The design, simulation and fabrication of microengineered silicon gyroscopes

Cooper, George

Cooper, George (1996) *The design, simulation and fabrication of microengineered silicon gyroscopes*, Durham theses, Durham University. Available at Durham E-Theses Online: http://etheses.dur.ac.uk/5297/

The Design, Simulation and Fabrication of Microengineered Silicon Gyroscopes

George Cooper BSc.
School of Engineering
University of Durham

A thesis submitted to the University of Durham
for the degree of Doctor of Philosophy
Summer 1996

Abstract

This thesis is concerned with the development of a low cost resonant gyroscope, or rate of turn sensor, which is capable of being mass produced.

The history and theory of the resonant gyroscope is reviewed, and then a survey of resonant gyroscope technology is presented.

Two novel designs of resonant gyroscopes are described. These designs are developed using the finite element analysis method. The fabrication procedure required to manufacture these devices is also developed and presented. The fabrication procedures are based upon silicon micromachining technology developed from the semiconductor industry. Prototype structures are fabricated. The first of these devices has been demonstrated to operate successfully as a gyroscopic rate of turn sensor.

A third design is also presented and developed using finite element analysis. This design demonstrates for the first time that it is possible to sense rates of turn about all three orthogonal axes independently, using just a single structure. A successful implementation of a structure of this type would eliminate the traditional requirement of one gyroscope per axis of rotation. The finite element simulations of the structure indicate that the design is suitable for mass production using silicon micromachining techniques.

Acknowledgements

Many people have helped in the completion of this thesis. A special thanks is owed to my supervisor Dr. Dave Wood for his support and contribution and especially for his patience in listening to some of the wilder ideas, also to our colleagues at the University of Newcastle; Jane Cruickshank and Dr. Alun Harris for their work on the testing of the structures and to Prof. Jim Burdess for both his ideas and robust discussion on gyroscope design.

In addition I would like to thank: John Gibson for his assistance in the fabrication of the structures, the staff of the engineering workshop who made a number of pieces of apparatus for the project, and the staff of the computing centre for their assistance in supporting the finite element package.

Closer to home a thanks to my parents, my sister and especially to my wife Ghadir, who has been very patient during the writing of this thesis.

Declaration

I declare that no material in this thesis has previously been submitted for a degree at this or any other university.

The research presented in this thesis is the result of a collaborative effort between the University of Durham and the University of Newcastle Upon Tyne. In particular the initial design of the gyroscope presented in chapter 4 is the work of Prof. J. Burdess of Newcastle and the testing of this device was performed by J.Cruickshank.

Contents

Chapter 1

Introduction

Chapter 2

Review of Resonant Gyroscope Technology

Chapter 3

The Bulk Machining & Material Properties of Single Crystal Silicon

Chapter 4

Membrane Gyroscope

Chapter 5

Bow-Tie Gyroscope

Chapter 6

Three Axis Gyroscope

Chapter 7

Conclusions and Suggestions for Future Work

Appendix A

Appendix b

Chapter 1

Introduction

In 1851 Jean Bernard Foucault suspended a 28 kg lead ball from a 67 metre long steel wire beneath the dome of the Pantheon in Paris, forming a huge pendulum[1]. Beneath the pendulum was arranged a circular railing, three metres in radius, on which was piled a ridge of sand. The sand was arranged so that a point protruding from the base of the pendulum would brush the sand with each swing. In this way the direction of the pendulum's swing could be recorded.

Foucault set the pendulum swinging and observed its motion. He found that the plane of motion of the pendulum appeared to rotate at a rate of about 11 degrees an hour in a clockwise direction, as viewed from above. In 32 hours the pendulum had undergone one full rotation. The figure of 32 hours corresponds to $24hours/Sin(48'51'')$ where 48'51" is the latitude of Paris[*].

Foucault recognised that he was not in fact observing the pendulum rotating, rather he was observing the earth rotating whilst the pendulum remained swinging in the same fixed direction. The difference between these two interpretations is subtle but important. Foucault's interpretation recognised that rotation rate has an absolute value and could be measured without reference to some external body. The ability to detect rate of turn without the need for an external reference can be considered as the definition of a gyroscope. Foucault's pendulum was not only the first resonant gyroscope but the first gyroscope of any type.

Scientifically the experiment was significant as it clearly put the earth spinning relative to the stars and not the other way round. On a practical level the pendulum also offered a method of measuring latitude, albeit a rather cumbersome one.

---

[*] The $24hours/Sin(48'51'')$ term comes from resolving the angular velocity vector of the earth along the direction in which the pendulum hangs. As the pendulum will always point to the centre of the earth, this angle is given by the latitude of the pendulum. If the pendulum were to swing at the north pole its direction of swing would rotate at a rate of one revolution per day, whilst at the equator no rotation would be observed.

A year later Foucault invented the more familiar spinning wheel gyroscope. This device was rather more practical than the pendulum and was soon developed into useful navigational instruments such as the gyrocompass and the familiar children's toy.

Foucault's pendulum remained a scientific curiosity, with little or no practical use, until the Sperry Gyroscope Company took up the idea again in the 1950's, almost exactly 100 years after the original experiments. The company set about constructing a practical version of the pendulum which could be used as a cheaper substitute for the rather complicated and expensive spinning wheel gyroscopes (see chapter 2).

The Sperry company succeeded in demonstrating that a practical resonant gyroscope could be made. However the Sperry gyroscope was a fairly complex design making the device expensive to produce. A number of other companies soon followed Sperry in attempting to develop resonant gyroscopes. Although these devices were to some extent technically successful, they did not find large enough markets to become commercially successful. At that time the big markets for gyroscopic sensors were in the military and aviation fields. These applications required high performance devices for flight control and inertial guidance systems. The resonant gyroscope failed to meet these stringent technical requirements making its price advantage largely irrelevant.

Over recent years there has been a resurgence of interest in the field of resonant gyroscope technology. This has largely come about as new applications for low cost small rate of turn sensors have been identified. As with the more conventional gyroscopes many of the applications are military[2]. Artillery round stabilisation and automatic weapons sighting systems both require methods of measuring rate of turn. The most significant potential market, however, is in the automotive industry.

As drivers become increasingly safety conscious car manufacturers have been encouraged to develop ever more advanced safety systems. Anti-lock braking and air bags which inflate to protect the passengers in the event of a crash are now commonly fitted as standard in new cars. Active suspension systems are now being developed as the next significant improvement in car safety. Some manufacturers have already introduced semi-active suspension systems on their top of the range models.

Conventional car suspension systems are essentially a spring and damper arrangement. The spring allows the wheel some freedom to move relative to the car body, isolating the body from much of the road roughness. The shock absorbers, or dampers, act to prevent the car from bouncing on its own suspension springs.

Choosing a suitable combination of spring and damper is difficult: make the system too stiff and handling will improve although the ride will become uncomfortable, whilst making the system too soft will lead to excessive body motion making the car difficult to control when braking hard or attempting to take rapid avoiding action. The ideal solution would be to have a suspension system which is able to tune itself to the given driving conditions, adjusting the strength of the dampers and springs as necessary. Such systems are known as 'Active' or 'Semi-Active' Suspension[3,4]. In the full active suspension system the springs and shock absorbers are both replaced or complimented with an hydraulic actuator. The actuator is able to move the position of the wheel relative to the chassis. In order to assess how to move the wheel's position measurements are made of the forces acting on each wheel and the motion of the car body. A computer control system then decides upon the optimum position for each wheel. This system requires advanced and expensive hydraulic components able to respond at high frequencies. The simpler semi-active suspension works in a similar way by measuring the motions of the car body, but in this case the control system adjusts a valve in each of the shock absorbers at each wheel. In this way the optimum damping force for a given situation may be set at each wheel. A simplified schematic of the semi-active suspension system is shown in figure 1.1. These systems have already been employed in Formula One racing cars.

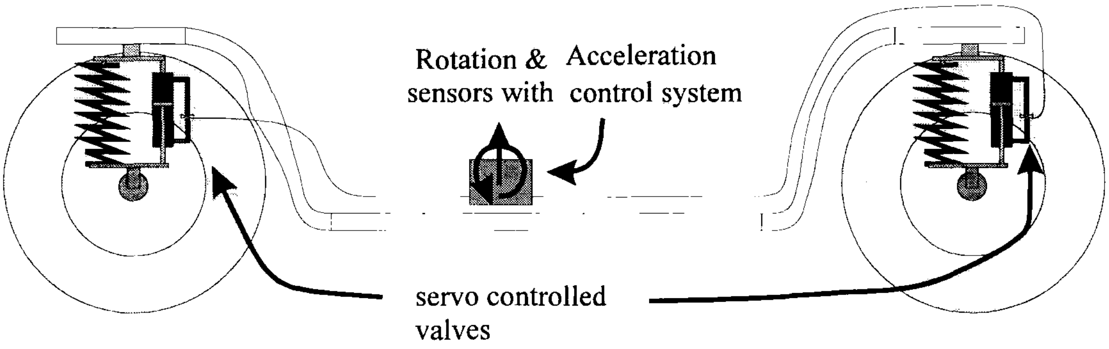

Fig 1.1 A simplified schematic of a semi-active suspension system.

The need to measure the motion of the wheels and the car body is common to both the active and semi-active systems. In order to adjust the parameters of a suspension system the system must first know what is happening to the car.

The car body has, like any solid body, six degrees of freedom: three translational and three rotational. Measuring the translational motions may be done using three accelerometers, one for each axis. The accelerometers needed for this application are already at a relatively advanced stage of development, largely as a result of being developed for use in air bag activation systems. The rotational motions are often referred to as the yaw, pitch and roll as shown in figure 1.2. These are essentially rates of turn and as such require a gyroscopic sensor.

Yaw, pitch and roll could be measured with an array of accelerometers distributed around the car body. However, this approach would require an array of nine accelerometers distributed around the vehicle's body. This approach is considered unattractive because of the amount of additional wiring that would be required[5].

With the large number of new cars manufactured each year, the automotive industry represents a very significant high volume market for gyroscopic sensors. The automotive sensor market is very demanding, requiring devices to be highly reliable, maintenance free and above all cheap.

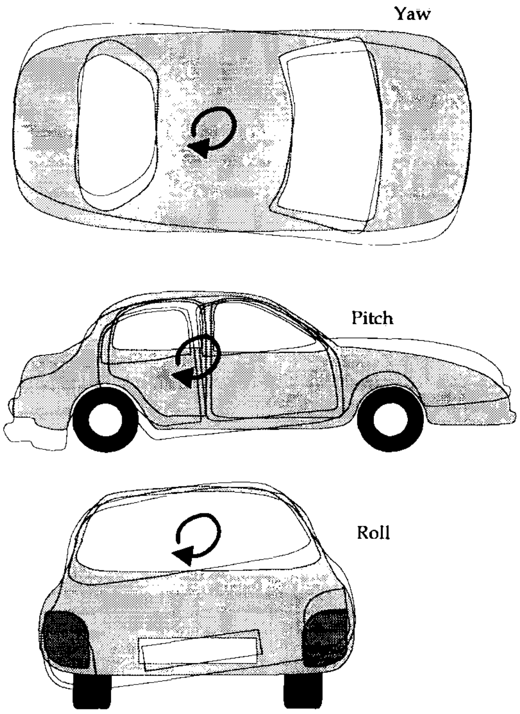

Fig 1.2 Showing the rotational degrees of freedom of a car.

Another area of application for low cost gyroscopes is the newly emerging field of virtual reality. Virtual reality simulators require a method of measuring the motion of the human body in order to simulate changes in the computer generated images. Advanced systems may well require a large number of sensors in order to measure rotations and accelerations at many differing locations of the body.

When looking for a system of mass producing such devices there can be few better examples than the semiconductor industry. By applying batch production technology, increased component integration and relentlessly shrinking device size the cost of electronic systems has continued to plummet whilst reliability has increased.

The success of these techniques has not gone unnoticed by the sensor industry. A number of manufacturers are now successfully using silicon chip technology to commercially manufacture pressure and acceleration sensors. For the sensor manufacturer using silicon processing has the additional attraction of offering the possibility of building the sensor and the electronics in the same process, all on one chip, thus eliminating assembly costs. The subject of this thesis is to apply the recently developed techniques of silicon micromachining to the manufacture of resonant gyroscopes of the type that may be suitable for automotive and other mass market applications.

It is perhaps worth saying something about the techniques employed in this thesis. Silicon micromachining can broadly be split into two areas, surface machining and bulk machining. Surface machining attempts to stick as closely as possible to conventional semiconductor processing, forming any mechanical components from thin deposited films of only a few µm thick. Bulk machining uses the full thickness of the silicon wafer to fabricate the mechanical elements.

Surface machining offers a greater compatibility with conventional silicon processing methods than does bulk machining. From a commercial stand point this is appealing as existing semiconductor factories should be able to manufacture the devices easily, without the need for a large amount of additional investment. Bulk machining on the other hand makes use of the remarkable mechanical properties of the single crystal silicon wafer (see chapter 3), but at the expense of requiring more 'custom' processing. At present both technologies are being developed actively and it is a subject of some debate which if any will eventually emerge as the clear winner.

The nature of a resonant gyroscope places some very demanding constraints on the types of material from which it is made. In the first instance the material must be able to undergo prolonged resonant vibrations without fatigue or ageing. The material must have extremely low internal damping as the Q factor of the resonances are all important to the device performance. The material properties must be controllable, to allow the resonant modes to be reliably matched without cross coupling (see chapter

2). Single crystal (bulk) silicon fulfils all of these criteria easily, whilst surface deposited layers,
such as polysilicon, still have significant problems in almost all areas. For these reasons bulk machining techniques were adopted for the work in this thesis[†].

1.1 Thesis Outline

The research presented in this thesis is concerned principally with developing resonant gyroscope designs suitable for mass production using the techniques of silicon micromachining and also with developing and demonstrating the necessary manufacturing techniques to make these designs. This research has however been carried out as part of a larger project to make a complete rate of turn measuring system. The mechanical structure of the gyroscope is just one half of the total system, the other half being the electronic systems needed to read the signals from the gyroscope and to correctly interpret these signals in terms of a rate of turn reading. Work on the electronics of the gyroscope has largely been carried out by colleagues at the University of Newcastle. The thesis would be incomplete without some explanation of the test and measurement systems used to evaluate the structures described here; this has been included and acknowledged where appropriate.

Naturally one of the first tasks of the research was to establish the current state of resonant gyroscope technology. To this end a literature review on gyroscope technology was carried out. The results of this search are presented in chapter 2. The necessary mathematical theory is also presented in this chapter.

Chapter 3 describes the techniques of micromachining which have been employed in the fabrication of the devices presented. A review of the properties of single crystal silicon as they relate to bulk micromachining is also given. Particularly, the arrangement of crystal planes and the elastic and piezoresistive properties of silicon are discussed in detail.

[†] Crystalline quartz has also been used to manufacture miniature resonant tuning fork structures. Although quartz has the advantage of being a piezoelectric material it was felt that the more developed fabrication techniques of the silicon industry coupled with the ability to fabricate integrated electronic circuits would ultimately make silicon a more suitable material for the fabrication of a resonant gyroscope.

In all, three novel gyroscope designs are presented in this thesis, the work carried out on each has been presented as a separate chapter (chapters 4,5 and 6). These chapters are presented in the order in which the research was carried out.

In chapter 4 a gyroscope fabricated from bulk {100} silicon is presented. Of the three designs this one has been under development for the longest time and is as a result at the most advanced stage of evaluation. Chapter 5 contains the design, computer simulation and fabrication of a second design, fabricated from {110} silicon. While the fabrication of this device has been demonstrated only a very limited amount of testing of the structure has been carried out. Chapter 6 contains the third design. This design is significant because it is theoretically capable of measuring rates of turn about all three orthogonal axes. This is believed to be the the first design of gyroscope, resonant or otherwise, with the ability to detect three orthogonal rates of turn. All previous designs of gyroscope have been limited to measuring a rate of turn about only one or two axes. Chapter 6 presents the design and the results of the computer modelling of the device. At the time of writing the fabrication techniques required to make this three axes device were still under development at Durham. For this reason the device could not be fabricated, however, an outline of one possible fabrication process has been included for completeness.

Within each of these chapters the work has, as far as possible, been presented in a manner that is easiest to follow for the reader, namely; design description, computer simulation, manufacturing and testing. In reality however the progress of the research was not quite such a clear cut progression. Inevitably as an understanding of the requirements of a resonant gyroscope was developed the design ideas were modified. Similarly as possibilities and limitations within the manufacturing processes became more obvious the designs also had to be modified.

It would have been satisfying to have been able to conclude the thesis saying that the research was complete, but this is not in the nature of research. There remains a great deal of work to be done before any of the designs reach commercial production. In chapter 7 the work is summarised and suggestions for future work are made.

1.2 References

---

[1] C. Kittel, W.Knight, M. Ruderman Mechanics Berkeley physics course volume 1 McGraw Hill

[2] J.T.Anders, R.Pearson Applications of the START VibratoryGyroscope GEC review Vo. 9 No. 3 (1994) pp 168-175

[3] K. Yi, K. Hendrick Dynamic Tire Force Control by Semiactive Suspensions Journal of Dynamic Systems, Measurement, and Control , 115 (1993) pp 465-474

[4] D. Horvat Applications of Optimal Control to Advanced Automotive Suspension Design Journal of Dynamic Systems, Measurement, and Control , 115 (1993) pp 328-342

[5] P.E.M. Frere Problems of Using Accelerometers to Measure Angular Rate in Automobiles Sensors and Actuators A, 25-27 (1991) pp. 821-824

Chapter 2

Review of Resonant Gyroscope Technology

2.1 Introduction

This chapter contains a review of gyroscope technology. Flywheel and optical gyroscopes are described in sections 2.2 and 2.3, these sections have been included both for completeness and to serve as a comparison with the resonant gyroscope sections. Section 2.4 covers the theory that is necessary to the understanding of resonant gyroscopes. Section 2.5 describes some of the many gyroscope designs that have been manufactured or patented.

2.2 Rotating Wheel Gyroscopes

Rotating wheel gyroscopes have been subject to a great deal of development, and as a result many design variations exist[1]. The most common is the gimballed gyroscope, as shown in figure 2.1. A heavy wheel is made to spin rapidly by an electric motor (not shown): this gives the wheel a large amount of angular momentum. The spinning wheel is then mounted inside a series of gimbals. This arrangement allows the base of the gyroscope to be rotated independently of the axis of rotation of the wheel. The effect of the gimbals is to isolate the wheel from any externally applied torques. Having isolated the spinning wheel from external torques, the wheel will remain oriented in the same direction in space even when the body to which it is attached is rotating. Used in this way the gyroscope can act as an attitude or direction reference, forming part of an inertial guidance system.

An alternative rotating wheel design is known as the 'strap down' gyroscope. In this design the gimbals are replaced with a solid but flexible support structure on which several strain gauges are mounted. As the gyroscope is turned the Coriolis forces are generated, these forces induce strains in the support structure. These strains are sensed by the strain gauges. The magnitude of these strains are then a measure of the rate of turn of the gyroscope. In this mode the gyroscope is referred to as a rate of turn, or rate, gyroscope. The output of the rate sensing gyroscope is the first time derivative of that of the attitude reference gyroscope. It is therefore possible to recover the attitude reference by integrating the signal of the rate gyroscope over time. Or in simpler terms, the attitude reference gyroscope measures the deviation from a fixed direction, while the strap down gyroscope measures the rate of change of direction.

Rotating wheel gyroscopes dominate the high cost, high performance market. Ultra high precision instruments are able to measure rotation rate with an uncertainty of less than 2×10^{-4} degree/hour. Typical applications for these devices include; precision azimuth alignment, ballistic missile guidance and inertial navigation. These ultra high performance devices can cost well in excess of £100,000. Unfortunately the rotating wheel gyroscope requires a high number of precision moving parts, making the device both expensive to build and to maintain. As a result these devices are unsuitable for applications requiring a low cost rotation sensor.

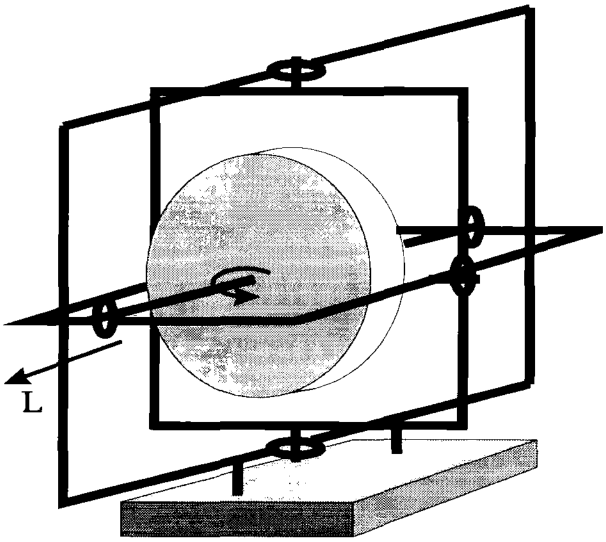

Figure 2.1 A simplified schematic of a fully gimballed gyroscope. The drive motor has been omitted.

2.3 Optical Gyroscopes

Optical gyroscopes work on an entirely different principle to the spinning wheel designs[2,3]. Instead of using the conservation of angular momentum to sense rotation they use the invariance of the speed of light: Imagine two photons travelling in opposite directions around a stationary circular closed loop. Both photons are travelling at the same speed and will take the same time to transverse the loop. If, however, the loop is made to rotate then the end of the loop moves nearer to one photon as it is travelling and further away from the other. The two photons see a different effective path length. This is known as the Sagnac effect, and can be used in various ways to measure rate of turn. Figure 2.2 shows a simplified schematic of a fibre optic gyroscope[1]. Light from a single source is initially split into two coherent components. The two separate beams are then fed into opposite ends of the same optical loop, in this case a coil of optic fibre. Using a coil increases the effective path length, increasing the time the light takes to traverse the coil and thus magnifying the overall signal. As the two beams re-emerge from the fibres they are recombined to form an interference pattern. This interference pattern allows the relative phase shift between the two beams to be measured, which in turn is a measure of the rotation of the loop while the light was passing through it. This signal may then be converted into a rate of turn.

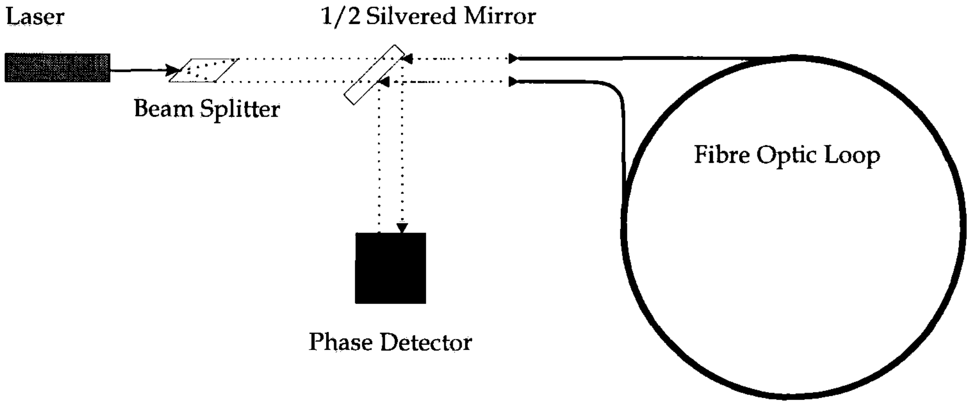

Figure 2.2 A typical fibre optic gyroscope.

---

[1] Another form of optical gyroscope is the 'Ring Laser Gyroscope'. This gyroscope also worked by passing light in opposite directions around an enclosed loop (the loop being defined by mirrors rather than a fibre optic). As with the FOG the sensitivity of the RLG is dependent upon the enclosed area of this loop, making successful miniaturisation extremely difficult.

Optical gyroscopes have received a great deal of development work. As a result some of the better designs are now considered to be inertial grade devices.

The optical gyroscope has the significant advantage of eliminating moving parts. Although this improves reliability and makes the device more rugged the high cost of the optical components and the device's relatively large size preclude its use in low cost applications.

2.4 Resonant Gyroscope Theory

All resonant gyroscopes work by sensing the Coriolis force. The Coriolis forces experienced by a rotating body are directly related to the angular velocity of that body and may therefore be used as a measure of angular velocity. An appreciation of the nature of the Coriolis force is essential to the understanding of resonant gyroscope design.

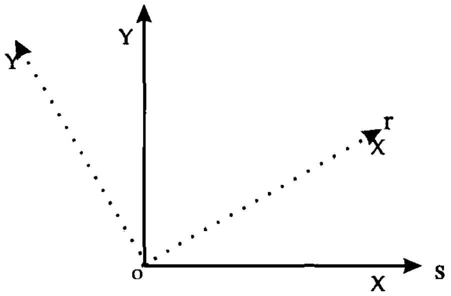

Figure 2.3 **Rotating and inertial frames**

Consider two reference frames, *s* and *r* with coincident origins. Frame *r* is rotating with an angular velocity Ω relative to the inertial frame *s*. A particle at position $\mathbf{r}$ has a velocity $\mathbf{V_r}$ measured in the rotating frame. The same velocity expressed in the inertial frame is given by[4]:

$$\mathbf{V_s} = \mathbf{V_r} + \Omega \times \mathbf{r} \qquad 2.1$$

It can be shown that the relationship between the rate of change of an arbitrary vector as measured in either frame is given by the following operator equation[4]:

$$\left(\frac{d}{dt}\right)_s = \left(\frac{d}{dt}\right)_r + \Omega \times \qquad 2.2$$

Applying operator 2.2 to equation 2.1 gives an expression for the acceleration of the particle in the inertial frame:

$$\left(\frac{d\mathbf{V}_s}{dt}\right)_s = \left(\frac{d\mathbf{V}_s}{dt}\right)_r + \boldsymbol{\Omega} \times \mathbf{V}_s \qquad 2.3$$

Equation 2.3 may be substituted into **F=ma**, giving the force acting on a particle in the inertial frame, $\mathbf{F_S}$.

$$\mathbf{F}_s = m(\left(\frac{d\mathbf{V}_s}{dt}\right)_r + \Omega \times \mathbf{V}_s) \qquad 2.4$$

Now substituting equation 2.1 into equation 2.4 and re-arranging, gives:

$$\mathbf{F}_s = m\left(\frac{d}{dt}(\mathbf{V}_r + \Omega \times \mathbf{r})\right)_r + m\Omega \times (\mathbf{V}_r + \Omega \times \mathbf{r})$$

$$\mathbf{F}_s = m\left(\frac{d\mathbf{V}_r}{dt}\right)_r + m\left(\frac{d}{dt}(\Omega \times \mathbf{r})\right)_r + m\Omega \times (\mathbf{V}_r + \Omega \times \mathbf{r})$$

$$\mathbf{F}_s = m\mathbf{a}_r + m\Omega \times \mathbf{V}_r + m\Omega \times \mathbf{V}_r + m\Omega \times (\Omega \times \mathbf{r})$$

$$\mathbf{F}_s = m\mathbf{a}_r + 2m\Omega \times \mathbf{V}_r + m\Omega \times (\Omega \times \mathbf{r})$$

$$\mathbf{F}_s = \mathbf{F}_r + 2m\Omega \times \mathbf{V}_r + m\Omega \times (\Omega \times \mathbf{r}) \qquad 2.5$$

Equation 2.5 relates the forces experienced by the particle as observed from the rotating and inertial frames. Re-arranging equation 2.5 in terms of the force in the rotating frame:

$$\mathbf{F}_r = \mathbf{F}_s - 2m\Omega \times \mathbf{V}_r + m\Omega \times (\Omega \times \mathbf{r}) \qquad 2.6$$

Equation 2.6 describes the effective forces felt on a body as measured in a rotating frame. The first term on the right hand side is the conventional force due to any acceleration of the particle, and the last term on the right hand side is the familiar centrifugal force. Note that the double cross product in this term means that the force is always acting normal to the rate of turn and pointing outwards. At first sight this force would appear to offer a method of measuring angular velocity. In practice, however, the presence of **r** in the term leads to some problems. In order to solve for **Ω** , the position of the sensor relative to the centre of rotation, must be known. In other words, the readings of a rotation sensor measuring centrifugal force would vary with the position of the sensor. This makes the centrifugal force unsuitable for the measurement to rotation in most situations. In addition the centrifugal force is proportional to Ω^2 and thus cannot distinguish between rotations in opposite directions. However, some speed governors on rotating machinery use the centrifugal force to sense and limit the rotation rate of spinning shafts.It is the second term in equation 2.6 that is of interest in the design of gyroscopic sensors. This term represents the Coriolis force.

$$\mathbf{F}_{Coriolis} = 2m\Omega \times \mathbf{V}_r \qquad 2.7$$

Clearly the Coriolis force, unlike the centrifugal force, is only manifest when a body is in motion relative to the rotating frame: that is $\mathbf{V_r}$ must be finite, hence the need for a moving or resonant device. As a consequence of the cross product in equation 2.7 the magnitude of the force is a maximum when the direction of this velocity is at right angles to the angular velocity vector Ω: in other words, when the velocity is in a radial direction to the centre of rotation. Also as a consequence of the cross product, the Coriolis force acts in a direction at right angles to both the velocity vector $\mathbf{V_r}$ and to the angular velocity vector Ω.

The action of the Coriolis force is well demonstrated by the following example: Consider a particle of mass *m* which is in orbit about an origin *O*, with an angular velocity **Ω,** at a distance **r**, from the origin. The particle will describe a circular path as observed from a non-rotating frame. Obviously in a frame having the same angular velocity as the particle, the particle will appear stationary, hence $\mathbf{V_r}$ is zero and no Coriolis force is observed. This situation is shown in figure 2.4.

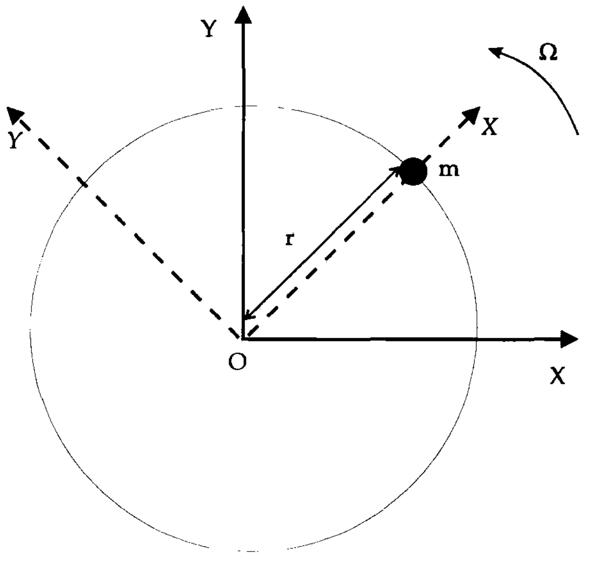

Figure 2.4 **A particle of mass m moving in a circular orbit.**

Now assume that the particle is not remaining stationary in the rotating frame, instead it is moving with a small sinusoidal vibration in a radial direction. For convenience the particle is assumed to lie on the x axis in the rotating frame and the vibration of the particle is assumed to be parallel to the x axis. The position of the particle in the rotating frame may then be expressed as :

$$\mathbf{R} = \mathbf{i}_x (r + a\sin(\omega t)) \qquad 2.8$$

where $\mathbf{i}_X$ is the unit vector in the x direction, a is the amplitude of the vibration and ω is the frequency of the vibration. The trajectory of the particle as observed from the inertial frame is shown in figure 2.5.

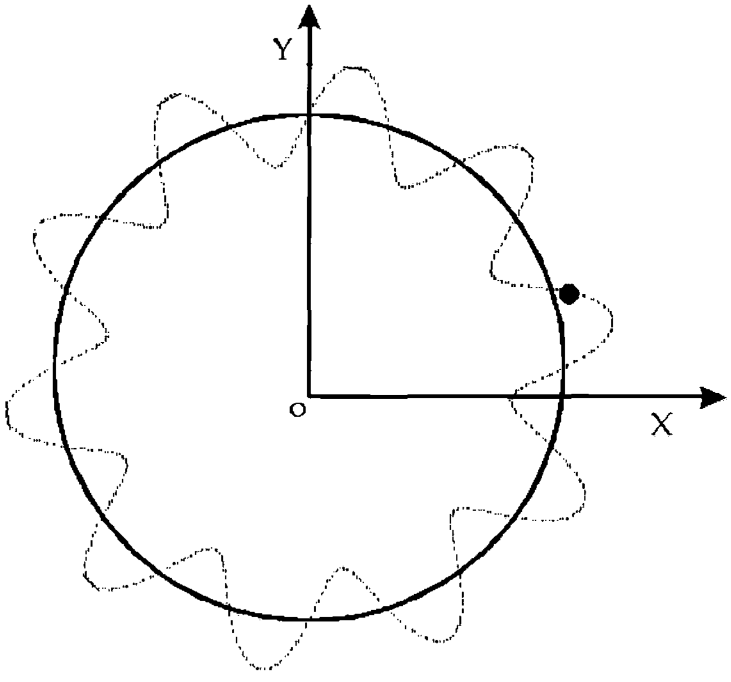

Figure 2.5 The trajectory of a vibrating and rotating particle as observed from a stationary frame.

Taking the time derivative of equation 2.8 and substituting it into equation 2.7 gives the Coriolis force acting on the particle:

$$\begin{aligned} \mathbf{F}_{Coriolis} &= 2m\Omega \times \mathbf{i}_x \frac{d}{dt}(r + a\sin(\omega t)) \\ \mathbf{i}_y F_{Coriolis} &= \mathbf{i}_y 2m\Omega\omega a\cos(\omega t) \end{aligned} \qquad 2.9$$

Note that the Coriolis force is acting in the **Y** direction, perpendicular to the velocity.

Equation 2.9 summarises many of the key issues which must be considered in the design of a resonant gyroscope. In order to maximise the sensitivity of the device it is necessary to maximise the amplitude of the Coriolis force being generated in the structure. This means maximising each of the terms on the right hand side of equation 2.9. This will occur when the structure is excited at its resonant frequency, where by definition the amplitude of vibration will be a maximum. This resonant vibration is conventionally known as the primary motion, or primary mode.

Also, equation 2.9 shows that Coriolis forces generated by a resonant structure are not constant, they are modulated by the $Cos(\omega t)$ term. The most efficient method of detecting this type of force is to allow it to excite an additional resonant mode in the structure, and then measure the amplitude of this secondary resonance. As the frequency of the Coriolis force is exactly the same as that of the primary motion it follows that the primary and secondary modes should have the same resonant frequency for maximum sensitivity. Achieving a design which allows these two resonances to be matched is essential to achieving a gyroscope with reasonable sensitivity.

It is, however, insufficient to simply produce a structure with matched resonant modes. Care must also be taken to ensure that these two modes are coupled only by the Coriolis force, and not by the structure itself or the electrical drive system. That is, it must be possible to excite one mode independently of the other. Any cross coupling of modes will lead to the secondary motion being excited even in the absence of a Coriolis force. This will then show up as a false measure of rate of turn, severely affecting the function of the sensor.

Resonant gyroscopes do not measure the Coriolis force directly: instead they measure the amplitude of the secondary resonance that it excites. This is an important distinction since the amplitude of the secondary motion is proportional to both the quality factor, Q_S, of the resonance and the amplitude of the driving force. What's more the magnitude of the Coriolis force is proportional to the amplitude of the primary mode.

Similarly the primary amplitude is governed both by the excitation force and by the Q_P of the primary mode. As a result the final signal of a resonant gyroscope is proportional to the product of Q_S and Q_P . Maximising the Q factors of these resonances has been the subject of a great deal of research. Generally a high Q requires that the material from which the gyroscope is manufactured has a very low damping factor and that the resonant structure be supported in a way that avoids dissipation of energy to the support structure. This is best achieved by supporting the structure at a node point of the vibration or, failing that, ensuring that the support structure is very rigid as it is the flexing in the support that allows energy to dissipate. Operating the device in a vacuum eliminates air damping, further increasing the Q. Finally, in order to fully solve equation 2.9 in terms of Ω, it is necessary to know the amplitude and frequency of the primary resonance. As a result it is necessary to measure the primary motion amplitude as well as the secondary mode.

2.5 Examples of Resonant Gyroscopes

The following section contains a summary of all significant novel devices which have been described in published work. Their method of operation is discussed and their applicability to silicon micromachining is discussed. Where possible details of their performance figures are also included.

2.5.1 A Resonant Cantilever Gyroscope

Next to the original Foucault's pendulum, is the simplest type of resonant gyroscope is the cantilever structure[5] of figure 2.6. The cantilever is made to resonate in its first flexural mode of vibration, this is the primary mode. If a rate of turn is then applied about the long axis of the cantilever, a Coriolis force will be generated. This Coriolis force will act at right angles to the primary motion and will therefore cause the beam to begin resonating at right angles to the primary motion. In order to match the resonant frequencies of the primary and secondary modes the beam should have a perfectly square cross section.

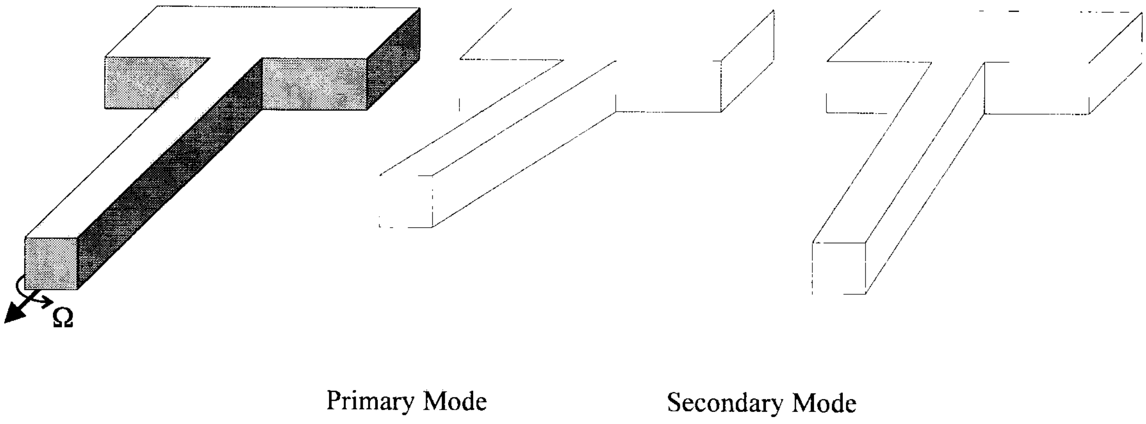

Figure 2.6 A vibrating cantilever gyroscope.

This type of vibrating cantilever design was described in a very interesting paper by Pringle[6] in 1948. The paper describes how the common house fly uses a resonant beam on either side of its' head to act as a gyroscopic sensor helping it maintain a controlled flight. This no doubt makes the cantilever design of gyroscope the most widely used miniature gyroscope!

More recently a simple cantilever gyroscope has been fabricated from {110} oriented silicon[7]. This device is significant as it is the only published gyroscope fabricated in {110} silicon apart from the design presented in this thesis. The basic structure is a cantilever wet etched from bulk silicon (see chapters 3 and 7). The primary mode is excited by mounting the whole structure on a piezoelectric disc, driving the beam to resonate out of the plane. The primary motion is sensed by a capacitor plate under the beam. The secondary motion is perpendicular to the primary mode and is therefore in the plane. The amplitude of the secondary motion motion is sensed with an additional pair of capacitor plates either side of the beam.

On first sight this design appears ideally suited to {110} silicon where beams of square cross section are easy to manufacture. Unfortunately, however, the wet etching process and the arrangement of the crystal planes cause a significant asymmetry in the support structure of this type of cantilever. As a result the beam is not symmetric about its long axis: this causes a mismatch in the two resonant frequencies, and importantly means that the two modes are not perfectly in and out of the plane of the wafer. The dynamics of this structure are discussed more fully in chapter 5. In addition the manufacture process of this device is relatively complex, requiring a three layer structure of PZT, Pyrex and silicon.

2.5.2 Resonant Beam Gyroscope (Square Cross Section)

This design operates in much the same manner as the cantilever design. The principle difference being that the beam is free at both ends and the support is arranged to coincide with the location of the node points of the resonance (figure 2.7). This design was produced in the late sixties by General Electric as a commercial device[8]. The beam was made from a single piece of solid metal (nickel chromium titanium alloy). Two models were made each having a length of 1.6 and 2.5 inches respectively, with a cross section of 0.15 inches square. The resonant frequencies of these devices were 10 and 4.5 kHz respectively. The node points were supported on pins through two opposite faces. The primary motion was driven by a piezoelectric plate fixed to the centre of one face and detected by a similar plate on the opposite face. The secondary mode was sensed and nulled by two piezoelectric plates attached to the orthogonal faces of the beam.

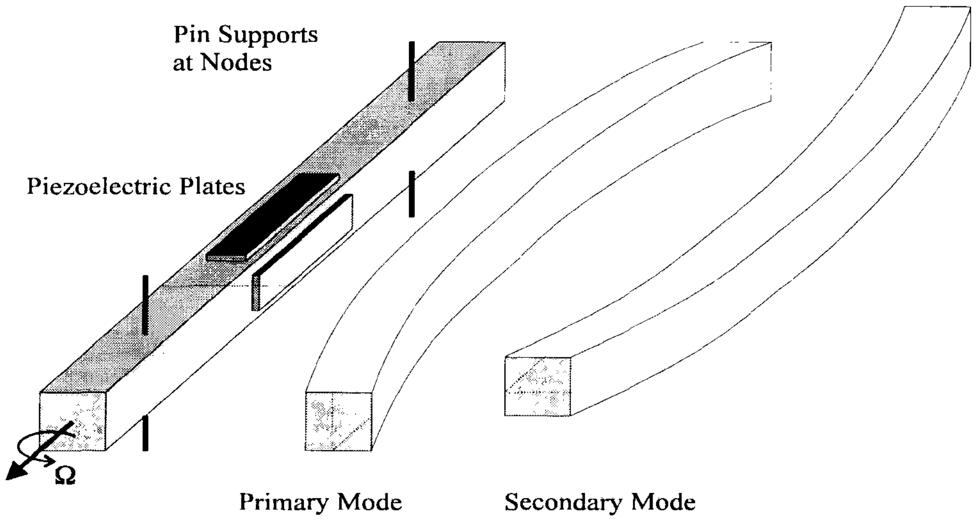

Figure 2.7 A Vibrating Beam Gyroscope (Square Cross Section)

Achieving the matched primary and secondary resonant frequencies requires that the beams are very precisely square in cross section. Additionally, the positioning of the piezoelectric plates and support structure are very important, any misalignment to the centre of the beam will tend to couple the primary and secondary modes.

Murata is currently marketing a very similar device[9]. The principle difference between the Murata and the General electric designs is that in the former the vibrating beam has a cross section which is an equilateral triangle (see figure 2.8). It is important to note that a beam with an equilateral triangle cross section will, like the square beam, have two orthogonal flexural resonant modes with the same frequency.

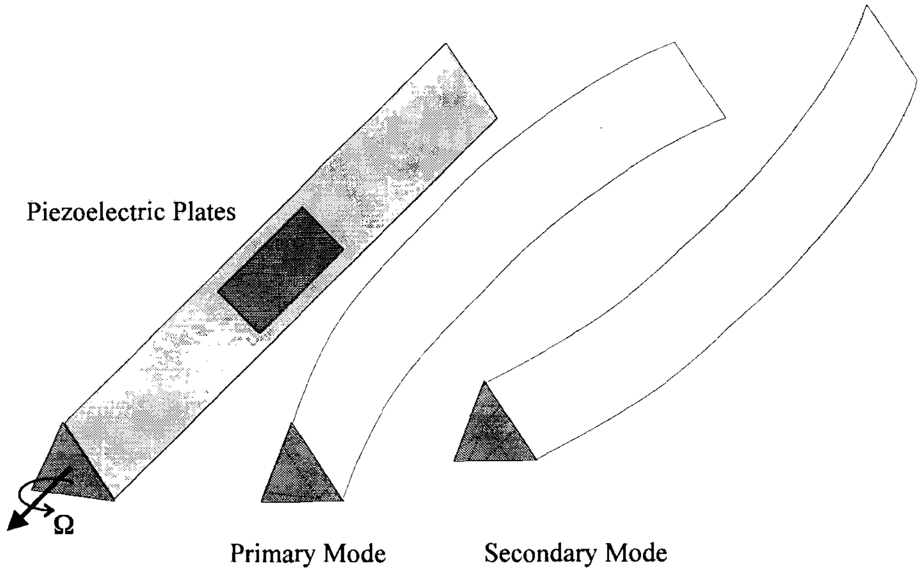

Figure 2.8 A Vibrating Beam Gyroscope (Triangular Cross Section).

This design is one of the few resonant devices which is currently commercially available, and its specification is shown in table 2.1

Maximum angular velocity (deg/sec)	±90
Scale factor(mV/Deg/sec)	22.2
Linearity (% full scale)	0.5
Response (Hz)	7

Table. 2.1 Performance data for the Gyrostar gyroscope.

Yet another device on the same theme has been published by the Tokin corporation[10]. This device uses a beam of circular cross section as the vibrating element. Drive and sense is achieved via six piezoelectric plates positioned around the outer surface of the beam.

2.5.3 Resonant Tuning Fork Gyroscope

The tuning fork gyroscope is essentially a pair of cantilever gyroscopes (figure 2.9). Each beam is made to vibrate as a cantilever at its fundamental frequency. The drive system is set up so that the beams vibrate at the same frequency, but 180° out of phase. In practice this means that the beams move towards and away from each other. Any rate of turn about the central stem of the tuning fork then causes equal, but opposite, Coriolis forces to be generated on each of the beams. These Coriolis forces form a torque about the axis of rotation. This torque is then a measure of the rate of turn.

2.5.3.1 Tuning Forks With Rectangular Sectioned Beams

One of the key design features in tuning fork gyroscopes is the cross section of the resonating tines. If the beams of the tuning fork have rectangular cross sections (figure 2.9), then clearly they will be much stiffer in one direction than the other. Invariably tuning fork gyroscopes with rectangular cross sectioned beams are configured so that the beams are able to flex most easily towards and away from each other: this is the primary mode. The Coriolis force is then generated at right angles to this motion. However, since the beams are stiffer in this direction, they tend not to flex under the effect of this force: instead they transmit the torque to the base of the tuning fork. The effect of this is to cause the entire tuning fork to resonate in torsion about the axis of rotation. One of the principle difficulties in manufacturing this type of sensor is to ensure that the two resonances have matched frequencies. This is done by adjusting the length and thickness of the support structure.

The first attempt to make a practical resonant gyroscopic sensor is credited to the Sperry Gyroscope Company[11] in 1953. The Sperry gyroscope was a tuning fork design with rectangular cross section beams. The fork itself was manufactured from a ferrous metal allowing the primary drive to be achieved by electromagnets positioned either side of the resonant beams. The primary amplitude is then sensed via a second set of coils on the inside of the fork. The torsional resonance is sensed by another set of coils either side of the beam protruding from the stem of the fork.

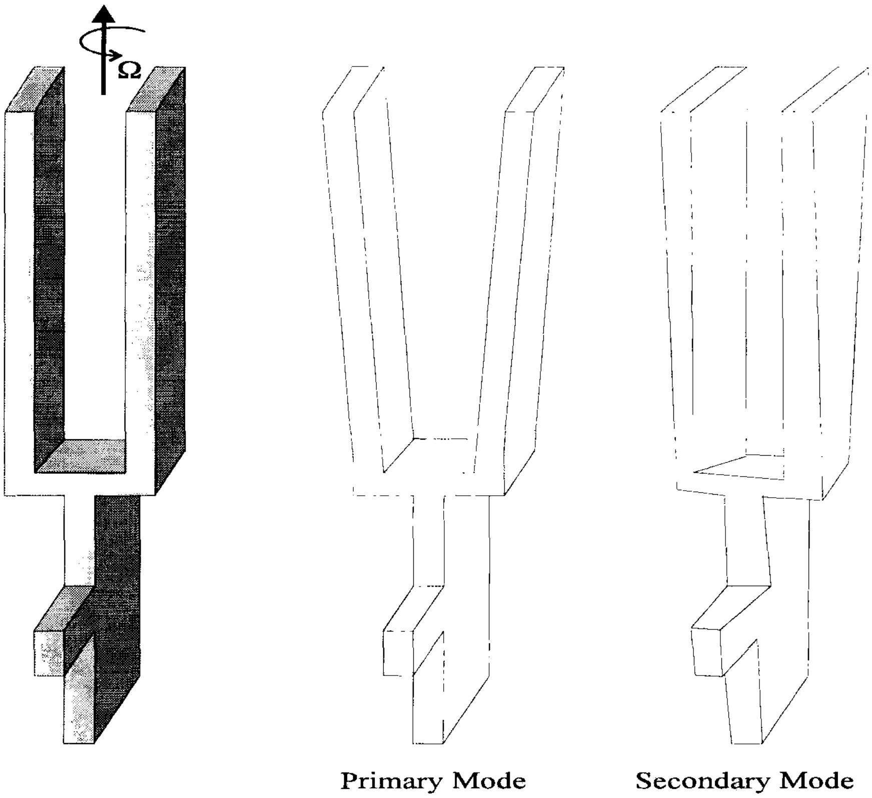

Figure 2.9 A tuning fork gyroscope with tines of rectangular cross section (Sperry type gyroscope).

2.5.3.2 Tuning Forks With Square Sectioned Beams

In this class of device the primary motion is exactly the same as for the previous device. The secondary motion, however, is somewhat different, (figure 2.10). The square cross section of the beams ensures that the resonant frequencies are the same in the direction of both the primary motion and in the direction of the Coriolis force.

The basic tuning fork arrangement is attractive for a number of reasons. Firstly, as the beams are vibrating in anti-phase they will generate signals which are similarly in anti-phase: by taking the difference between these two signals twice the output signal amplitude is achieved, and simultaneously many sources of error are eliminated. Also, as the design is symmetric and the beams resonate in anti-phase, there is a natural node point along the centre line of the fork where there is zero displacement on the primary resonance. By fixing the mounting structure to this point it is possible to minimise the energy dissipated in the support structure. This results in an increase in the Q of the primary resonance and a corresponding improvement in the performance of the device, as discussed in section 2.1.

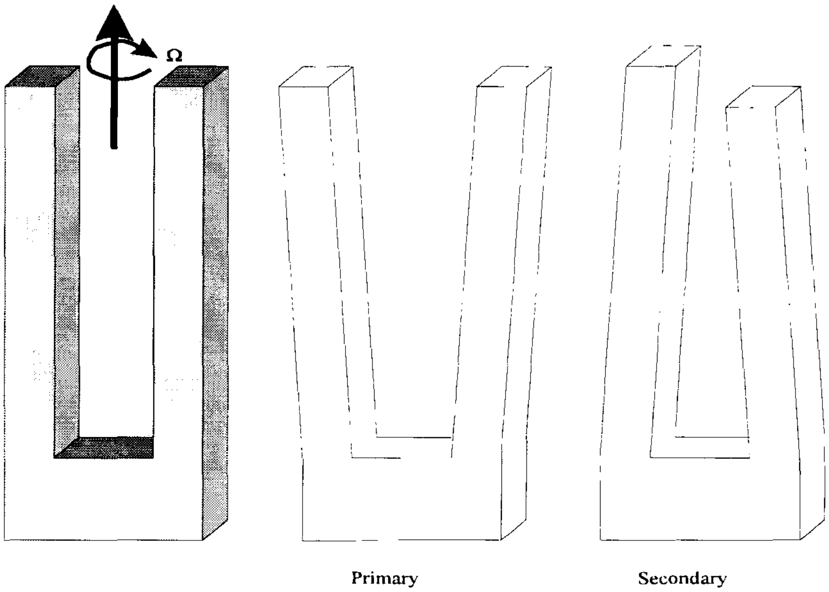

Figure 2.10 A tuning fork gyroscope with tines of square cross section.

2.5.3.3 Tuning Forks With Beams of Varying Section

An interesting variant on the tuning fork design is currently being marketed by Watson Industries[12,13]. It is worth discussing as it shares an important feature with one of the devices presented in this thesis. In the Watson design the beams are composed of two rectangular sections joined end to end with their principle axis of flexure being rotated by 90 degrees relative to each other (figure 2.11).

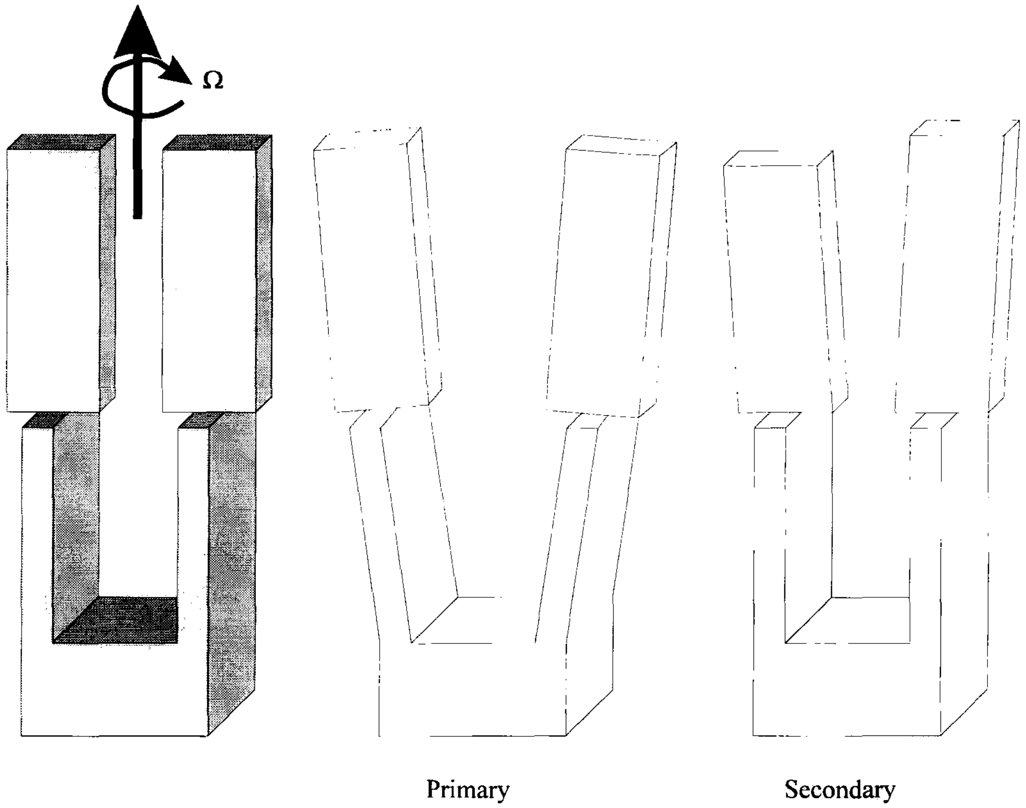

Figure 2.11 A tuning fork gyroscope with tines of variable cross cection.

The primary motion is achieved by causing the base section of the beam to flex. The top section of each beam does not flex in the primary mode as it is stiff in this direction. Application of a rate of turn generates the Coriolis force which is sensed by this same upper sections of the beams. These upper sections of the beams may be thought of as accelerometers, sensitive to force only in a direction perpendicular to the direction of the primary motion. This design allows the use of standard piezoelectric plates for the beams.

The design presented in chapter 5 shares some features with this structure: in both cases the secondary motion is sensed via a pair of 'accelerometers' whose shape allows them to flex only in the direction of the Coriolis force.

Range (4 options) deg/sec	±30,±100,±300,±1000
Output V	±10
Output Impedance W	1K
Bandwidth Hz	50
Noise mV rms	< 15
Temp range °C	-20 + 50
Temp Drift	< 10% FSD
Drift (constant temp)	<2% FSD
Scale Factor Error	<2%
Shock Survival g	200
Linearity	> 0.1% FSD

Table 2.2 performance figure of the Watson gyroscope.

2.5.4 Double tuning fork Gyroscopes

The basic tuning fork arrangement creates a node of zero displacement for the primary mode but not the secondary mode. Achieving a structure with a node point for the secondary resonance is achieved by mounting two tuning forks mounted on the same base, pointing in opposite directions . Each tuning fork is made to resonate in the normal way as described, but with a 180° phase shift between each of the forks. The effect of this arrangement is to create a node point at the centre of the device where the secondary torques created by the Coriolis force also cancel .

Range deg/sec	±10 to±1000
Output V	±2.5 FSD
Bandwidth Hz	60
Scale factor calibration	<1% of reading
S.F. temp coefficient	<0.003%/deg
Resolution threshold	<0.002 deg/sec
Operating Life	< 10 years
Shock survival	100g

Table 2.3 Systron Donner Gyroscope performance figures.

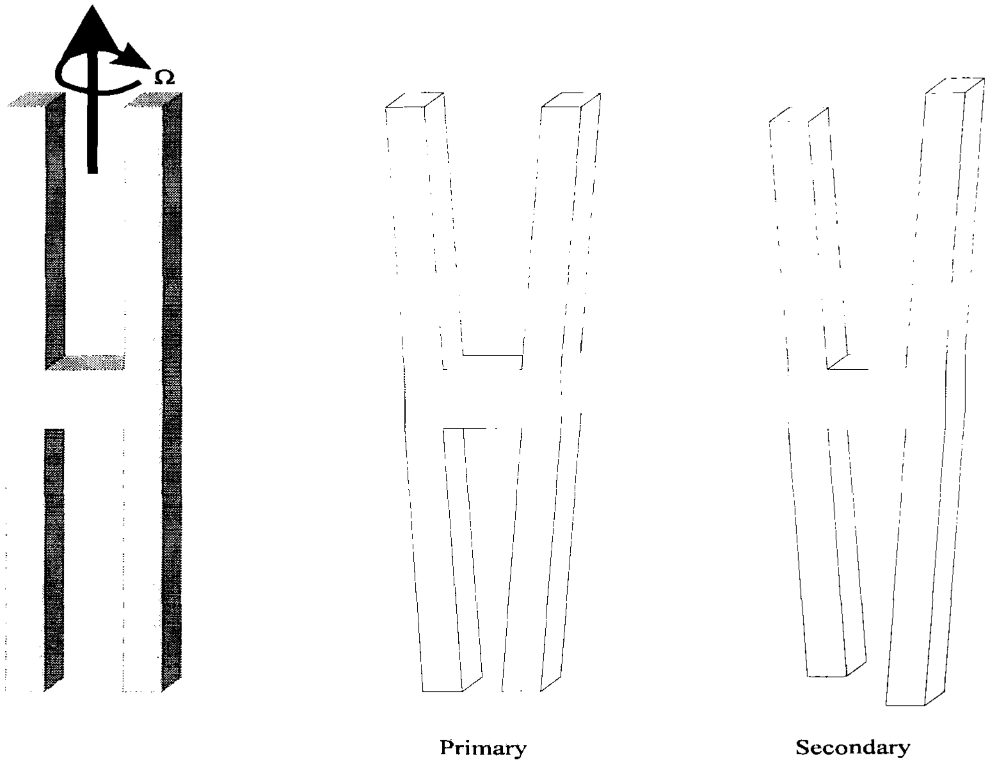

Figure 2.12 A Double Tuning Fork Gyroscope

The Systron Donner corporation are currently marketing a double tuning fork device made from quartz crystal[14] . Quartz has the useful properties of being both a high Q material and also a piezoelectric.

2.5.5 A Surface Micro Machined Tuning Fork Gyroscope

The Charles Stark Draper labs and Murata have independently carried out research into manufacturing a gyroscope on the surface of a silicon wafer[15]. Figure 2.13 shows a simplified drawing of this type of device. The central mass is excited into resonance across the surface of the silicon wafer by an electrostatic force applied via the comb drive arrangement. A rate of turn then causes the mass to move up and down away from the surface of the wafer. The secondary motion is sensed via capacitor plates beneath the structure.

It is critiacal to obtain the correct material properties right for this type of device. Any strain in the material of the structure will cause it to buckle[2], severely affecting its

---

[2] Surface machined devices are typically fabricated from 'Chemical Vapour' deposited films. These films often have large pre-stresses built into them during the deposition process.

mechanical performance. Even slight buckling could cause the two modes to be coupled, or worse cause the device to stick to the wafer surface. In addition the material must have a low damping factor and must be able to withstand resonant vibration for long periods. These qualities are not as yet well tested in thin film deposited layers such as polysilicon or electroformed metals.

These type of devices are attractive from the commercial point of view as they offer the possibility of CMOS integration and the basic manufacture technique is similar to some designs of surface machined accelerometers.

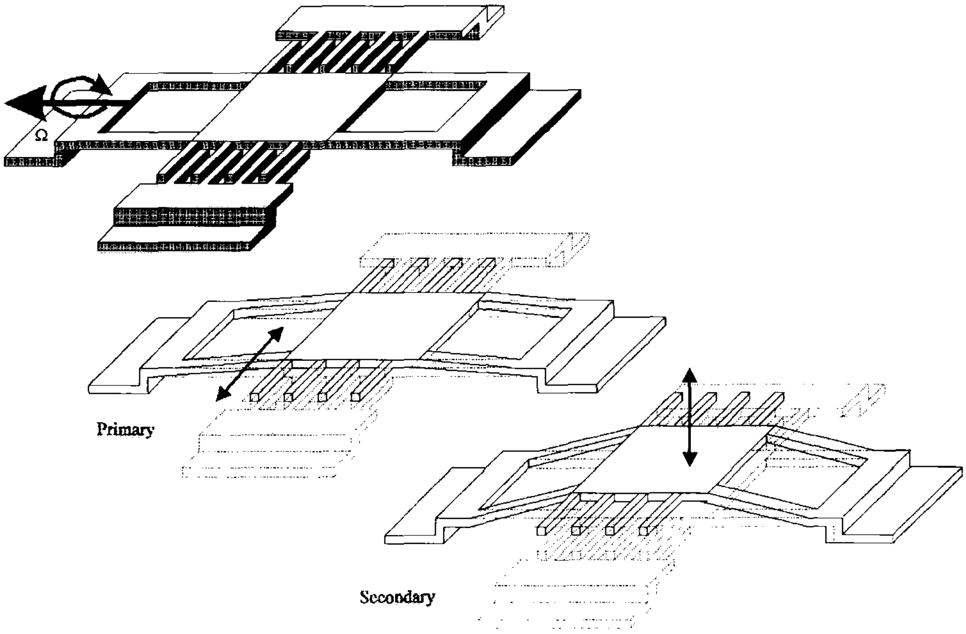

Figure 2.13 A micromachined gyroscope

2.5.6 Vibrating Gimballed Plate Gyroscope

This is another design from the Draper labs and again is a design suitable for silicon machining[16,17]. The primary motion of the device, see figure 2.14, is excited capacitively, and causes a bouncing motion of the whole structure. In the presence of a rate of turn this mode is coupled into a rocking motion of the inner plate. This device has been fabricated on a silicon wafer though its manufacture process is extremely complex, requiring a combination of surface machining, bulk machining and electrochemical deposition.

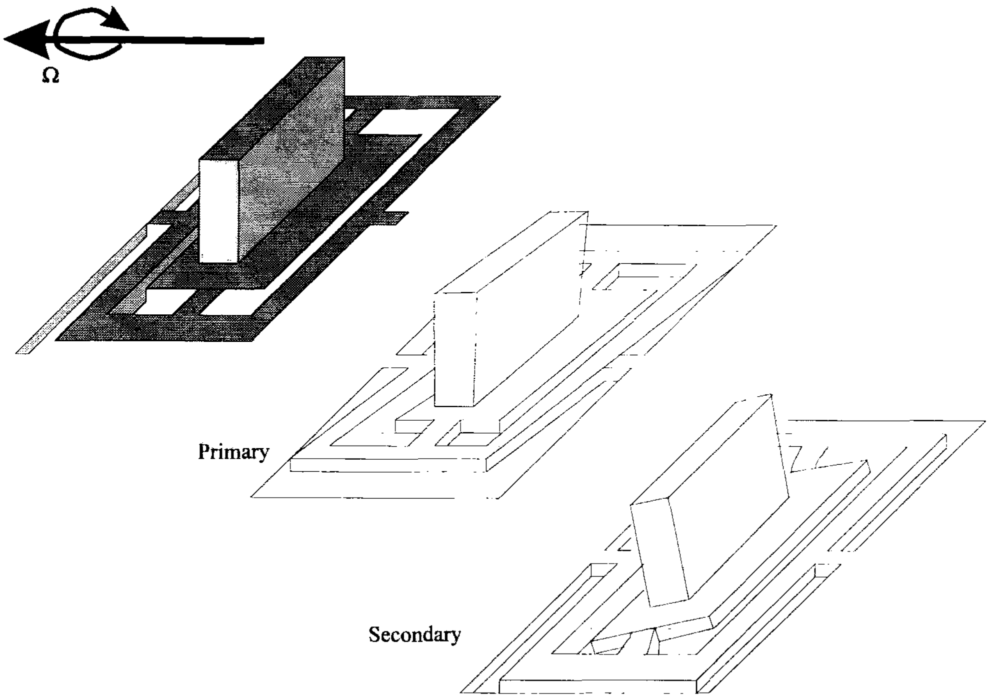

Figure 2.14 A Double Rocking Plate Gyroscope.

This device, in common with the design presented in this thesis, has two orthogonal rotational modes.

2.5.7 Shear Plate Gyroscope

Bosch of Germany have developed another variant of the vibrating gyroscope[18]. In this case the vibrating component is a square, X cut, PZT piezoelectric plate. The plate is made to vibrate in shear, as shown in figure 2.15, by the application of an ac signal across the plate . A rate of turn about an axis perpendicular to the plane causes a second shear motion to be generated, figure 2.15.

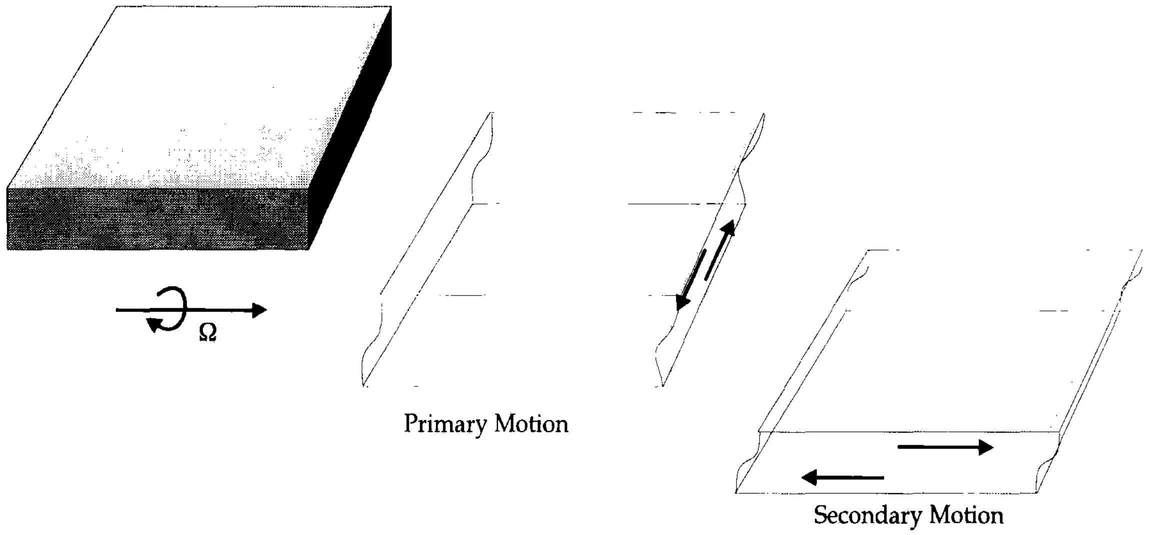

Figure 2.15 A piezoelectric plate gyroscope.

This gyroscope has a very simple construction but is difficult to sense and any support structure is likely to dampen the resonance. The resonant frequency of this device is 170 kHz.

2.5.8 Vibrating Wire Gyroscope

In this design the resonant component is a metal wire[19]. An ac current is passed along one half of the wire, which is in the presence of a magnetic field. This in turn generates a lorentz force causing the wire to vibrate. The frequency of the current is chosen to excite the second mode of the wire. In the absence of a rate of turn the wire will resonate perpendicular to the magnetic field. Once a rate of turn is applied about the long axis of the wire the direction of the resonance rotates. This is sensed inductively via coils close to the second half of the wire. This device has been patented, but no working device appears to have been made. The device is shown in figure 2.16.

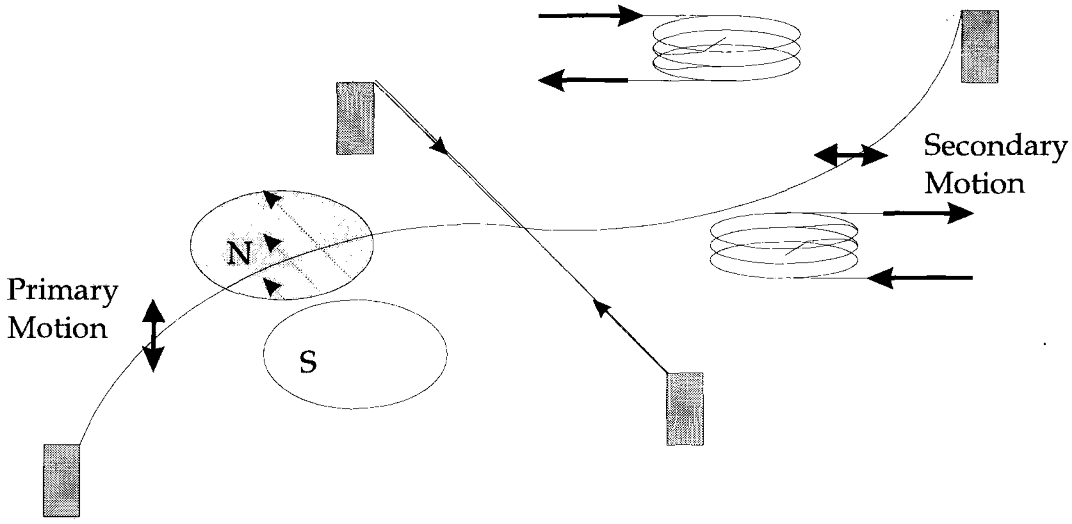

Figure 2.16 A Vibrating Wire Gyroscope.

2.5.9 Cylinder gyroscopes

This is another class of resonant gyroscope. The resonant component is a thin walled tubular shell. The shell is made to vibrate in a radial cos2q mode as shown in figure 2.17 . In the presence of a rate of turn about the long axis of the cylinder the nodes of maximum displacement tend to move around the shell.

The theory behind this design of gyroscope will not be covered here as it is quite involved and is not directly related to the work of this thesis. A full treatment is given by Burdess[20].

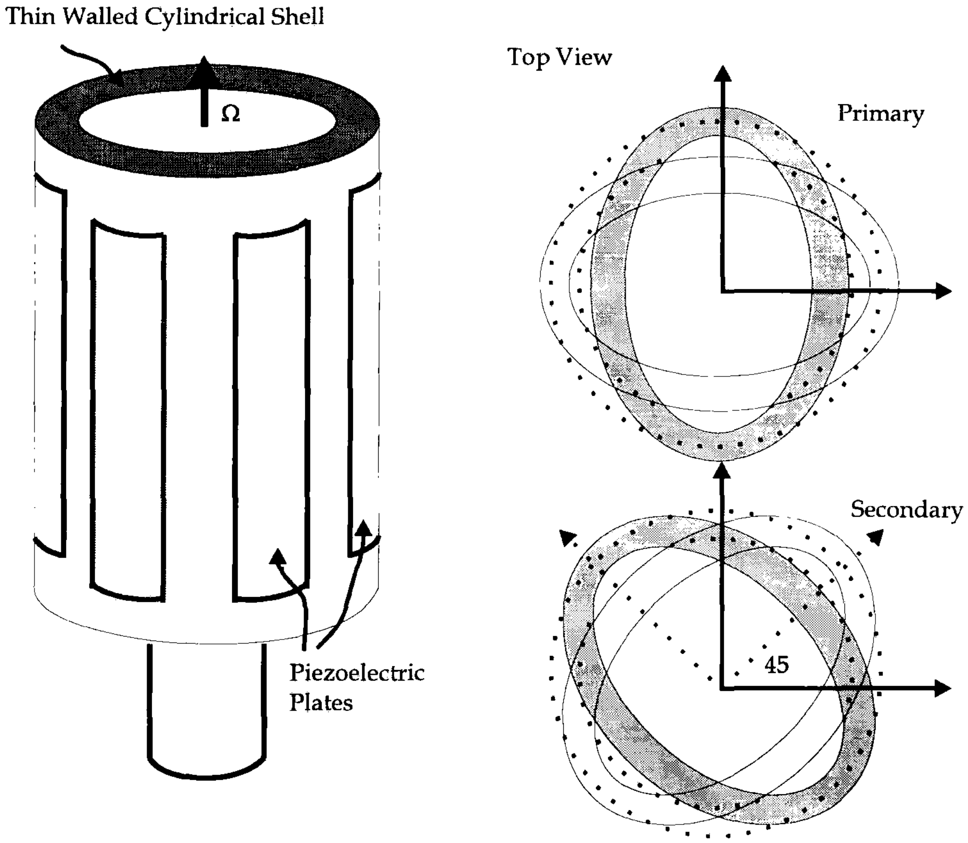

Figure 2.17 A Cylinder Gyroscope .

The cylinder gyroscope has the advantage that it is relatively easy to manufacture a precisely balanced cylindrical structure. This ensures that the resonant modes are of the same frequency. A number of commercial devices based on this design have been made: the specifications of one such device is contained in table 2.4.

A number of groups are working on making similar cylindrical designs using silicon surface machining techniques[21]. Most groups appear to be using electrochemically deposited metal for the resonant structure.

Linearity	±0.3%
Range	>60 deg/sec
Resolution	±0.02 deg/sec
Bandwidth	90 Hz
Cross axis sensitivity	<0.1%
Shock survival	<1000g

Table 2.4 performance figures of the GEC cylinder gyroscope

2.6 Conclusions

Due to the highly complex nature of both flywheel and optical gyroscopes it is highly unlikely that they will ever be successfully utilised in mass market applications. The resonant gyroscopes have no independently moving parts and therefore offer the possibility of reliable, rugged, cheap devices.

To date resonant gyroscopes have been hindered by relatively expensive manufacturing costs. The requirement of matching the two resonant modes of the device frequently leads to expensive precision engineered components. In addition many of the structures are quite complex requiring involved assembly processes.

Applying microelectronics technology, where tolerances of a fraction of a micron are routinely achievable, to bulk silicon machining offers the possibility of achieving precisely machined components at a low cost, an integrated silicon device would require a minimum of complex assembly proceedures. In addition single crystal silicon is known to be a good material for the manufacture of resonant components, having a low damping factor and few defects for cracks to propagate.

	Gyrostar	Watson	Systron Donner	GEC
Operating Range	$\pm 90^{o}s^{-1}$	$\pm 30^{o}s^{-1}$ to $\pm 1000^{o}s^{-1}$	$\pm 10^{o}s^{-1}$ to $\pm 1000^{o}s^{-1}$	$>60^{o}s^{-1}$
Scale factor[3]	$22.2mV/^{o}s^{-1}$	$0.3V/^{o}s^{-1}$ to $0.01V/^{o}s^{-1}$	$0.25V/^{o}s^{-1}$ to $22.5mV/^{o}s^{-1}$	-
Scale factor linearity	0.5%fsd	0.1%fsd	-	0.3%fsd
Bandwidth	-	50 Hz	60 Hz	90 Hz

Table 2.5 Summary of published performance figures

---

[3] The change in output for each degree/second change in the rate of turn of the gyroscope.

2.7 References

---

[1] R.Arnold,L.Maunder, Gyrodynamics and Its Engineering Applications Academic Press, 1961.

[2] E.Post Sagnac Effect Rev.mod.Phys., vol.39, 1967. P475-481

[3] B.Culshaw et. al. Fibre Optic Gyroscopes J.Phys. E:Sci.Instrum., vol 16, no.5, 1983

[4] H.Goldstein Classical Mechanics Addison -Wesley Publishing, 2nd Ed. 1980, pp. 166-187.

[5] M.O'Conner, " Vibrating Beam Rotation Sensor," European Patent Application 82400351.1, 02.03.1982.

[6] J.W.S.Pringle, "The Gyroscopic Mechanism of the Halters of Diptera," *Phil.Trans.Roy.Soc.London, Ser.B,* vol 233, 1948, pp.347-384

[7] K.Maenaka,T.Shiozawa, "A Study of Silicon Angular Rate Sensors Using Anisotropic Etching Technology," *Sensors & Actuators A,* 1994

[8] W.Gates, " Vibrating Angular Rate Sensor May Threaten The Gyroscope," *Electronics,* June 10, 1968, pp.130

[9] Murata Ltd., "Gyrostar," Murata Ltd. Product Brochure, 1991.

[10] H.Abe,T.Yoshida,K.Tugara, "Piezoelectric-Ceramic Cylinder Vibratory Gyroscope," *Jpn.J.Appl.Phys.,* vol.31, 1992, pp.3061-3063

[11] J.Lyman, " A New Space Rate Sensing Instrument," *Aeronaut.Eng'g.Review.,* vol.12,1953, pp-24-36

[12] Watson Industries Ltd., "Inertial Sensor Technology," Product Catalogue November 1993.

[13] G.Hunt, A.Hobbs, "Development of An Accurate Tuning Fork Gyroscope," *Proc.Instn.Mech.Engrs.,* Vol 179, pt.3E, 1964-65, pp. 129-139

[14] Systron Donner Ltd., " Quartz Rate Sensor Model QRS11-C1 Summary Specifications," Product Data Sheet 5-11-1992

---

[15] J.Bernstien,S.Cho,A.King,A.Kourepenis,P.Meciel,M,Weinberg, "A Micromachined Comb-Drive Tuning Fork Rate Gyroscope," *Proc. IEEE Micro Electro Mechanical Systems Conference,* Florida, USA, Feb., 1993, P.143

[16] B.Boxenhorn, "Planar Inertial Sensor," UK Patent GB 2,156,523,B., Mar.15, 1985

[17] P.Greiff,B.Boxenhorn,T.King,L.Nliles, " Silicon Monolithic Micromechanical Gyroscope," *IEEE,* 1991 pp. 966-968

[18] M.Boruschewitz,S.Gartner,H.Hamisch,H.Kaiser,G.Pfaff, "The Development of an Inexpensive Gyroscope Based on The Principle of a Vibrating Piezoelectric Plate, " *DGON Symposium on Gyro Technology,* Stuttgart, 1988, Paper 6.

[19] J.Johnston,R.Mass, " Vibrating Wire Attitude Reference Sensing System," US. Patent 3,903,747., Sept.9, 1975.

[20] J.Burdess, "The Dynamics of a thin Piezoelectric Cylinder Gyroscope," *Proc.Instn.Mech.Engrs.,* vol 200, no.C4, 1986 pp. 271-280

[21] M.Putty,K.Najafi, "A Micromachined Vibrating Ring Gyroscope," *Solid state Sensor and Actuator Workshop,* Hilton Head, South Carolina, June 1994 pp. 213-220

Chapter 3

The Bulk Machining & Material Properties of Single Crystal Silicon

3.1 Introduction

This chapter is divided into two sections. In the first section the manufacturing processes used to fabricate the gyroscopes is presented. The designs presented in the thesis have been specifically chosen to be manufacturable with existing micromachining technology.

In the second section of the chapter, the mechanical and piezoresistive properties of single crystal silicon are discussed in some depth. The orthotropic nature of silicon is discussed. Particular attention is paid to the properties of {110} oriented silicon, which is less well documented. The stiffness, compliance and piezoresistive matricies for {110} silicon are calculated from the published {100} values. These results are used in the finite element analysis of the design described in chapter 5.

3.2 Micro Machining of Bulk Silicon

Modern silicon chips are extremely complex and their fabrication can involve well over 100 different manufacturing stages or processes. Silicon micromachining borrows many of these proceses. However, the work contained in this thesis is concerned only with the bulk machining of silicon. Bulk machining requires only a few of these processes. In the following section only the processes concerned with the bulk machining of silicon are described: a more complete review of the manufacturing techniques used in the microelectronics industry may be found in Wolf[1] and Sze[2].

3.2.1 Wet Anisotropic Etching of Silicon

The process of bulk silicon micromachining, uses the etching process to fabricate mechanical components. This is achieved by selectively removing, dissolving or etching away certain regions of the silicon wafer leaving behind the desired structure. This can be achieved in one of two ways: wet chemical etching, or plasma etching. The work described in this thesis was carried out exclusively using the wet etching process: this procedure is described below.

Single crystal silicon may be etched by a number of alkaline solutions. EDP and KOH being the most commonly used formulations.The EDP etchant recipe used for most of the work in this thesis was 30g Catechol: 175 ml diaminoethane and 125 ml deionised water. The preparation of the etchant bath was found to be important in order to achieve a reproducable etch.

EDP and KOH solutions have similar properties: in both cases the solution attacks {111} planes at a significantly slower rate than the {100}, {110} or higher planes. This fact allows the {111} planes to be used to control the direction in which the etch front proceeds through the wafer. These {111} planes allow the initially two dimensional mask patterns to be transferred into the third dimension in a precisely controlled manner: the relative orientations of the crystal planes to the wafer surface dictate the nature of the shapes that may be formed with this process. Section 3.3 describes this in more detail.

The EDP solution was found to oxidise with atmospheric oxygen while it was being prepared. This in itself does not appear to prevent the etch from proceeding: it does however render the solution a very dark brown colour making it difficult to observe the sample during the etch process. In order to minimise the amount of oxygen absorbed whilst preparing the solution, the following procedure was adopted:

- clean all components of the reaction chamber thoroughly with deionised water and then dry the components with a hot air blower
- weigh out the desired quantity of catechol (30 g for the flask used) place the catechol in the reaction vessel with the magnetic stirrer and seal the reaction vessel.
- measure out 175 ml of Diamenothene and add this through a small port into the vessel. At this stage the solution should appear light orange.
- finally add the 125 ml of water again through a small port, place the reflux condenser into the port.

After the addition of the water the vessel will fill with opaque fumes these should clear leaving behind a clear tea coloured solution. This solution should be heated and stirred during the etching procedure. The etchant was maintained at a temperature of 100 degrees during the process. The solution should be left for about 1/2 an hour before adding the silicon sample. When first mixed the solution forms a three phase mixture, as the temperature is increased the mixture becomes homogenous forming a single solution.

Even with careful preparation the etch rate of silicon in the EDP was found to be very variable. Typically a 300 μm thick {100} wafer would take around 5 hours to etch fully through and a similar {110} wafer would take around 3 hours. The total etch time required was highly dependent upon the nature of the structure being etched. The etch rate of different regions of the structures varied considerably. Usually large exposed regions of silicon would etch more rapidly than would narrow deep trenches, indicating that the etch rate is to some extent controlled by the flow of fresh etchant over the silicon surface.

As a result of the non-uniformity of the etching process a considerable over-etch was often necessary. In practice the most reliable way to contol the etch was found to be to regularly inspect the sample: for the most part this could be done without removing the sample from the etchant.

3.2.2 Etch masking & Oxidation

The EDP solution will dissolve silicon: in order to fabricate a mechanical structure there must be a way of controlling the regions that are dissolved. This requires selectively masking, or protecting from the etchant, certain regions of the surface of the wafer .

If the silicon wafer is placed in an oxygen rich atmosphere at high temperature the surface of the silicon will combine with the oxygen, forming a thin layer of silicon dioxide around the wafer, see Figure 3.2. This is achieved by placing the wafer inside a quartz lined furnace with a constant stream of oxygen passing through it. Typical furnace temperatures range from 800 to 1250^0C. Silicon dioxide is used both as an electrical insulator and for its ability to withstand chemical attack. The oxidation process forms silicon dioxide over the whole surface of the wafer. In order to etch the mechanical structure this oxide must be selectively removed, thus exposing the desired areas of the silicon to the EDP etchant. This procedure is carried out with a combination of the photolithographic process and hydrofluoric acid etching.

The hydrofluoric acid does not significantly attack the silicon but etches the silicon dioxide very rapidly.

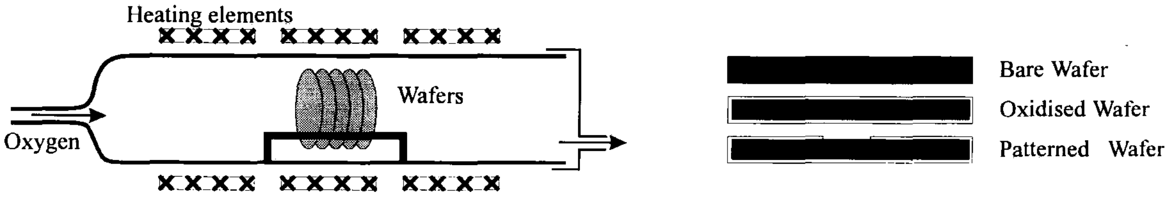

Figure 3.1 The oxidation process

3.2.3 Photolithography

Photolithography is the process by which all of the shapes of the microstructures are defined. In the first stage of the process the silicon wafer is coated with a thin layer, typically around 1μm thick, of a photosensitive material, known as photoresist. The photoresist is applied in liquid form and the wafer is then spun at high speed to drive off the excess liquid, producing a uniform coating over the wafer surface. After this the wafer is baked to drive off the solvent in the photoresist.

The photoresist is a polymeric material whose chemical properties are changed by UV light. In positive resist the UV light acts to break some of the chemical bonds rendering the resist soluble in developing solution.[*] As a result defined areas of the photoresist may be removed by selectively exposing these areas to UV light and then dissolving away the resist in developer. This selective exposure is achieved by placing a mask between the UV source and the wafer. A typical mask would be a quartz plate covered with a layer of patterned chromium. The chromium covered areas reflect the light preventing the photoresist from being exposed and therefore developed. This process is shown graphically in Figure 3.2.

---

[*] **Negative photoresists are also available, where exposure to UV light renders the resist insoluble in the developing solution. These resists are no longer widely used: all work described here uses positive resist.**

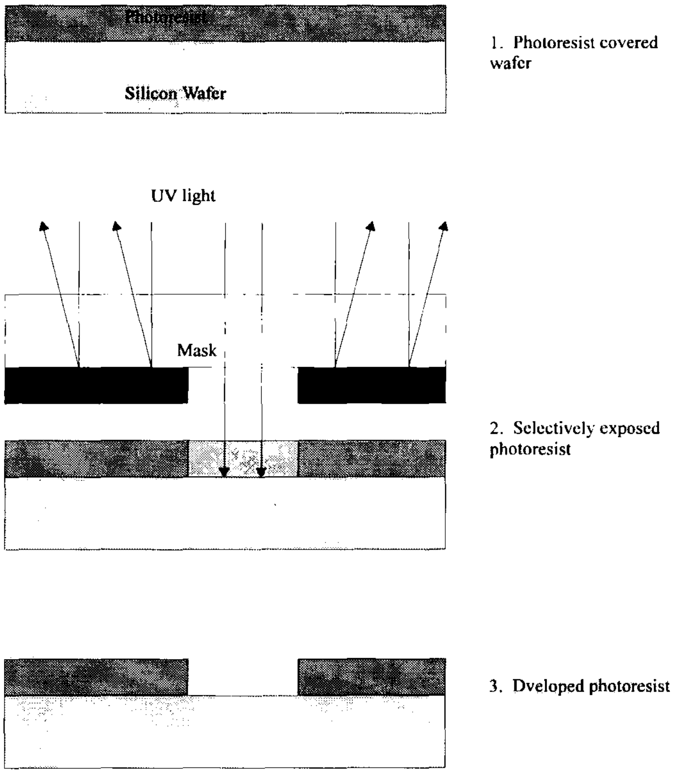

Figure 3.2 The photolithography process

The patterned photoresist then acts to protect the selected regions of the wafer surface from future processing; chemical etching, for example. The photoresist is not able to resist the EDP etchant and therefore may not be used directly as an etching mask for the anisotropic etching process.

The photolithography carried out in this thesis was performed with Shipley-S1813 positive photoresist. The wafers were pre-baked for 10 minutes at 120 ^{o}C to drive off any surface moisture prior to spinning, this process improves the adhesion of the photoresist to the wafer surface.

The photolithographic process is only able to define two dimensional patterns: this is ideal for electronic circuitry but is a serious limitation to the design of micromechanical structures.

3.2.4 Mask Making

The photolithographic process requires a mask patterned with the desired design. Commercially produced masks are typically made using an electron beam to directly write the desired image onto a chrome covered quartz plate. This technique is expensive and unsuitable for research work where by definition the device designs are changing rapidly requiring new masks for each modification.

A simple, cheap mask making technique was developed for the purpose of this research: The masks themselves were high resolution black and white photographic plates (Agfa millimask plates were used), this range of plates are specifically produced for the photolithography industry. The mask image was generated by photographically reducing a master image directly onto the plate. To do this a photo reduction table was made: a plate camera was positioned at one end of the table while on the other end the mask design was mounted on an illuminated base plate. The set up was rather like the reverse of a conventional dark room enlarger. The position of the base plate and the camera could be adjusted so as to vary the degree of the reduction between a maximum of 12.4:1 down to 5:1.

The master images themselvs were then drawn with the aid of a computer aided design, CAD, package[†]. The images were then simply printed on a high resolution printer[‡]. This technique gave satisfactory results allowing the formation of lines with a minimum width of 50 μm. This resolution was adequate for the designs described in this thesis.

3.2.5 Diffusion

The diffusion process is a method of introducing dopant atoms into the silicon to modify its electrical properties. Diffusing boron atoms into the silicon makes the silicon p type, meaning that the conduction is via holes. If phosphorus, arsenic or antimony is used then the silicon becomes n type, meaning that the conduction method is via electrons. The diffusion process is very similar to the oxidation process: the principle difference being the gas atmosphere within the furnace. In the diffusion process the oxygen atmosphere is replaced with an inert carrier gas, usually nitrogen and some additional source of the dopant atoms. The dopant atoms may be intoduced in gas form, or as used for the work in this thesis, from a solid source placed alongside the wafer in the furnace. The Boron diffusion process used in this thesis was performed with boron nitride plates as the dopant source.

For micromechanical purposes the boron diffusion serves two quite different purposes. In the first instance it is used to make a region of silicon conductive to act as a strain

---

[†] Autocad version 11 was used.

[‡] An Agfa A3 high resolution colour plotter was used, the plots being sent in postscript format.

sensitive piezoresistor. Secondly the addition of high levels of boron atoms to the silicon renders the silicon immune to attack by certain silicon etchants, in particular to the EDP etchant. This latter feature is extremely useful as it allows the diffused silicon to remain intact while the region around it is dissolved away[3]. The boron diffused regions act as an etch mask in the same way as oxidised regions. In order to achieve this etch protection a very high doping concentation must be used. Figure 3.3 shows the dependence of etch rate on doping concentration for one of the commonly used etchants.

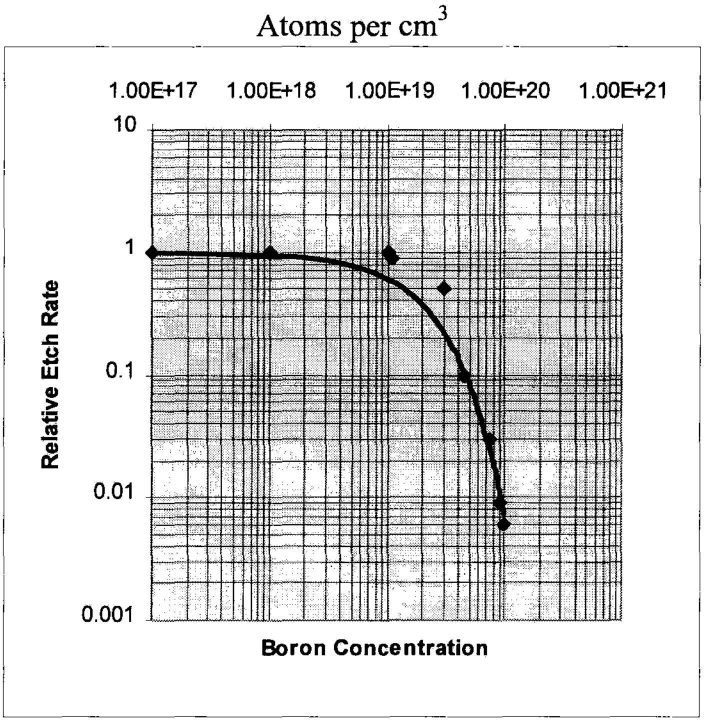

Figure 3.3 **Etch rate of silicon as a function of boron concentration in EDP etchant. (Taken from reference 3 Figure 4)**

The regions into which the boron is diffused can be defined using a patterned layer of silicon dioxide. The boron is able to diffuse into the exposed silicon but is unable to diffuse through the silicon dioxide layer.

3.2.6 Metalisation

Metal tracks were deposited using the evaporation method. The wafer is placed inside a sealed chamber (see figure 3.4). The chamber is then evacuated and a sample of metal is heated up to evaporation point inside the chamber. The metal vapour then condenses on the first surface that it meets, the inside of the vacuum chamber and the silicon wafer.

The deposition of multiple layers is possible by using two separate heated crucibles each containing a different metal. For the purposes of fabricating the test structures described in chapters 4 and 5 a layer of chromium was deposited first followed by a layer of gold. The chromium acted as a interface between the gold and silicon improving the adhesion of the gold to the substrate. The gold was used for its high conductivity and good resistance to the EDP etchant.

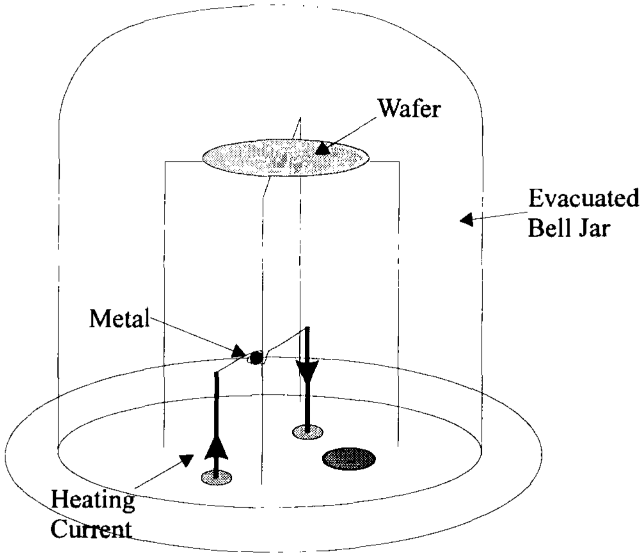

Figure 3.4 Schematic of a conventional metal vaporation system.

The evaporations were performed using a Varian dual e-beam evaporator, this system differs from the one shown in figure 3.4 in that the sample is heated by a focused beam of electrons. The system was pumped with a combination of turbo molecular and ion adsorption pumps, giving a base pressure of 3×10^{-7} Torr. The deposited metal layers were patterned using photolithography and wet etching processes.

3.3 Single Crystal Silicon

Figure 3.5 shows the three most important crystal planes in silicon.

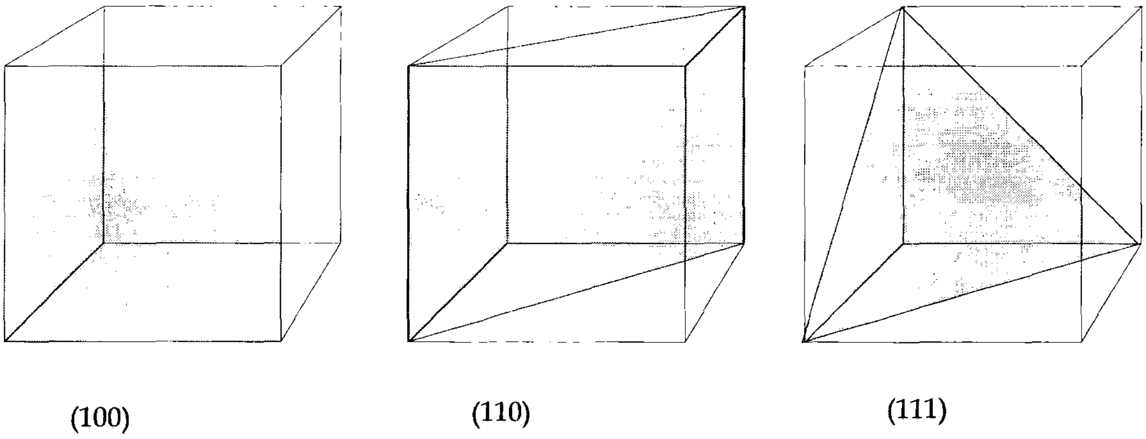

Figure 3.5 Crystal Planes of Silicon

Wet anisotropic etching of silicon relies heavily upon using the etchant's selectivity to various crystal planes to define the micromechanical structure. With EDP or KOH etchant the {111} planes are highly resistant to the etchant. If a wafer having a surface cut parallel to a {100} plane is used, then typically V groove trenches, square nozzles and square based pyramids may be formed. These structures are simple and have been described extensively in the literature[4]. The design described in chapter 4 is fabricated using {100} silicon.

The design on chapter 5 has been developed to take advantage of the arrangement of the {111} planes as they relate to a {110} plane. The literature on anisotropic etching of {110} wafers is much less clear, than for {100} silicon, and it is therefore worth describing the orientation of the {111} planes relative to the {110} planes. Figure 3.6 and 3.7 show some of the {111} planes as viewed from the (100) and (110) planes respectively.

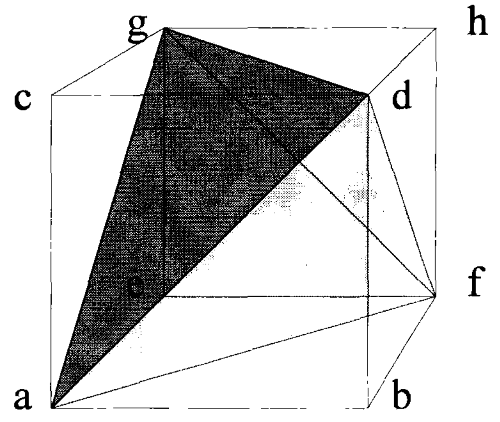

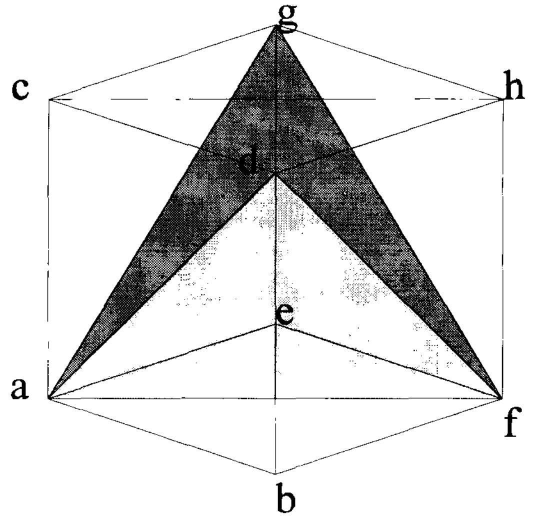

Figure. 3.6 {111} Planes viewed from a (100) plane   Fig 3.7 {111} Planes viewed from a a,b,c,d.
(110) plane a,f,c,h.

For clarity some of the {111} planes have been omitted. Consider figure 3.6, the plane a,b,c,d represents a (100) plane, while the planes a,g,d and a,f,d represent (111) planes. It can easily be calculated that both of these (111) planes intersect the (100) plane at an angle of $Tan^{-1}(\sqrt{2})$ or 54.74 degrees. In figure 3.7, which is simply a rotation of figure 3.6, the (110) plane is represented by a,f,c,h, as in figure 3.6 the (111) planes are a,g,d and a,f,d , in addition d,f,g also represents a (111) plane. Clearly the planes a,g,d and d,f,g intersect the a,f,c,h (110) plane at 90^{0}. While the plane a,f,d intersects the (110) plane at an angle of $Tan^{-1}(\sqrt{2}/2)$ or 35.26 degrees. The two vertical (111) planes a,g,d and d,f,g make an angle of $2Tan^{-1}(\sqrt{2}/2)$ or 70.53 degrees to each other. The angle at which the vertical {111} plane a,g,d meets the inclined {111} plane a,f,d is $Tan^{-1}(\sqrt{2})$ or 54.74[§].

The result of this arrangement of crystal planes is that it is possible to etch a six sided pit in the surface of the silicon (Figure 3.8), four of the side walls being vertical and two inclined to the wafer surface. The shape of the pit may be varied allowing the formation of diamond shapes, trenches, and V grooves. Note that a V groove formed on a (110) surface may be formed in only one direction, whereas two perpendicular V grooves may be formed on a (100) surface.

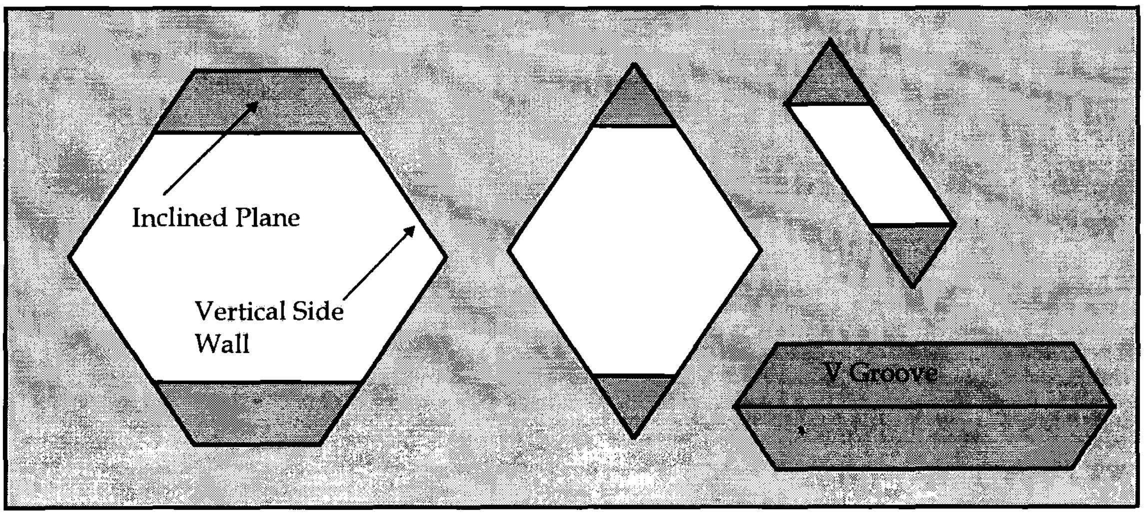

Figure 3.8 Anisotropically etched {110} silicon

The ability to etch a V groove into the (110) surface has been used in the design of the structures described in chapters 4 and 5.

3.3.1 Finite Element Analysis of Crystal Structures

Extensive use of Finite Element Analysis, or FEA, method has been made in this thesis. A general description of FEA is given by Fagan[5] and Hitchins[6]. This will not be repeated here. However a few general words on issues specific to silicon microstructure modelling are needed.

The FEA method requires that the structure to be modelled is divided into small sub-sections or elements. The FEA method works best when these elements are as close to

---

[§] **All of these angles may be calculated exactly as the unit cell is a perfect cube.**

cubic as possible. As the aspect ratio of a structure increases it is necessary to use more elements to describe the structure in order to avoid deforming the individual elements too severely. In microstructures the aspect ratio of the devices can be extremely high: this can become a serious problem in constructing a reasonable FEA mesh. For this reason a number of approximations in the analysis of the structures were made. Where very thin silicon beams have been used they have been approximated to "tension bar elements". These elements have the advantage of requiring only two nodes to define them. Tension bar elements, as the name suggests, are only able to sustain tensile or compressive forces, and any bending moment is neglected. A full description of these elements can be found in the published literature[7].

The finite element analysis was carried out using the PAFEC suite of programs mounted on a 64 bit Hewlett Packard UNIX based workstation. Double precision was used for all calculations. PAFEC, like other FEA packages is organised into a 3 stage program; pre-processing (data input), calculation and post-processing (results output). As an alternative to the pre-processor PAFEC allows the user to write a data file with all of the model details defined within it. This approach was adopted as it allowed for more accurate positioning of the node points. The node positions were calculated with a combination of AutoCad and Microsoft Excel . For most models a precision of better than 1μm was used for the node positions.

In order to model single crystal devices accurately it is necessary to take into account the anisotropy of the material stiffness. In order to do this PAFEC had to be given the coefficients of the compliance matrix for silicon. This is discussed in the following sections.

3.3.2 Co-ordinate Systems

Silicon, being a crystal with a cubic unit cell[**] has a natural co-ordinate system defined by the crystallographic directions [100], [010] and [001]. Due to the symmetry of the silicon crystal these directions are orthogonal and equivalent.

This natural co-ordinate system is unfortunately inconvenient when working with wafers of {110} orientation, as only one of the axes lie in the (110) plane. A more natural axis set for these wafers is [101], [010], [10-1]. This axis set corresponds to a -45^0 rotation about the Y direction, using right handed axis convention. The two co-ordinate systems are shown in Figure 3.9. This new co-ordinate system has both X and

---

[**] Silicon has a diamond crystal structure consisting of two interlocking face centred cubes displaced by (1/4,1/4,1/4) relative to one another.

Y directions in the plane of a {110} wafer and also retains mirror symmetry of the crystal properties about both X and Y axes. The 90^0 rotational symmetry about the Z axis is, however, reduced to 180^0 symmetry. The axis set chosen is not unique, other co-ordinate systems are equivalent for example [10-1],[010], [101].

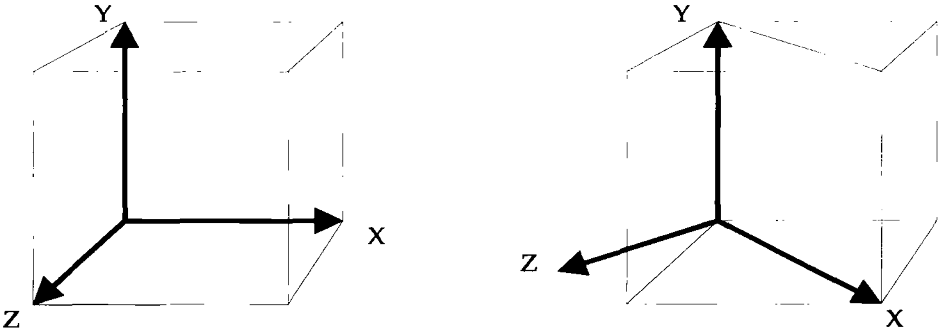

Figure 3.9 co-ordinate systems for {100} and {110} silicon (The axis set shown above has been chosen to coincide with the axis set shown on the FEA plots in chapters 4-6)

3.3.3 Young's Modulus of {110} Silicon[††]

Single crystal silicon is an orthotropic material, as such its Young's modulus is direction dependent and cannot be described by a single number, rather the full generalised version of Hooke's law should be used[8]. This may be expressed in tensor notation as follows:

$$S_{ij} = s_{ijkl} T_{kl} \qquad 3.1$$

or

$$T_{ij} = c_{ijkl} S_{kl} \qquad 3.2$$

Where T_{ij} represent the nine components of the stress tensor and S_{kl} the nine components of the strain tensor. s_{ijkl} is the fourth rank compliance tensor and c_{ijkl} is the corresponding stiffness tensor. The suffixes can take values of 1,2 or 3 corresponding to the X,Y and Z directions. As a result the stress and strain tensors have nine components, 3x3, while the full stiffness and compliance tensors each have 81 components, 3^4. Due to the crystal symmetry these 81 components are not independent and many are zero. In general there are only 21 independent coefficients[9] and in the case of a crystal with cubic symmetry like silicon the number of independent coefficients is reduced to only three. In most situations the full tensor notation is dropped and replaced with a more compact matrix notation, where only a 6x6 matrix is shown. Much of the literature on both silicon stiffness and piezoresistive coefficients uses the term tensor to describe what is in fact the matrix notation. This

---

[††] **The notation in this chapter is consistent with that used by R.F.S.Hearmon[9].**

can causeconfusion and is particularly important when attempting to use rotated reference frames as is the case when rotating the frame of reference of the tensors as is required when performig FE calculations on silicon of {110} orientation. The following section outlines how the two notations relate to one another.

$$T_{ij} = \begin{bmatrix} T_{11} & T_{12} & T_{13} \\ T_{21} & T_{22} & T_{23} \\ T_{31} & T_{32} & T_{33} \end{bmatrix} \qquad 3.3$$

The full stress tensor is shown in equation 3.3. T_{11},T_{22},T_{33} correspond to the stresses in the X,Yand Z directions respectivly and T_{12},T_{13},T_{23} represent the shear stresses. Given that T_{ij} =$T_{ji,}$ (the matrix is symmetric) then the stress tensor only has six independent components. Thses are conventionally shown in the form of a column matrix, Whose components are given by:

$$T_1 = T_{11},\ T_2 = T_{22},\ T_3 = T_{33},\ T_4 = T_{23},\ T_5 = T_{13},\ T_6 = T_{12}, \qquad 3.4$$

The strain tensor is abbrieviated in a similar way:

$$S_1 = S_{11},\ S_2 = S_{22},\ S_3 = S_{33},\ S_4 = 2S_{23},\ S_5 = 2S_{13},\ S_6 = 2S_{12}, \qquad 3.5$$

Tensor notation suffix pairs	**11**	**22**	**33**	**23,32**	**31,13**	**12,21**
Matrix Equivalent	1	2	3	4	5	6

S_{ijkl}=S_{mn} when both m and n are 1,2 or 3.
S_{ijkl}=0.5S_{mn} when either m or n are 4,5 or 6.
S_{ijkl}=0.25S_{mn} when both m and n are 4,5 or 6.

Table 3.1 Rules to Convert between tensor and matrix notation.

It is imortant to note the factors of 2 which have been introduced in equation 3.5[‡‡]. S_4,S_5 & S_6 are referred to as the engineering strains as opposed to the tensor strains. Having defined these two new column matrices equations 3.1 and 3.2 can be re-written in matrix notation:

[‡‡] The factor of 2 is introduced to allow for the double summation which would occur in the true tensor notation but is omitted in the simplified matrix notation.

$$S_i = s_{ij} T_j \qquad 3.6$$

$$T_i = c_{ij} S_j \qquad 3.7$$

As an example equation 3.6 has been shown explicitly below:

$$\begin{pmatrix} S_1 \\ S_2 \\ S_3 \\ S_4 \\ S_5 \\ S_6 \end{pmatrix} = \begin{pmatrix} s_{11} & s_{12} & s_{13} & s_{14} & s_{15} & s_{16} \\ s_{21} & s_{22} & s_{23} & s_{24} & s_{25} & s_{26} \\ s_{31} & s_{32} & s_{33} & s_{34} & s_{35} & s_{36} \\ s_{41} & s_{45} & s_{43} & s_{44} & s_{45} & s_{46} \\ s_{51} & s_{52} & s_{53} & s_{54} & s_{55} & s_{56} \\ s_{61} & s_{62} & s_{63} & s_{64} & s_{65} & s_{66} \end{pmatrix} . \begin{pmatrix} T_1 \\ T_2 \\ T_3 \\ T_4 \\ T_5 \\ T_6 \end{pmatrix} \qquad 3.8$$

where s_{ij} and c_{ij} are known as the compliance and stiffness matrices respectively. formed from the tensor components by the rules in table 3.1. For silicon the coefficients of the compliance and stiffness matrices are shown in equations 3.9 and 3.10 respectively [10,11]:

$$s_{ij} = \begin{pmatrix} 0.768 & -0.214 & -0.214 & 0 & 0 & 0 \\ -0.214 & 0.768 & -0.214 & 0 & 0 & 0 \\ -0.214 & -0.214 & 0.768 & 0 & 0 & 0 \\ 0 & 0 & 0 & 1.26 & 0 & 0 \\ 0 & 0 & 0 & 0 & 1.26 & 0 \\ 0 & 0 & 0 & 0 & 0 & 1.26 \end{pmatrix} \times 10^{-11} Pa^{-1} \qquad 3.9$$

$$c_{ij} = \begin{pmatrix} 1.657 & 0.639 & 0.639 & 0 & 0 & 0 \\ 0.639 & 1.657 & 0.639 & 0 & 0 & 0 \\ 0.639 & 0.639 & 1.657 & 0 & 0 & 0 \\ 0 & 0 & 0 & 0.7956 & 0 & 0 \\ 0 & 0 & 0 & 0 & 0.7956 & 0 \\ 0 & 0 & 0 & 0 & 0 & 0.7956 \end{pmatrix} \times 10^{11} Pa \qquad 3.10$$

Note that in each of these matrices there are 12 non-zero coefficients of which only three are unique.

The coefficients in these matrices are dependent upon the axis set used. The values given are for an axis set based on [100],[010] and [001] directions. However, as described in the previous section this is not the most convenient axis set to define structures made from {110} wafers; the choice of axis set becomes particularly important when constructing complex FE models. It is therefore necessary to calculate the equivalent matrices for the axis set described in figure 3.9.

However, it is important to note that these matrices do not represent tensors and do not transform as tensors. The matrices as shown cannot be transformed directly. In order to perform the transformation they must be converted back to the full tensor notation. This is done using the relations shown in table 3.1.

Once the full tensor is reconstructed it may be transformed according to the tensor transformation rule:

$$T'_{ijkl} = a_{im} a_{jn} a_{ko} a_{lp} T_{mnop} \qquad (3.11)$$

where a_{ij} represent the direction cosines between the new and old axis set. Equation 3.11 uses the summation convention, i.e. it is assumed that all free indices are to be summed over. For the axis set described in section 3.3.2 the a_{ij} are given by equation 3.12.

$$a_{ij} = \begin{pmatrix} 1/\sqrt{2} & 0 & 1/\sqrt{2} \\ 0 & 1 & 0 \\ -1/\sqrt{2} & 0 & 1/\sqrt{2} \end{pmatrix} \qquad 3.12$$

The transformation calculations were performed using a spread sheet. The transformed tensors, were then re-formed into the conventional matrix notation, again using the relations in table 3.1. In this form they were suitable for use with the finite element package. The resultant compliance and stiffness matricies are given in equation 3.13 and 3.14.

$$s_{ij} = \begin{pmatrix} 0.592 & -0.214 & -0.038 & 0 & 0 & 0 \\ -0.214 & 0.768 & -0.214 & 0 & 0 & 0 \\ -0.038 & -0.214 & 0.592 & 0 & 0 & 0 \\ 0 & 0 & 0 & 1.26 & 0 & 0 \\ 0 & 0 & 0 & 0 & 1.96 & 0 \\ 0 & 0 & 0 & 0 & 0 & 1.26 \end{pmatrix} \times 10^{-11} pascal^{-1} \qquad 3.13$$

$$c_{ij} = \begin{pmatrix} 1.994 & 0.639 & 0.352 & 0 & 0 & 0 \\ 0.639 & 1.657 & 0.639 & 0 & 0 & 0 \\ 0.352 & 0.639 & 1.994 & 0 & 0 & 0 \\ 0 & 0 & 0 & 0.796 & 0 & 0 \\ 0 & 0 & 0 & 0 & 0.509 & 0 \\ 0 & 0 & 0 & 0 & 0 & 0.796 \end{pmatrix} \times 10^{11} \mathit{pascal} \qquad 3.14$$

As an alternative to this approach, it was also possible in the PAFEC package to use the conventional untransformed matrix and define a rotated axis relative to the matrix axis. The model may then be defined in this new rotated axis set. This approach is valid for dynamic calculations but leads to problems when trying to extract directional stress data and can become extremely complex when applying directional forces to the model. Both approaches were tested for the dynamic modelling and the resonant mode shapes and frequencies were in good agreement, indicating that the two approaches are consistent. Utilising the transformed matrix also reduced the time taken to process the model.

The variation in the stiffness of the silicon as a function of orientation on the {110} plane is significant in the design of resonant structures. It can be shown[15] that Young's modulus on a {110} plane is given by equation 3.15 .

$$Y(\theta) = \left[0.768 + \left[0.768 + 0.214 - \left(\frac{1.26}{2}\right)\right] \cdot \left[\left(\cos(\theta)\cdot\frac{1}{\sqrt{2}}\right)^4 + \left(\cos(\theta)\cdot\frac{1}{\sqrt{2}}\right)^4 + \sin(\theta)^4 - 1\right]\right]^{-} \mathrm{x}10^{11}\mathrm{pa} \qquad 3.15$$

A plot of the equation 3.15 is shown in figure 3.10. As can be seen from this plot the Young's modulus posesses lines of mirror symmetry about both the X and Y axis, if correctly chosen, and 180° rotational symmetry.

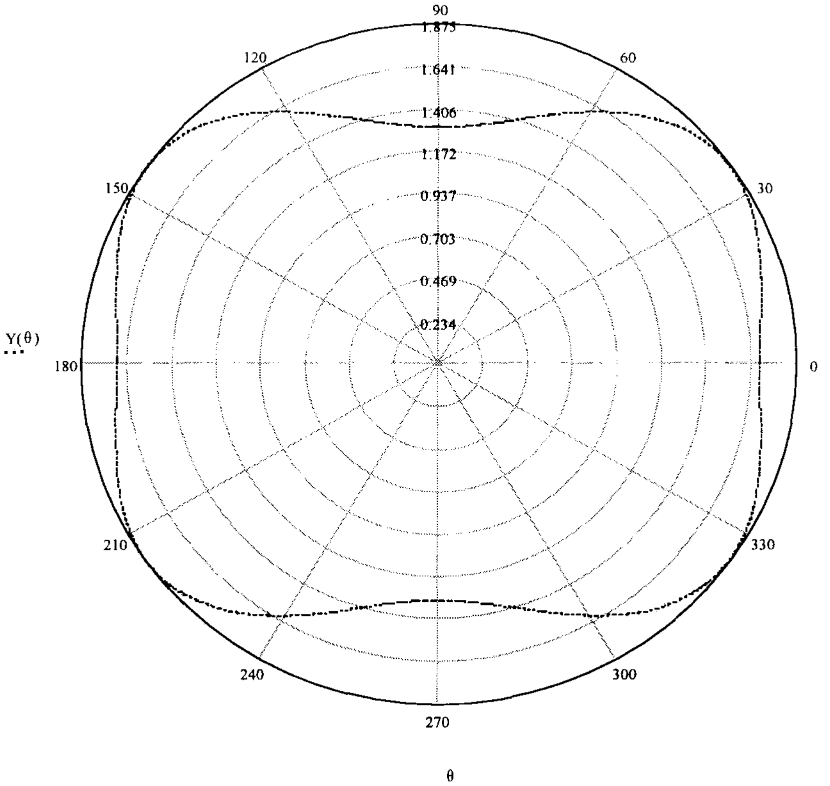

Figure 3.10 Young's Modulus as a Function of Angle on a {110} plane[12] ($x10^{11}$Pascals)

In figure 3.10 θ=0 corresponds to the Y direction of the axis set described in 3.3.2. Note that the Young's modulus is a maximum at θ=35.26°, corresponding to the direction in which the vertical {111} planes lie.

3.3.4 Piezoresistive Properties of {110} silicon

The maths required to describe the piezoresistive properties of silicon is much the same as that used in the previous section. Once again the general law governing piezoresistance is in the form of a tensor:

$$\frac{\Delta\rho_{ij}}{\rho} = \pi_{ijkl} T_{kl} \qquad (3.16)$$

where $\Delta\rho_{ij}/\rho$ is the 3x3 tensor describing the fractional change in resistivity and π_{ijkl} is the 3^4 tensor containing each of the 81 piezoresistive coefficients. As with the compliance and stiffness tensors, the piezoresistive tensor contains only three independent coefficients when the natural co-ordinate system is used. As a result it is once again possible to employ the shortened matrix notation used in the previous section. The equivalent that equation to 3.5 may be expressed as:

$$\begin{pmatrix}\rho_1\\ \rho_2\\ \rho_3\\ \rho_4\\ \rho_5\\ \rho_6\end{pmatrix} \Big/ \rho_0 = \begin{pmatrix}\pi_{11} & \pi_{12} & \pi_{13} & \pi_{14} & \pi_{15} & \pi_{16}\\ \pi_{21} & \pi_{22} & \pi_{23} & \pi_{24} & \pi_{25} & \pi_{26}\\ \pi_{31} & \pi_{32} & \pi_{33} & \pi_{34} & \pi_{35} & \pi_{36}\\ \pi_{41} & \pi_{45} & \pi_{43} & \pi_{44} & \pi_{45} & \pi_{46}\\ \pi_{51} & \pi_{52} & \pi_{53} & \pi_{54} & \pi_{55} & \pi_{56}\\ \pi_{61} & \pi_{62} & \pi_{63} & \pi_{64} & \pi_{65} & \pi_{66}\end{pmatrix} \cdot \begin{pmatrix}T_1\\ T_2\\ T_3\\ T_4\\ T_5\\ T_6\end{pmatrix} \qquad 3.17$$

In this case in order to maintain consistency between the tensor and matrix notation the following conversion rules must be observed:

$\pi_{ijkl}=\pi_{mn}$ when both m and n are 1,2 or 3.
$\pi_{ijkl}=0.5\pi_{mn}$ when m and n are both 4,5 or 6.

The piezoresistive properties of silicon vary with crystal direction in much the same way as the mechanical properties. The piezoresistive coefficients are conventionally represented in a 6x6 matrix. This matrix has the same form as the compliance matrix discussed in section 3.3.3: if the conventional axis set is used only three independent coefficients are required, π_{11},π_{12},π_{44}. The numerical values of these components are dependent upon a number of factors, most important of which are the dopant type and the dopant density[13,14,15]. For the work described in this thesis all of the piezoresistors were fabricated with boron diffusion and are therefore p type. The most significant piezoresistive coefficient for p type silicon is the π_{44} coefficient: at surface concentrations of boron in the range $3x10^{18}$ this coefficient is about $120x10^{-12}$ cm^2/dyne. As the surface concentration of the dopant increases this value falls to $35x10^{-12}$ cm^2/dyne at a dopant concentration of $2x10^{21}$ atoms m^2 . It is an unfortunate consequence of the manufacturing process used in the fabrication of the devices in this thesis that a high boron concentration had to be used. For the purposes of estimating resistance changes as a function of applied stress the values given in equation 3.18 have been used.

$$\pi_{mn} = \begin{pmatrix}1 & -0.5 & -0.5 & 0 & 0 & 0\\ -0.5 & 1 & -0.5 & 0 & 0 & 0\\ -0.5 & -0.5 & 1 & 0 & 0 & 0\\ 0 & 0 & 0 & 35 & 0 & 0\\ 0 & 0 & 0 & 0 & 35 & 0\\ 0 & 0 & 0 & 0 & 0 & 35\end{pmatrix} \times 10^{-11} pa^{-1} \qquad 3.18$$

Showing the piezoresistive coefficients for heavily Boron doped silicon, using the conventional axis set, these results were taken from Tufte[8].

In the rotated axis set, equation 3.18 becomes:

$$\pi_{mn} = \begin{pmatrix} 17.75 & -0.5 & -17.25 & 0 & 0 & 0 \\ -0.5 & 1 & -0.5 & 0 & 0 & 0 \\ -17.25 & -0.5 & 17.75 & 0 & 0 & 0 \\ 0 & 0 & 0 & 35 & 0 & 0 \\ 0 & 0 & 0 & 0 & 1.5 & 0 \\ 0 & 0 & 0 & 0 & 0 & 35 \end{pmatrix} \times 10^{-11} pa^{-1} \qquad 3.19$$

In this form the coefficients are consistent with the stresses produced by the finite element models using the compliance matrix given in equation 3.13.

It can be shown that the π_{11} coefficient as a function of θ on a $\{110\}$ plane is given by:

$$\pi(\theta) = 1 - (2\cdot(1 + 0.5 - 35))\cdot\left[\left(\frac{1}{\sqrt{2}}\cdot\cos(\theta)\right)^2\cdot\sin(\theta)^2 + \sin(\theta)^2\cdot\left(\frac{1}{\sqrt{2}}\cdot\cos(\theta)\right)^2 + \left(\frac{1}{\sqrt{2}}\cdot\cos(\theta)\right)^4\right] \qquad 3.20$$

A plot of equation 3.20 is given in figure 3.10 This plot shows the optimum orientation for a piezoresistor on the (110) surface to be at 35.26 degrees to the Y axis, this is parallel to the direction in which the vertical $\{111\}$ planes intersect the $\{110\}$ planes. In addition figure 3.10 shows the symmetries of the $\{110\}$ silicon plane.

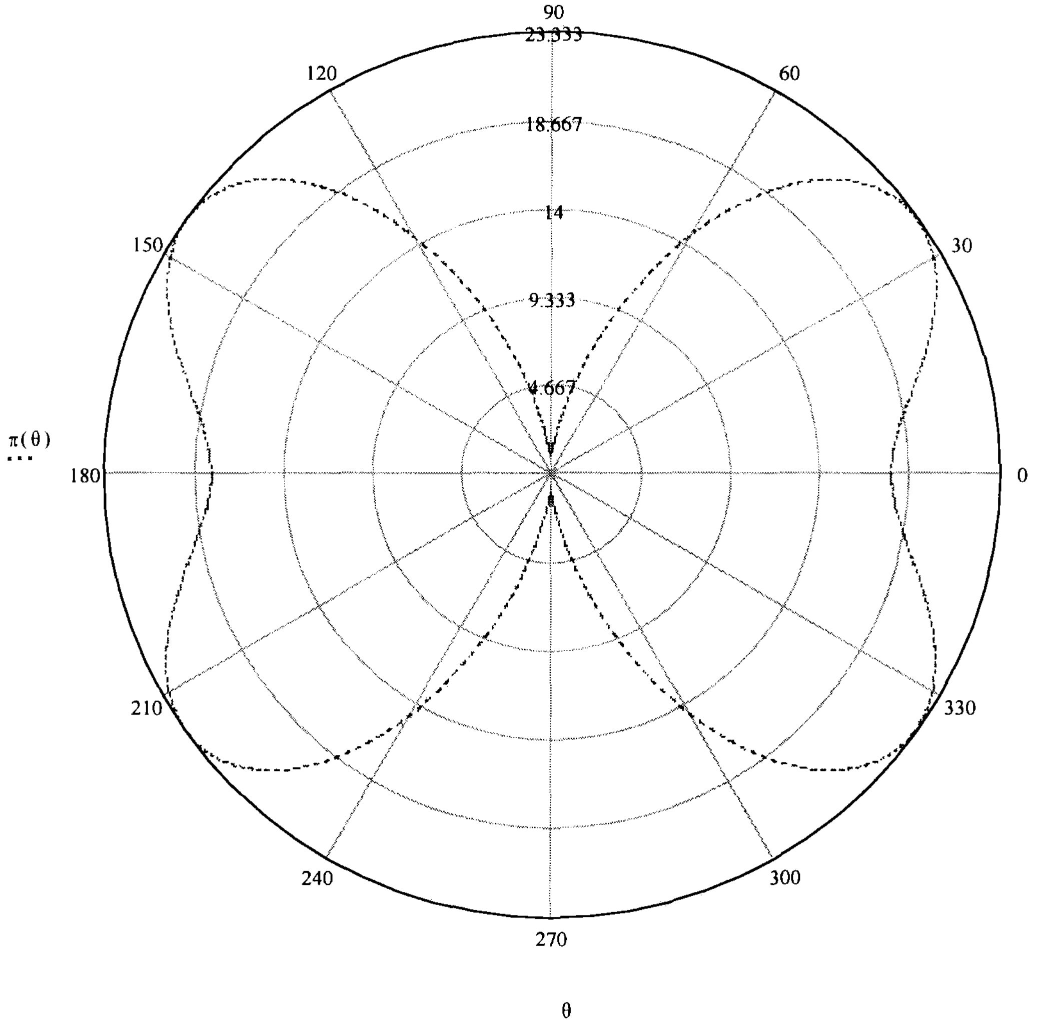

Figure 3.10 The variation of π_l with θ on the {110} plane. θ=0 corresponds to the Y axis.

Clearly the piezoresistive properties of silicon have a much stronger dependence upon crystallographic orientation than do the elastic properties.

3.4 Conclusions

The mechanical properties of single crystal silicon wafers have been reviewed, with particular attention to {110} oriented silicon. The transformed compliance tensor and corresponding matrix has been calculated for an axis set natural to {110} silicon. A plot of piezoresistance as a function of orientation on a {110} surface has also been made.The gyroscope described in chapter 5 has been specifically designed to reflect the symmetries of {110} silicon. This helps to minimise any cross coupling of the resonant modes of the gyroscope.

3.5 References

---

1 S.Wolf, R.N.Tauber Silicon Processing for the VLSI Era Volume 1- Processing Technology (1986) Lattice Press

2 S.M.Sze VlSI Technology 2nd ed. (1988) McGraw Hill

3 H.Seidel L.Cesprgi H.Herberger H.Baumgartel Anisotropic Etching of Crystalline Silicon in Alkaline Solution II the influence of Dopants J.Electrochem.Soc. 137 (1990) pp. 3626-3632

4 J.W.Gardener Microsensors (1994) Wiley Chapter 2.

5 M.J.Fagan Finite Element Analysis (1992) Longman

6 D. Hitchins A Finite Element Dynamics Primer (1992) NAFEMS

7 PAFEC Version 7.4 Users Manual

8 J.F.Nye, Physical properties of Crystals (1957) Oxford Press pp. 131 149

9 R.F.S. Hearmon An Introduction to Applied Anisotropic Elasticity (1961) Oxford University Press pp. 7-26

10 J.J. Wortman, R.A.Evans, Young's Modulus Shear Modulus and Poisson's ratio in Silicon and Germanium J.Appl.Phys, 36 (1965) pp. 153-156

11 W.Brantly Calculated Elastic Constants for stress problems associated with semiconductor devices J.Appl.Phys, 44 (1973) pp. 534-535

12 Wortman and Evens Young's Modulus, Shear Modulus, and Poisson's Ratio in Silicon and Germanium J.Appl.Phys, 36 (1964) pp. 153-155

13 O.N.Tufte, E.L.Stelzer Piezoresistive Properties of Silicon Diffused layers J.Appl.Phys, 34 (1962) pp. 313-318

14 C.S.Smith Piezoresistance Effect in Germanium and Silicon Phys.Rev 94 42 (1954) pp 313-318

15 Y.Kanda Piezoresistance Effect of Silicon Sensors and Actuators A 28 (1991) pp 83-91

Chapter 4

Membrane Gyroscope

4.1 Introduction

In this chapter the first of three gyroscope designs is presented. The structure is described and its method of operation as a gyroscope is explained. The fabrication process developed to make the test samples is also described. The mode shapes of the structure have been calculated, using the finite element technique, and are presented. Results of the testing of the device are given. The device has been shown to work successfully as a gyroscope. However the resonance of the device has been shown to be strongly non-linear. This non-linearity is explained in terms of a simplified model of the structure.

4.2 Design Description

The basic structure of the gyroscope is shown in figure 4.1. A pyramid shaped mass of solid silicon is supported in the centre of a thin square silicon membrane. The outer edge of the membrane remains attached to the silicon wafer (not shown).

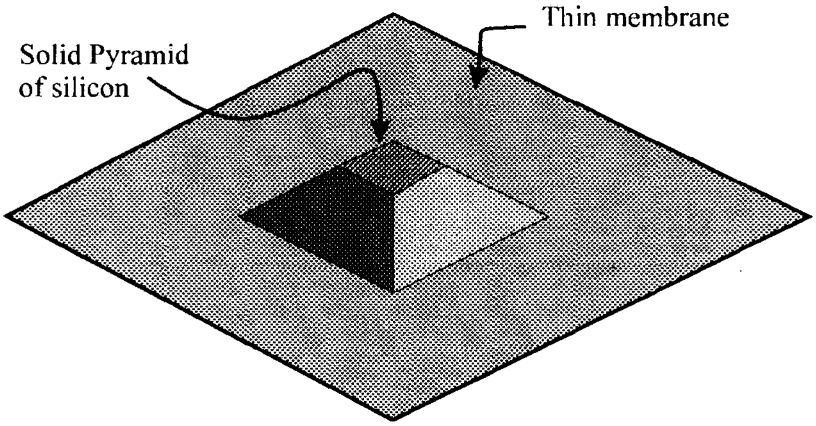

Figure 4.1 **Membrane Gyroscope**

The flexibility of the membrane allows the pyramid some freedom to rock from side to side. By applying equal and opposite forces on either side of the membrane, in a direction normal to the membrane, it is possible to excite this rocking motion. This situation is shown in figure 4.2a, where the primary resonance is shown as a rocking motion about the X axis. As a result of the rocking motion the centre of gravity of the pyramid is made to move back and forth along the Y axis.

Now if the whole structure is made to rotate about the Z direction, figure 4.2b, then a Coriolis force will be generated. The direction of the Coriolis force will be orthogonal to the rate of turn and to the direction of motion of the centre of gravity of the pyramid, as described in chapter 2, and will therefore act along the X direction. The Coriolis force will therefore cause the structure to begin resonating with the same rocking mode but about the Y axis. This situation is shown in figure 4.2b. The motion of the device is not dissimilar to the original Foucault pendulum, with the pyramid being the equivalent of the pendulum bob.

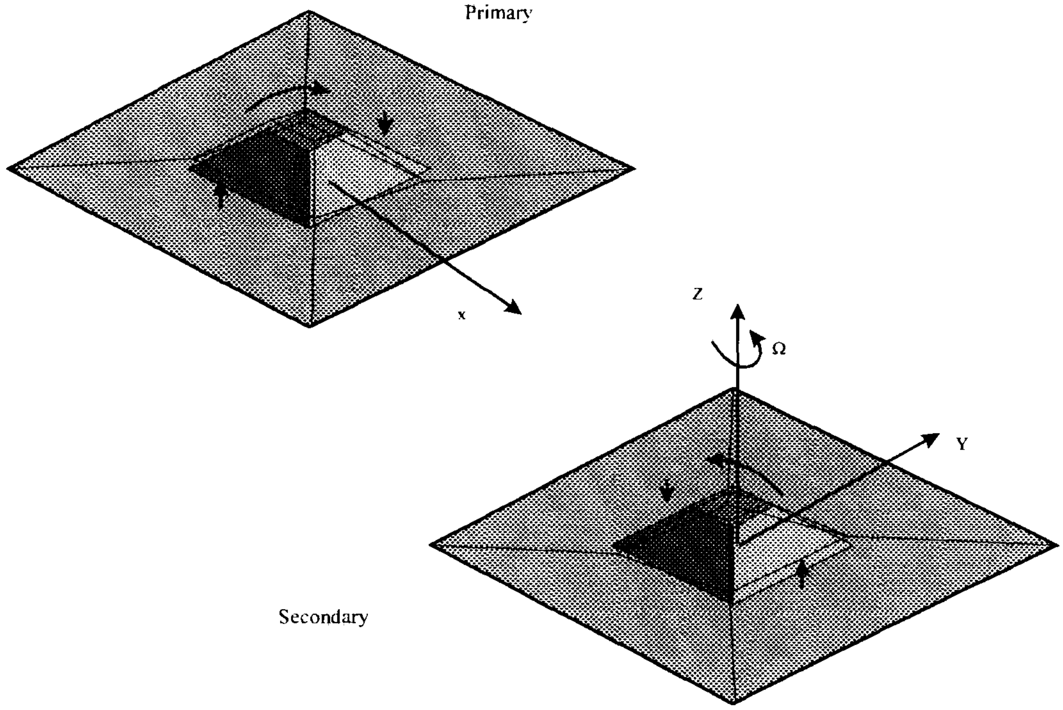

Figure 4.2 **The Primary and Secondary Resonances of the Gyroscope**

Due to the symmetry of the design the primary and secondary modes of the structure are interchangeable. This automatically means that in theory they will have exactly matched resonant frequencies, the optimum condition to ensure a maximum transfer of energy from the primary to secondary modes.

4.2.1 Drive and Sense Arrangement

Driving the gyroscope into resonance is achieved via a pair of electrodes positioned underneath the membrane on either side of the pyramid. These electrodes are close to, but not in contact with, the membrane. The membrane itself is also metallised and acts as a third electrode. With this arrangement it is possible to electrostatically drive the membrane into resonance by applying sinusoidal voltages to the electrodes (figure 4.3).

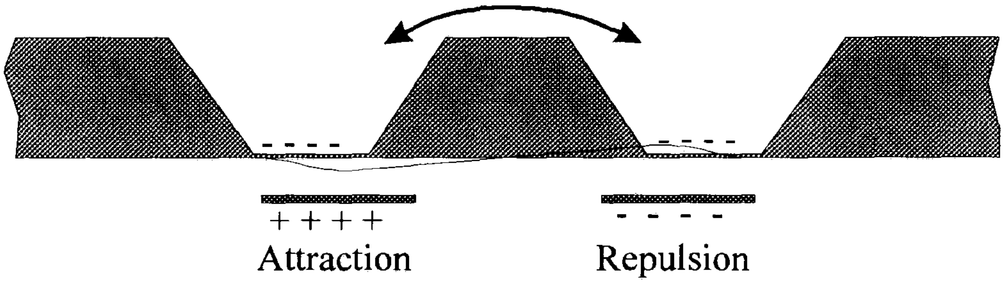

Figure 4.3 **A cross section of the gyroscope showing the electrostatic excitation/detection arrangement.**

A similar pair of electrodes positioned on the other two sides of the membrane act as capacitive displacement sensors to measure the amplitude of the secondary resonance, giving the measure of rate of turn.

4.3 Finite Element Analysis (FEA)

In order to check that the structure would move in the manner described a finite element (FE) model of the device was constructed. Figure 4.4 shows the FE mesh. Working from the centre of the structure outwards the pyramid is constructed from a combination of 20 node brick elements and 15 node wedge elements. This is then attached to the membrane which is modelled using thin shell elements. The shell elements that were used were able to simulate the bending stiffness as well as the in-plane tensile forces. The outer edge of the membrane is then attached to a frame of wedge and brick elements. All nodes on the four outermost faces of the structure were

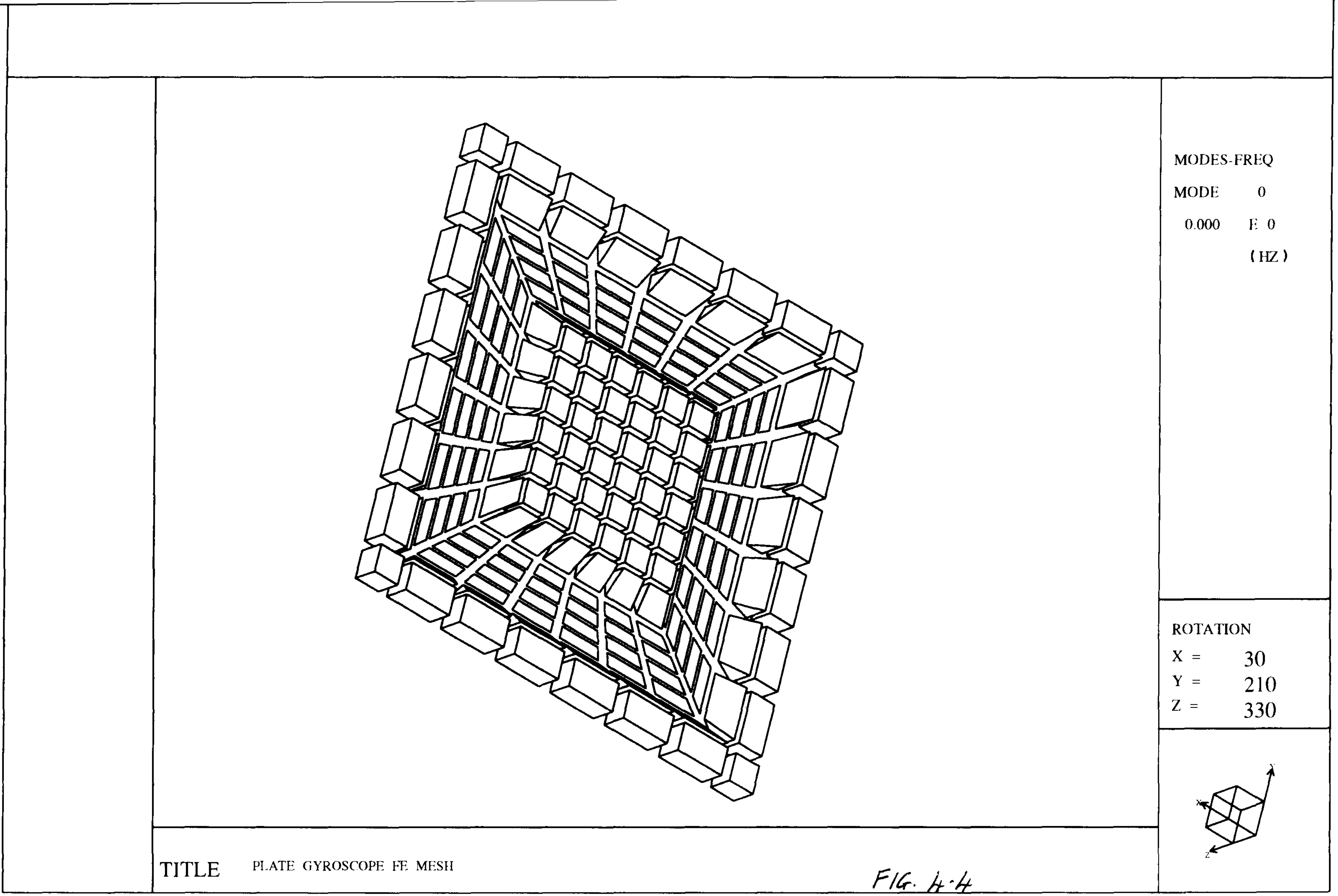
MODES-FREQ
MODE 0
0.000 E 0
(HZ)
ROTATION
X = 30
Y = 210
Z = 330
Y
X
Z
TITLE PLATE GYROSCOPE FE MESH

FIG. 4-4

MODES-FREQ

MODE 0

0.000 E 0

(HZ)

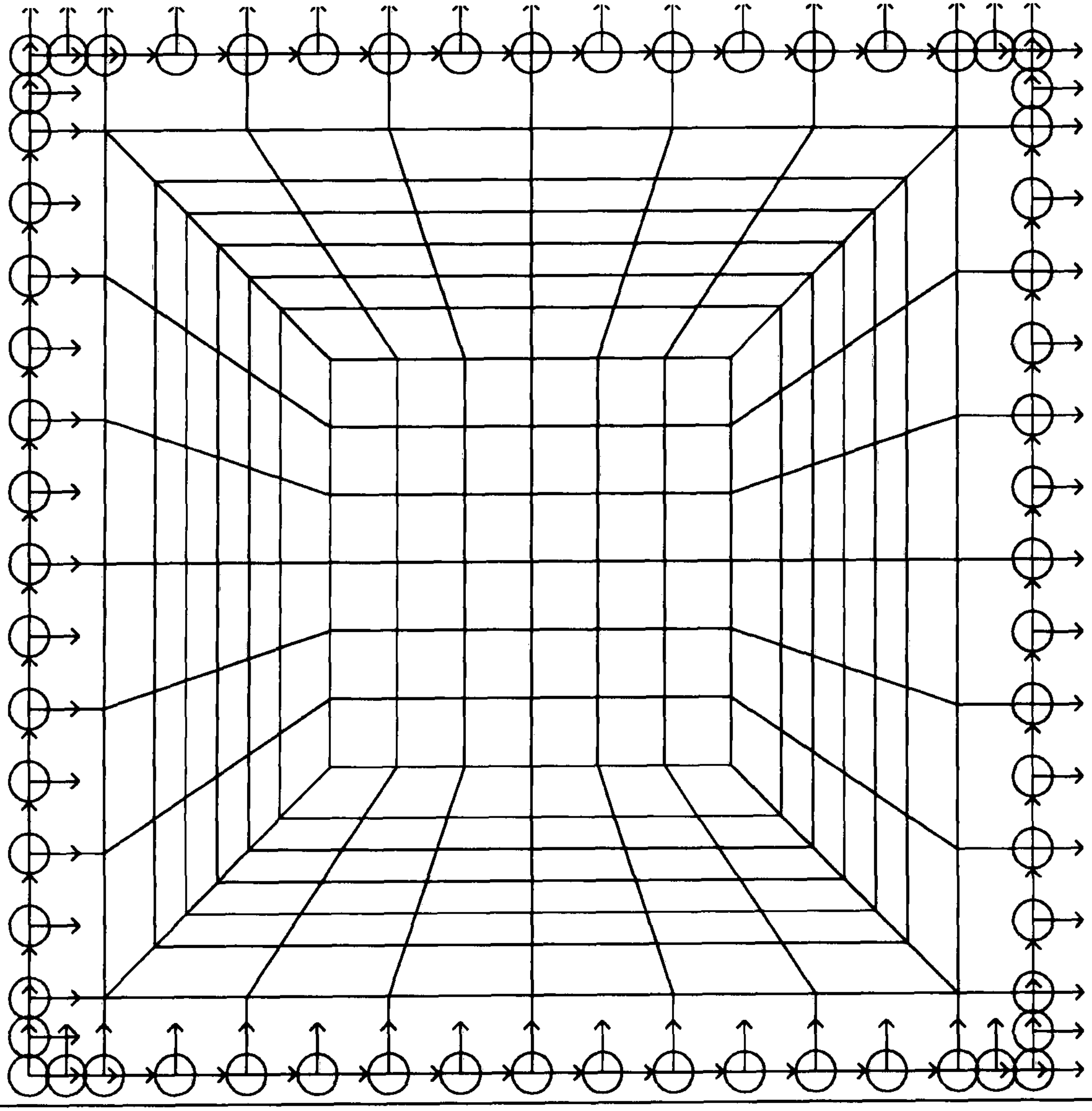

ROTATION

X = 0

Y = 0

Z = 0

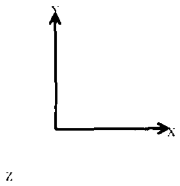

TITLE PLATE GYRO RESTRAINTS

FIG. 4.5

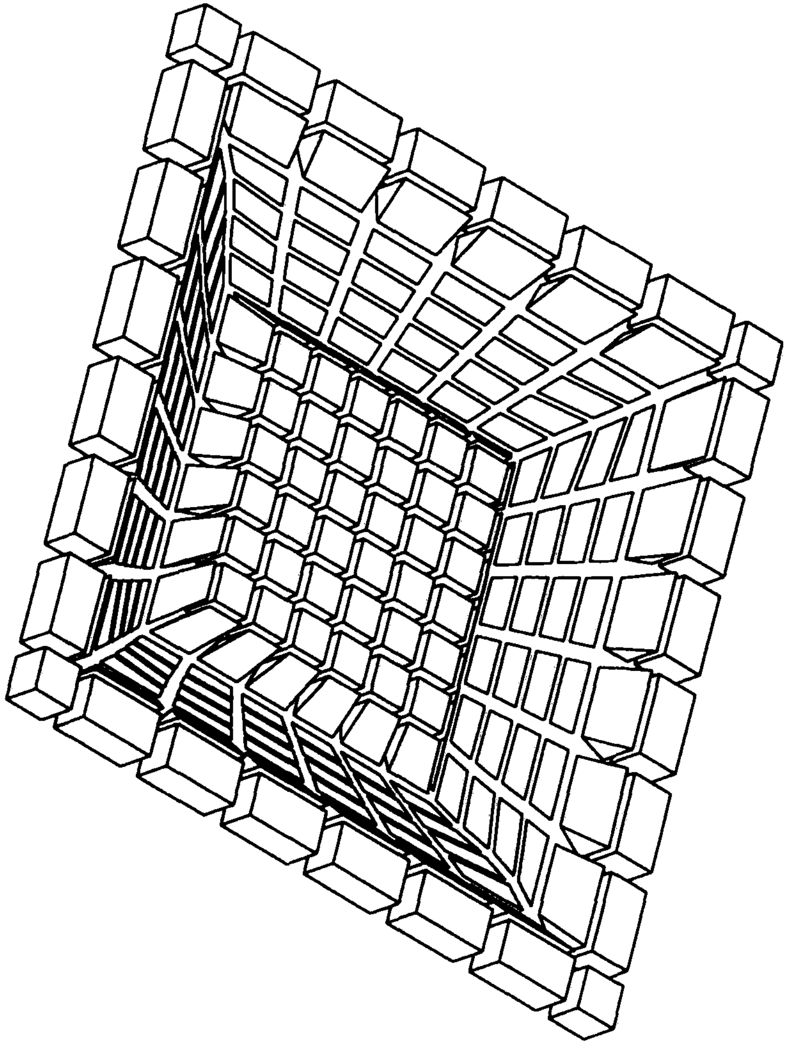

MODES-FREQ

MODE 1

0.617 E 3

(HZ)

ROTATION

X = 30

Y = 210

Z = 330

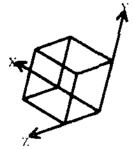

TITLE MODE 1

FIG 4·6

MODES-FREQ

MODE 2

1.420 E 3

(HZ)

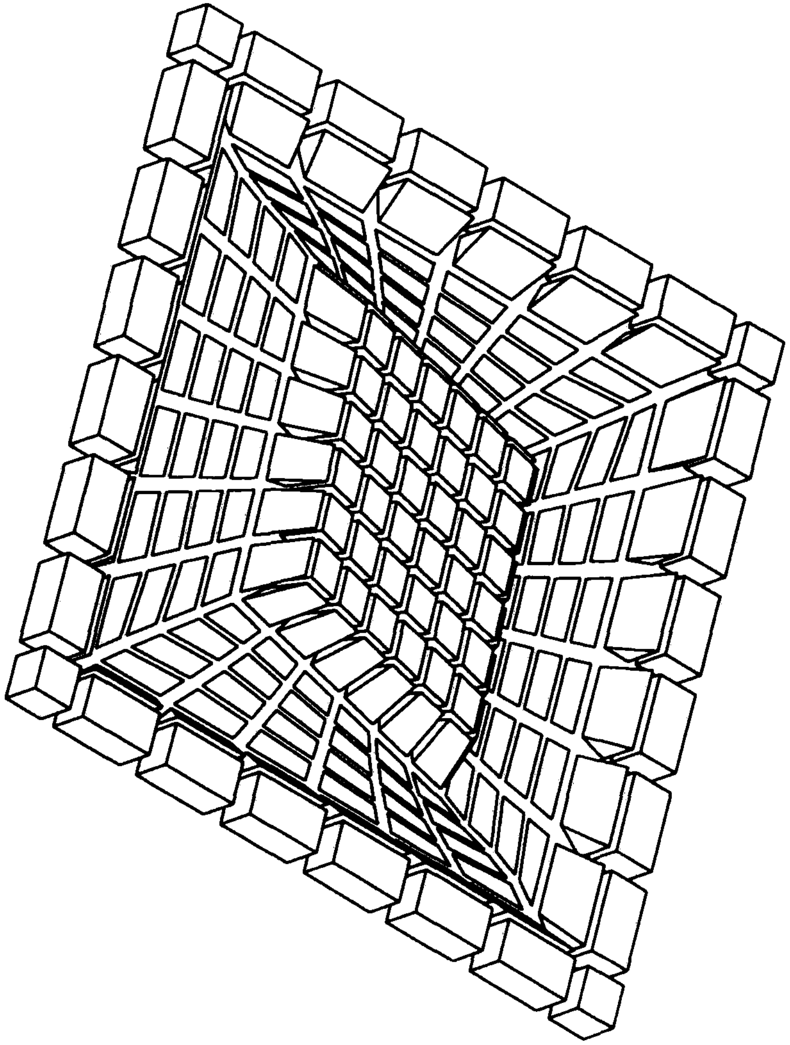

ROTATION

X = 30

Y = 210

Z = 330

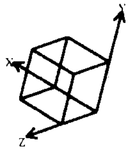

TITLE MODE 2

FIG 4·7

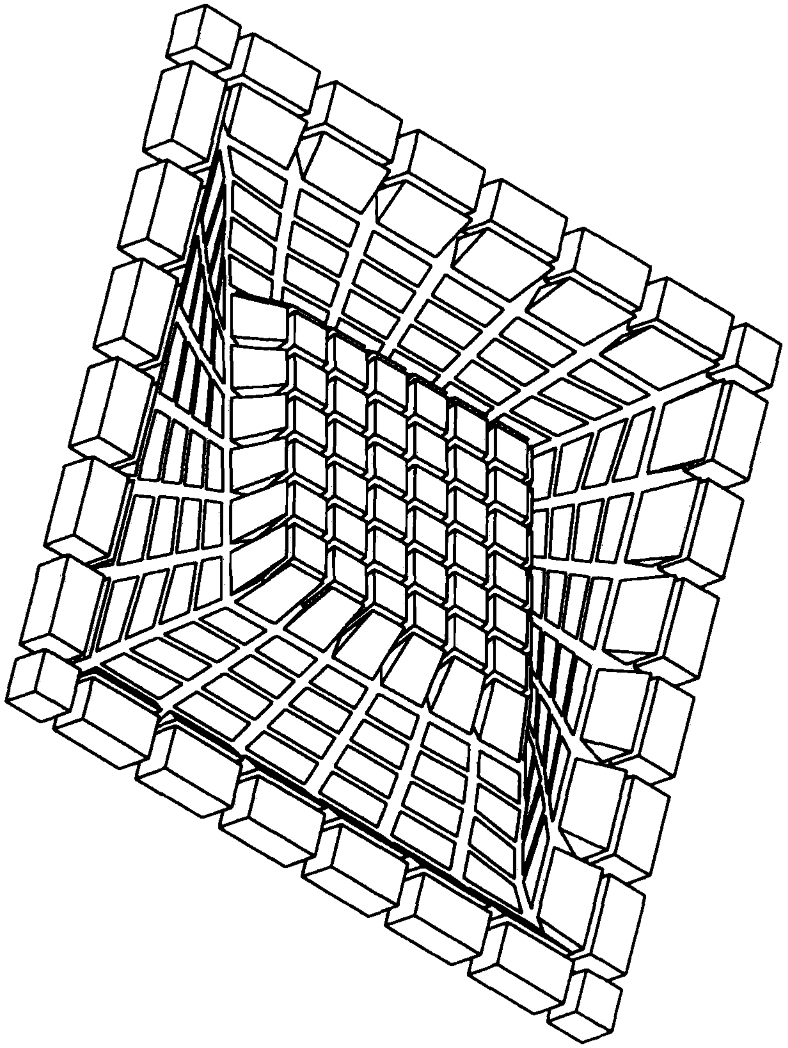

MODES-FREQ

MODE 3

1.432 E 3

(HZ)

ROTATION

X = 30

Y = 210

Z = 330

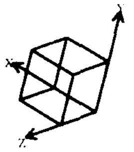

TITLE MODE 3

FIG 4·8

MODES-FREQ
MODE 2
1.420 E 3
(HZ)

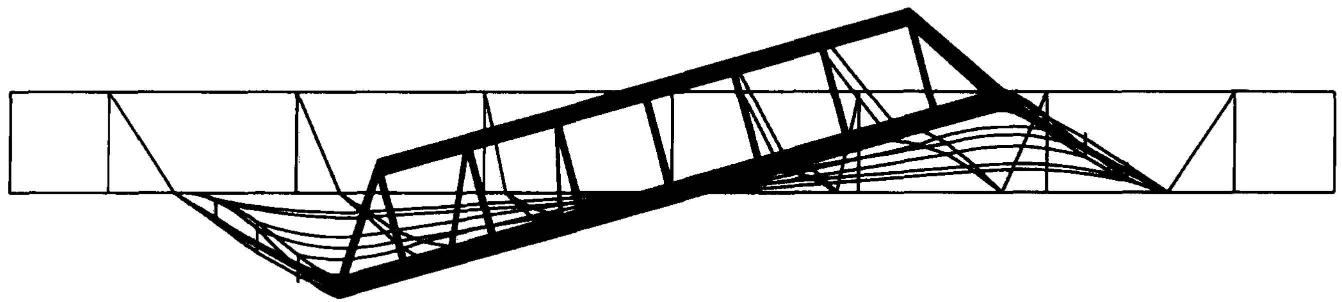

ROTATION
X = 90
Y = 0
Z = 0

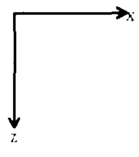

TITLE PLATE GYRO MODE 2

FIG 4.9

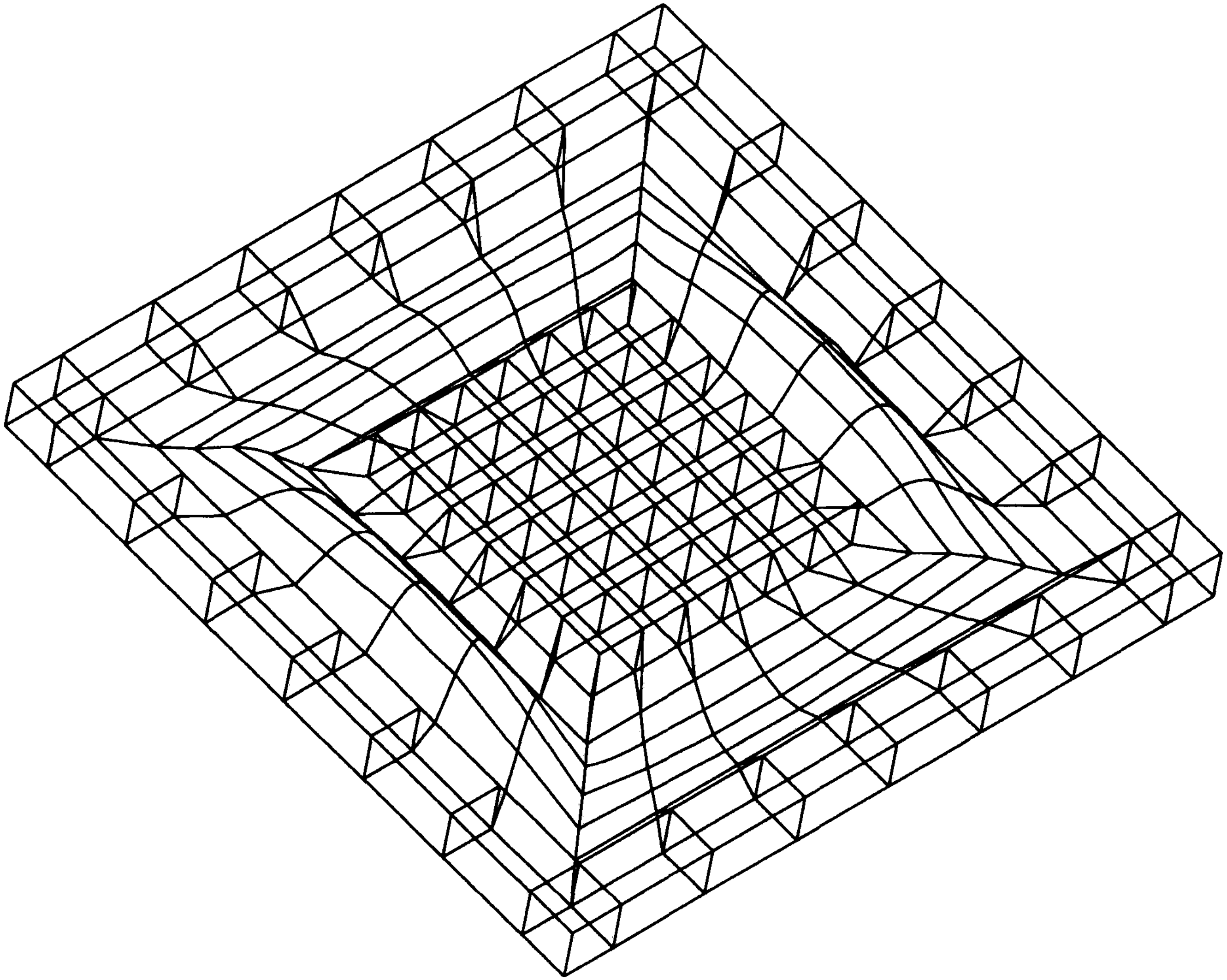

MODES-FREQ

MODE 4

0.494 E 5

(HZ)

ROTATION

X = 30

Y = 330

Z = 30

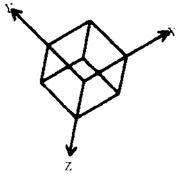

TITLE PLATE GYRO MODE 4

Fig 4.10

restrained in all directions giving an idealised mechanical ground: the restrained nodes are shown in figure 4.5.

The elastic material properties of all the elements, including those of the membrane, were described by the matrix 3.9, corresponding to the orthotropic properties of {100} silicon. Calculations were performed for a membrane 3 mm square with a pyramid in the centre whose base is 2 mm square and height is 300 μm, with a membrane thickness of 2.5μm. Figure 4.4 shows the finite element model of the structure with the central mass in the centre of the membrane. Figure 4.5 shows the restraints imposed upon the model, the outer most edge of the region being restrained in all 3 axes. Figure 4.6 shows the first resonant mode of the structure, a bouncing motion in the Z direction[*]. Figure 4.7 shows the primary mode[†], the central mass moves in a rocking motion about the Y axis. The secondary mode, figure 4.8, is a rocking mode about the X axis. Figure 4.9 shows these two modes in cross section. Figure 4.10 shows the next highest mode in which the central mass remains mainly stationary while the membrane resonates. The primary and secondary modes have equal resonant frequencies (the small difference of 12 Hz is due to numerical errors in the FEA).

In order to fabricate the membranes it is necessary to dope the wafer with boron. This doping process is known to cause a large tensile stress within the silicon. The level of the tensile stress is known to be dependent upon the doping concentration but its exact value is unknown. In the models described above no account of this pre-stress has been made. As a result the values of the predicted resonant frequencies were well below those measured on the real devices.

4.4 Fabrication

The fabrication of this device involves three stages. In the first stage the resonant element is manufactured. The electrodes are fabricated on a separate wafer and finally the two components are assembled.

---

[*] All of the finite element plots contain a labled axis in the bottom right hand corner: the directions described in the text agree with these axes.

[†] The primary and secondary modes are interchangeable in this device.

4.4.1 Membrane fabrication

The gyroscope structure was fabricated from wafers of single crystal silicon. The wafers were circular, having a diameter of 50mm and a thickness of 300μm. The wafers had been cut so as to make the faces parallel to a {100} plane. A small flat was ground on the outside edge of the wafer, this flat was oriented parallel to the direction of a {111} plane, this allowed the mask patterns to be correctly oriented to the crystal lattice on the wafer surface. One side of the wafer was polished to a mirror finish.

The first stage of the fabrication process was to clean the wafer, in order to remove any surface contamination which can adversely effect the thickness and quality of the oxide. The cleaning procedure involved boiling the wafers for one hour in a 1:1 mixture of hydrogen peroxide (H_2O_2) and sulphuric acid (H_2SO_4). Immediately following this the wafers were rinsed in deionised water twice and then place in a recirculating bath of de-ionised water for a further half hour before being dried in a centrifuge.

The wafers were then placed in an oxidation furnace, as described in section 2.2. The wafers were allowed to remain in the furnace for three hours during which time a constant flow of oxygen and steam was allowed to flow through the furnace. The furnace was maintained at a constant temperature of 1100° C.

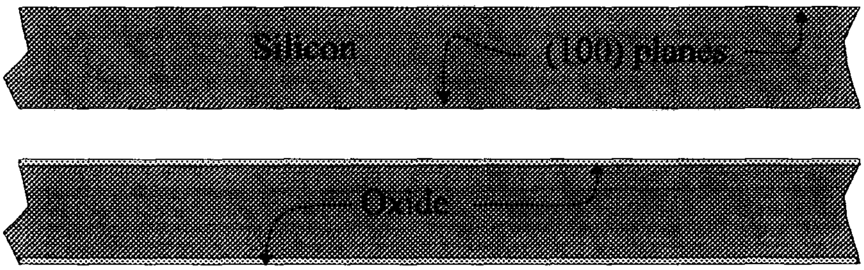

Fig 4.11 A cross section of the silicon wafer before and after the oxidation process.

This procedure produced an oxide thickness of about 0.8μm on both sides of the wafer. The oxide thickness was measured with an alpha step height measurement system described in section 3.6. A typical example of the step profile is shown in figure 4.12. The thickness of this oxide layer is not critical as it serves only as an etch mask and does not form part of the final structure.

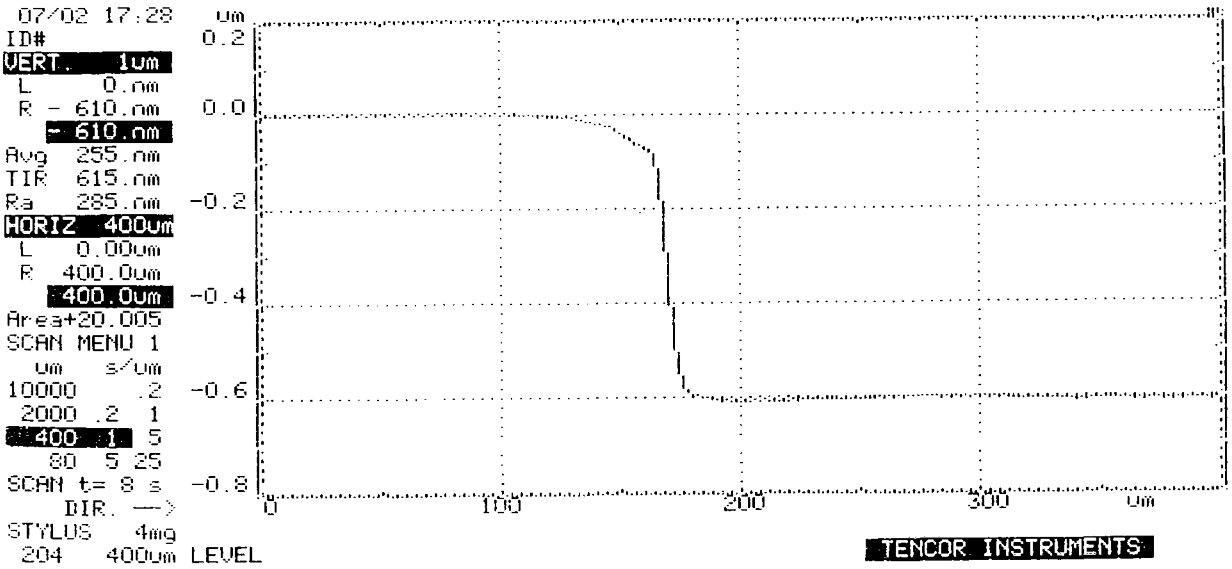

Figure 4.12 An Alphastep profile of the initial oxidation stage.

The next stage of the process was to remove the silicon dioxide from the mirrored surface of the wafer. The oxide was removed using a 40% solution of hydrofluoric acid (HF) and a 40% solution of ammonium fluoride in a ratio of 1:4 parts HF to NH_4OH. This solution would dissolve the silicon dioxide layer in around 4 minutes. The wafer was left in contact with the solution until the surface of the wafer became hydrophobic indicating that the oxide had been fully removed[‡]. This etchant does not significantly attack silicon so it is not necessary to control the process precisely .

During the oxide removal stage the wafer was clamped between two O rings in a custom made PTFE jig. The etchant could then be applied to only one surface of the wafer at a time allowing the oxide to be removed from the front surface without damaging the oxide on the reverse side.

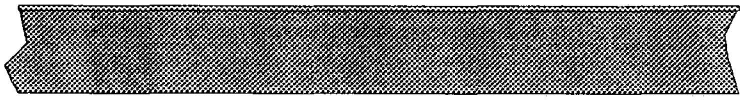

Figure 4.13 An oxidised wafer after the front side oxide has been removed.

[‡] Silicon dioxide is strongly hydrophilic whereas silicon is hydrophobic.

Following the oxide etch the wafer was again rinsed in de-ionised water and placed in a recirculating bath for half an hour before being centrifuged.

In the next stage boron dopant was diffused into the front surface of the wafer: at high concentrations the boron renders the silicon immune to etching in subsequent stages[§]. This process was carried out in a furnace similar to the one described in 3.2.2. The main difference being that the gas ambient in the furnace was 97% nitrogen and 3% oxygen. During the diffusion the bare face of the silicon wafer was held at a distance of a few mm from a disc of boron nitride, using a quartz jig. The boron atoms diffuse out of the boron nitride and into the silicon wafer. The process is carried out for 4 hours at a temperature of 1100° C. During this process the silicon dioxide on the reverse side of the wafer acted as a diffusion barrier, preventing the boron from entering the back of the wafer.

An unfortunate by-product of this process is the formation of a thin layer of heavily boron doped silicon oxide on the wafer surfaces. This layer was found to cause severe problems in subsequent processing as it adversely effected the adhesion of both the photoresist and the metal layers. The layer was also found to be highly resistant to attack by HF making subsequent patterning of oxide layer difficult. As a result the following procedure was developed to remove the layer: The wafer was boiled in a 1:1:1 mixture of Nitric, Hydrochloric and Sulphuric acids for 1 hour, then rinsed in de-ionised water before being etched in 10% HF solution for 30 seconds. Usually at this stage the front surface of the wafer was predominantly hydrophobic with a hydrophilic area in the centre. The wafer was then placed in the oxidation furnace in a steam ambient at 1100° C for 20 minutes. It was found that this last stage changed the nature of the film and rendered it soluble in HF solution. The final oxdation step also improved the photoresist and metal adhesion.

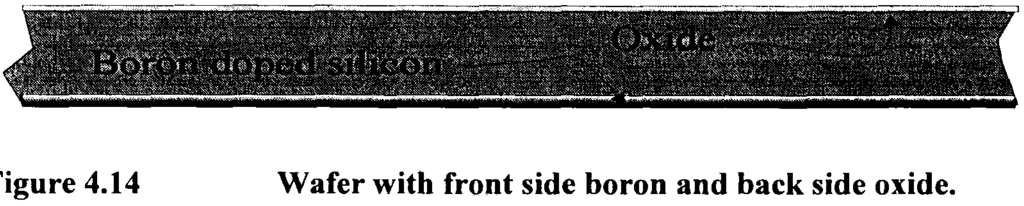

Figure 4.14 **Wafer with front side boron and back side oxide.**

[§] No equipment for measuring dopant concentration was available, as a result the required doping process was determined by trial and error.

The next phase of the fabrication process was to open a window in the oxide layer on the back side of the wafer. The purpose of this window was to expose selected areas of silicon on the back side of the wafer allowing the silicon to be etched by the anisotropic etchant. This was done using the photolithographic technique described in section 3.2.3. This was followed by another oxide etch process as described previously. The mask used for this pattern is shown in figure 4.20. The etching of the silicon oxide on the back of the wafer was done without the use of the PTFE jig described above. As a result the thin oxide layer, formed by the 20 minute oxidation process on the mirrored surface, was also removed.

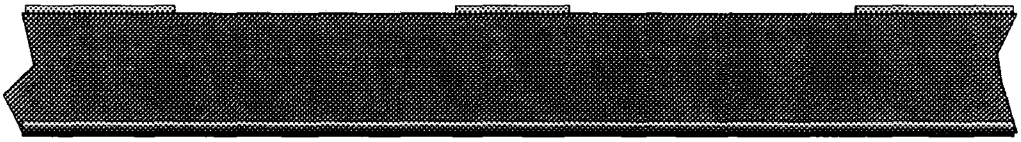

Figure 4.15 The wafer after the patterning of the silicon dioxide

The next stage of the process was to metallise the boron diffused side of the wafer. This metal layer acts as the top electrode in the capacitive drive/sense arrangement shown in figure 4.3. The metal layer was formed by evaporating first a layer of chrome and then gold, using the electron beam evaporation apparatus described in section 3.2.6. The chrome/gold combination was used as they were both resistant to the subsequent anisotropic etch process.

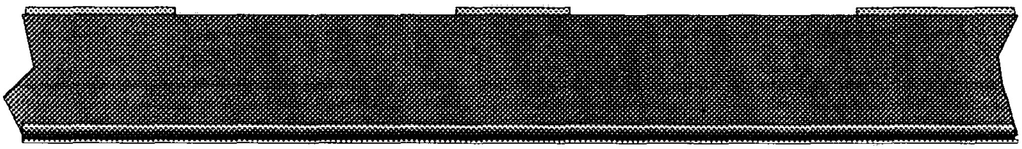

Figure 4.16 Wafer after the addition of the chrome & gold.

The first layer of chrome was used to act as an interface between the silicon and the gold. The adhesion of gold to silicon is very poor and the gold would tend to peel off the silicon during the final anisotropic etching if chrome was not used as an interface between the gold and silicon. The total thickness of the deposited metal layer was typically 0.3μm. An example of the step height of the two layers is shown in figure 4.17.

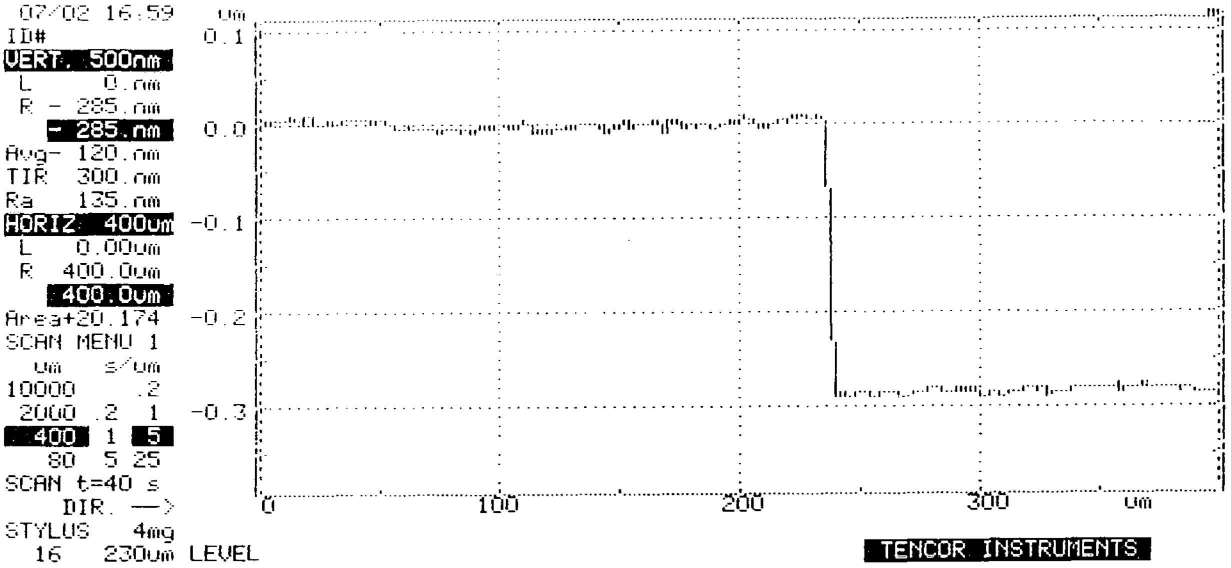

Figure 4.17 Alphastep of the chrome/gold combination

4.4.2 Anisotropic etching

The wafer was now ready for the anisotropic etch process which forms the structure of the device. All of the devices were made using the EDP etch solution described in section 3.2.1. During the etch process the silicon is gradually dissolved away as shown in figure 4.18.

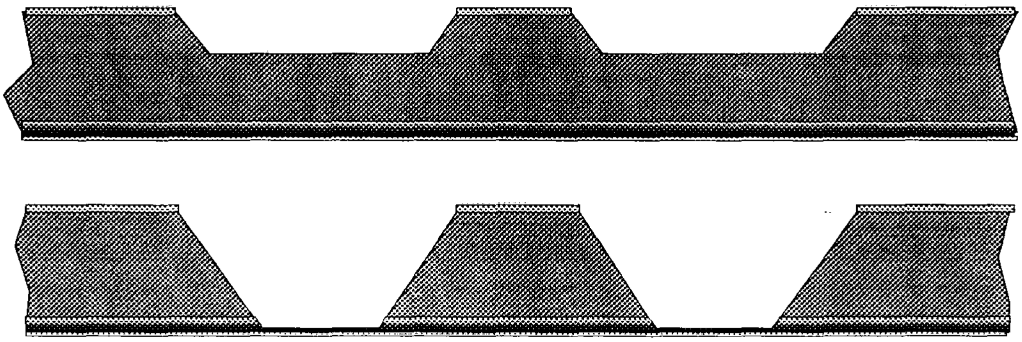

Figure 4.18 The etch partially and fully completed.

The etch proceeds vertically through the wafer until it reaches the boron diffused region on the front side of the wafer. Once the etch front has reached a region of sufficiently high boron concentration the etch rate is dramatically reduced and the etch effectively stops: the boron etch stop is described in section 3.2.5. In the horizontal direction the etch is controlled by the inclined {111} planes which run through the wafer at 54.7 degrees to the wafer surface and attacked at a much slower rate than the horizontal {100} planes. The resulting structure is shown in figure 4.18. This process typically took around 5 hours to produce a boron doped membrane free of any residual silicon.

The orientation of the wafer within the etch bath was found to be important. During the etch bubbles of hydrogen are formed on the surface of the silicon. These remain on the surface for a finite time and appear to hinder the etching process. If the wafer is held vertically the top of the wafer tends to etch more rapidly: this is thought to be due to the lower bubbles moving up the wafer surface disturbing those above it. As a result bubbles formed on the bottom section of the wafer tend to remain on the wafer surface longer and the etch proceeds more slowly in this region. To avoid this problem the wafer was held in a horizontal orientation within the bath. This arrangement produced a more uniform etch.

The point at which the etch front is stopped by the boron diffusion controls the thickness of the silicon membrane. This point depends upon both the diffusion profile, which itself depends upon length, time and temperature of the diffusion as well as the doping method, and also on the etchant used. Different etchants are stopped at different boron concentrations. However, a typical etch front will be stopped at a few microns from the front of the wafer.

In order to measure the thickness of the membrane a section of the membrane was pressed into contact with a cleaned wet glass slide. The glass slide was then allowed to dry naturally for a few hours before being placed on a hot plate at 80°C for an hour. After this process the membrane remained stuck to the surface of the slide and no Newton's rings or air bubbles could be seen at the interface between the membrane and the slide, when observed from the back of the slide. This indicated that the two surfaces were in contact. The Alphastep was then used to measure the step height of the membrane to the glass substrate. The Alphastep plot is shown below. With a 4 hour diffusion the resultant membrane thickness was 2.3μm.

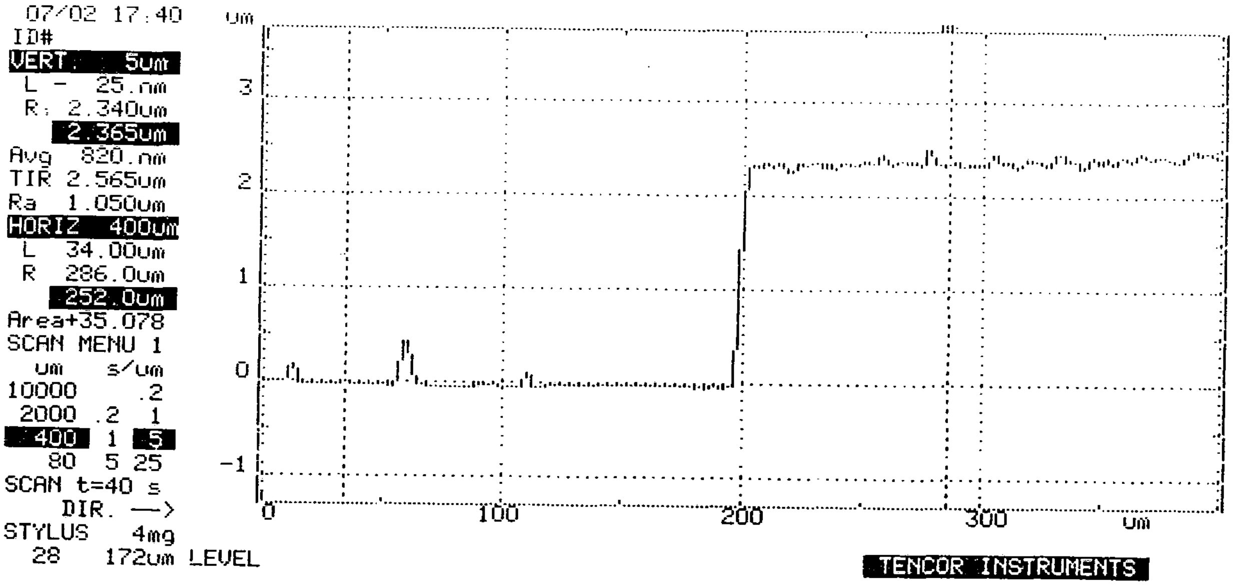

Figure 4.19 The step height of the membrane

Figure 4.20 shows the mask design that was used to define the membrane and the central mass. The structure has both convex and concave corners, the pyramid being bounded by 4 {111} planes meeting at convex corners and the membrane being bounded by 4 planes meeting at concave corners. A feature of the etch process is that these convex corners are attacked at a significant rate. This has the effect of reducing the size of the pyramid and making it non-square. In order to correct for this problem the corners were built out as shown: these areas are etched away during the process but they remain in place long enough to protect the corners of the pyramid.

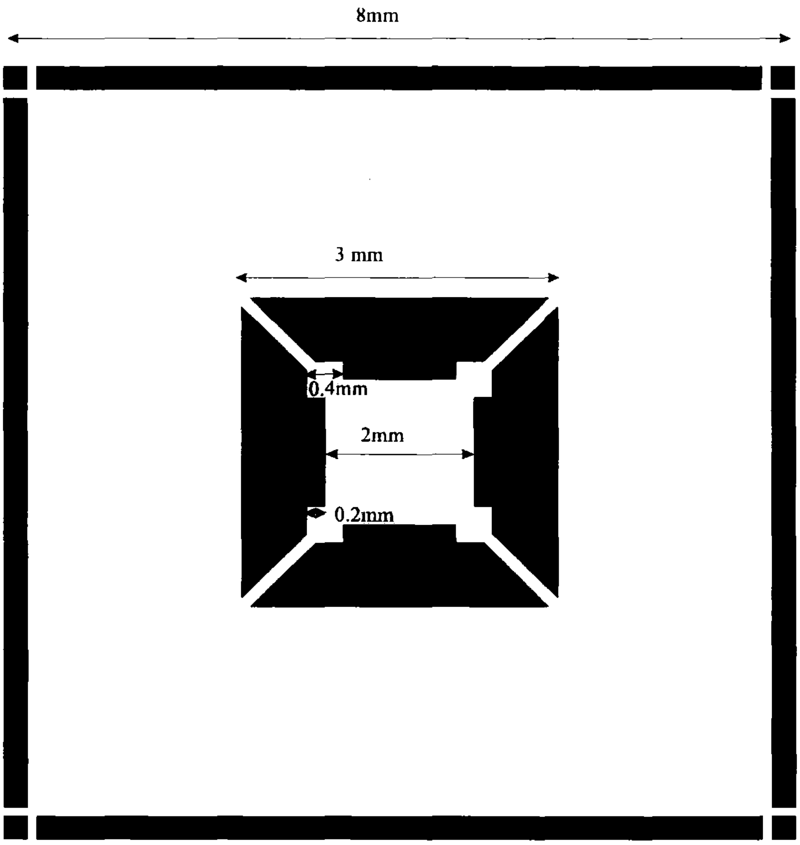

Figure 4.20 The mask pattern used to etch the membrane. The dimensions shown correspond to those of the final structure

In the mask shown all of the areas coloured black will be etched away. The black lines around the edge of the structure are etched into V grooved trenches and allow the central square containing the gyroscope to be separated from the silicon wafer. In addition to the corner compensation figure 4.20 shows four diagonal beams running from the corners of the pyramid across the membrane. These beams also contribute to the corner compensation. However their main purpose is to provide mechanical support to the structure during the assembly process.

As the beams are not aligned with the crystal planes the silicon beneath them is dissolved away, leaving a free standing beam. These beams are left in place during the assembly process and help to prevent the membrane from fracturing while the wafer is diced. Once the membrane is assembled with the drive electrodes the whole structure becomes more robust and the beams may be removed. This a done by touching the beams with a pin to fracture them and then blowing the broken beam away with a nitrogen gun.

Six membranes were fabricated at the same time on each wafer that was processed.

4.4.3 Fabrication of the Electrode arrangement

The second component of the structure is the electrode arrangement containing the drive and sense electrodes. The electrode arrangement was fabricated onto a Pyrex glass disc, 50 mm in diameter and 1.5mm thick[§].

The first stage of the process was again to clean the glass discs: this was done in the same manner as used for the silicon wafers. After this stage the disc was metallised, again with the gold on chrome layer previously described.

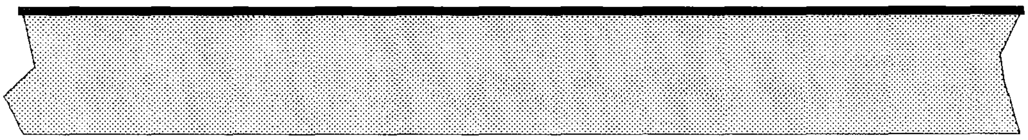

Figure 4.21 Glass disc with first metal layer

This metal layer was used as an etch mask in order to form the spacing trench in the surface of the disc. A more conventional technique would have beene to use a simple photoresist mask as used to pattern silicon dioxide. This technique was originally tried. However the adhesion of the photoresist to the Pyrex was found to be insufficient to survive the long etch time used to make the trench. In addition the pattern transfer from the mask to the photoresist was poor. One possible cause of this poor pattern transfer may be the fact that the glass is transparent to UV light, allowing light passing through the mask to be internally reflected inside the wafer causing masked areas to be exposed from the back. The gold was patterned using a wet etching process: A solution of KI : I_2 : H_2O in a ratio of 4:1:8, by volume, was used. This solution dissolved the gold without attacking either the photoresist or the chrome layer. The photoresist was then removed. Finally the exposed chrome was removed using a two

---

[§] Pyrex glass was used as pyrex allows the silicon to glass anodic bonding technique to be used. This technique has not been used in the current proces however a final device would most likely employ the technique in the assembly stage.

part chrome etchant: Solution A consiting of 83.5g NaOH: 167ml H_2O , solution B consisting of 167g $K_3[Fe(CN_6)]$: 500ml H_2O. Solutions A and B were mixed just prior to etching in a ratio of 1A:3B.

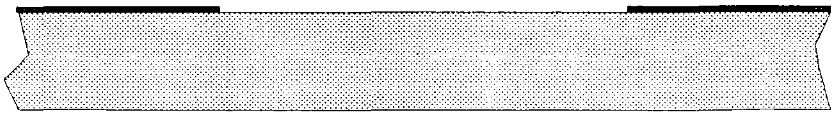

Figure 4.22 The glass disc with a patterned metal layer.

The next stage was to etch the trench, this process was done using a 1:4 solution of HF to ammonium fluoride. The disc was left in the solution for 1 hour. This etch time produced a trench depth of about 1.8μm. An alpha step plot of the trench step height is shown in figure 4.23. Following the trench etch the remaining metal was removed, leaving a bare disc with a trench patterned in its surface.

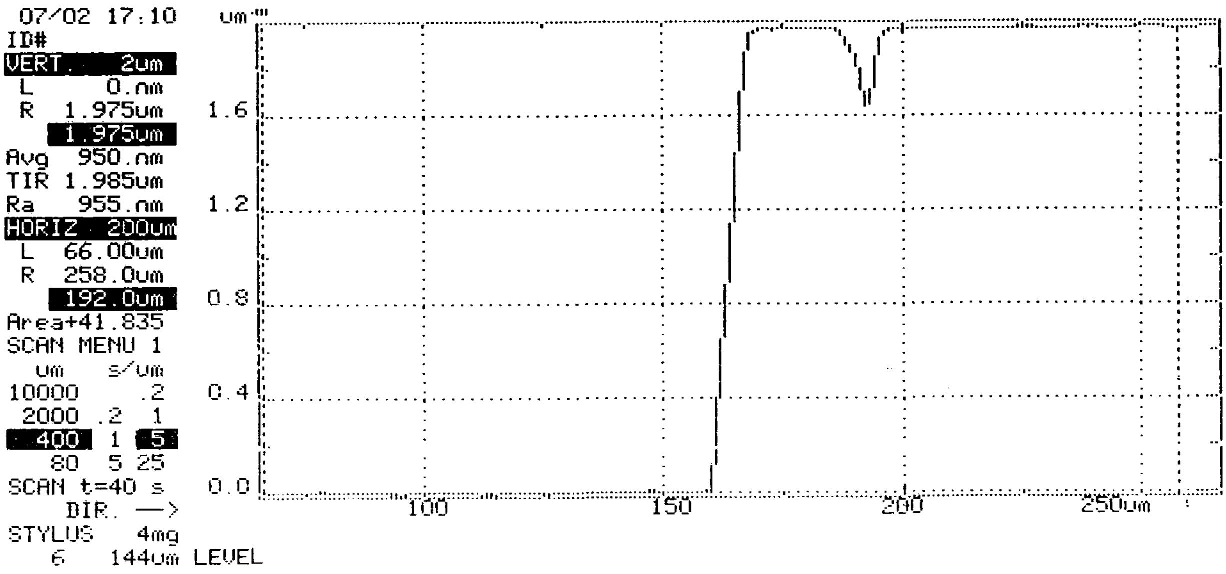

```
 07/02 17:10
ID#
VERT.    2um
 L     0.nm
 R  1.975um
    1.975um
Avg  950.nm
TIR 1.985um
Ra   955.nm
HORIZ  200um
 L  66.00um
 R  258.0um
    192.0um
Area+41.835
SCAN MENU 1
  um    s/um
10000     .2
 2000  .2  1
  400   1  5
   80   5 25
SCAN t=40 s
     DIR. —>
STYLUS   4mg
   6   144um LEVEL
```

Fig 4.23 Trench depth profile

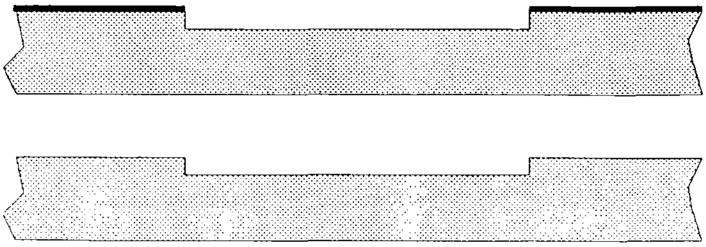

Fig 4.24 Disc with etched trench before and after the first metal layer is removed.

The pattern of the trench is shown in figure 4.25. The central square region sits immediately below the membrane while the arms extending from this region are there to act as channels along which the tracks connecting to the capacitor plates are routed.

The etched disc was then metallised again with gold and chrome and the metal is patterned into the desired arrangement for the electrodes. The electrode arrangement has a total of 8 connections as shown in figure 4.26. Four of these go directly to the drive/sense plates and another two are connected to a guard ring running between all of the electrodes. All of these are positioned in the bottom of the etched trench. The two other connections are not in the trench, but instead sit on the wafer surface. This allows an electrical contact to be made with the metal on the membrane.

The guard ring was found to be necessary in order to minimise electrical coupling between the 4 plates.

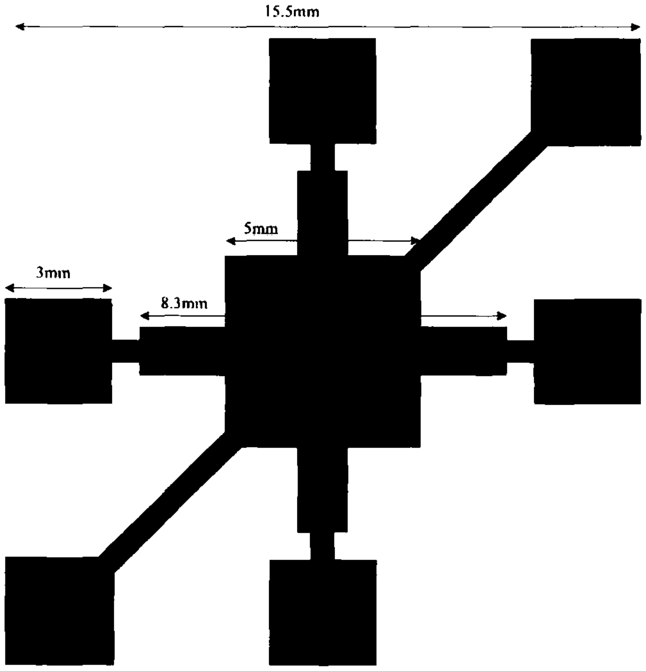

Figure 4.25 Mask pattern of the trench pattern

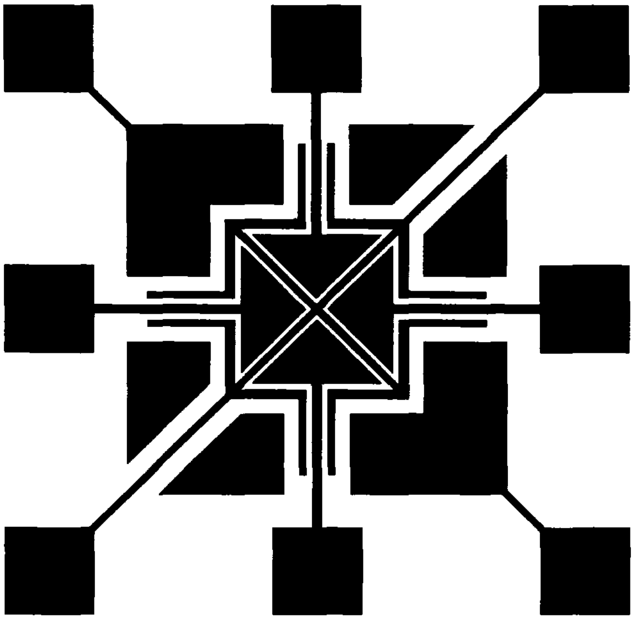

Figure 4.26 The electrode arrangement.

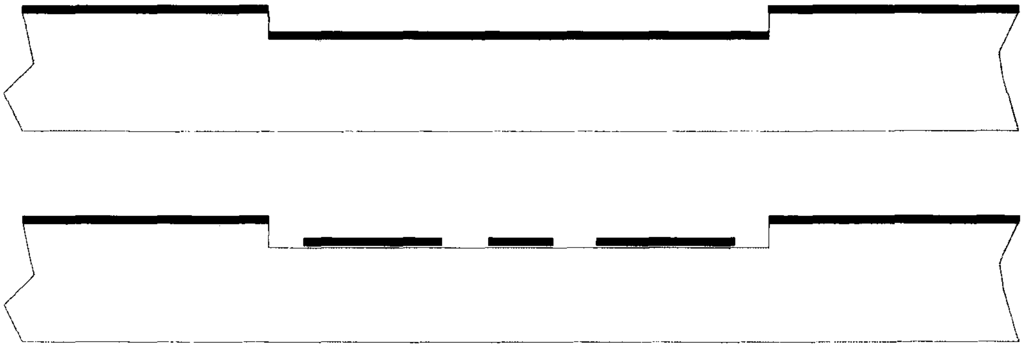

Figure 4.27 After the final metallisation and patterning stages.

The final stage was in assembling the membrane and electrodes. For the test structures this was done simply by eye and the membranes were fixed in place with a drop of adhesive at each corner. Figure 4.28 shows a cross section of the completed device.

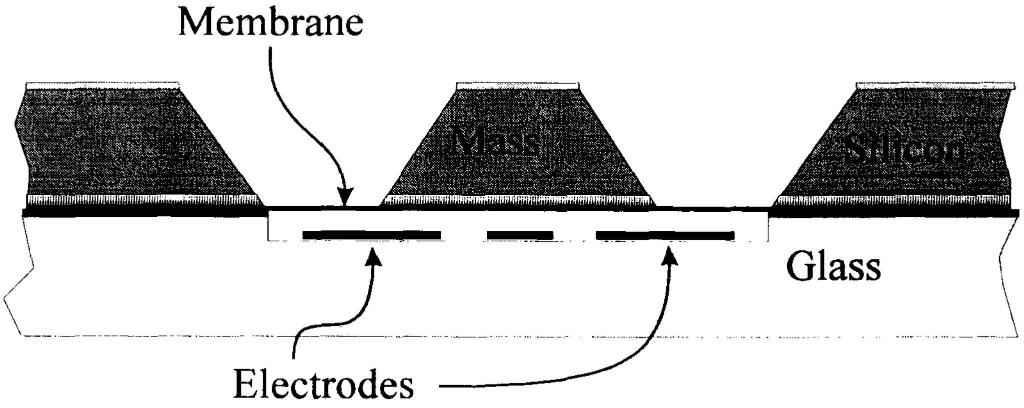

Figure 4.28 A cross section of the completed device.

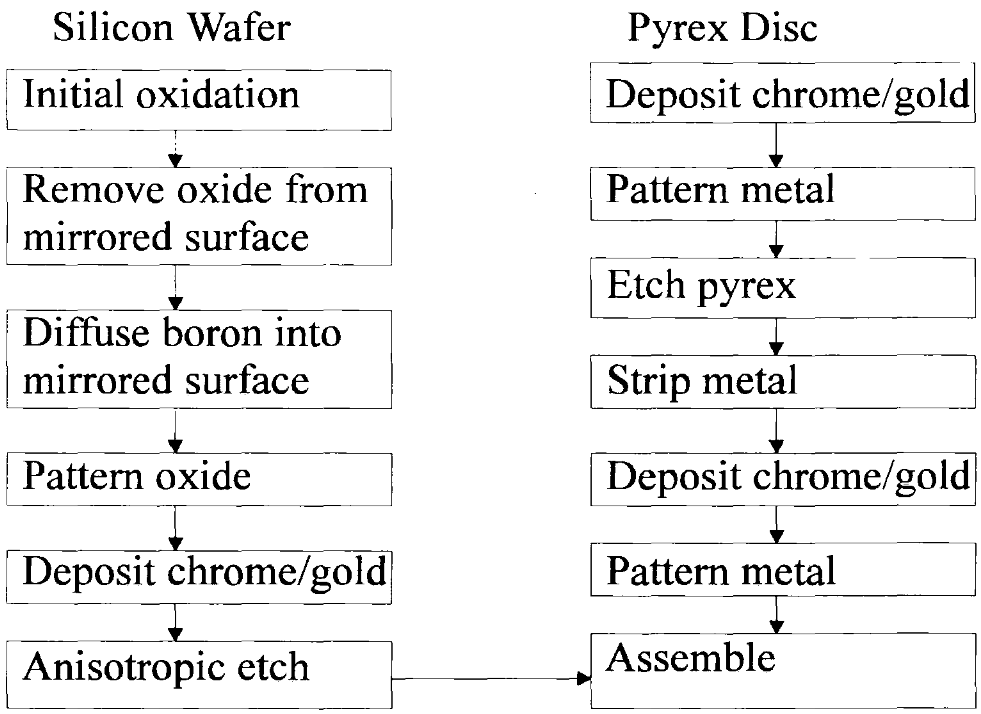

Figure 4.29 Flow chart of the fabrication process

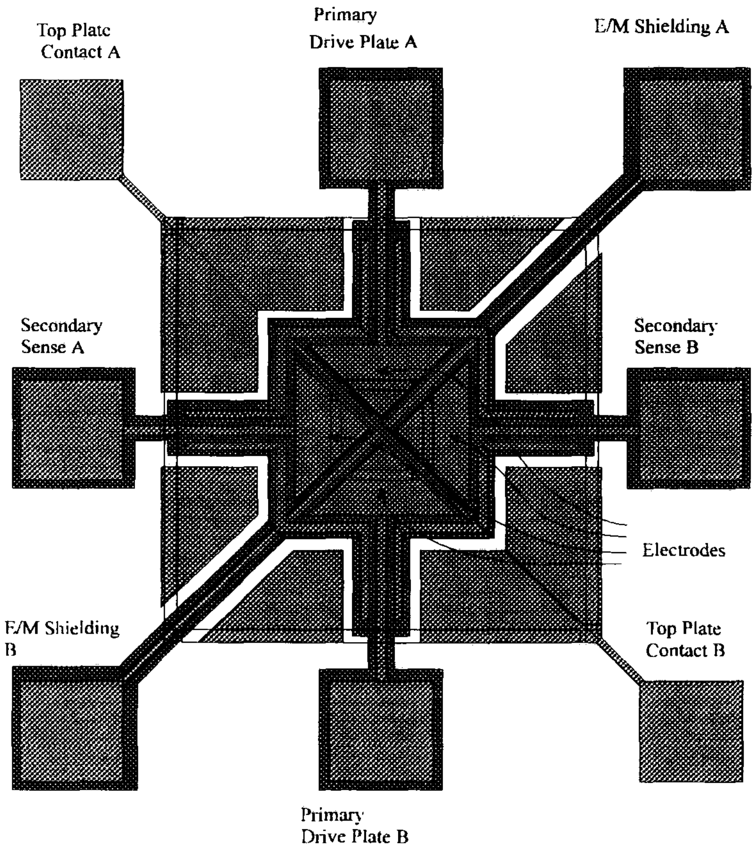

Figure 4.30 A plane view of the complete structure.

Figure 4.30 shows the electrode arrangement, light grey, superimposed on the trench pattern in dark grey. Note that the electrodes marked top plate contact are not lying in a trench.

4.5 Testing[**]

The completed device was tested both optically, electrically and finally on a turntable. During testing the device was held in a vacuum chamber at pressures from 1.6 to 1.8 mbarr. It was necessary to hold the device under vacuum in order to prevent air from damping the resonance. The need to operate the device in vacuum is common to most resonant gyroscopes.

4.5.1 Laser Doppler Tests

Measuring the amplitude of the resonance was done with a laser Doppler interferometer system. The system used passed a laser beam down an optic fibre. The beam was focused onto the membrane surface using a lens on the end of the fibre optic. The reflected light was transmitted back along the same fibre. The laser Doppler system could directly measure velocity and displacement. A block diagram of the system is shown in figure 4.31.

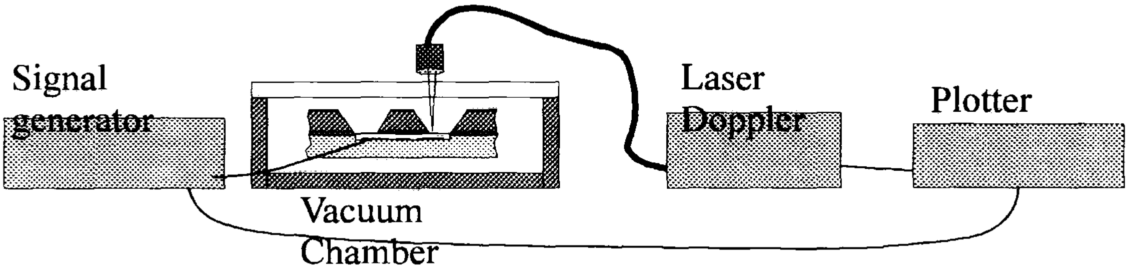

Figure 4.31 Laser Doppler interferometer

In order to ascertain that the membrane was moving in the desired manner a constant amplitude sinusoidal signal of 0.6V was applied to one electrode and measurements of the phase and displacement of the membrane were taken at 5 different points on the

---

[**] The following measurements were performed by Jane Cruickshank at Newcastle University.

structure. One point in the centre of the pyramid and one point on the membrane immediately adjacent to the pyramid half-way along each of its four sides. The Nyquist plot of the displacements at each of the 5 points is shown in figure 4.32. The phase angle is with respect to the drive voltage. The largest lobe, on the left hand side, corresponds to the measurement taken above the drive electrode, while the second largest lobe was measured immediately above the opposite electrode. The maxima of these two lobes are 180^0 degrees out of phase with each other, indicating that the points are moving in antiphase. The measurement taken on the pyramid itself correspond to the smallest of the five lobes, indicating that it is moving with a small amplitude. These three results indicate that the membrane is rocking in the desired mode. The remaining two lobes correspond to measurements taken above two remaining electrodes. In theory, if the measurement point were positioned exactly along the centre line of the device, that is on the node point of the resonance, then these two lobes should vanish. Their relatively large size is probably due to asymmetry in the structure, which will tend to cause the mass to couple both primary and secondary modes, and to misalignment of the laser spot to the node of zero displacement.

4.5.2 Non-Linearity of the gyroscope

Figures 4.33 to 4.37[‡‡] show plots of amplitude against frequency around the resonance peak. Each plot was made with a successively higher drive voltage. Figure 4.38 shows a plot of the peak displacement against drive voltage for the five traces. All of these measurements were taken at the same point. Figure 4.33 shows a fairly standard resonance peak, having a largely symmetric shape. As the drive force and hence the amplitude is increased the peak becomes gradually skewed towards the high frequency side. In figure 4.37 the shape of the peak is distorted into a 'shark fin' having a discontinuity on the high frequency side.

[‡‡] **The vertical axis of figures 4.33 to 4.37 represent displacement, each division being 1.25μm.**

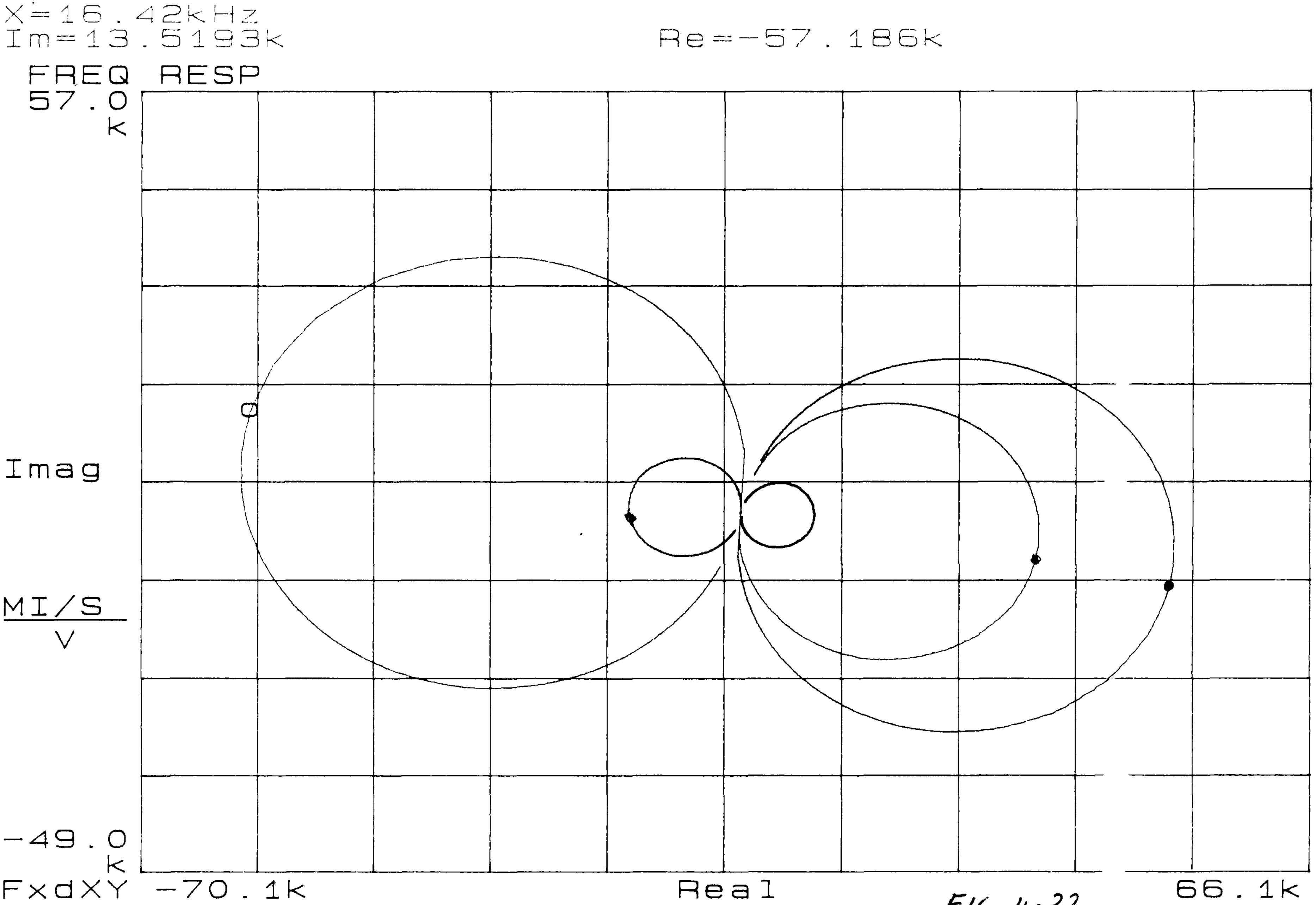
X=16.42kHz
Im=13.5193k
Re=-57.186k
FREQ RESP
57.0
k
Imag
MI/S
V
-49.0
k
FxdXY -70.1k
Real
66.1k

FIG 4-32

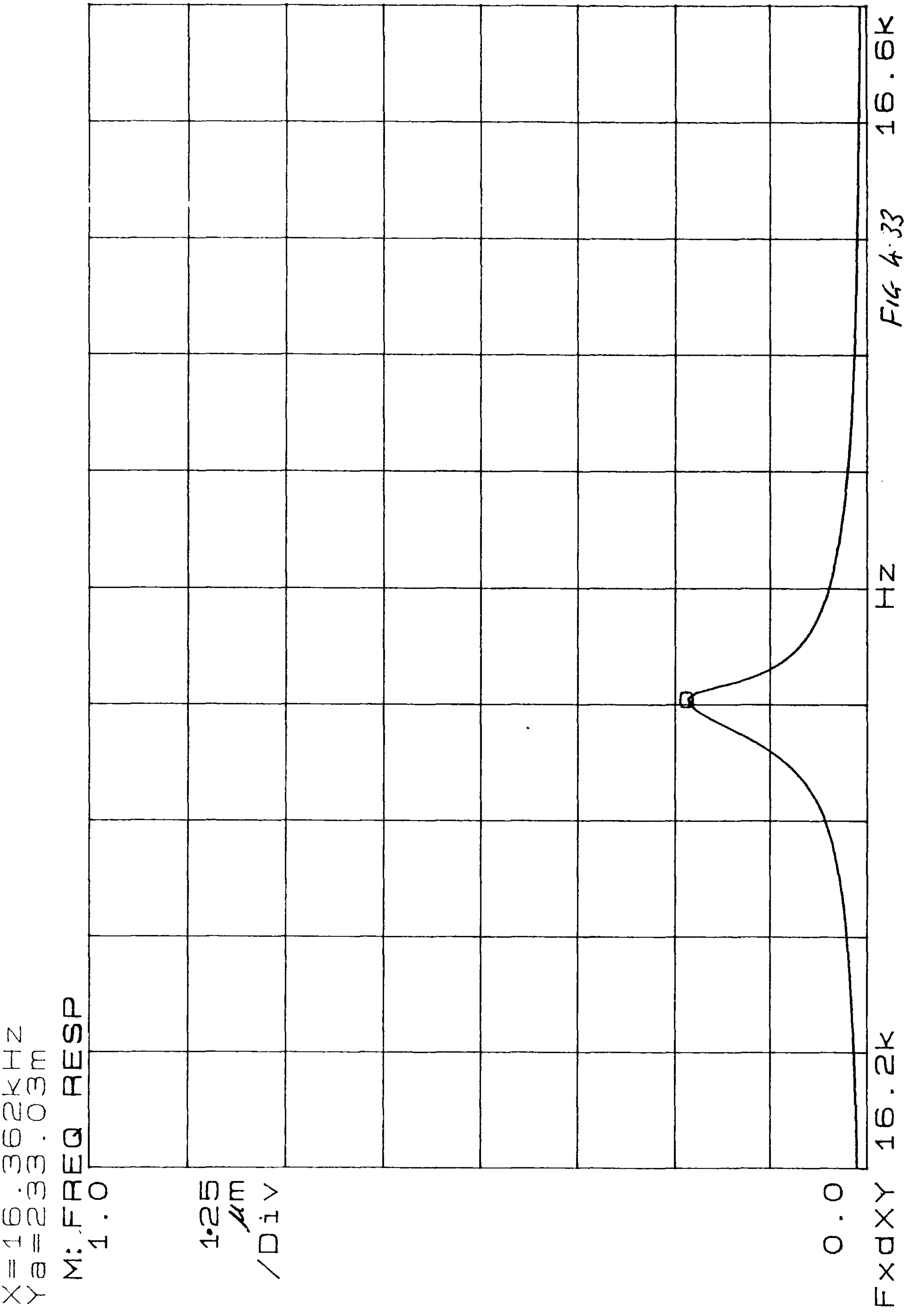
X=16.362kHz
Ya=233.03m
M: FREQ RESP
1.0
1·25
μm
/Div
0.0
FxdXY
16.2K
Hz
16.6K

FIG 4·33

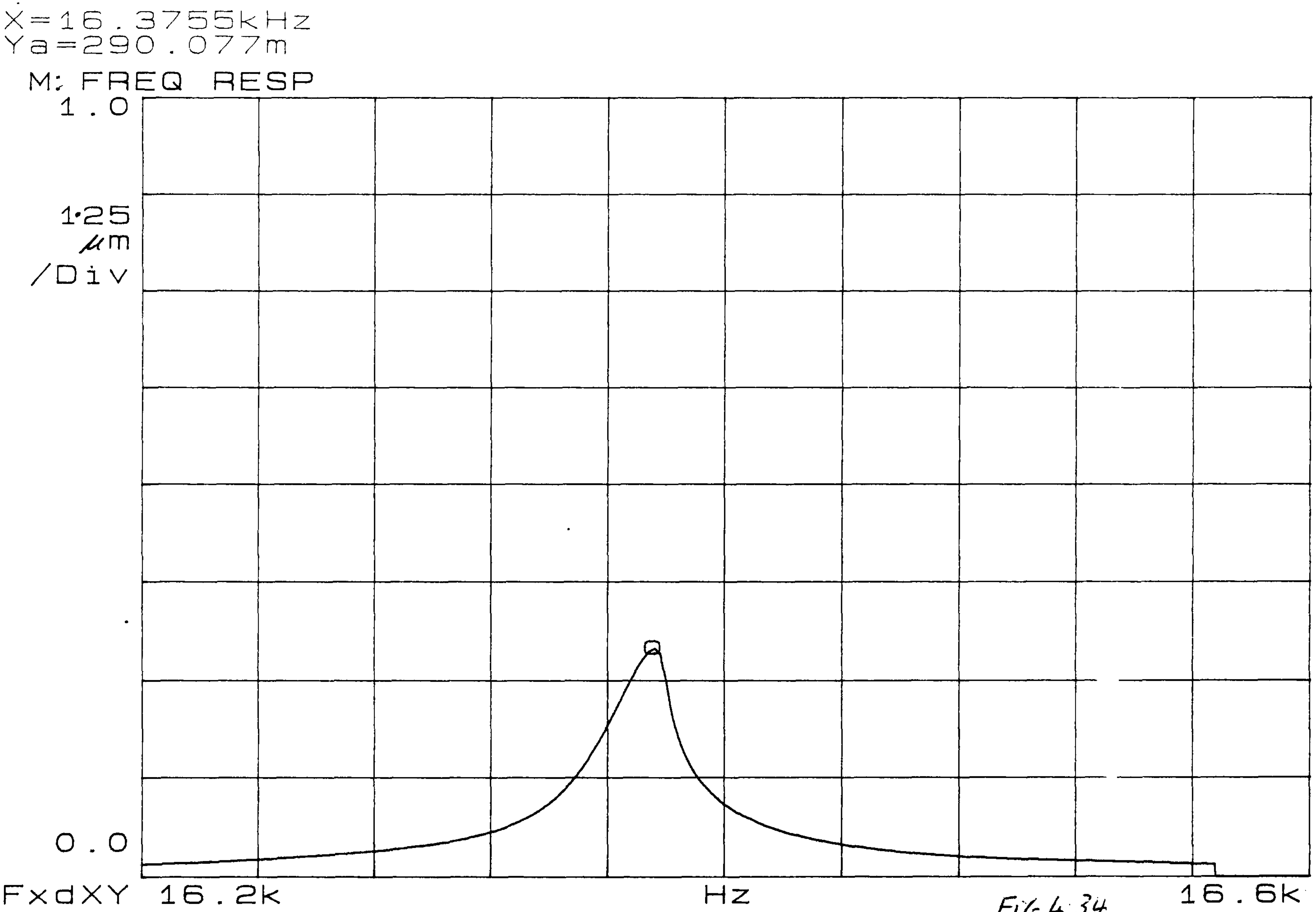
X=16.3755kHz
Ya=290.077m
M: FREQ RESP
1.0
1·25
µm
/Div
0.0
FxdXY 16.2k
Hz
16.6k

Fig 4·34

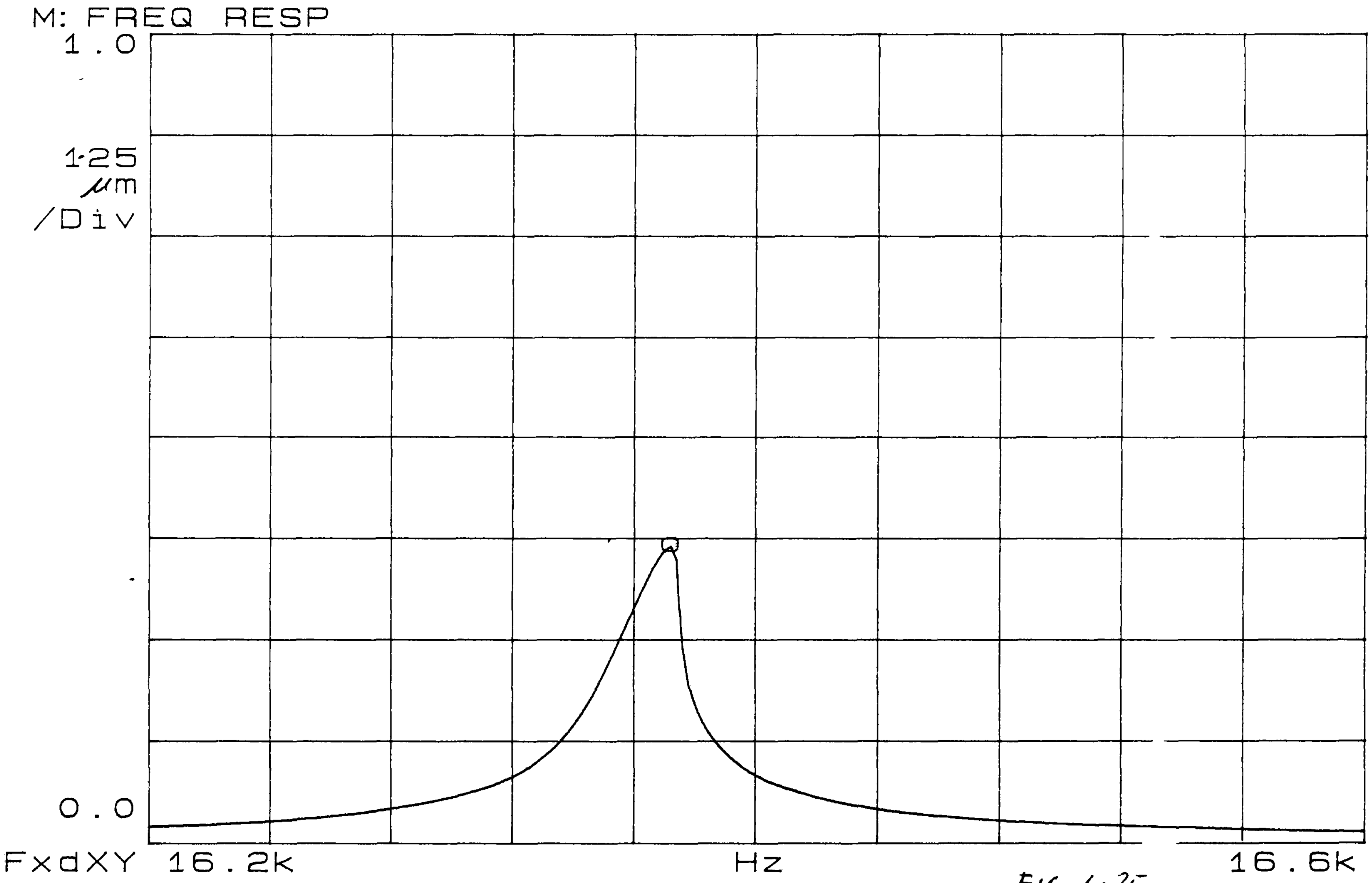

FIG 4·35

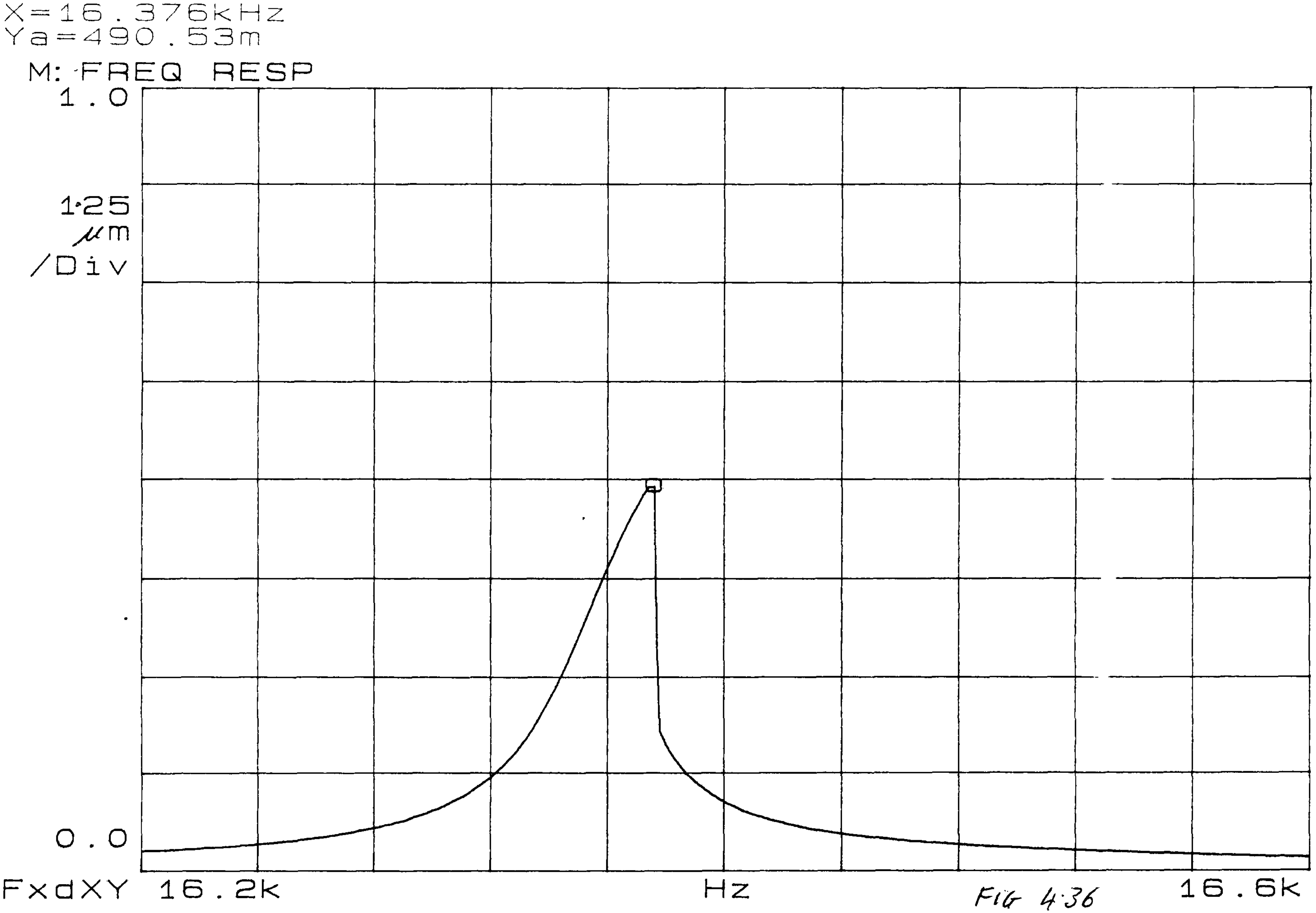
X=16.376kHz
Ya=490.53m
M: FREQ RESP
1.0
1·25
μm
/Div
0.0
FxdXY 16.2k
Hz
16.6k

FIG 4·36

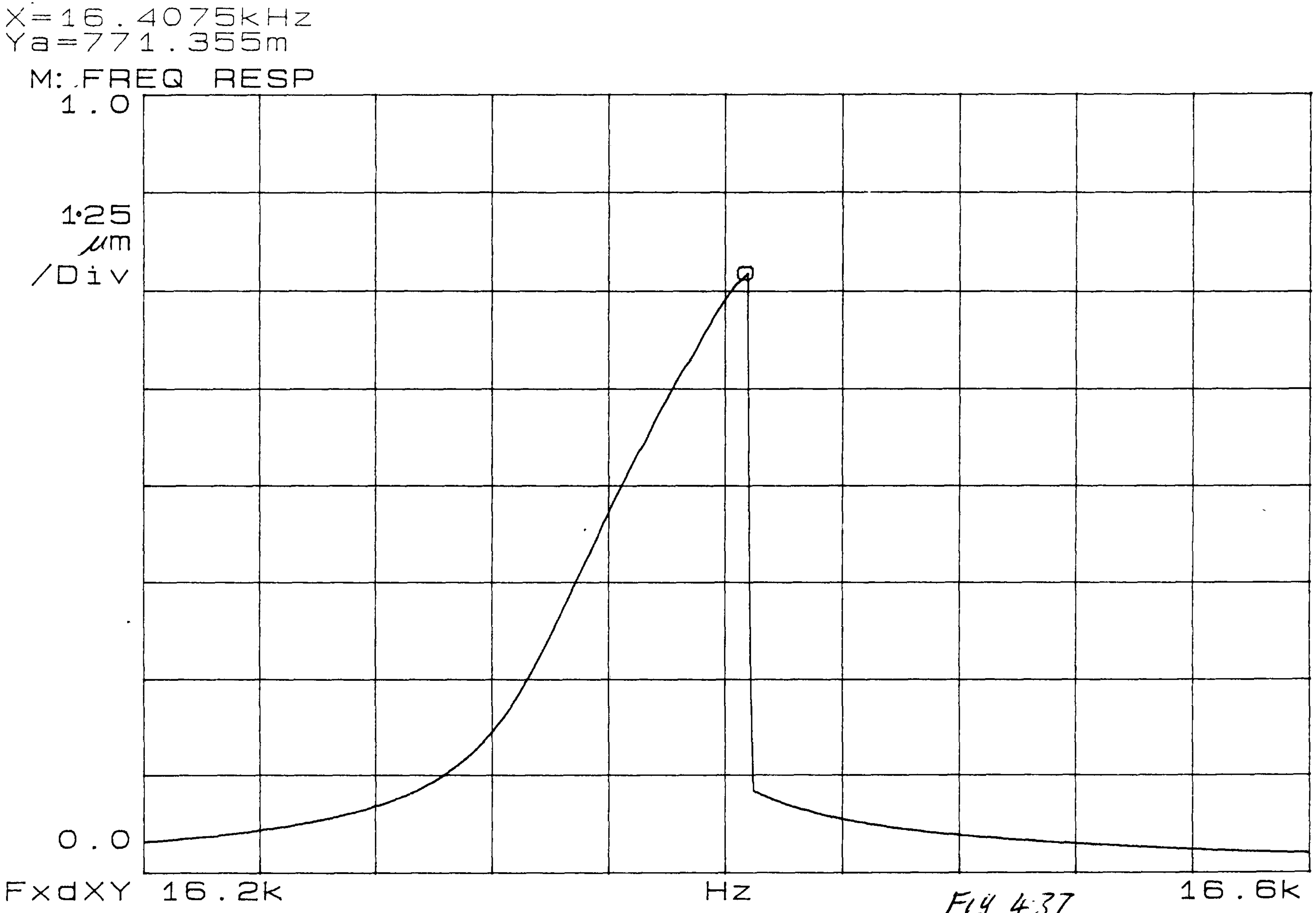
X=16.4075kHz
Ya=771.355m
M: FREQ RESP
1.0
1·25
µm
/Div
0.0
FxdXY 16.2k
Hz
16.6k

Fig 4·37

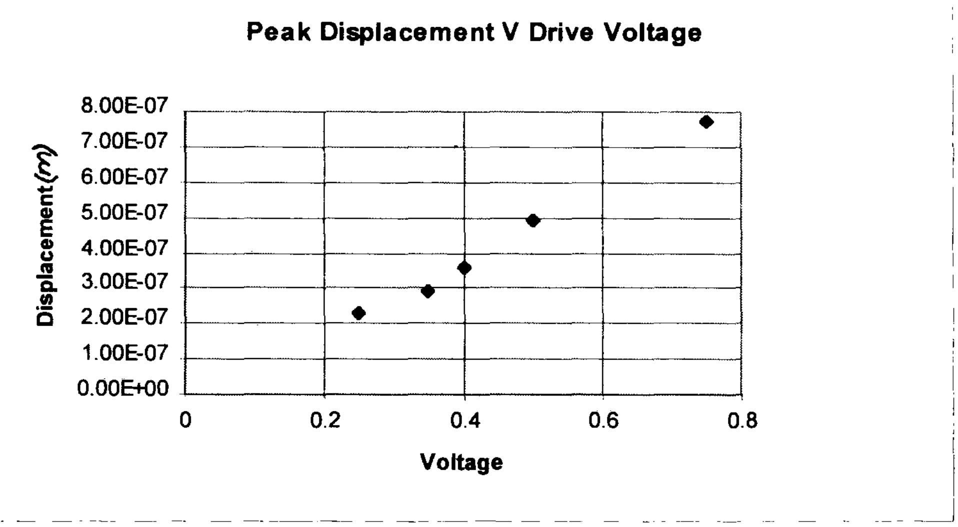

Fig 4.38 A Plot of amplitude against drive Voltage

This change in the shape of the resonance peak from the symmetric to the shark fin shape as the amplitude increases is typical of a non-linear hardening resonance[12]. A typical force displacement curve for a system with a hardening restoring force is shown in figure 4.40. As the displacement of the system increases the restoring force in the system increases disproportionately, the system becomes stiffer or harder.

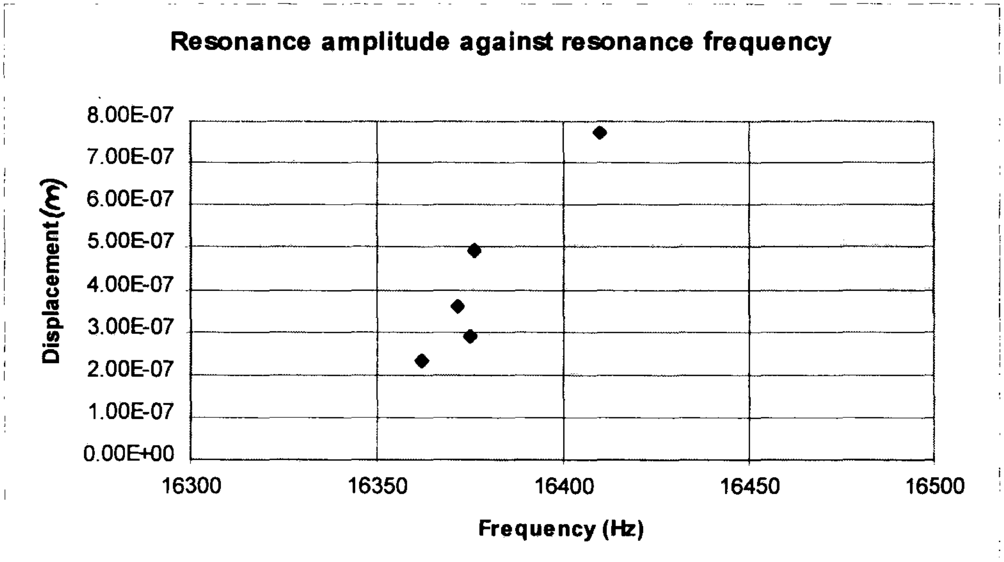

Fig 4.39 The relationship between amplitude and resonant frequency.

Systems having a restoring force of the type shown in figure 4.41 are known to generate resonance peaks with a discontinuity on the high frequency side.

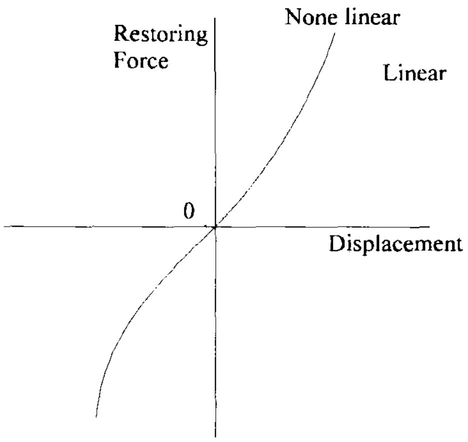

Figure 4.40 Showing the restoring force as a function of displacement for a hardening system.

4.5.3 A Simplified model to explain the origin of the non-linear response

The non-linearity in this device is almost certainly caused by the geometry of the structure rather than the material properties of the silicon. Single crystal silicon is known to have linear elastic properties up to its fracture point[3].

The source of the non-linearity can be understood at least qualitatively by considering a slice through the centre of the gyroscope. The cross sections of the deformed and undeformed structure are shown in figure 4.41.

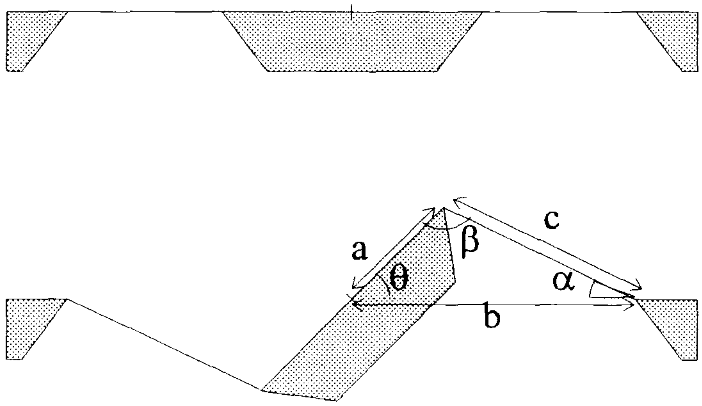

Fig 4.41 Showing a cross section through the gyroscope structure

Figure 4.41 should be compared with figure 4.9. Ignoring any bending stiffness in the silicon membrane the restoring torque exerted by the membrane on the central pyramid may be calculated as a function of θ in terms of the geometry of the structure and the pre tension in the membrane. This calculation is described fully in appendix A. A plot of the restoring torque acting on the pyramid is shown in figures 4.42 and 4.43

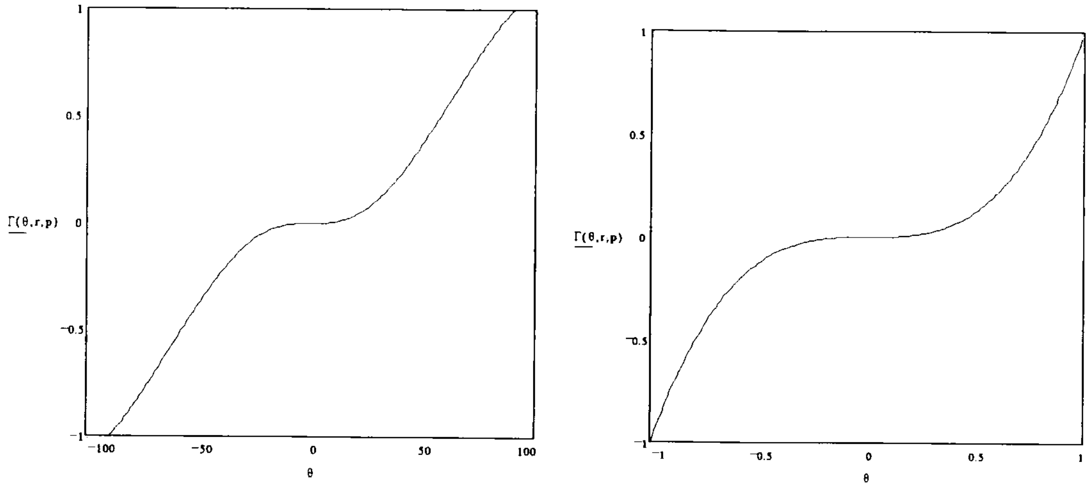

Figure 4.42 **Figure 4.43**

Plots showing the shape of the function describing the restoring torque on the pyramid as a function of θ over two different ranges of θ. (The vertical scale has been normalised to 1)

Figure 4.42 shows the restoring torque over the range -90,+90 degrees while figure 4.43 covers just the range -1,+1 deg. Clearly the none linearity of the function does not decrease with reduced amplitude of vibration.

The addition of pre tension into the model is also interesting. Figure 4.44 shows a series of curves with increasing pre-tension. The steeper curves are the ones with the larger pre tension. These steeper curves are also the most linear ones, indicating that the tension in the membrane introduced by the boron diffusion is actually improving the linearity of the device, at least for small vibrations.

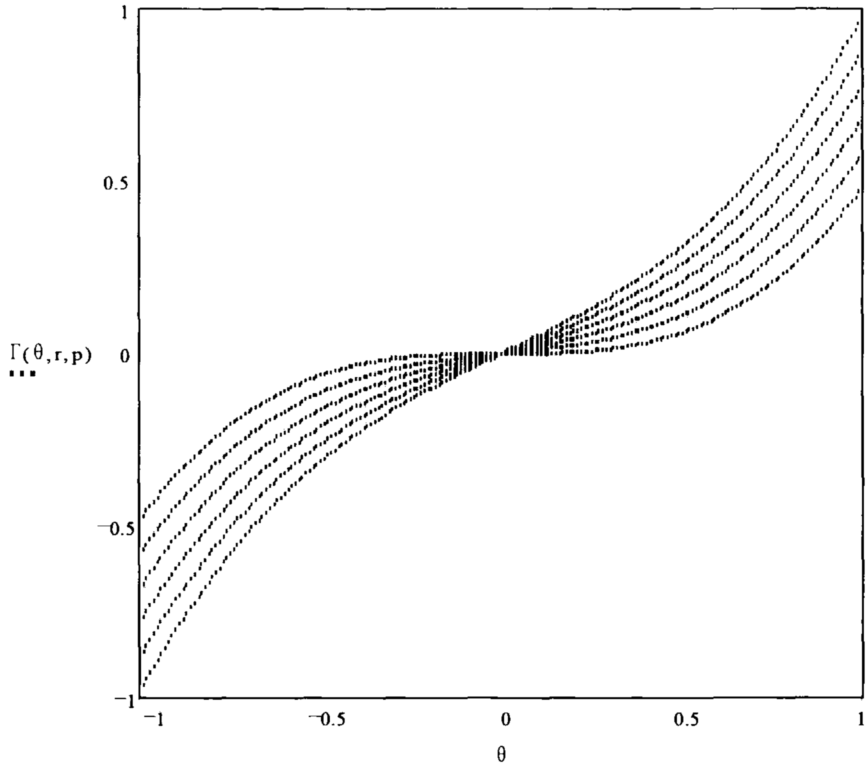

Figure 4.44 Plots showing the effect of increased pre-tension in the membrane (The vertical scale has been normalised to 1)

The non-linearity problem has a number of effects on the device as a gyroscope. If the device is driven into the non-linear region then the effect of the hardening is to push the peak of the resonance to a higher frequency. This effect is also evident from figure 4.40. As a consequence if the resonant modes of the device were to be initially matched, driving the primary mode to a large amplitude will cause the modes to move apart. This is a problem for the design as the amplitude of the secondary resonance will always be much smaller than that of the primary mode. In this situation the non-linearity will cause the two modes to have a different resonant frequency even in a perfectly symmetric structure.

The shape of the resonance peak is a potential problem for the electronics that drive the system. The usual way to drive a resonant gyroscope is to employ a phase locked loop (PLL). The PLL circuit works by sensing the amplitude of a resonance and then adjusting the drive frequency to maximise the sensed amplitude. This is fine when the displacement is a smoothly varying function like a linear resonance curve, where the circuit can approach the peak from either side and should eventually converge to the top of the resonance. With a severely distorted resonance like the one shown in figure 4.38 it is possible to imagine the phase locked loop moving up the peak from the left hand side in return for ever increasing signal, as desired, and then overshooting the peak, at which point the amplitude will drop dramatically. In the worst case the PLL may not be able to find the peak from the high frequency side, or may even continually move back and forth across the discontinuity resulting in an unstable primary amplitude and correspondingly unstable gyroscopic signal.

4.5.4 Rotation Sensitivity

Despite the problems of non-linearity and the mismatch in the resonant modes, it was possible to operate the device as a gyroscope. The output voltage as a function of rotation rate is shown in figure 4.45.

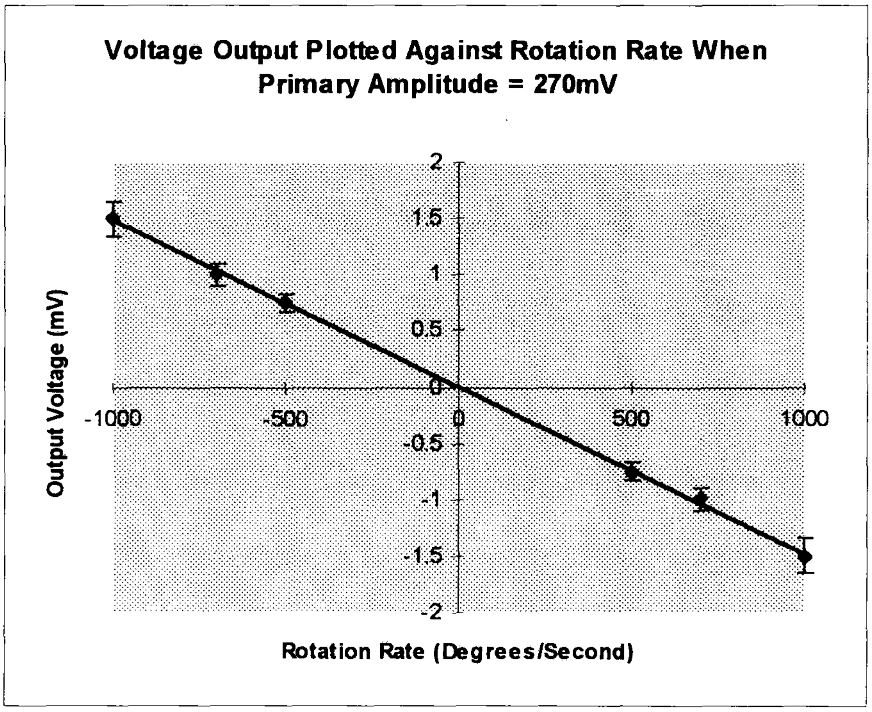

Figure 4.45 Showing the results of the rotation rate tests

4.6 Conclusion

The design described has been manufactured tested and shown to work as a gyroscope, albeit with a rather low sensitivity. The resonance tests have revealed a strong non-linearity at a relatively low amplitude of vibration. The origin of this non-linearity has been explained in terms of a simplified model of the structure. This simplified model has given some insight into the nature of the non-linearity and what influences its magnitude.

4.7 References

---

[1] W.Weaver, S.P.Timoshenko, D.H.Young Vibratiion Problems In Engineering 5th ed. 1990 John Wiley

[2] J.J.Stoker Non-linear Vibrations in Mechanical and Electrical Systems 1950 Interscience Publishers.

[3] Wortman and Evens Young's Modulus, Shear Modulus, and Poisson's Ratio in Silicon and Germanium J.Appl.Phys, 36 (1964) pp. 153-155

Chapter 5

Bow-Tie Gyroscope

5.1 Introduction

This chapter describes a second design of resonant gyroscope. The structure is more complex than the design described in chapter 4. The evolution of the device is described in section 5.2. It is hoped that this will help explain some features of the final design. Section 5.3 gives a detailed description of the final structure and its method of operation. The design does not possess symmetry between the primary and secondary modes. For this reason it has been necessary to perform a more extensive finite element analysis of the structure, in order to confirm that the primary and secondary modes could be matched: this work is presented in section 5.4. In section 5.5 the development of the manufacturing process is described. At the time of writing only the most preliminary tests have been performed on the finished structure. These are reported in section 5.6 and finally the conclusions are contained in section 5.7.

5.2 Initial Design

Since the Sperry company introduced the tuning fork resonant gyroscope in the early 1950's there have been numerous redesigns of the same basic tuning fork idea: many of these are presented in chapter 2. The tuning forks' main advantage is that the two tines are moving in opposite directions at any given instant. Thus anti-parallel Coriolis forces are generated: this allows the sensing electronics to take the difference of the signals from each tine. This effectively doubles the electrical signal, allowing for a greater device sensitivity, whilst also allowing any electrical noise appearing across both to be subtracted out of the signal.

An alternative to the tuning fork design is shown in figure 5.1. In this design a single ridged beam is supported at its centre and allowed to vibrate in torsion about the supporting point. Applying a rate of turn about the long axis of the beam will then excite the beam to begin vibrating at 90^0 to the primary motion, as shown.

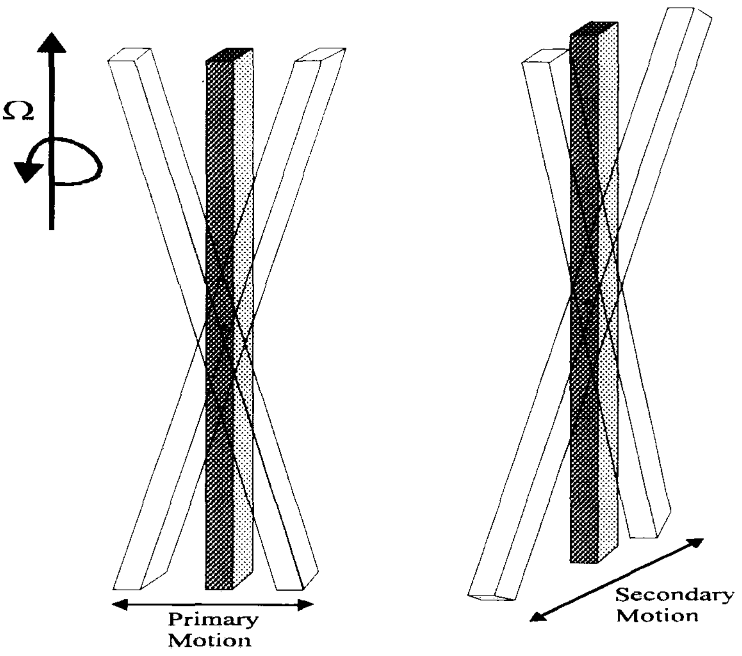

Figure 5.1 The primary and secondary motion of a rocking beam design under the action of a Coriolis force about its long axis.

The tips of the beam, like those of the tuning fork, are always moving in opposite directions, preserving the possibility of making a device with a differential sensing system.

It was felt that this design offered a few potential advantages over the conventional tuning fork arrangement. The tuning fork design relies on accurately machining each tine of the fork to have precisely the same dimensions, in order that they will resonate at the same natural frequency. Any mismatch between the two tines will lead to the tines having different natural frequencies. Under the influence of the single frequency drive signal this will mean that the two tines will have different amplitudes of vibration in the primary mode, and correspondingly different secondary amplitudes. This in turn will lead to some loss of sensitivity when taking the difference of the two signals.

With the design in figure 5.1 the resonant element is a single ridged beam: as a result the resonant element moves as a single body, ensuring that the tips of the beam move with the same frequency and amplitude of vibration and always 180^0 out of phase. This is the optimum condition for taking the difference of the two signals.

Another potential advantage of this design is in its sensitivity to external vibrations. By placing the support structure of the beam at the centre of gravity of the device, rather than at one end, the device will be less influenced by external vibrations or accelerations, as any inertial forces generated on one half of the beam will cancel those generated on the other half of the structure, as shown in figure 5.2. This could be an significant advantage in the automotive environment where vibration levels may be very high.

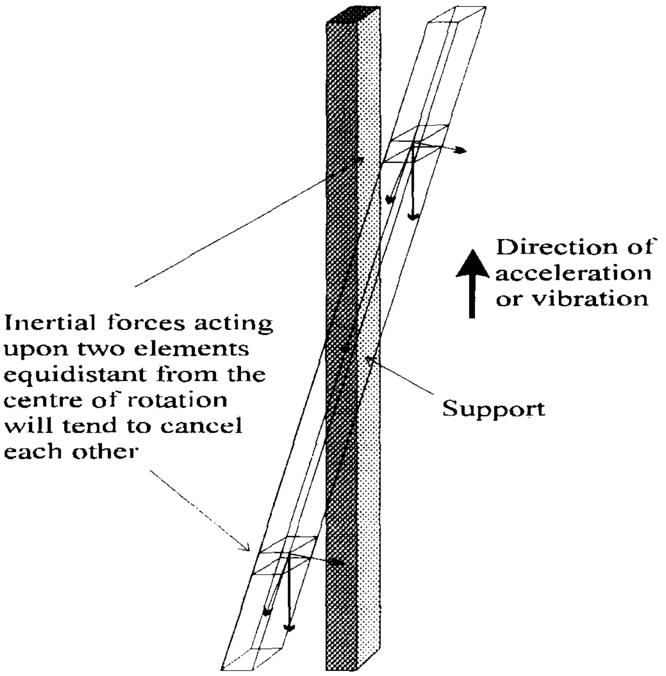

Figure 5.2 **The forces acting on either end of a beam rocking about its' centre point.**

5.2.1 Revision 1

This simple beam design lends itself to fabrication in {110} silicon where parallel sided square and rectangular cross sectioned beams are easily made by anisotropic etching (section 3.7). The first design of resonant beam device is shown in figure 5.3. The inclined geometry of the device is dictated by the relative orientation of the {111} crystal planes (section 3.2). In order to make the structure resonate in the desired manner the whole structure is placed in a magnetic field, with the field lines running normal to the plane of the page. A sinusoidal current is then passed along the top beam, which causes a sinusoidal Lorentz force in the plane of the wafer acting perpendicular to both the current and magnetic field directions. This force is then applied to the gyroscope beam via the cross member , causing the beam to vibrate in a rocking mode.

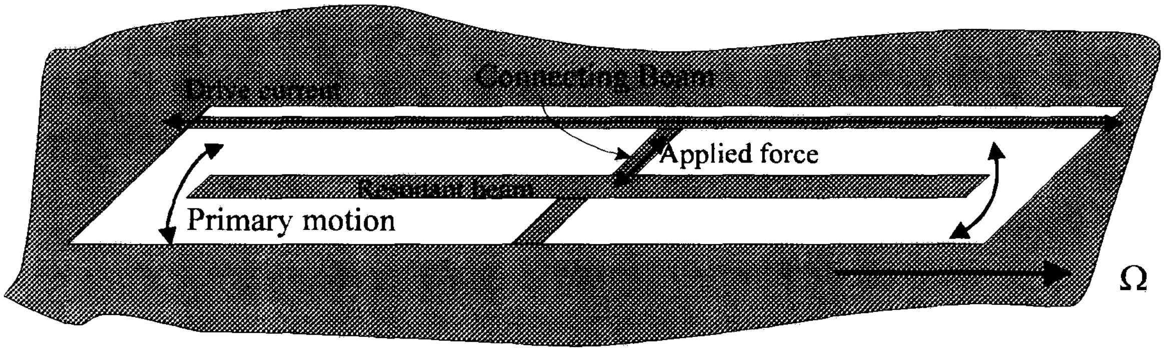

Figure 5.3 The first stage design

The decision to utilise the Lorentz force rather than the more commonly used capacitive drive method was motivated by the desire to simplify the manufacture process. As shown with the design in the previous chapter capacitive excitation involves the positioning of two plates close together: this in turn requires a wafer bonding process, doubling the number of wafers used. Using the Lorentz drive the function of the second wafer can be replaced with a permanent magnet. The alignment of the magnet to the device is not critical as is the case with a capacitive excitation method.

The structure shown in figure 5.3 was etched and a photograph of the resulting device is shown in figure 5.4. Four structures are shown in two pairs.

5.2.2 Revision 2

The structure shown in figure 5.4 has no method of detecting the out of plane Coriolis forces. The next stage of development was to attempt to fabricate sensing elements, which could be built into the tips of the beam to detect the Coriolis forces. These sensing elements are essentially accelerometers. For maximum sensitivity these devices must be placed at the tip of the resonating beam, where the primary motion and the corresponding Coriolis force would be a maximum.

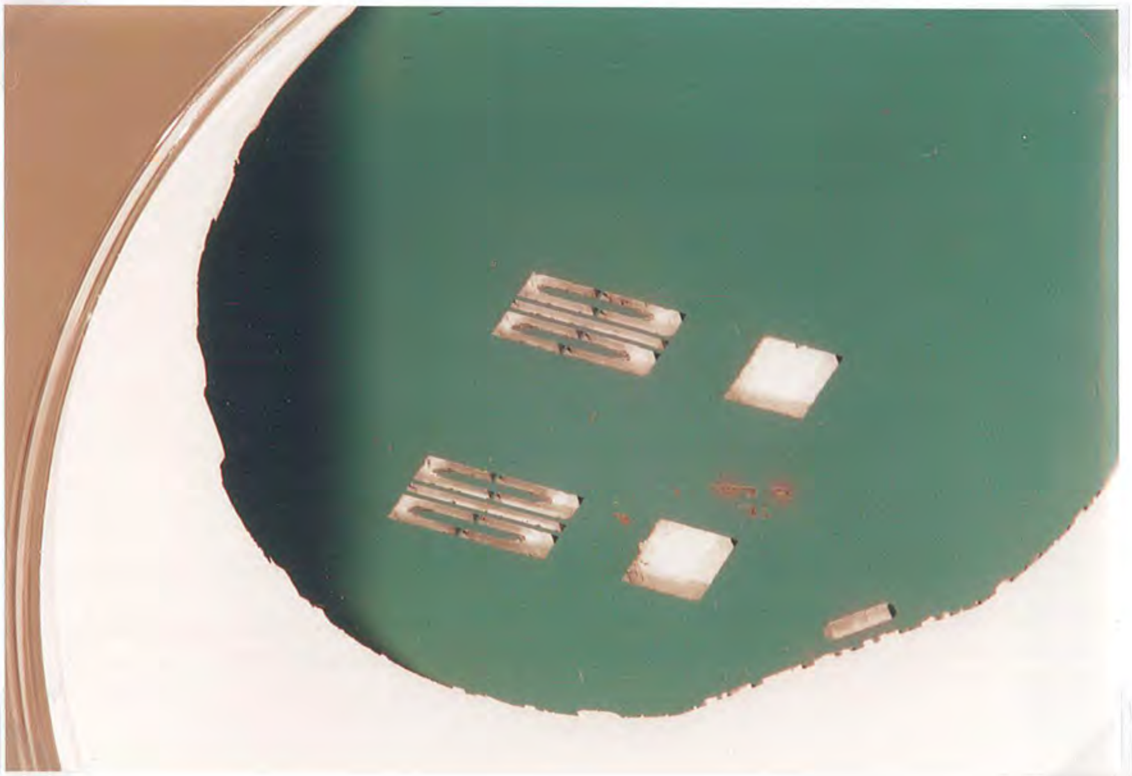

Figure 5.4 Photograph of revision 1, one of the first trial structures etched in {110} silicon.

The first design of sensing element that was attempted was an inertial mass supported on two beams as shown in figure 5.5. Any out of plane acceleration force would cause the mass to deflect inducing a strain in the top surface of the support beams. This strain

MODES-FREQ

MODE 1

1.361 E 4

(HZ)

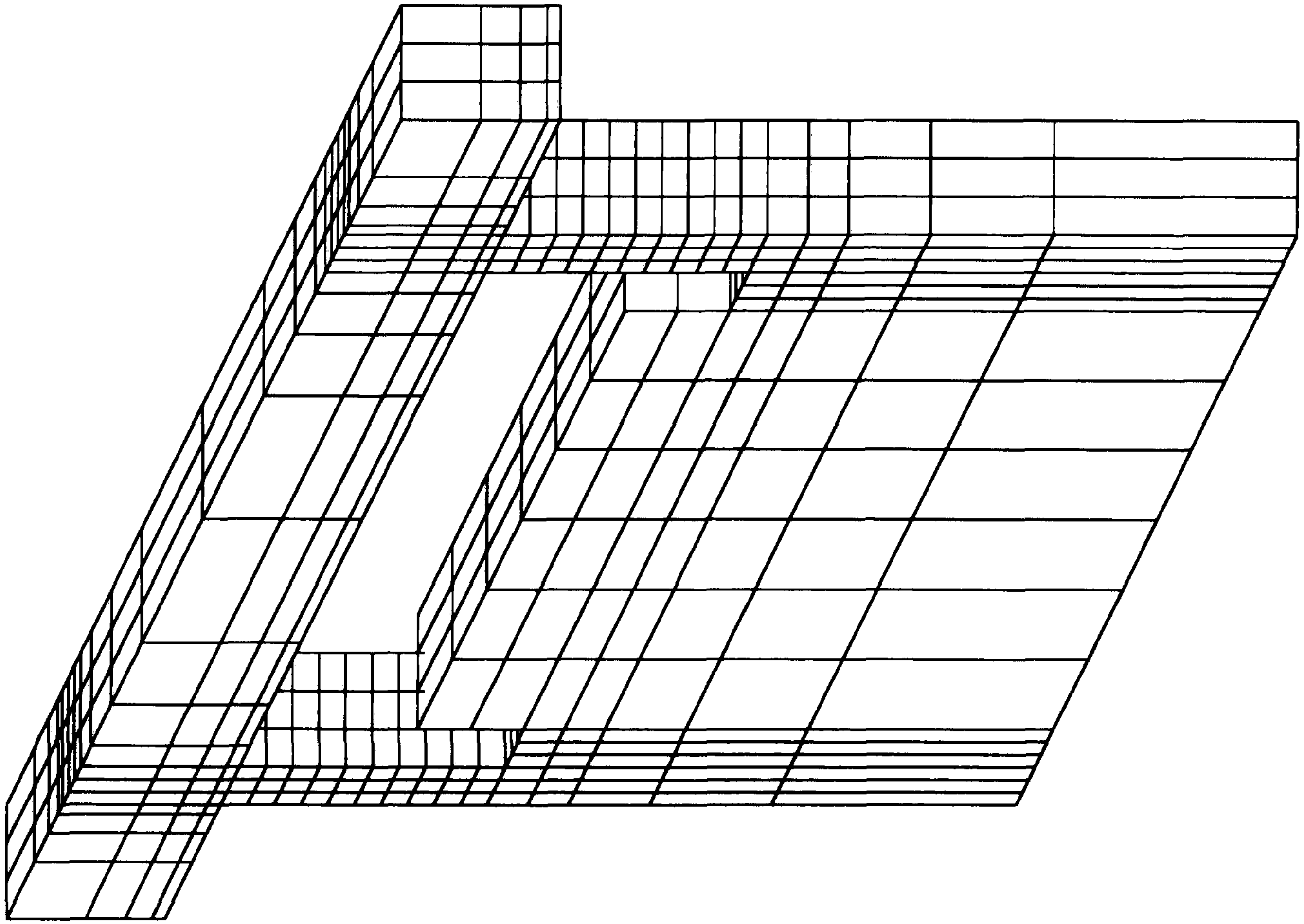

ROTATION

X = 45

Y = 0

Z = 0

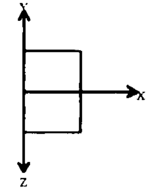

TITLE UNDEFORMED SENSOR STRUCTURE

FIG 5-5

could then be measured using piezoresistors diffused into the beams. These sensors were incorporated into the basic beam structure as shown in figure 5.6.

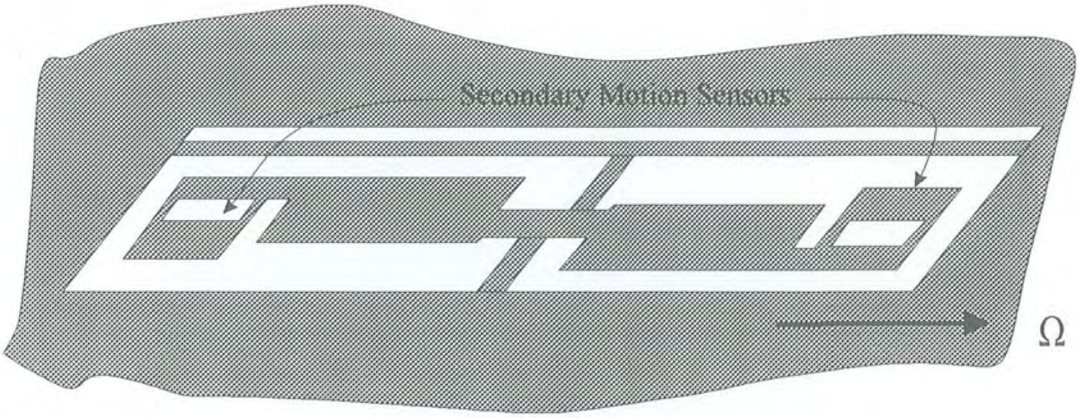

Figure 5.6 **Revision 2, with secondary sensing elements.**

The fabricated version of the structure is shown in photograph 5.7

Figure 5.7 **A Photograph of revision 2**

The etching of this structure revealed a serious limitation to the bulk machining of {110} silicon, namely the presence of the inclined {111} planes. These inclined planes cause a trapezoidal solid mass of silicon to remain in each acute corner of the etched structure. In figures 5.5 and 5.7 these regions show up as dark grey triangular regions in the acute corners of the device. This effect is inherent to wet etched structures made in {110} silicon, though it is often ignored in the literature. The size of these masses is significant in comparison to the overall dimensions of the structure and their effect is to increase the structures stiffness considerably. As a result of this the etched sensor structure, fig 5.7, does not exactly replicate to the desired structure shown in figure 5.6.

5.2.3 Revision 3

It was decided that the design of secondary sensor described above would not be suitable for Coriolis force detection because of the residual silicon located in the acute corners of the structure. In order to overcome this problem the sensing element was redesigned into a triangular form as shown in figures 5.8 and 5.9. Two edges of the triangle are formed by the vertical {110} planes and the third by the inclined {111} plane. This design fits more naturally with the arrangement of the {111} planes. The triangular design allowed the support beams to be made much thinner increasing the out of plane flexibility without causing excessive flexibility in the plane. It is important to minimise the in-plane flexibility of the device since the primary motion will itself generate inertial forces on the sensor. These forces will act in the plane: it is necessary that the sensor is not influenced by in-plane forces. Finite element analysis of this design was carried out and the results indicated that the resonant frequencies of the device may be suitable for the gyroscope application.

This device was incorporated into the beam structure: figures 5.10 and 5.11 show a plan layout and photograph of the etched structure.

MODES FREQ

MODE 1

1.500 E 4

(HZ)

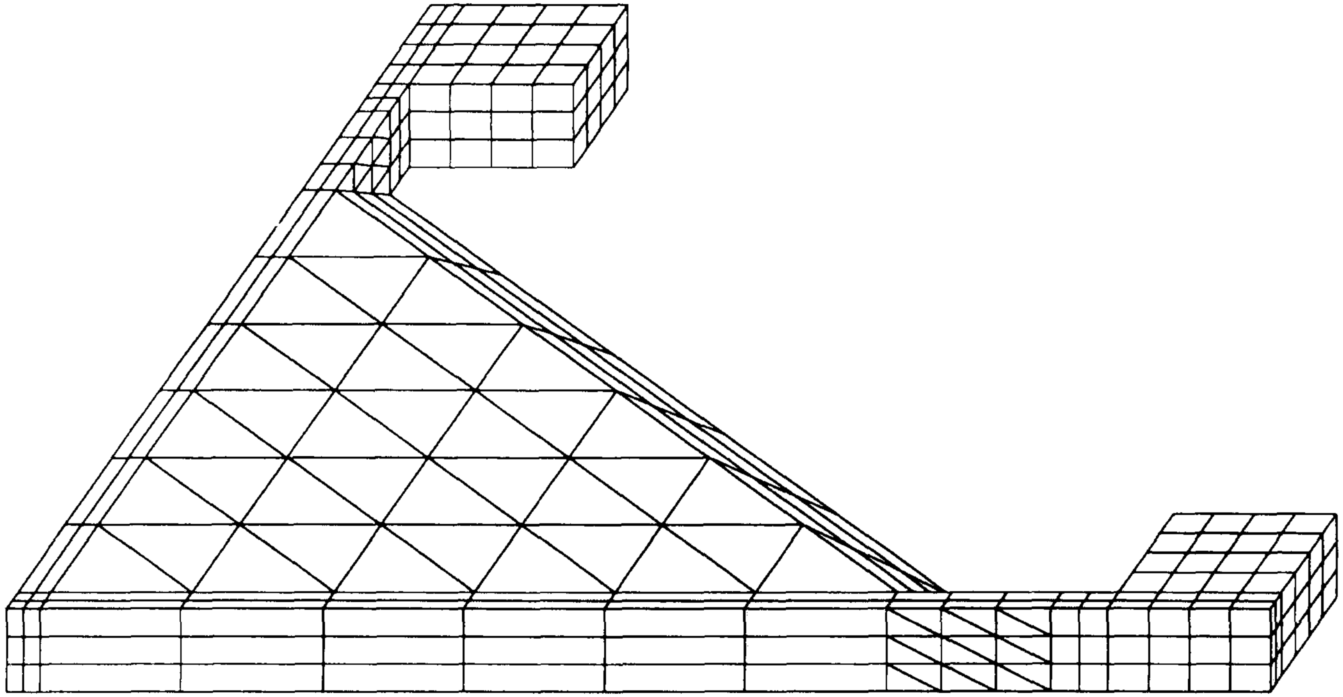

ROTATION

X = 300

Y = 0

Z = 0

TITLE RUN 3 UNDEFORMED STRUCTURE

FIG 58

MODES-FREQ

MODE 1

1.500 E 4

(HZ)

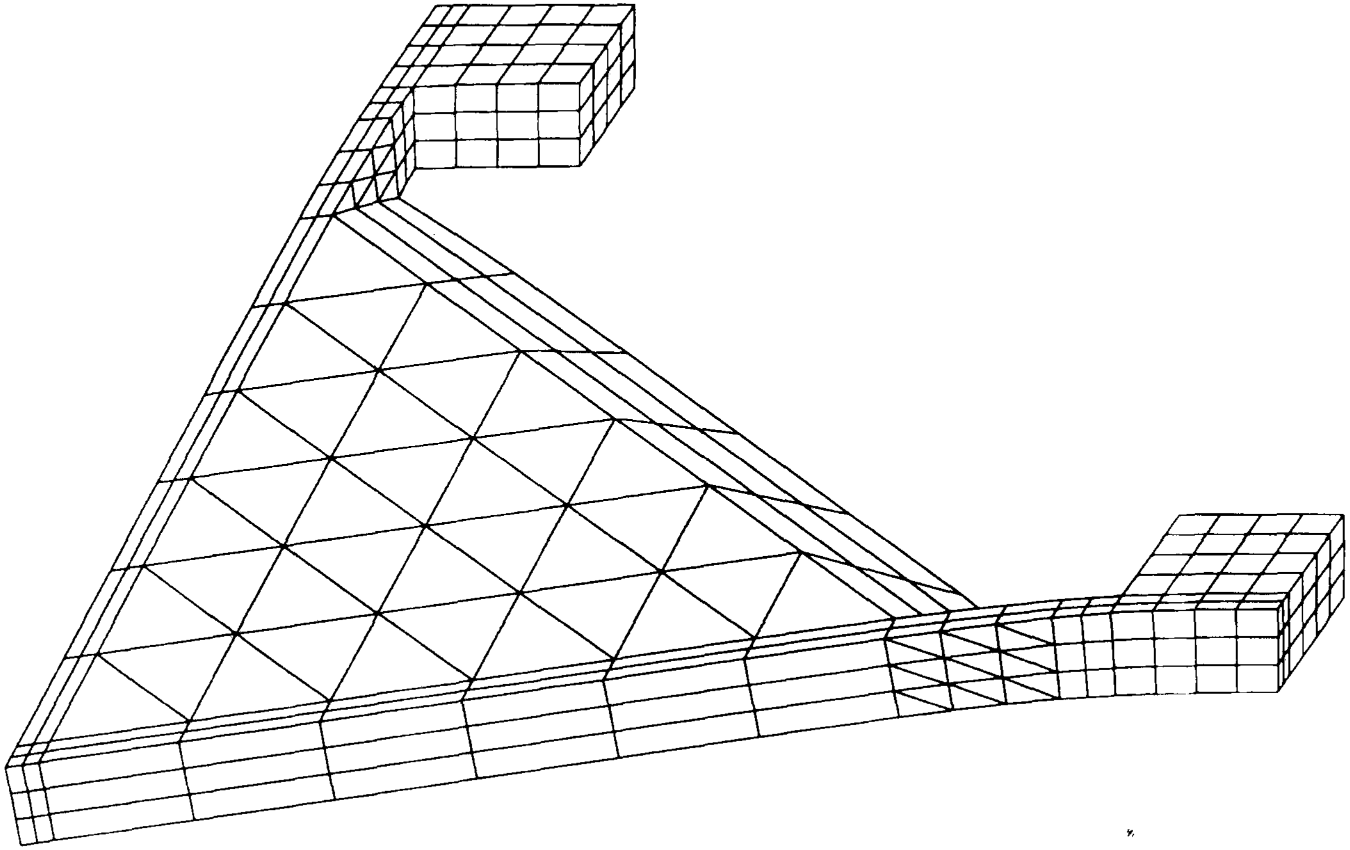

ROTATION

X = 300

Y 0

Z 0

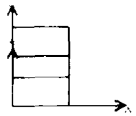

TITLE RUN 3 MODE 1

FIG 5·4

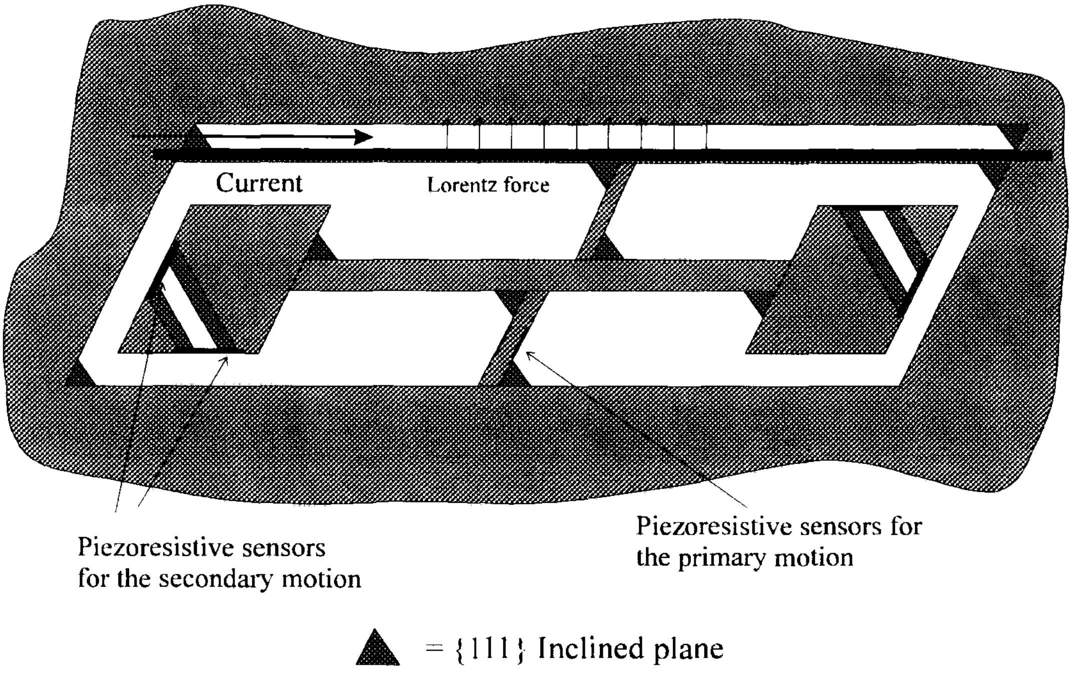

Figure 5.10 Structure with modified Coriolis sensors.

This design was fabricated into a full device, with piezoresistors and metal interconnects and the resulting device was then tested. It was found that the device could be excited into resonance at a frequency of around 7 kHz using Lorentz activation. This resonance was audible and was additionally detected with a laser Doppler interferometer and via the piezoresistors diffused into the support beam as shown. The laser Doppler interferometer did however indicate that there was a significant out of plane motion of the device. The device was not resonating purely in the plane of the wafer as desired.

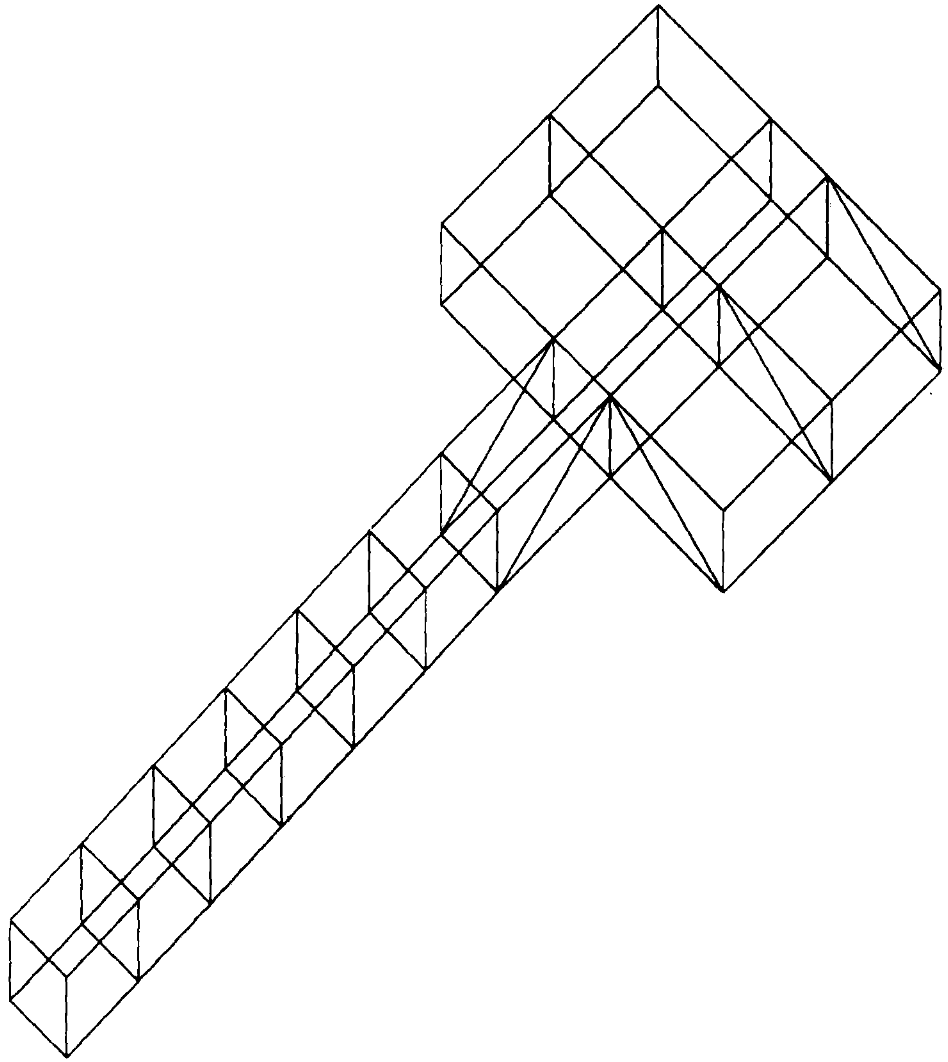

MODES-FREQ

MODE 0

0.000 E 0

(HZ)

ROTATION

X = 225

Y = 180

Z = 0

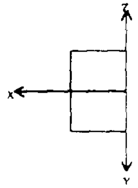

TITLE BEAM WITHOU CORNER WEDGE

FIG 5.12

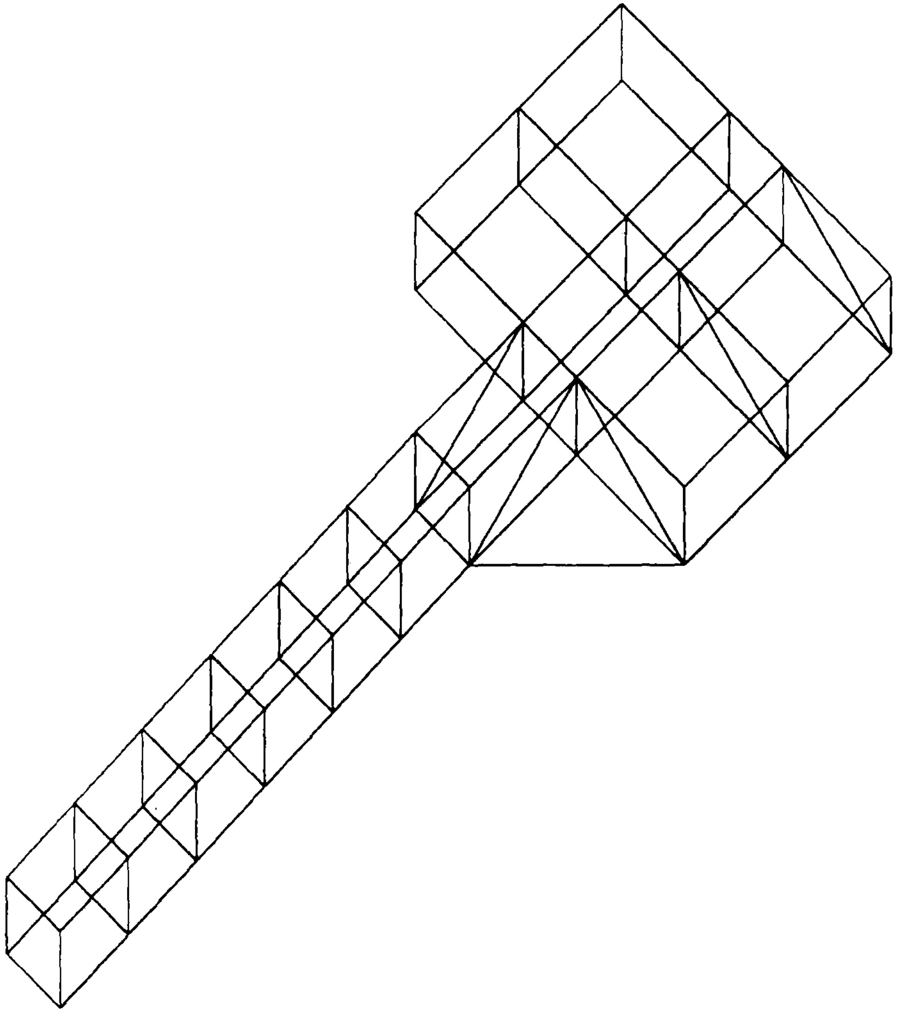

MODES-FREQ

MODE 1

0.567 E 5

(HZ)

ROTATION

X = 225

Y = 180

Z = 0

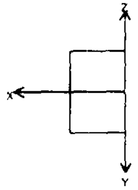

TITLE UNDEFORMED {110} BEAM

FIG 5-13

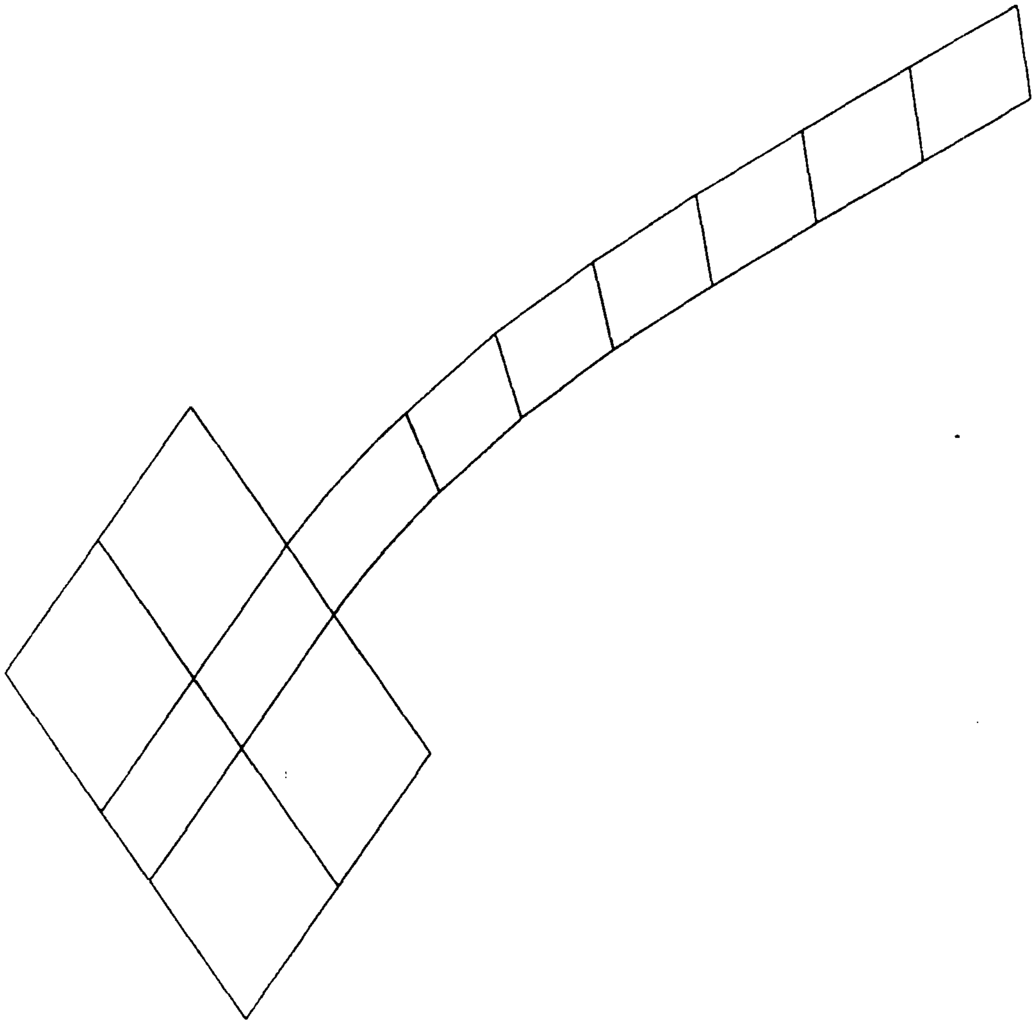

MODES-FREQ

MODE 1

0.482 E 5

(HZ)

ROTATION

X = 0

Y = 0

Z = 0

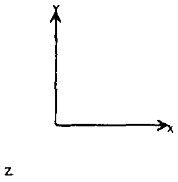

TITLE IN PLANE MOTION WITHOUT CORNER WEDGE

FIG 5·14

MODES-FREQ

MODE 1

0.482 E 5

(HZ.)

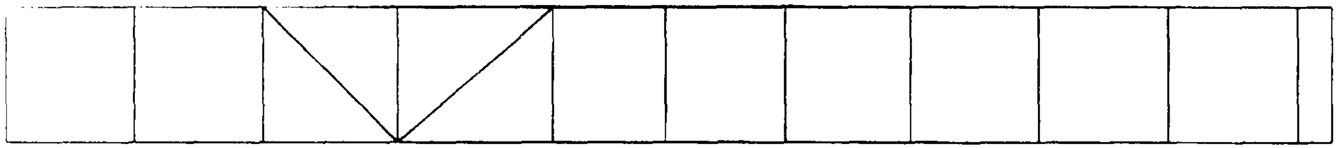

ROTATION

X = 90

Y = 0

Z = 0

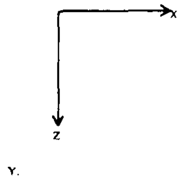

TITLE OUT OF PLANE MOTION, WITHOUT CORNER WEDGE

FIG 5.15

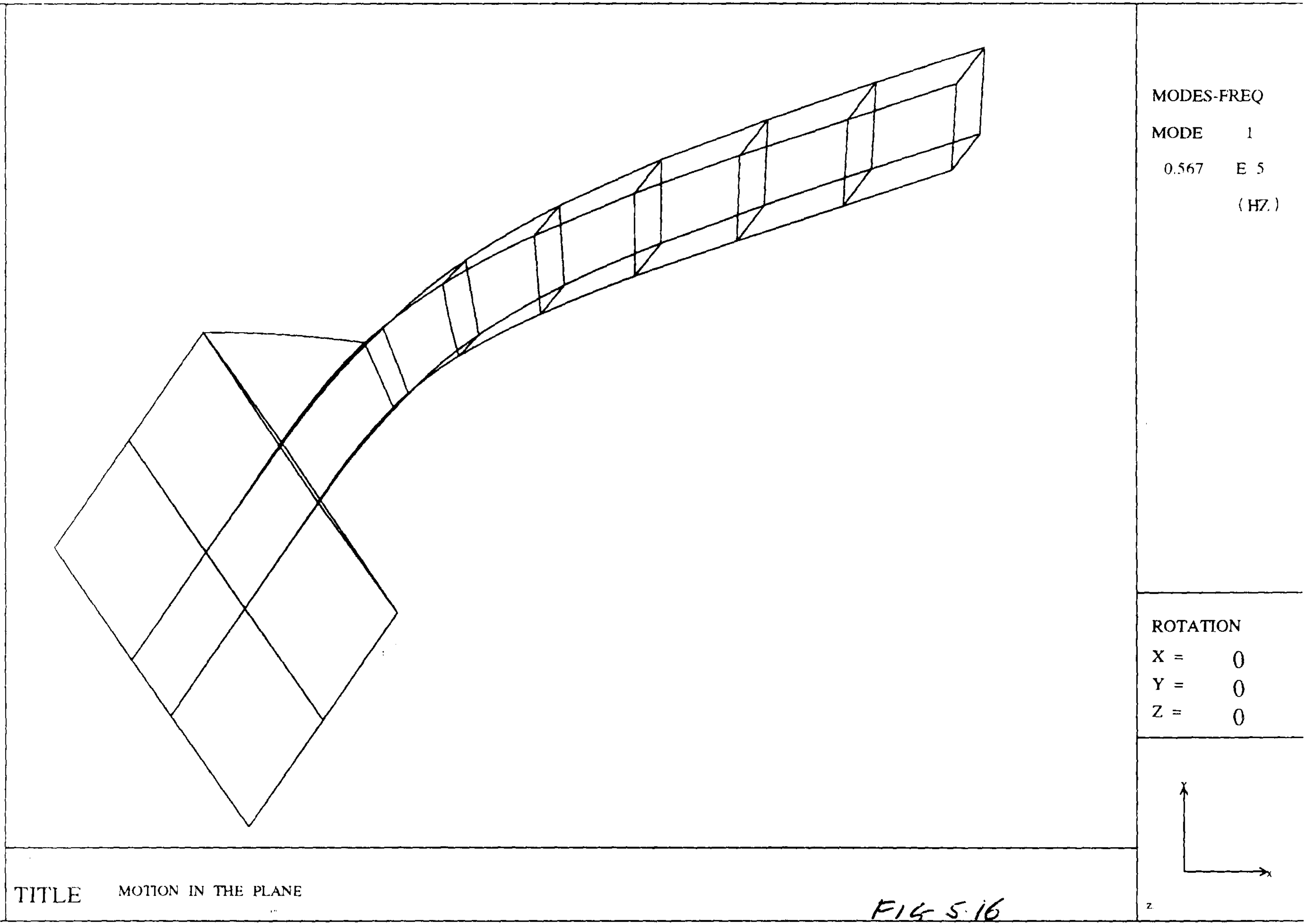
MODES-FREQ
MODE 1
0.567 E 5
(HZ.)
ROTATION
X = 0
Y = 0
Z = 0
Y
X
Z
TITLE MOTION IN THE PLANE

FIG 5.16

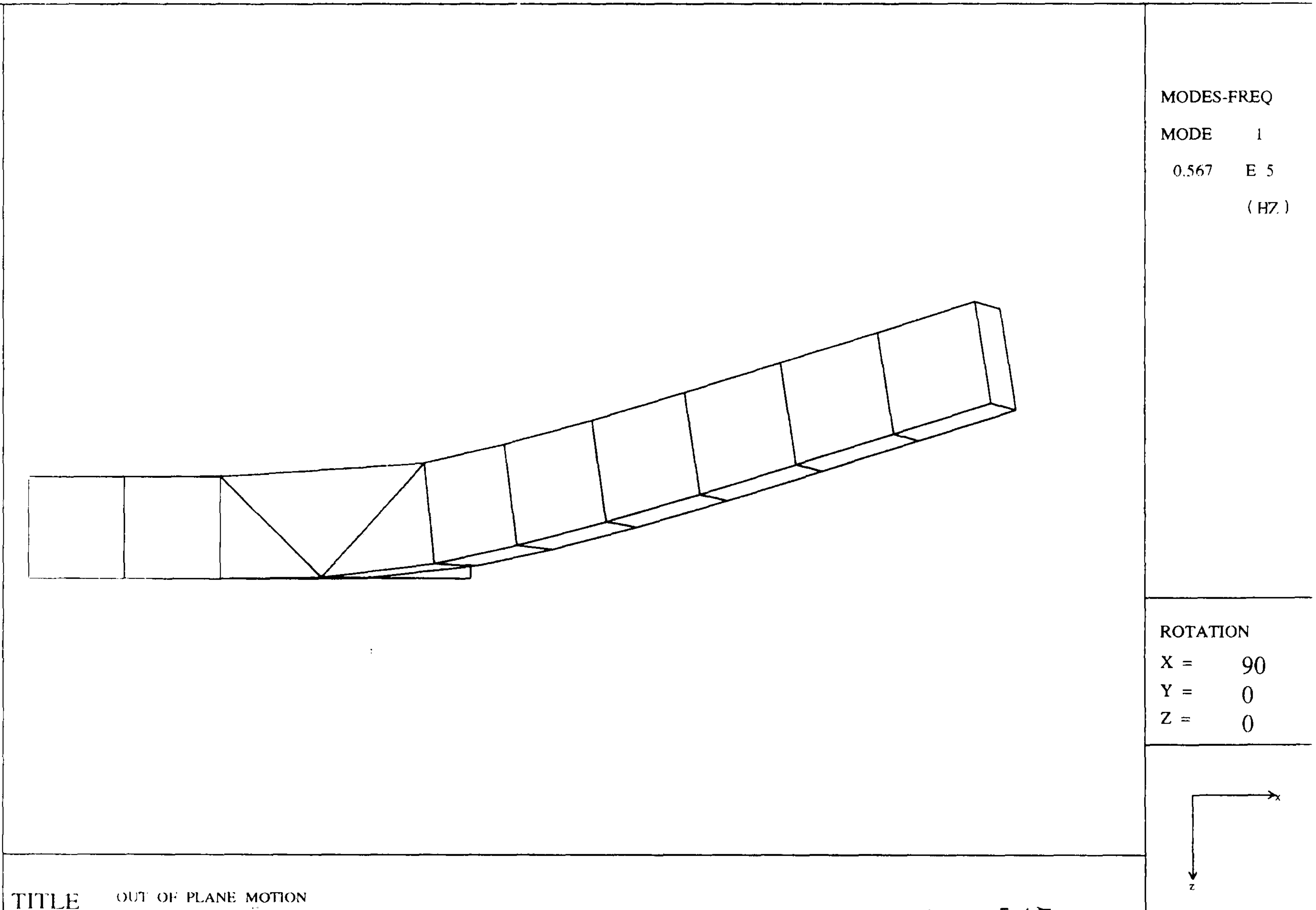
MODES-FREQ
MODE 1
0.567 E 5
(HZ)
ROTATION
X = 90
Y = 0
Z = 0
x
z
y
TITLE OUT OF PLANE MOTION

FIG 5.17

that the tip of the beam now has a rotational component as well as the translational component to the mode shape. The addition of the wedge shaped block has stiffened the bottom surface of the beam more than the top surface: as a consequence the beam twists as well as bends. Figure 5.17 shows the same motion from the Y axis: in this plot it can be seen that the beam has also acquired an out of plane component to its motion.

These mode shapes indicate that a cantilever fabricated from {111} silicon using wet etching will not naturally have a bending mode in the plane of the wafer. The tip of the beam will move at some angle to the wafer surface, with an additional rotational component to the motion. This model implies that the centre point 'A' shown in figure 5.10 would also have an out of plane component in the primary motion. As the stiffness of the device is not symmetric due to the presence of the second beam connecting to the upper drive beam, this out of plane motion would in turn generate an out of plane rotational component to the primary mode. This component would be indistinguishable from the Coriolis induced secondary mode. In short, the effect of these silicon wedges on the device shown in figure 5.10 is to make it impossible to excite the primary mode without simultaneously exciting the secondary mode.

5.2.4 Revision 4, Symmetric Design

In order to remove this mechanical coupling of primary to secondary motion it was necessary to make the device symmetric about the centre of the structure. The result of this redesign is best described with reference to figures 5.18 and 5.19, which show a photograph of the etched structure and a finite element mesh of the design respectively. In this design the centre line of the resonating beam is no longer parallel to either of the {111} planes: instead it lies exactly mid-way between them. The beam itself is now a pair of diamonds joined in the centre, forming the 'bow-tie' shape. The sensing elements form the tips of the bow-tie. The support structure is formed by four beams leading from the centre of the structure which are in turn connected to another four beams. The ends of these outermost beams are connected to the silicon wafer.

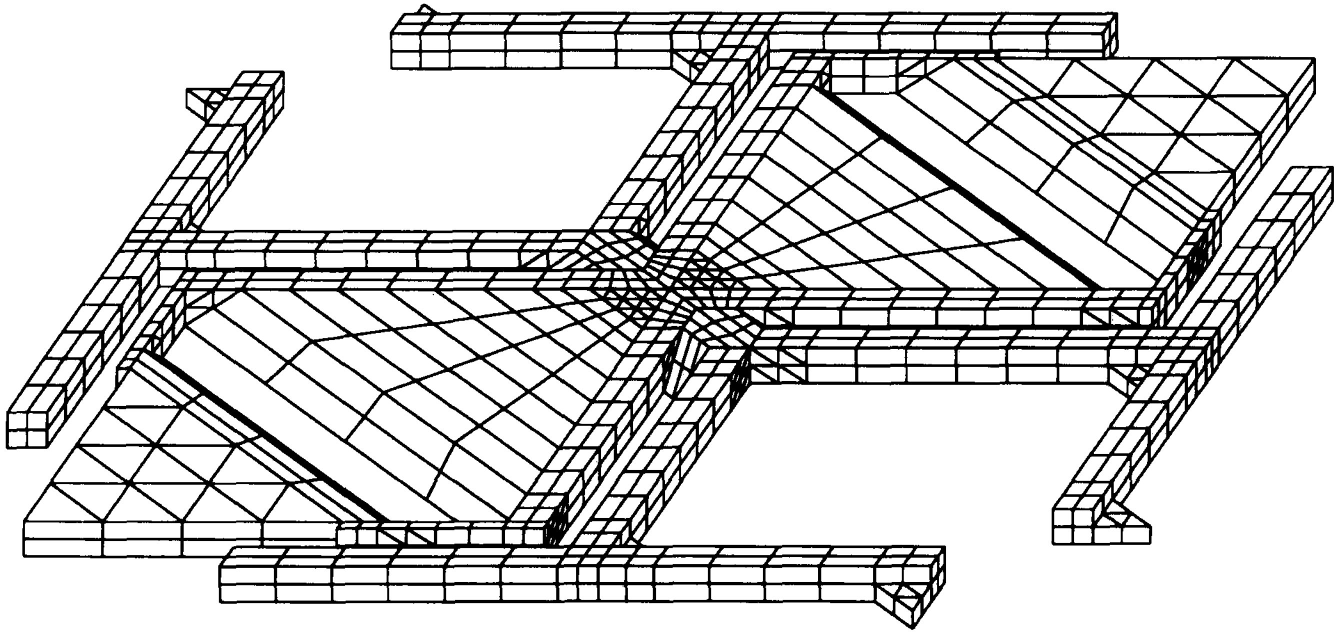

MODES-FREQ

MODE 2

0.790 E 4

(HZ)

ROTATION

X = 300

Y = 0

Z = 0

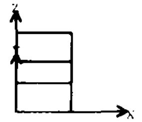

TITLE UNDEFORMED STRUCTURE

FIG 5 19

This design possesses all of the symmetries of the crystal itself, both elastic and piezoresistive (see figures 3.3 and 3.4). With this device two of the supporting beams are used as drive beams. By ensuring that the same current flows through each beam in an opposite direction it is possible to eliminate any undesired transitional motion of the centre of gravity of the structure, ensuring that all of the energy is translated into rotational motion.

The design also achieves the initial aim of making the centre of gravity of the structure coincide with the geometric centre. As a result, linear accelerations and vibrations should be unable to couple into the two rotational modes which form the primary and secondary resonances. The symmetry of this structure implies that the primary and secondary modes would be uncoupled in this design. A test structure was etched and is shown in figure 5.18.

The finite element models confirmed that the primary and secondary modes of the structure were orthogonal and uncoupled. However, the FE models also showed that the beams supporting the sensors at either end of the bow-tie device would have to be made extremely thin, less than 50μm, in order to reduce resonant frequency of the secondary mode to match that of the primary. This was beyond the ability of the available lithography process.

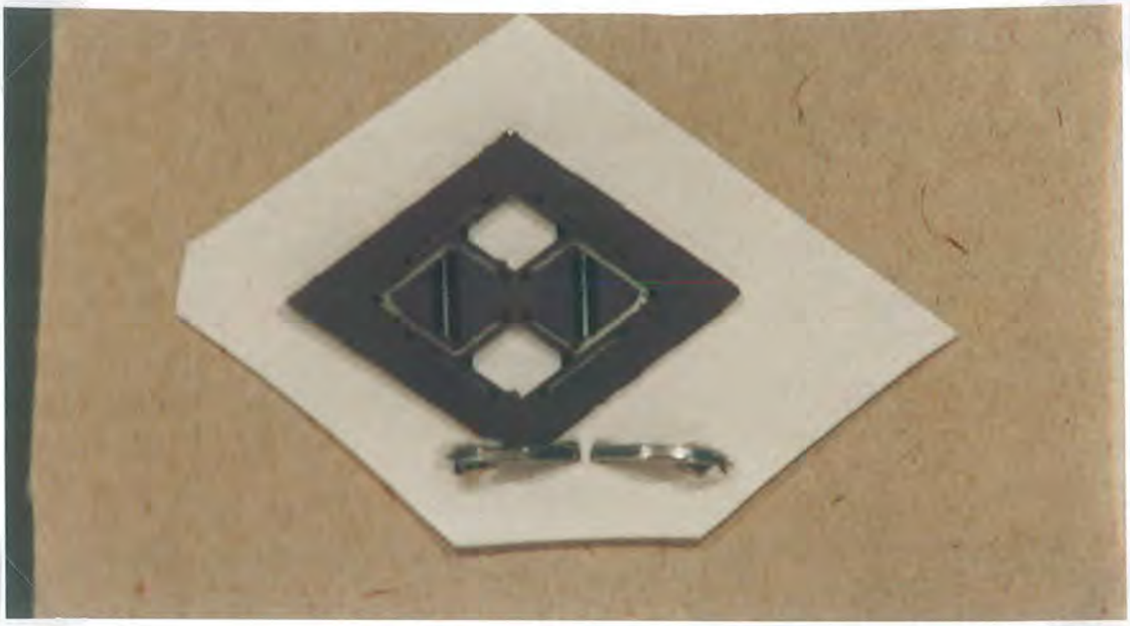

Figure 5.18 Photograph of revision 4

5.2.5 Revision 5

In order to achieve the matching of the modes one last revision of the sensing element was made. The two support beams were dispensed with and the V groove separating the sensor from the main structure was made narrower so that the resulting V groove would not go all the way through the wafer. The sensing element was then supported on a thinned hinge of silicon.

This in turn required the piezoresistors that had previously been diffused into the support beams be repositioned. The orientation of the piezoresistors was changed from being parallel to the {111} plane to being parallel to the {100} plane. This allowed the etchant to dissolve the silicon from beneath the piezoresistors leaving the resistors as a bridge structure running across the V groove. The piezoresistors themselves remain unaffected by the etching due to their boron doping.

This design of sensing element required that the doping level in the resistors be sufficiently high to stop the silicon etchant. This, combined with the reorientation of the resistors away from the optimal {111} direction, had the effect of reducing the gauge factor of the resistors. The calculated gauge factor is discussed in section 3.4.

5.3 Description of the method of operation

Figure 5.20 shows a plan view of the structure. The device is driven into resonance by the Lorentz force generated on the top right and bottom left hand beams. A sinusoidal drive current is passed along each beam in the direction shown by the arrows, so that the current flowing in each beam is always moving in opposite directions.

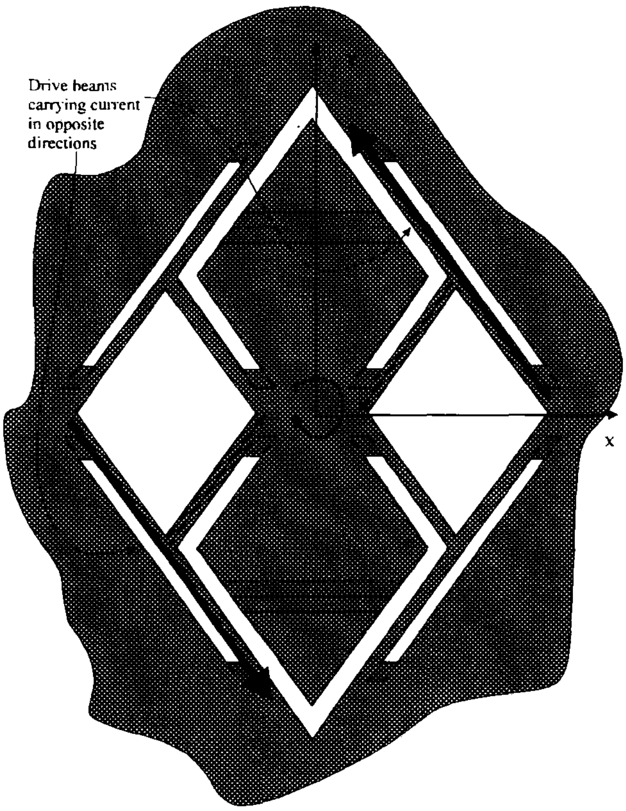

Figure 5.20 The method of Lorentz excitation used in revision 5

The Lorentz force is then transmitted along the two connecting beams to produce a couple on the centre, which drives the central structure into a torsional resonance about the Z axis, normal to the page. In the presence of a rate of turn about the long axis of the device, the Y axis, the secondary motion is excited. The secondary motion corresponds to a second torsional vibration, this time about the X axis. In this mode one tip of the gyroscope is moving out of the plane while the other moves into the plane. These modes are best demonstrated by the finite element analysis plots in the following section.

5.4 Finite Element Analysis of the Structure

5.4.1 Introduction

In this section the results of the finite element analysis of the final version of the 'Bow tie' gyroscope are presented. The finite element analysis has three main aims:-

DYNAMICS

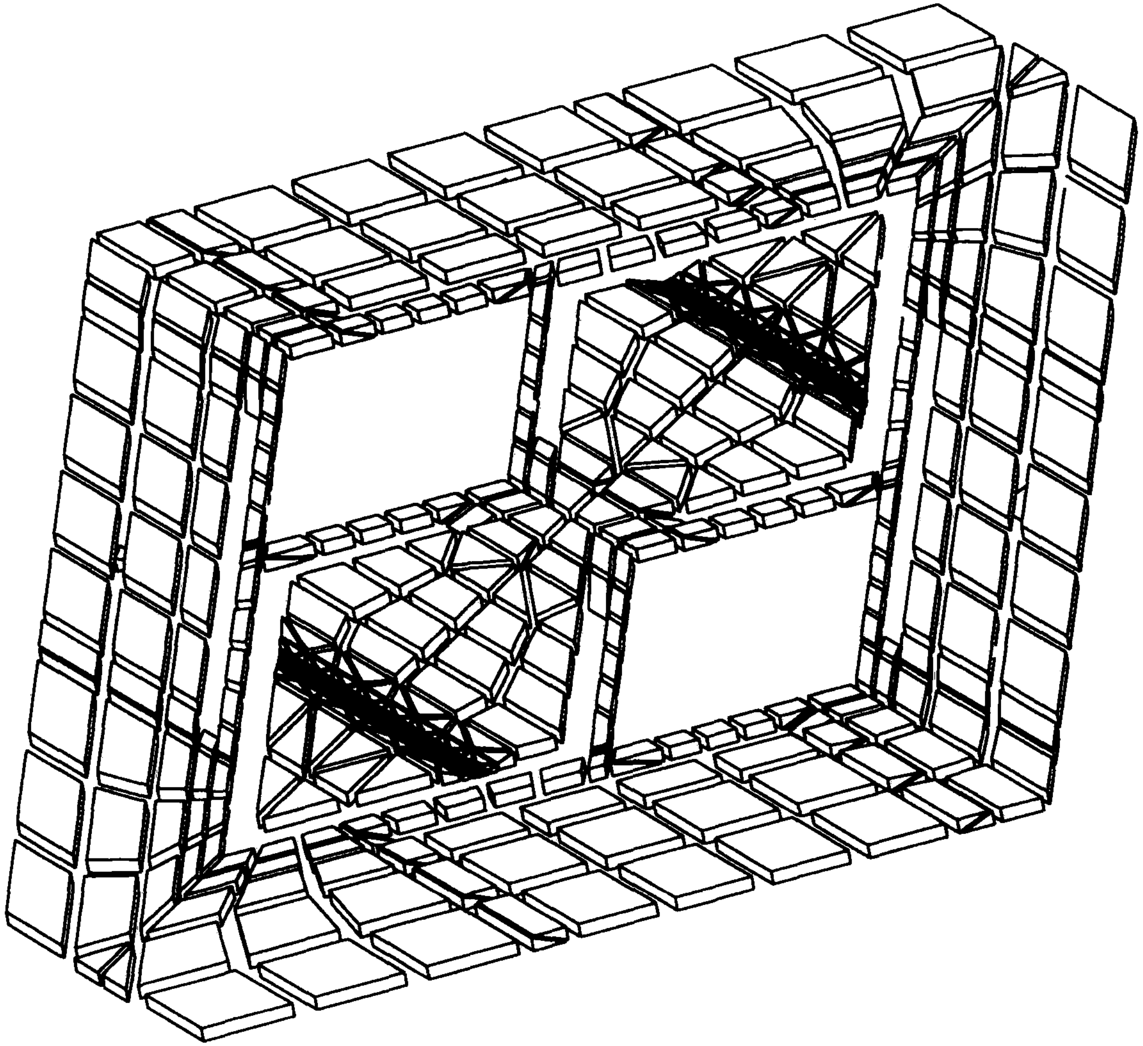

TITLE

FIG 5.21

ROTATION
X = 330
Y = 330
Z = 330

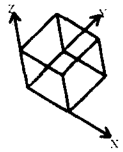

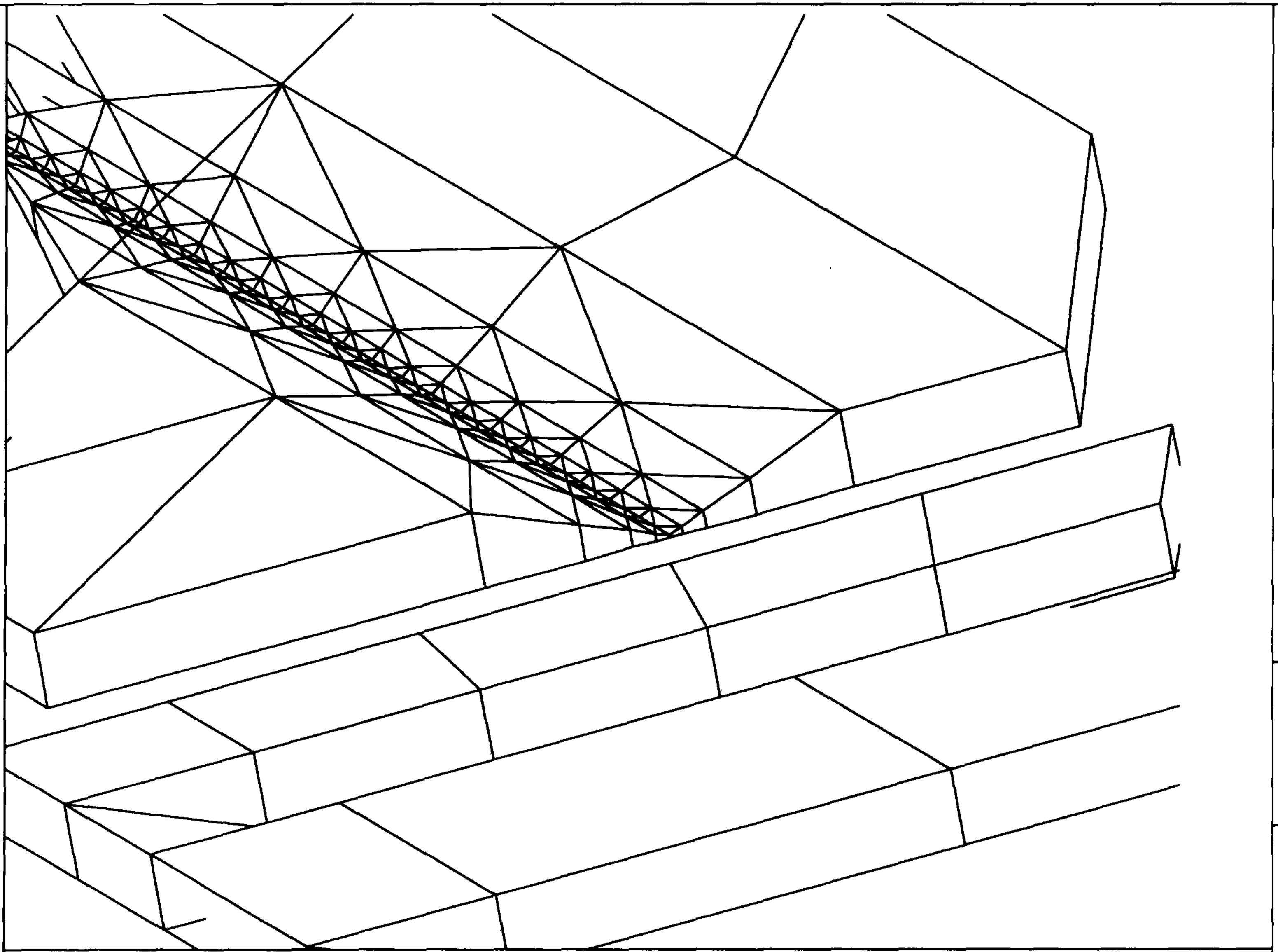

FIG 5·22

- to confirm that the design has the desired resonant modes and that the design dimensions can be adjusted to make the primary and secondary modes have equal frequency.
- to establish that the primary mode could be excited by the Lorentz force in the manner previously described .
- to establish whether the device is likely to be sensitive enough to operate as a gyroscope.

5.4.2 The Finite Element Model

The finite element model is best described with reference to figures 5.21-5.36. Figure 5.21 shows the construction of the FE mesh broken down into its constituent elements. The model was principally constructed with solid three dimensional elements; 20 node bricks, 15 node wedges and 10 node quadrilaterals each having nodes at the corners and midway along each edge. All of the elements used were able to take account of the orthotropic nature of the crystal structure. The rotated compliance matrix , equation 3.14 calculated in chapter 3 was used to define the elastic properties of the material. Using this matrix the rotated reference frame described in chapter 3 agrees with the reference frame shown in the bottom right hand corner of each of the FE plates. The piezoresistive strain gauges running across the V groove were modelled with a single beam element running along the centre line of the structure: this element is represented as a single straight line and is visible in figure 5.22.

The two V groove regions required a very great increase in the mesh density, particularly towards the bottom of the V groove (see figure 5.22). This is a consequence of the very high aspect ratio at the bottom of the groove. The need for such a large number of elements in this region effectively limited the ability to model devices with V grooves deeper than about 296μm in a wafer of 300μm thick (a remaining thickness of only 4μm).

The mesh shown has over 1600 nodes and close to 7000 degrees of freedom. A full dynamic analysis of the model with the rotated orthotropic material properties took

DYNAMICS

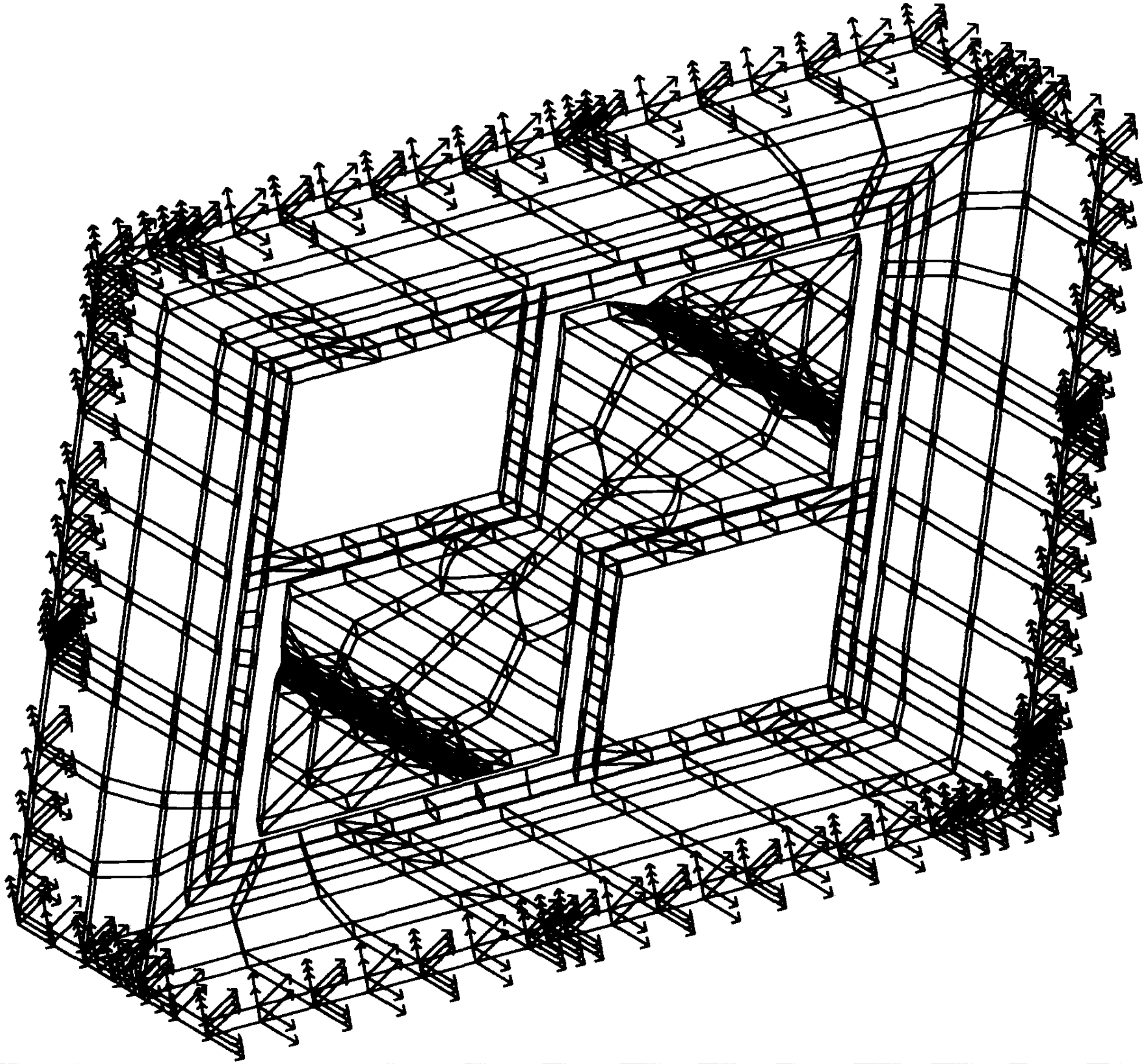

ROTATION
X = 330
Y = 330
Z = 330

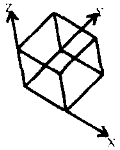

TITLE

FIG5·23

MYDAEMFRSEQ

MODE 1

0.526 E 4

(HZ)

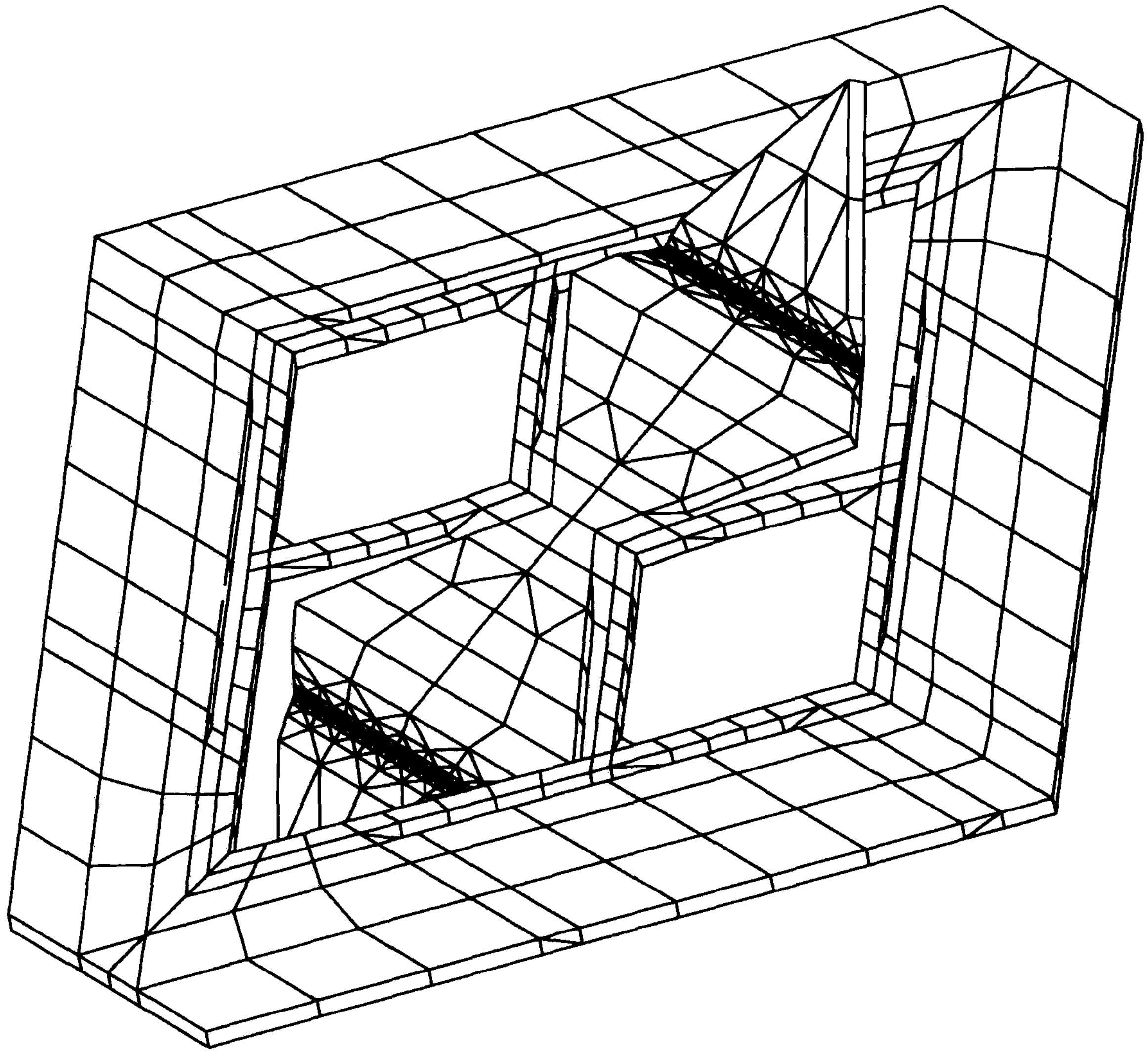

ROTATION

X = 330

Y = 330

Z = 330

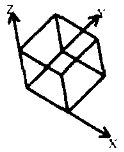

TITLE

FIG 5.24

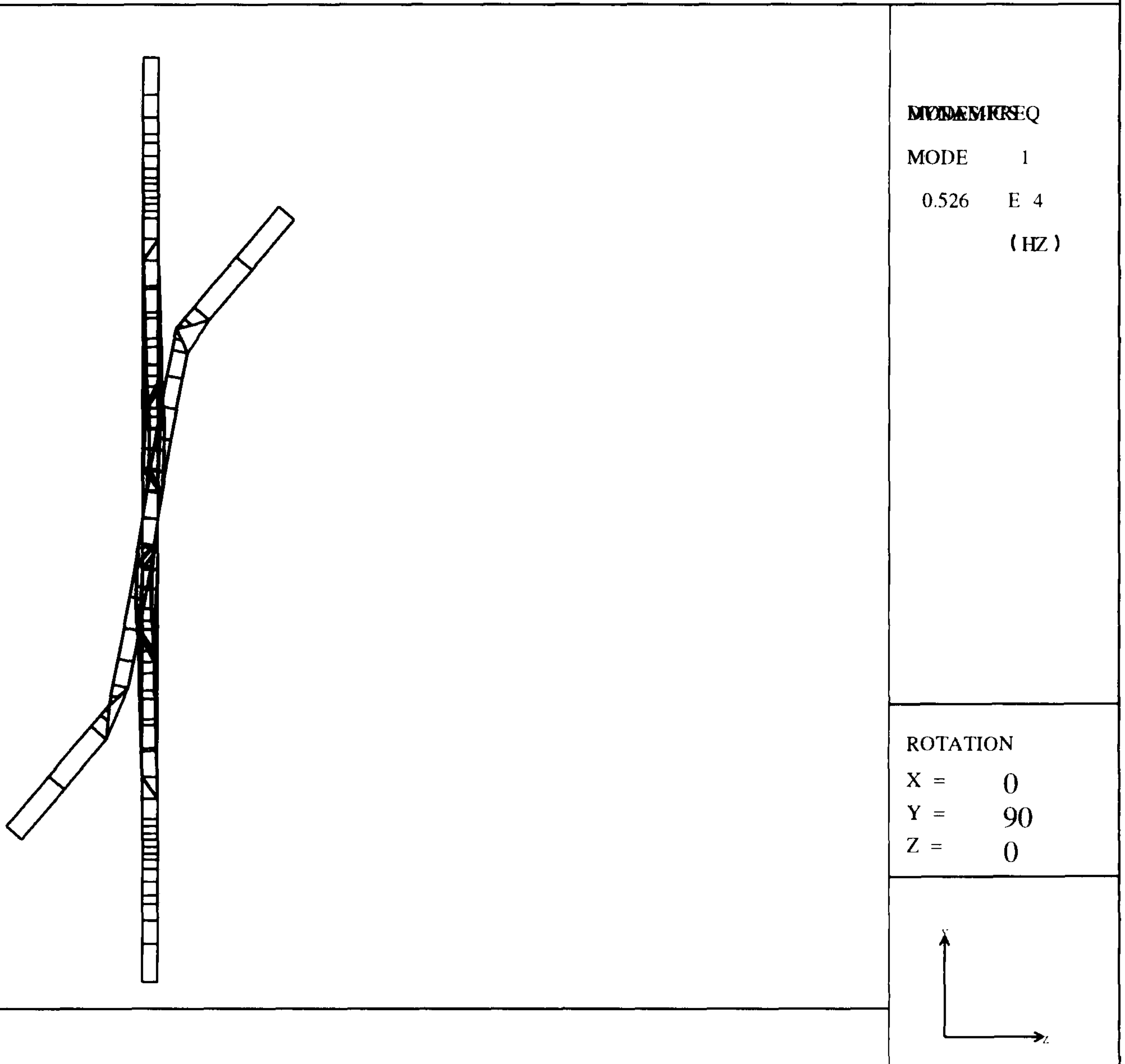

FIG 5.25

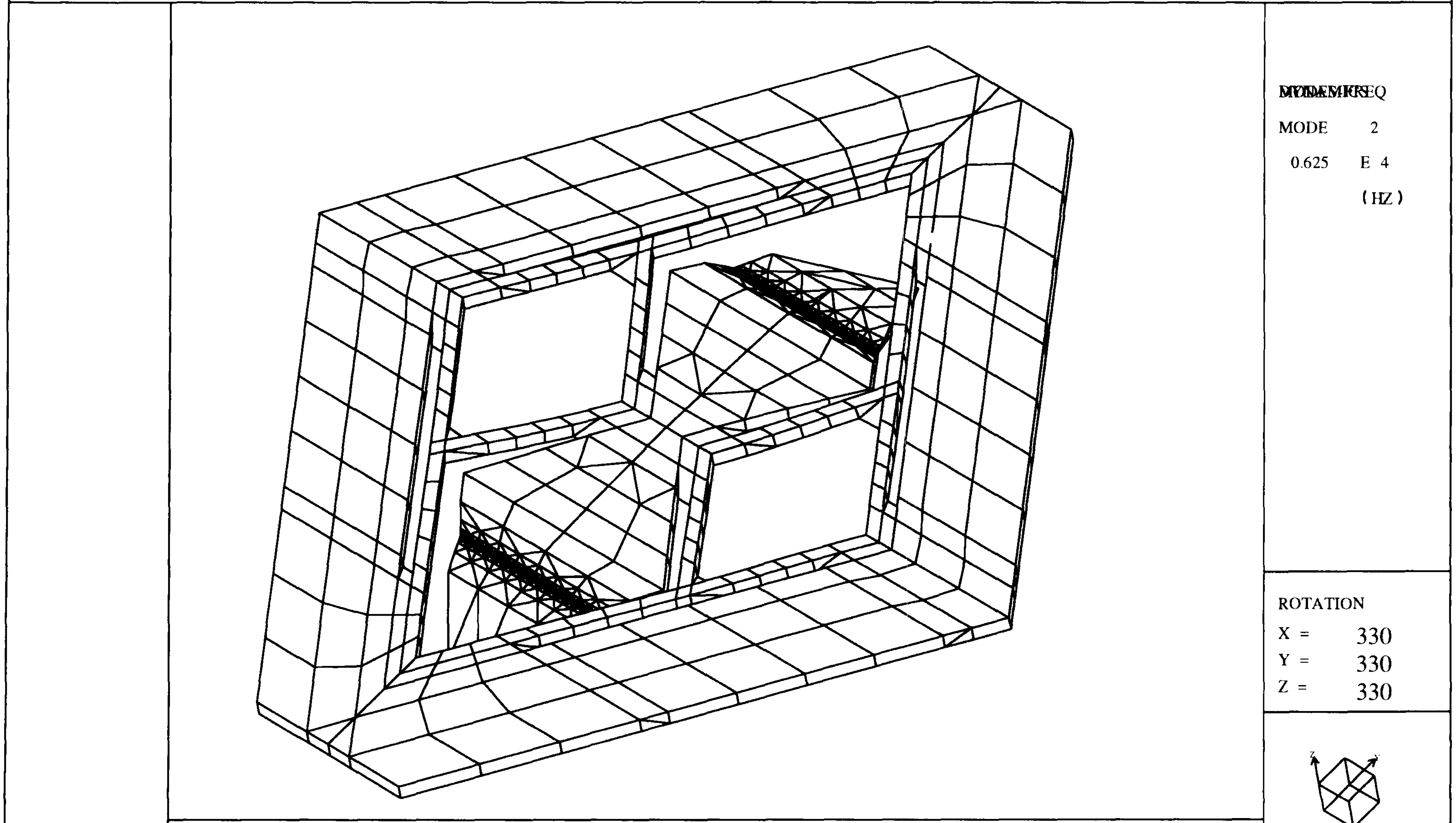

TITLE

FIG 5.26

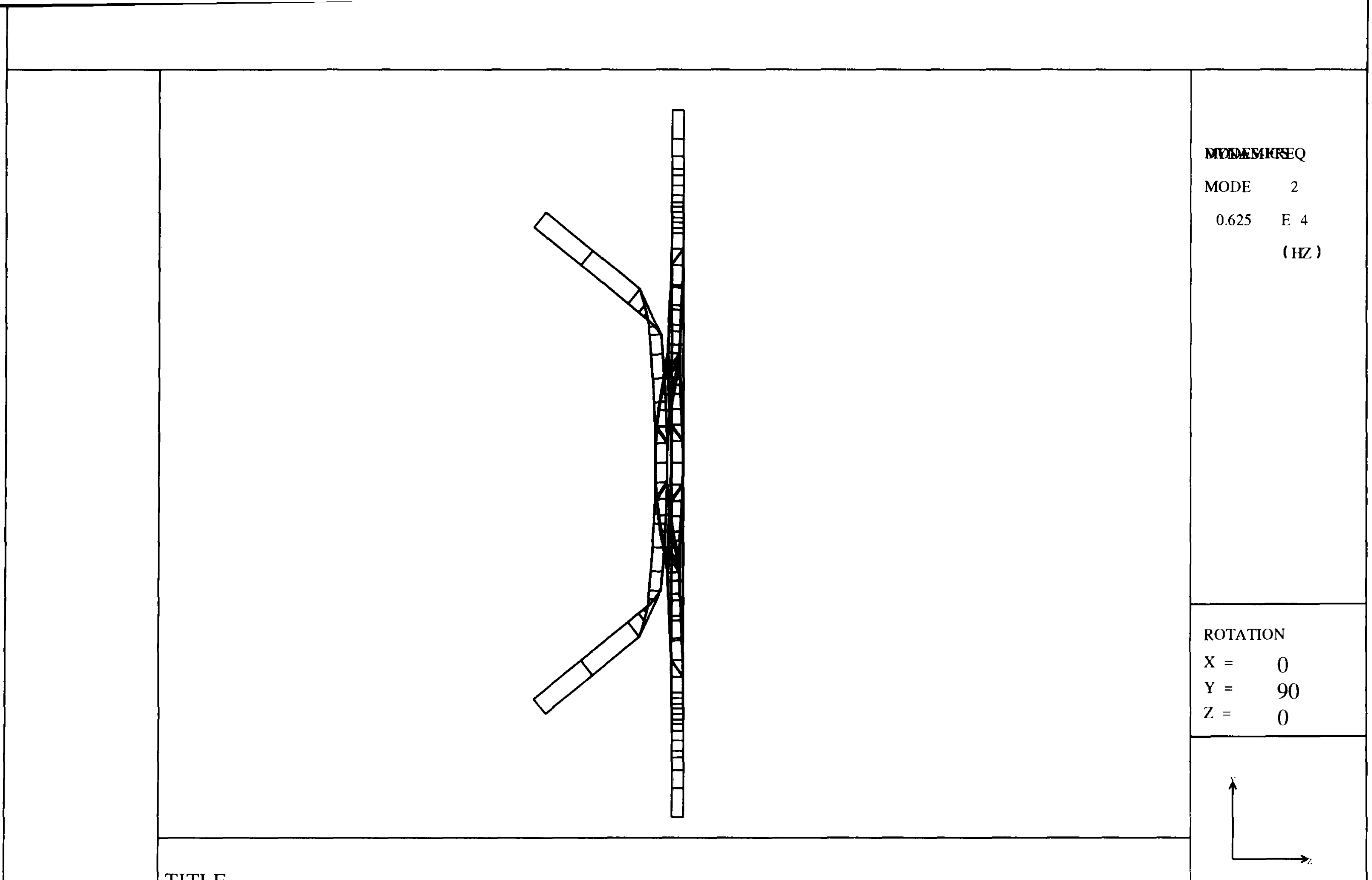

FIG 5·27

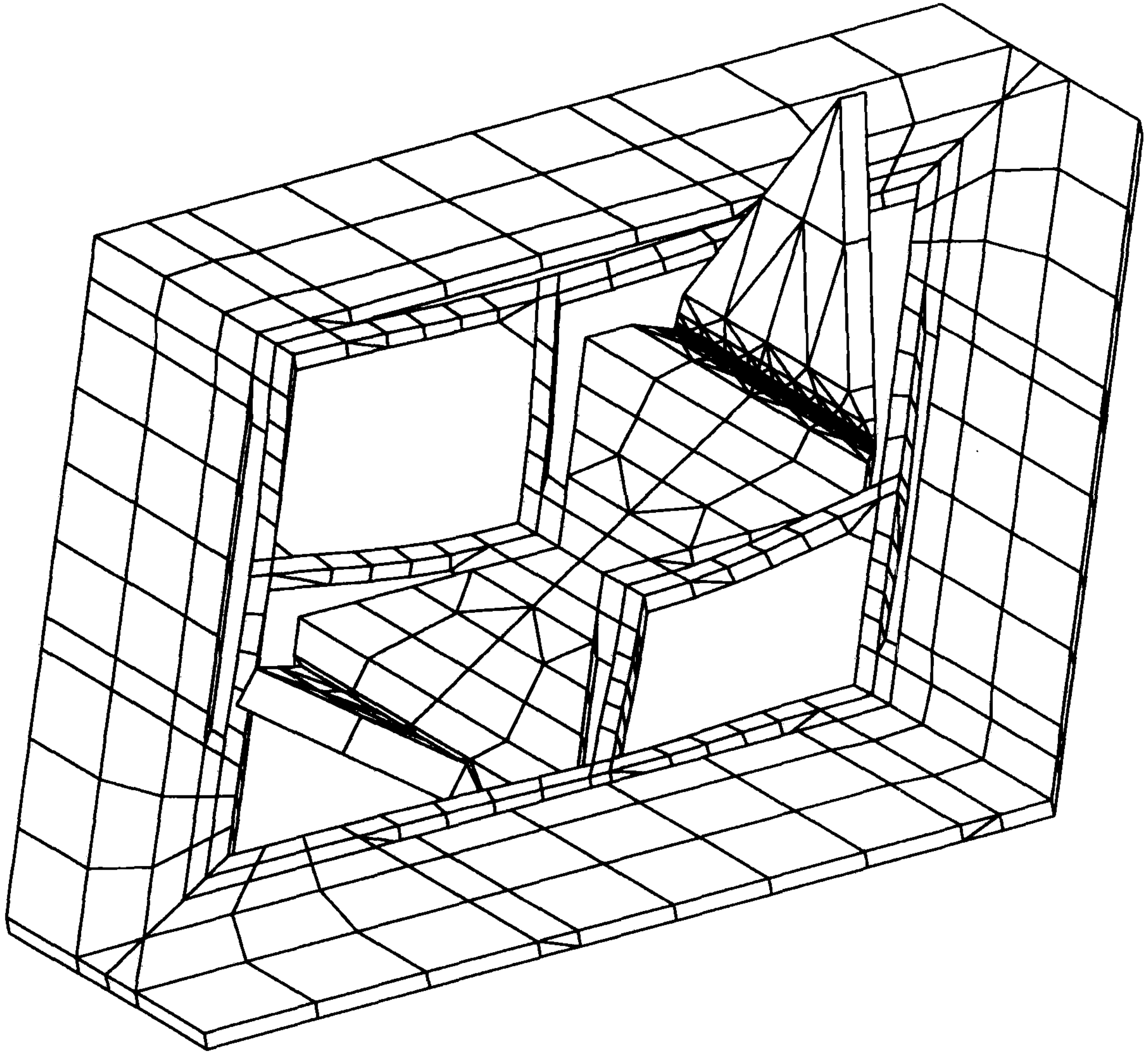
DYNAMICS
MODE FREQ
MODE 3
1.031 E 4
(HZ)
ROTATION
X = 330
Y = 330
Z = 330
Z
Y
X
TITLE

FIG 5.28

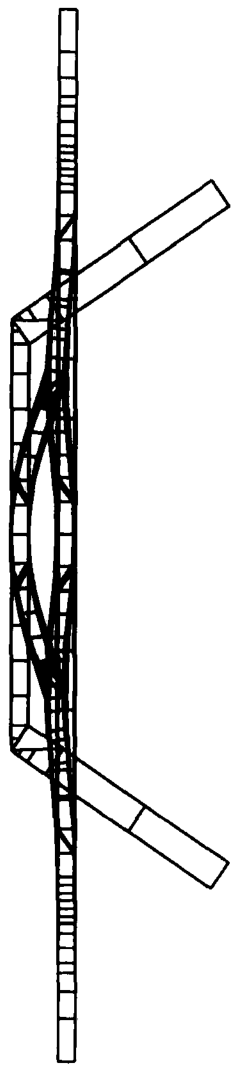

FIG 5.29

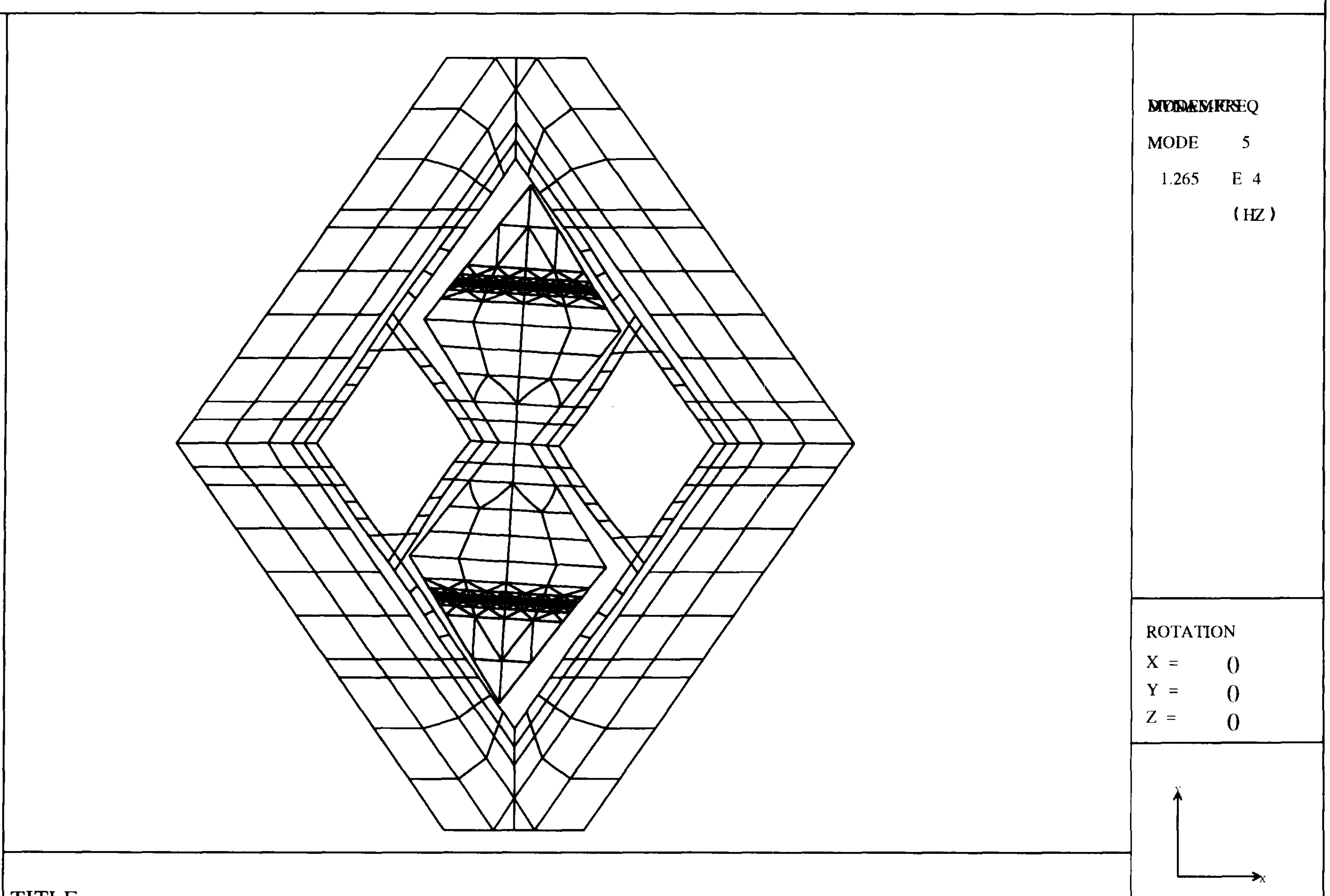

FIG 5:30

MODAL FREQ
MODE 5
1.265 E 4
(HZ)

ROTATION
X = 0
Y = 90
Z = 0

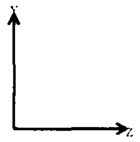

TITLE

FIG 5.31

around 18 hours of CPU time and generates output files of almost 0.5 Gbyte. Limitations on both file space and CPU time prevented running models with a significantly denser mesh. However the mesh density could be increased if the V grooves were omitted. This was done to assess the effect of increasing mesh density on the numerical results. The resultant frequency changes were only of the order of a few percent indicating that a higher mesh density would not produce significantly different results from the ones given below.

The restraints on the structure were applied to all of the nodes around the outer edge of the structure as shown in figure 5.23, where the directions of the arrows indicate a restrained freedom.

5.4.3 Matching the Primary and Secondary Modes

The dynamics of this device are quite complex: figures 5.24 to 5.36 show the first eight resonant modes of the structure. Figure 5.24 shows first resonant mode of the structure: this mode corresponds to a torsional resonance about the X axis as shown in the bottom right hand corner of the plot. Figure 5.25 shows this same mode in cross section. The cross sectional plot also shows the V-grooves cut along each of the tips of the resonant section.

Figure 5.26 shows the second resonant mode: this is a straightforward bouncing mode with the direction of motion of each of the sensors being in phase as shown in figure 5.27. Figures 5.28 and 5.29 show the third resonance. This mode differs from mode 2 in that the centre of the structure is moving in anti-phase with the tips of the structure. The difference between these modes is most clearly shown by comparing figures 5.27 and 5.29.

The primary mode of operation is shown in figure 5.30 and 5.31. Figure 5.30 shows the primary mode shape viewed perpendicular to the wafer surface. The central bow-tie shaped structure is resonating in a rocking mode about the geometric centre of the structure and in the plane of the page (around the 'Z' axis). Figure 5.31 shows the

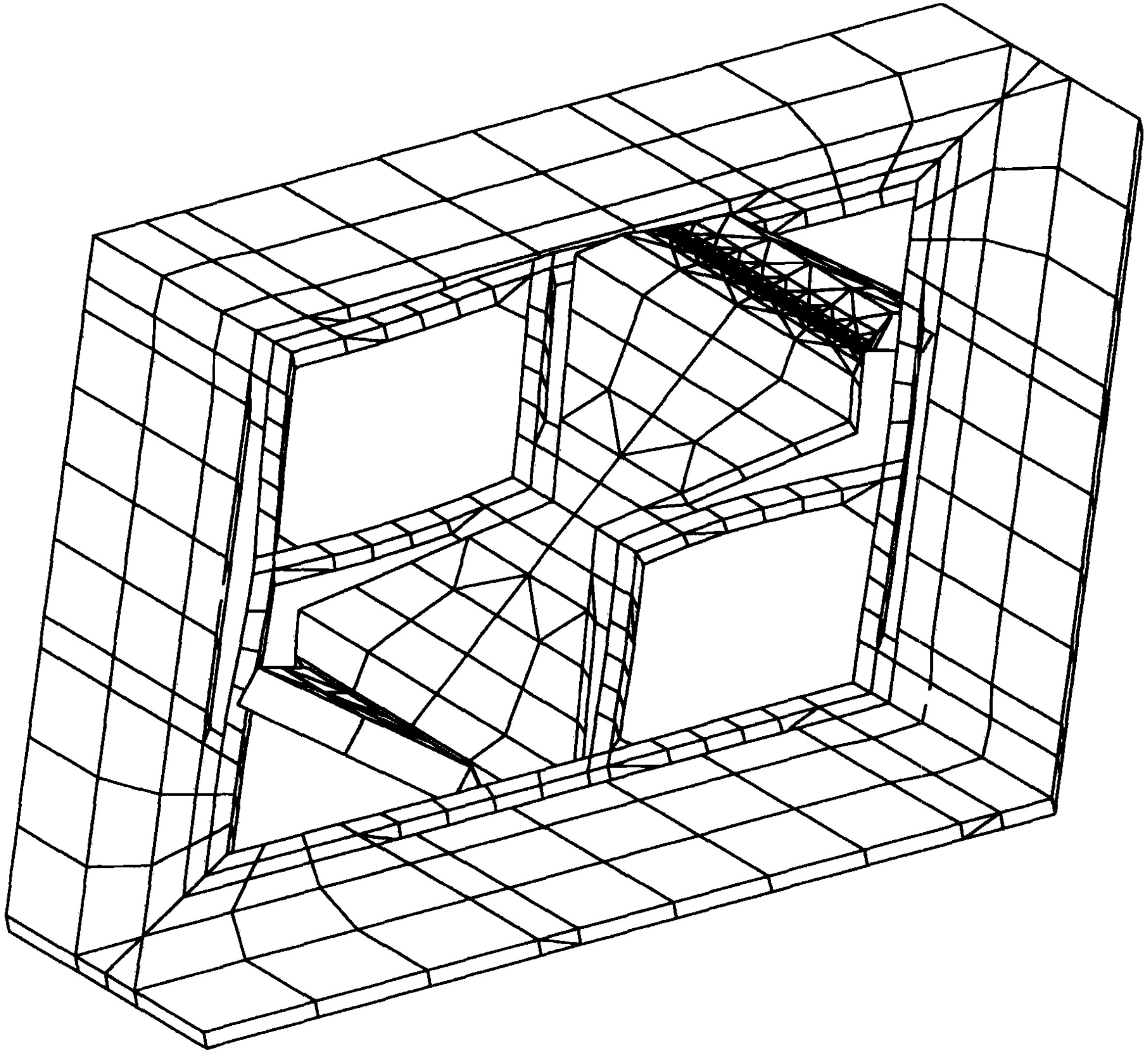

MODAL FREQ

MODE 4

1.265 E 4

(HZ)

ROTATION

X = 330

Y = 330

Z = 330

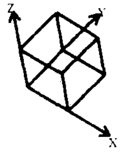

TITLE

FIG 5.32

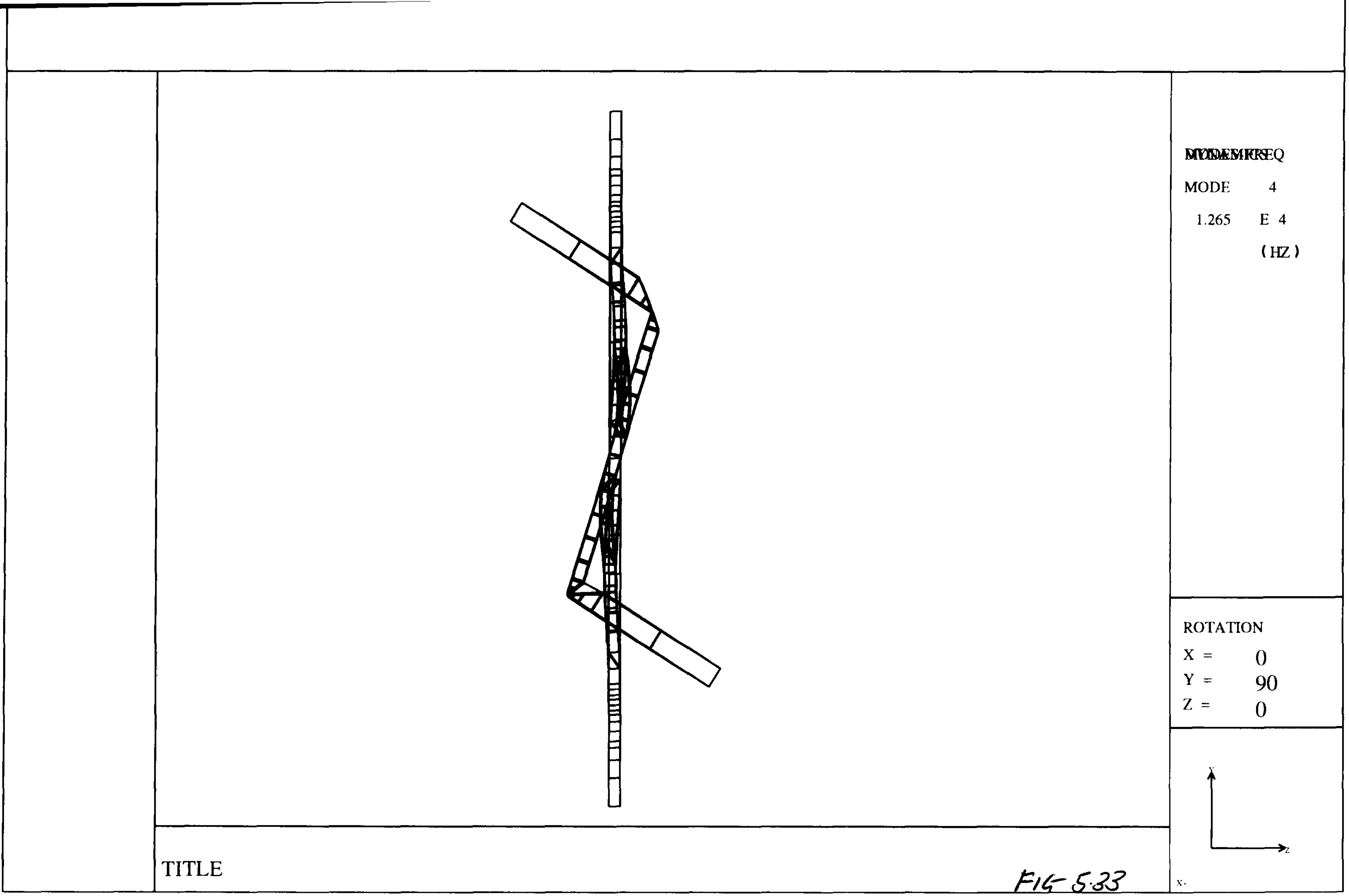

FIG 5.33

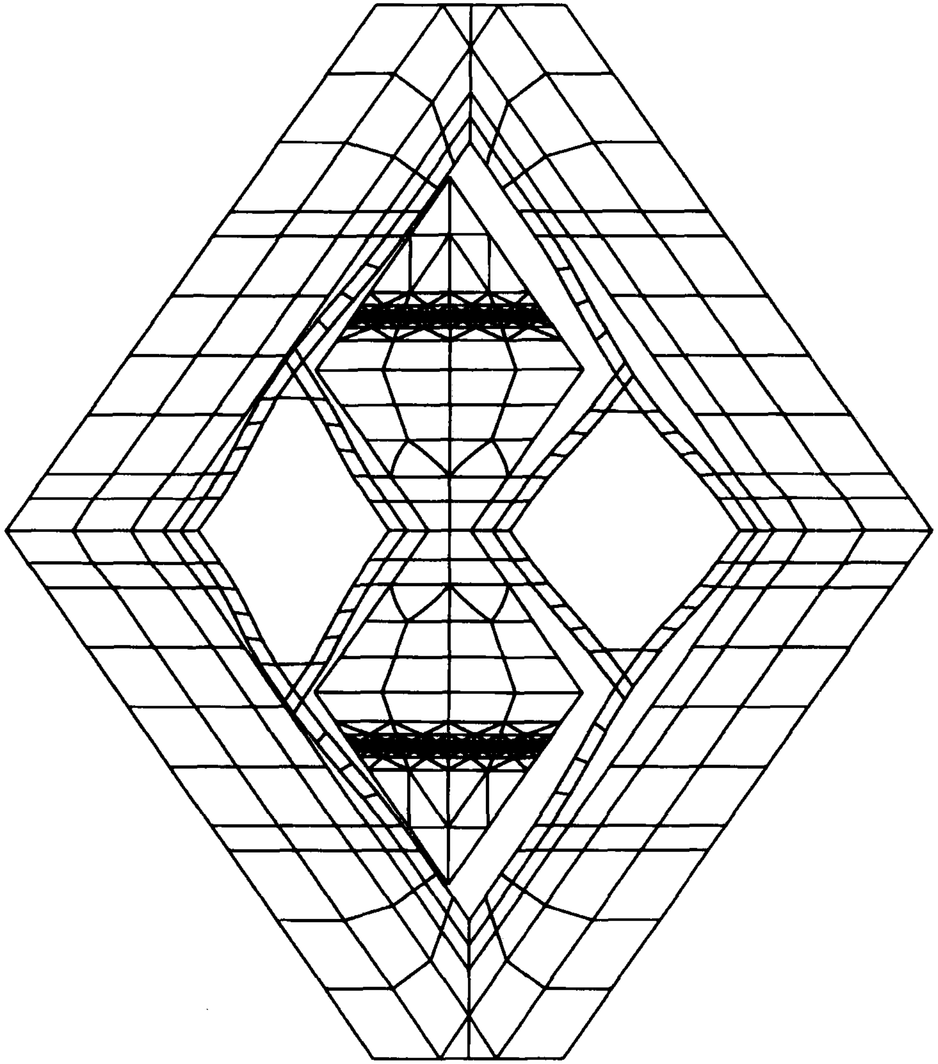

MODAL FREQ

MODE 6

1.591 E 4

(HZ)

ROTATION

X = 0

Y = 0

Z = 0

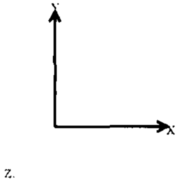

TITLE

FIG 5·34

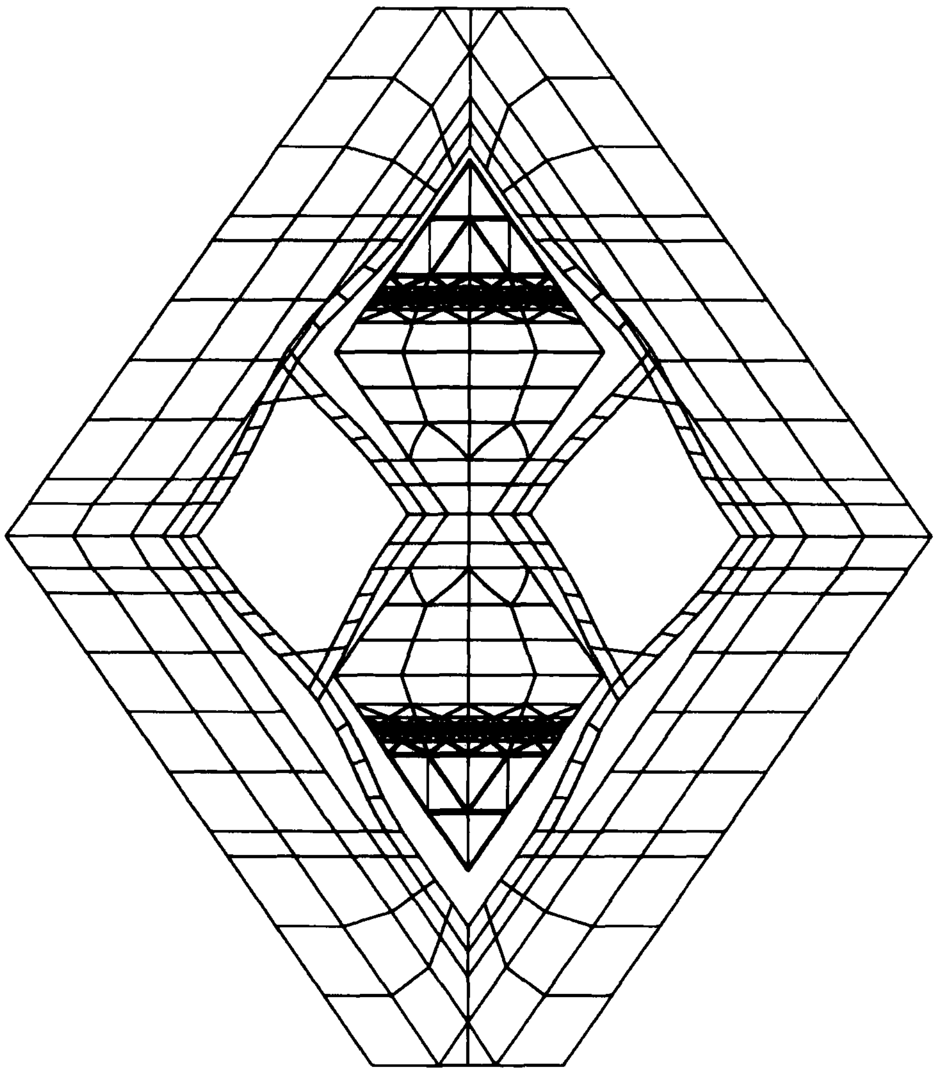

FIG 5.35

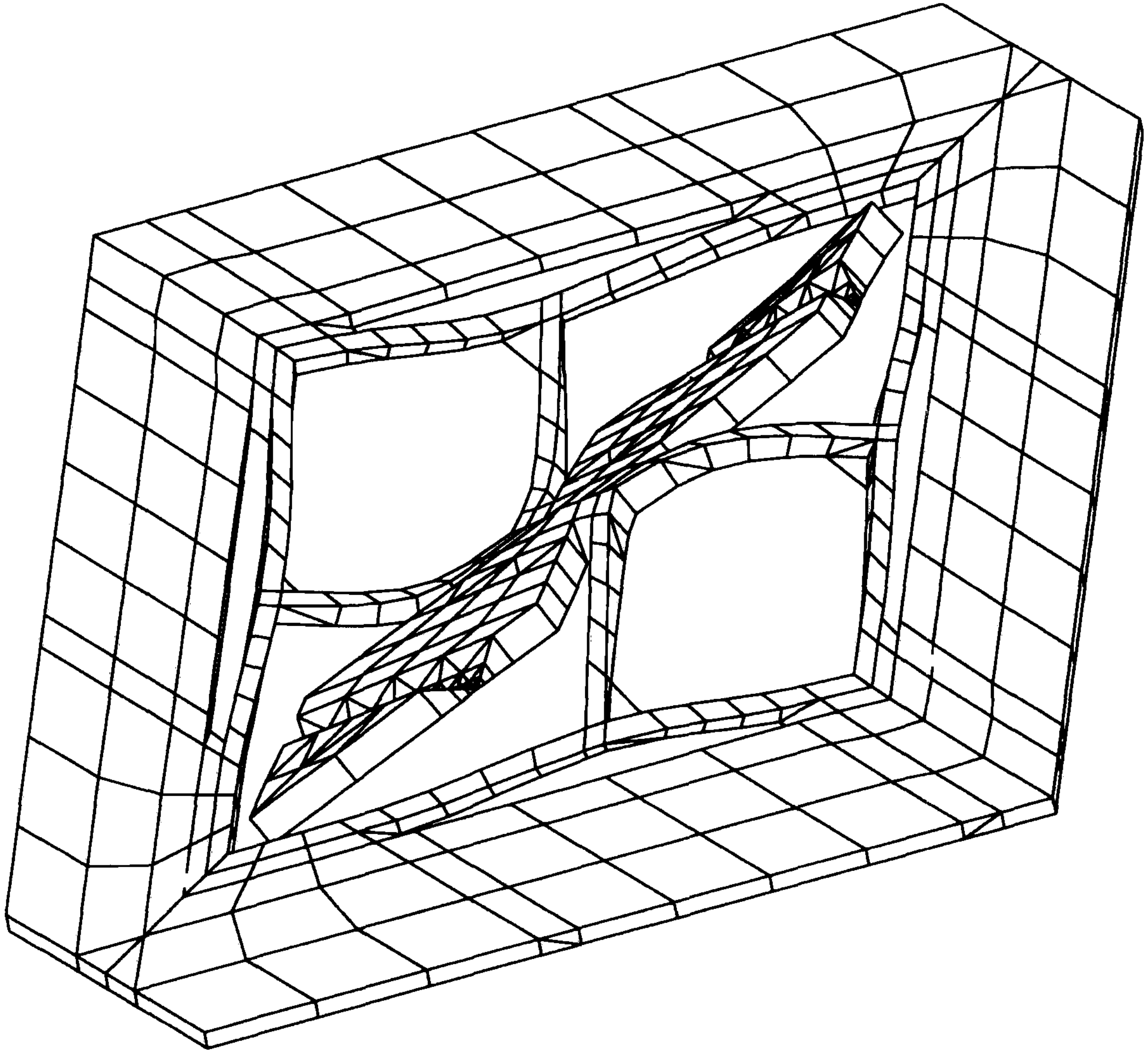

MYMESH MODE FREQ

MODE 8

2.385 E 4

(HZ)

ROTATION

X = 330

Y = 330

Z = 330

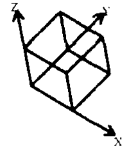

TITLE

FIG. 5:36

same resonant mode viewed parallel to the 'X' axis, demonstrating that the motion of the primary mode is indeed in the plane of the wafer.

Figures 5.32 and 5.33 show the secondary mode. Figure 5.32 shows how the two triangular sensor elements are moving in opposite directions, when one moves into the plane the other moves out of the plane of the wafer. This motion is more clearly shown in figure 5.33, looking along the 'X' axis. This plot clearly shows how the strain gauge sensors running across the 'V' groove, are alternately put into tension and compression. In the bottom half of the figure the structure is bending so as to close up the 'V' groove thus compressing the strain gauge, shown as a thin line crossing the groove. In the top half of the figure the structure is flexing in the opposite direction causing the 'V' groove to widen putting the strain gauge into tension (the strain gauge is obscured in this section of the plot).

The secondary mode of the structure is, at first sight, similar to mode one shown in figures 5.24 and 5.25. Comparing figures 5.25 and 5.33 clearly show the difference between these two modes. In mode one, figure 5.25, each point on the bow-tie structure is rotating in the same direction at any given time. The motion in the secondary mode, figure 5.33, differs in that while the two sensing elements rotate in the same direction the central supporting section rotates in the opposite direction.

Figures 5.34, 5.35 and 5.36 show the next three resonant modes in ascending order of frequency. These plots have been included for completeness only, as the motions shown are not directly of interest to the operation of the structure as a gyroscope . Figure 5.34 corresponds to a resonance in which the bow-tie moves in the plane of the wafer along the 'X' direction. Similarly figure 5.35 corresponds to a resonance in which the bow-tie moves in the plane of the wafer along the 'Y' direction. Figure 5.36 is a rotational resonance about the 'Y' axis.

The resonant frequencies of each of these modes are shown on the right hand side of the mode shape plots. As can be seen from figures 5.30 and 5.32 the primary and secondary modes both have exactly matched frequencies at 12.65 kHz. This was only achieved after a number of adjustments to the design dimensions. This section describes the procedure that was employed to achieve the matching of these two modes.

The structure has numerous parameters that may be varied in order to adjust the resonant frequencies. Due to limitations on computing time and file space only a limited number of parameters could be investigated.

Preliminary results indicated that the primary mode of the structure would be largely independent of the depth of the V-groove and thickness of the sensor beams. This would be expected given that the V-groove does not flex in the primary mode. This fact meant that it was possible to adjust the geometry of the device to give the primary motion a suitable resonant frequency, and then tune the secondary motion to match the primary by varying the V-groove depth .

Tuning of the primary mode was limited to varying one parameter, namely the width of the support and drive beams. This parameter, β, was measured parallel to the x axis as this was most convenient for the finite element calculations. Figure 5.37 shows this graphically.

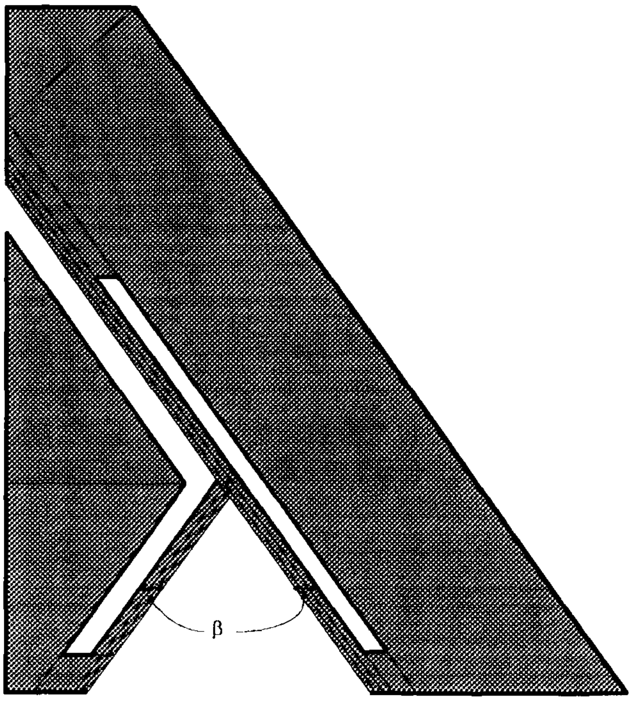

Figure 5.37 **FE models were run with beams of differing widths.**

The FE model was run with 3 different values of β: 100,200 & 300 μm. Figure 5.38 shows how the primary mode varied as a function of β. For the purposes of manufacturing a test device the thickest beam width was chosen, 300 μm. This was dictated by the limits of the lithographic process and the need to pass three wires along the support beams. With better lithography this dimension could be reduced: this in turn would increase the amplitude of the primary mode and lead to a more sensitive device.

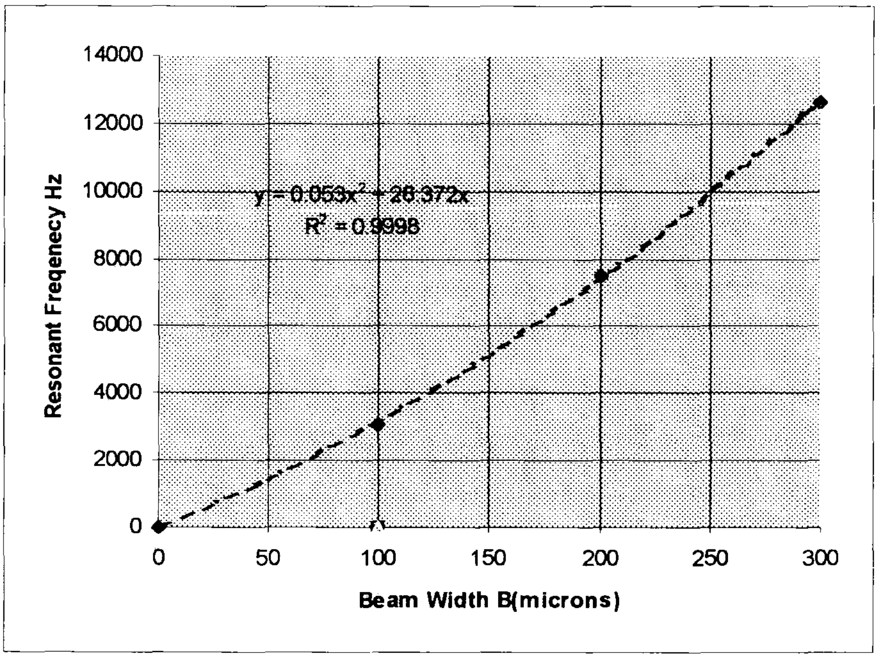

Figure 5.38 The primary frequency as a function of beam width

Having found the frequency of the primary mode it was then possible to adjust the secondary frequency to match that of the primary. This was achieved by adjusting the depth of the V groove running across each of the wings and also by adjusting the thickness of the piezoresistive bridges. After a few iterations of the process the two modes were matched at 12650 Hz with a V-groove depth of 290 μm and a total cross sectional area of the secondary sensing resistors being 169 μm^2.

5.4.4 Post manufacture resonance tuning

Manufacturing the device to have exactly matched resonant frequencies requires a very precise and well controlled process. The electronics industry regularly uses methods of post manufacture tuning to adjust the parameters of electronic circuits. These methods include laser trimming, where tracks are selectively cut using a high power laser. This design of gyroscope also lends itself to this type of process, by placing a number of extra beams across the V-groove on each wing. Once the final device has been manufactured the resonance modes would be measured and these spare beams then broken, so as to adjust the frequency of the secondary mode downwards to meet the primary mode. This method would of course only work if the secondary mode were above the primary in the first place: however the design parameters could be adjusted to make this more likely. These sacrificial beams were incorporated into the final design revision and can be seen later in fig 5.48.

5.4.5 Lorentz and Coriolis loading

Having demonstrated that the device could be fabricated with matched resonant frequencies, the next stage was to assess the effect of the Lorentz force on the device in order to establish if it could realistically be expected to excite the structure.

The magnitude of the Lorentz force is easily calculated from the magnetic field strength and the drive current. Miniature samarium cobalt earth permanent magnets are available with very high field strengths. For the test structures a number of these magnets were purchased.. The magnets were 10x9x6mm with a quoted field strength of 1T. Neodymium iron magnets with a field strength of 1.2T are also available[1]. The Lorentz force is given by:

$$F_{lorentz} = \mathbf{B} \times (\mathbf{I} \cdot \mathbf{L}) \qquad 5.1$$

Assuming a maximum drive current of 100mA equation 5.1 gives an estimated force of 0.1 N per metre. For the purposes of manufacturing the test structure only a single wire was used on each of the drive beams. In a final design the single wire could be replaced with a multi-turn coil having a large number of tracks running along the beam. This would allow the drive current to be reduced by a factor of N, with N being the number of tracks on the beam.

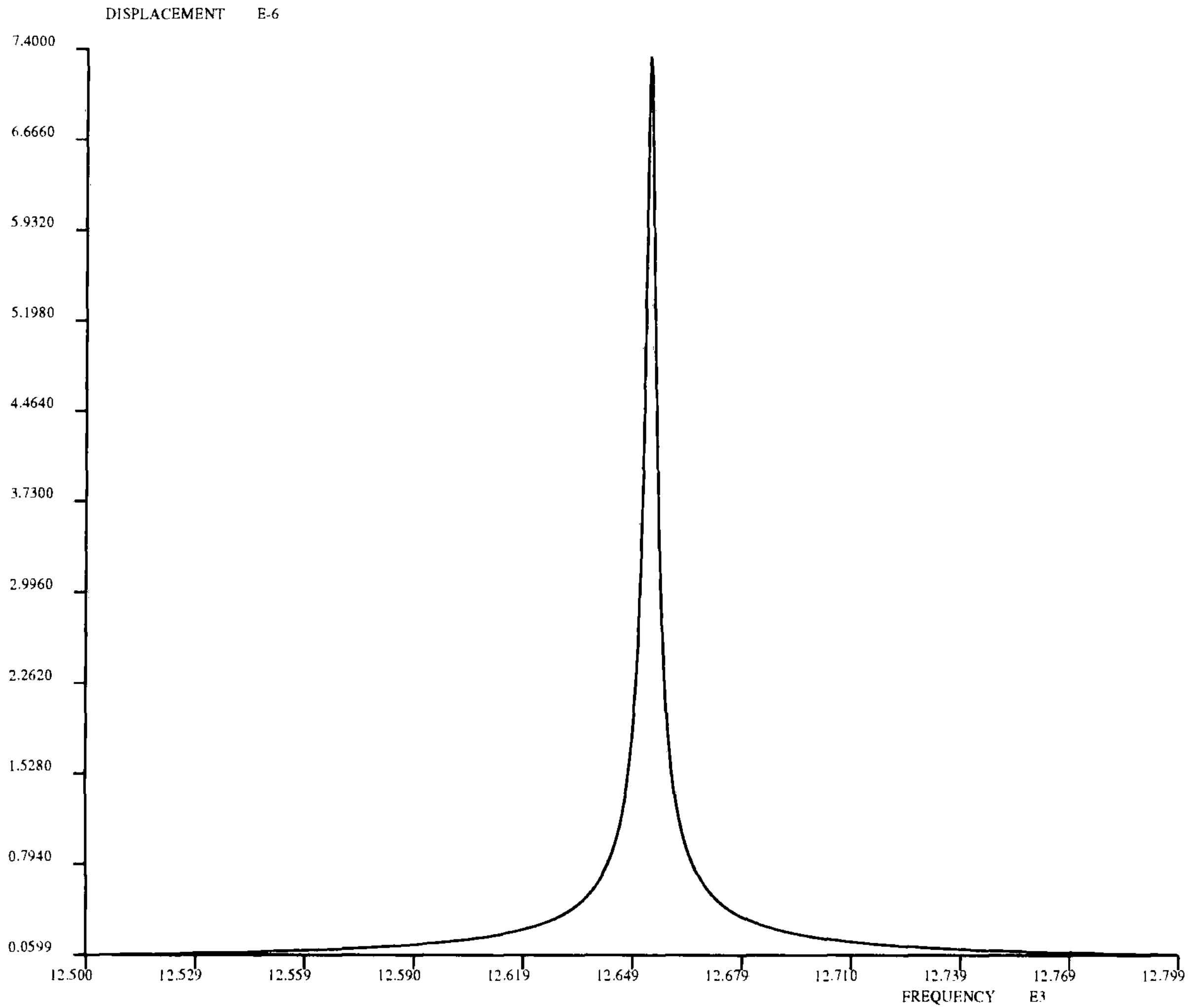

ROTATION

X = 330

Y = 330

Z = 330

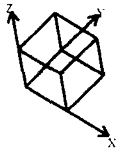

TITLE PRIMARY NODE 43 DIRECTION X

FIG 5·40·

The length of each of the drive beams was 8mm, so giving a Lorentz force 8×10^{-4} newtons acting on each beam. A 50% margin of error was allowed on this figure and a force of 4×10^{-4} N per beam was assumed[*]. This force was then divided appropriately between the nodes on the top surface of the two drive beams. The force was applied as a sinusoidal force acting in the plane of the wafer at right angles to the direction of the drive wire: this is consistent with a magnetic field perpendicular to the wafer. The forces on each of the two drive beams were applied 180° out of phase, consistent with the currents running in opposite directions. A plot of the displacement of the tip of the structure as a function of applied frequency is shown in figure 5.40, predicting a peak displacement of 7.4 microns. This plot was made using an estimated value of Q to be 10,000 [†]. The finite element package used was a linear one, as a result the calculated resonant displacement was directly proportional to the estimated value of Q.

5.4.6 Estimation of the Coriolis force displacement

Having made an estimation of the primary mode displacement it was then possible to estimate the magnitude of the Coriolis force. The finite element package was not capable of calculating the Coriolis force directly. It was therefore necessary to calculate the Coriolis force manually and apply the results to the model directly. The magnitude of the Coriolis force is dependent upon the mass of the structure and the amplitude of its motion (equation 2.3). The estimated Coriolis force was calculated by dividing each of the wings into strips running parallel to the V-groove. The mass of each strip was calculated as was the displacement of the centre of gravity of the strip in the primary mode. This gave a figure for the applied Coriolis force acting on each section of the wing. Figure 5.39 shows the magnitude of the estimated Coriolis force for each node of the structure lying on the Y axis (as shown in figure 5.20).

---

[*] This large margin of error was allowed to take account of the loss of magnetic field strength caused by the spacing between the magnets and the samples.

[†] Values of Q up to 640,000 have been reported in silicon, so this estimate is probably conservative.

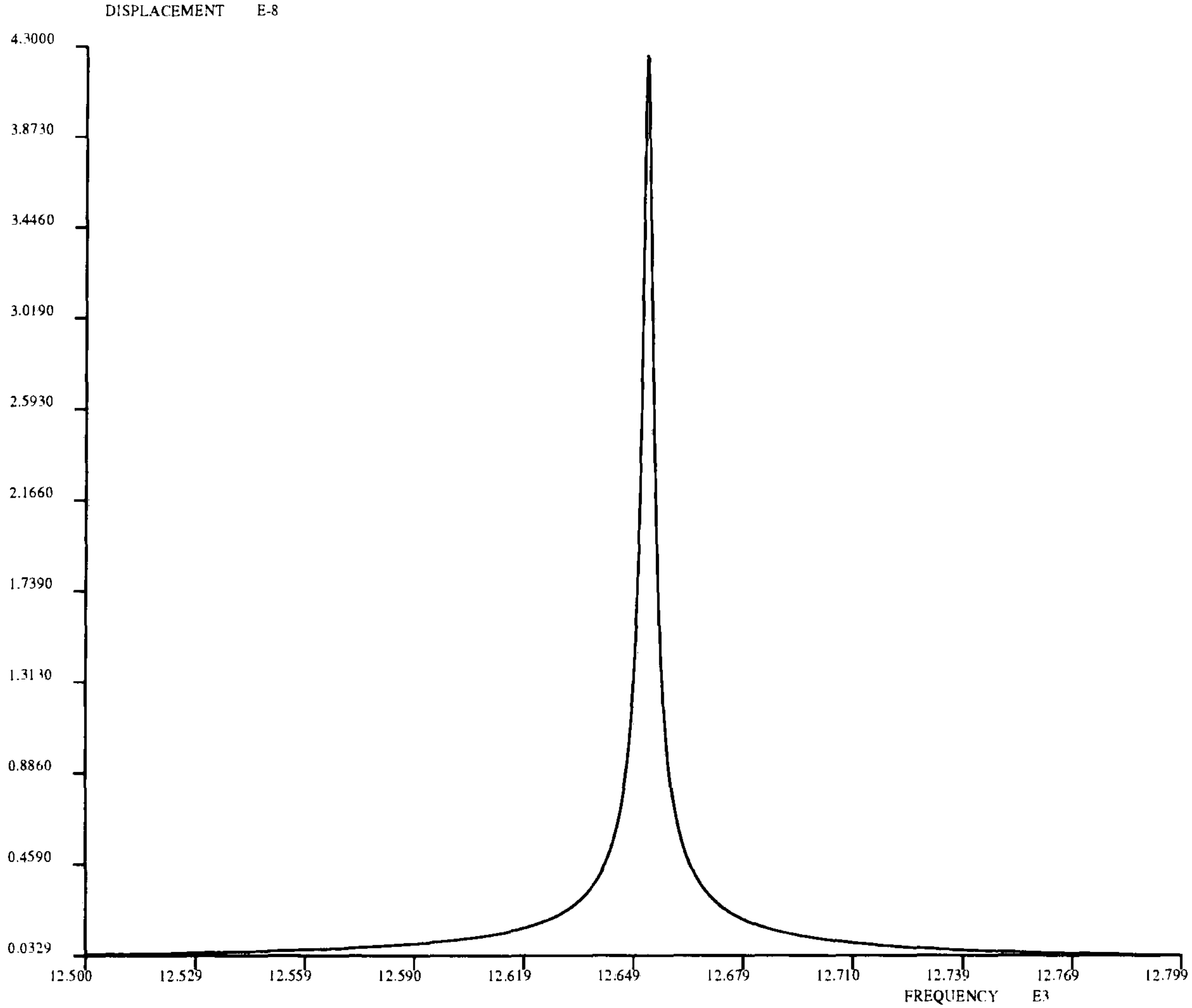

ROTATION
X = 330
Y = 330
Z = 330

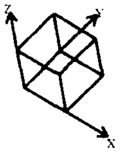

TITLE NODE 43 CORIOLIS RESPONSE Z DIRECTION

FIG 5·41

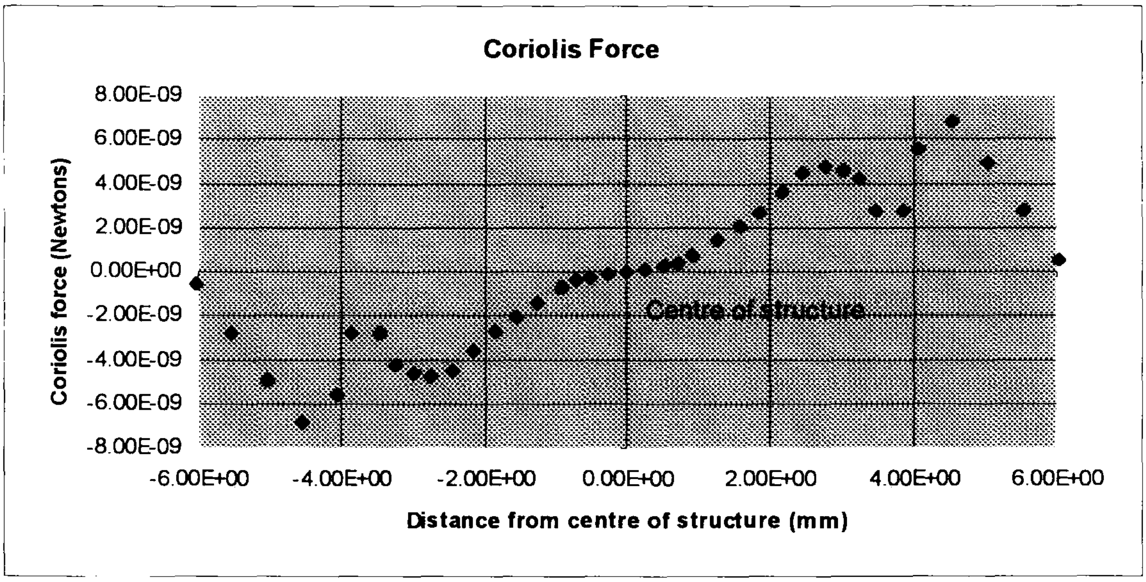

Figure 5.39 **The applied Coriolis force.**

The values shown in figure 5.39 correspond to the Coriolis force generated by a 7.4μm primary displacement at resonance of 12.65 kHz under the influence of a rate of turn corresponding to one revolution per second. The unusual form of the function in figure 5.39 is because both the mass distribution and the vibration amplitude is varying across the device.

This calculated Coriolis force was applied to the nodes lying along the centre line of each wing of the structure. Figure 5.40 shows the estimated displacement of one of the sensor tips under the influence of the applied Lorentz force estimated in section 5.4.5. Figure 5.41 shows the estimated displacement of the sensor tip as caused by the Coriolis force described in figure 5.39. The calculated strain in the secondary piezoresistors under the influence of the simulated Coriolis force was 11μσ/rev/sec.

Using the gauge factor of 30, as estimated in section 3.5, it is possible to calculate the fractional change in resistivity of the secondary sensors under the influence of this strain:

$$\frac{\Delta R}{R} = 30 \times 11e - 6 = 330 \times 10^{-6} \,/\, \text{rev/s} \qquad \textbf{5.2}$$

This figure can now be used to indicate the likely voltage output from the bridge circuit. The two secondary sensing resistors form a natural half bridge arrangement as shown, with both resistors in the half bridge varying in anti-phase.

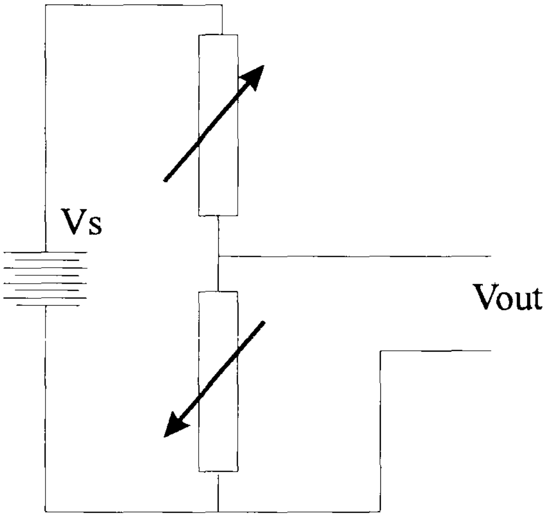

Figure 5.42 **Half bridge.**

The voltage V_{out} is given by:

$$V_{out} = \frac{R_1}{R_1 + R_2} V_s \qquad \textbf{5.3}$$

If both resistors change resistance then 5.3 becomes:

$$V_{out} + \Delta V_{out} = \frac{R_1 + \Delta R_1}{R_1 + \Delta R_1 + R_2 + \Delta R_2} V_s \qquad \textbf{5.4}$$

and solving for ΔV_{out}

$$\Delta V_{out} = \left(\frac{R_1 + \Delta R_1}{R_1 + \Delta R_1 + R_2 + \Delta R_2} - \frac{R_1}{R_1 + R_2} \right) V_s \qquad \textbf{5.5}$$

In this case $R_1 = R_2$ and $\Delta R_1 = -\Delta R_2$ thus equation 5.5 reduces to:

$$\Delta V_{out} = \left(\frac{R + \Delta R}{2R} - \frac{R}{2R} \right) V_s = \left(\frac{1}{2} \cdot \frac{\Delta R}{R} \right) \cdot V_s = 0.5 \times 330 \times 10^{-6} V_s \qquad \textbf{5.6}$$

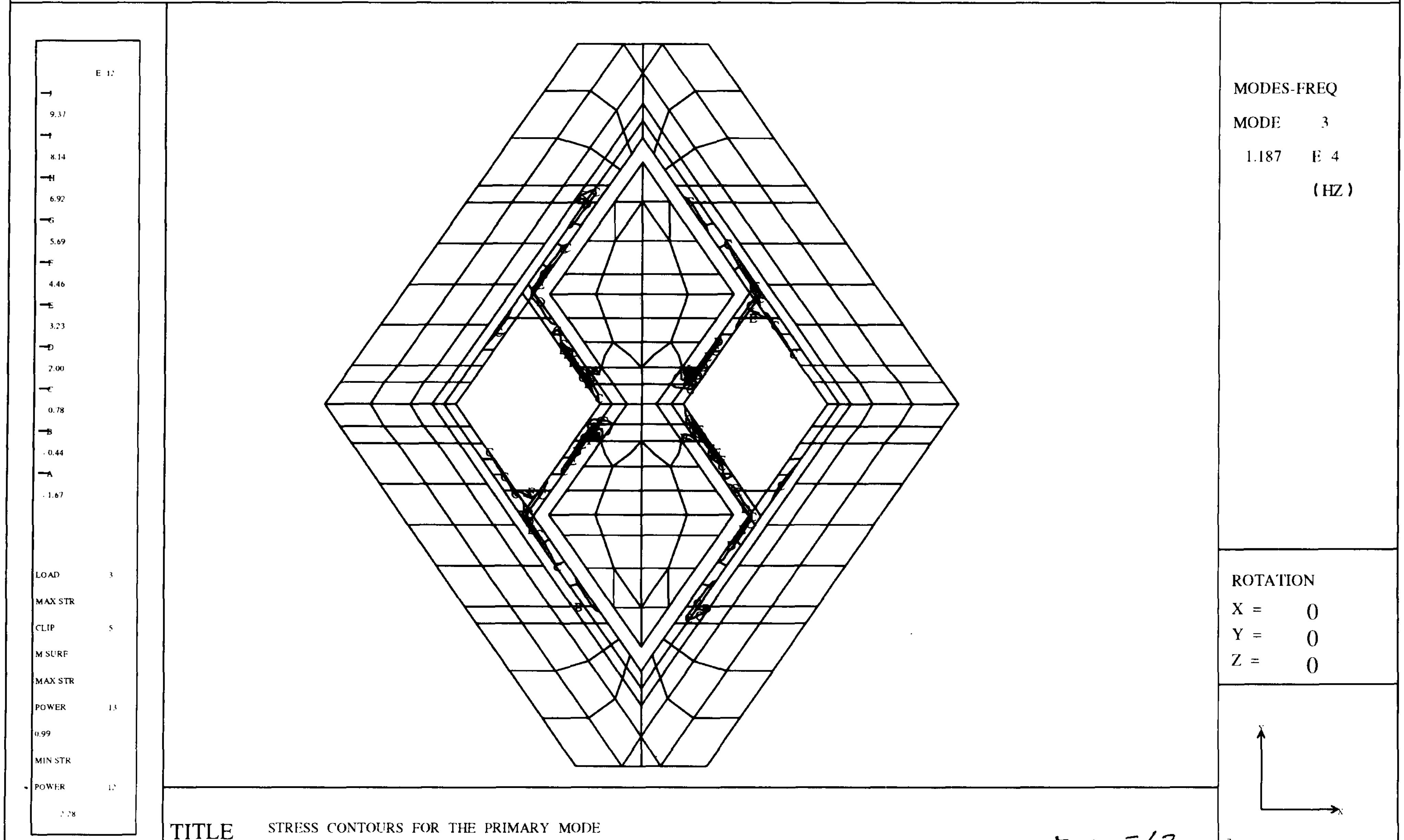

TITLE STRESS CONTOURS FOR THE PRIMARY MODE

FIG 5.43

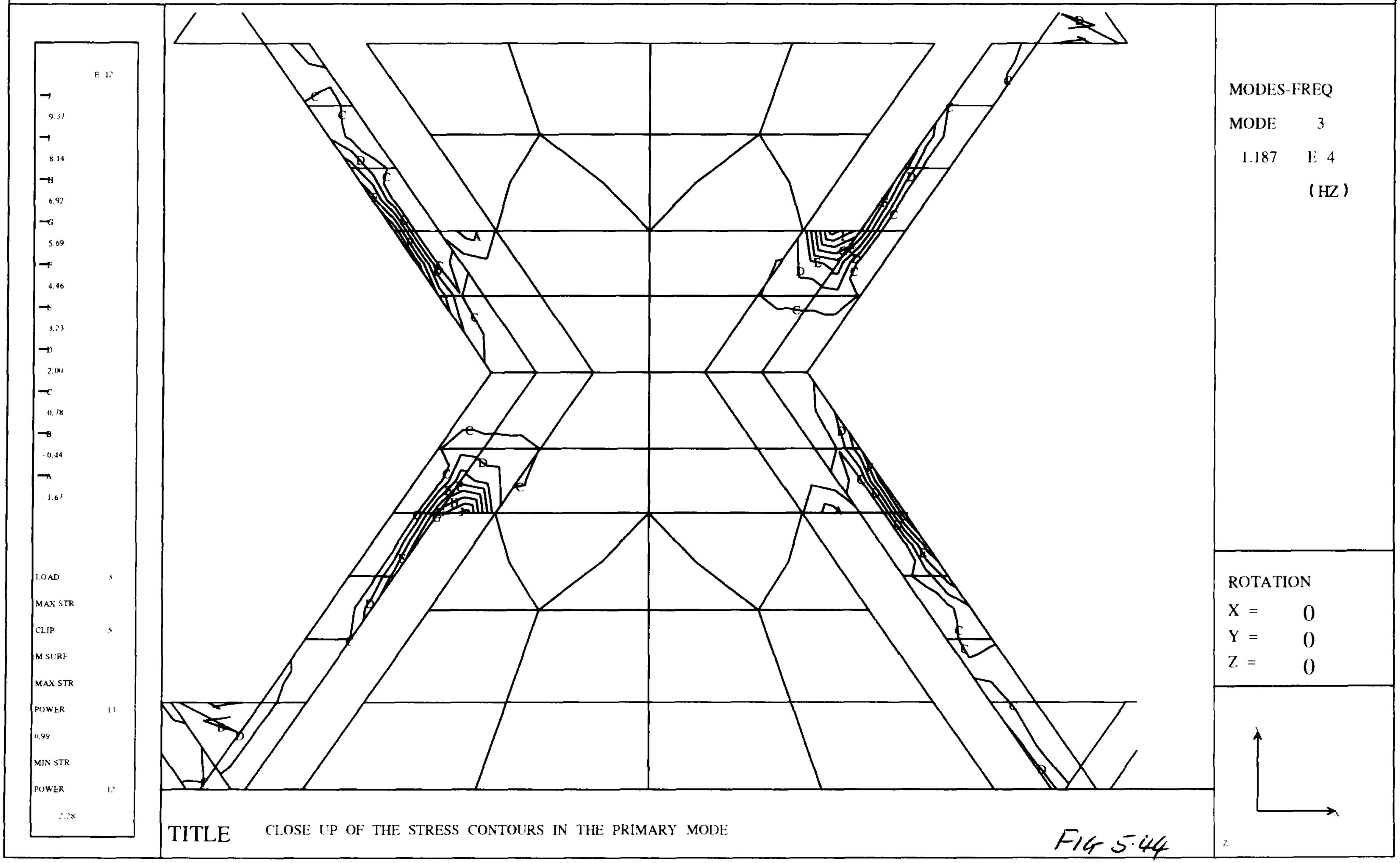

TITLE CLOSE UP OF THE STRESS CONTOURS IN THE PRIMARY MODE

FIG 5·44

Assuming an applied voltage of 10 V then the half bridge should give an output of about 1.65mV per revolution per second[‡]. A signal of this level should be large enough to allow reasonable sensitivity.

5.4.7 Locating the Primary Piezoresistors

The mode shape of the primary motion was used to decide the location of the piezoresistors which were to sense the primary motion. Figures 5.43 and 5.44 show stress contours of the structure as it vibrates in the primary mode. These diagrams indicate that the peak stress will occur in the beams connected to the centre of the structure. The piezoresistors were located on either side of one of those beams in order to coincide with these peak strain regions.

5.5 Manufacturing Process

The manufacturing process of this device involves only a single wafer and is therefore less complex than that of the previous design. Some of the processes involved in the manufacture of this device are common with those described previously: the details of these processes will not be described again.

5.5.1 Wafers

Figure 5.45 shows a diagram of the wafers used to fabricate this device: the relative orientations of the {111} planes are shown. The {111} planes running at 35.26° to the orientation flat are also perpendicular to the wafer surface, those at 90° to the flat are at 35.26° to the wafer surface. The wafers used in all of the manufacturing trials were 300 μm thick. The first stages of the manufacture process were the same as described previously in section 4.4, resulting in an oxidised silicon wafer as shown in figure 5.46a.

[‡] This estimation is dependent upon the product of the Qs of both resonances. Individual Qs of 10,000 have been assumed. If these figures are as low as 1000 then the sensitivity would drop to 16.5μV per rev/per sec.

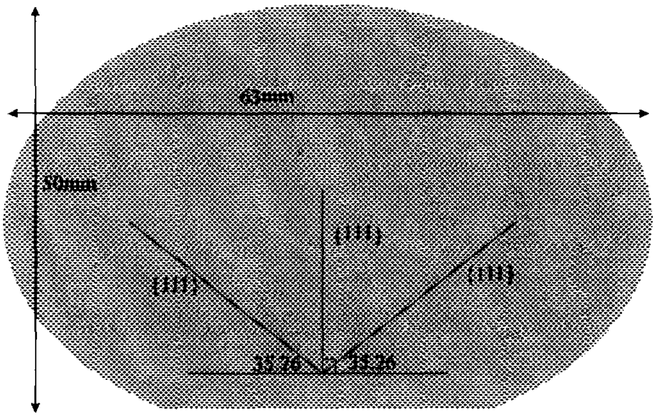

Figure 5.45 Showing a figure of the silicon wafers used

5.5.2 Cleaning and Oxidation and Diffusion

Following the oxidation process windows were opened in the oxide on the polished side of the wafer. These windows served to define the subsequent diffusion stage. Figure 5.46 shows the wafer following the oxidation stage, the first mask stage and after the diffusion stage. The diffusion time used was 3 hours. Following the diffusion process the same boron glaze removal procedure as described in section 4.4 was followed. The diffusion process served to form the piezoresistors for the primary mode detection and for the piezoresistive bridges which formed the secondary sensing elements.

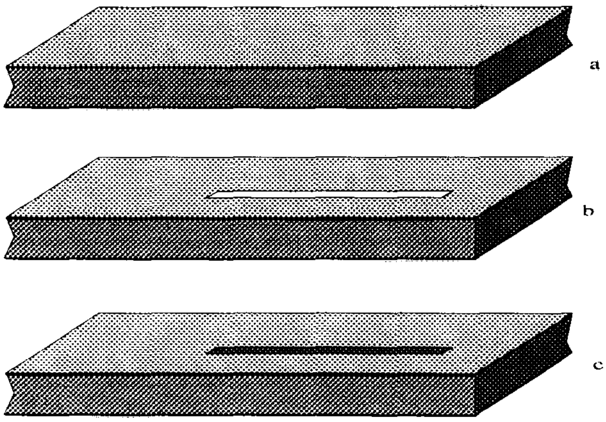

Figure 5.46 The diffusion mask and diffusion process

a: The wafer is oxidised, b: the oxide is selectively removed, c: boron is diffused into the exposed regions of silicon.

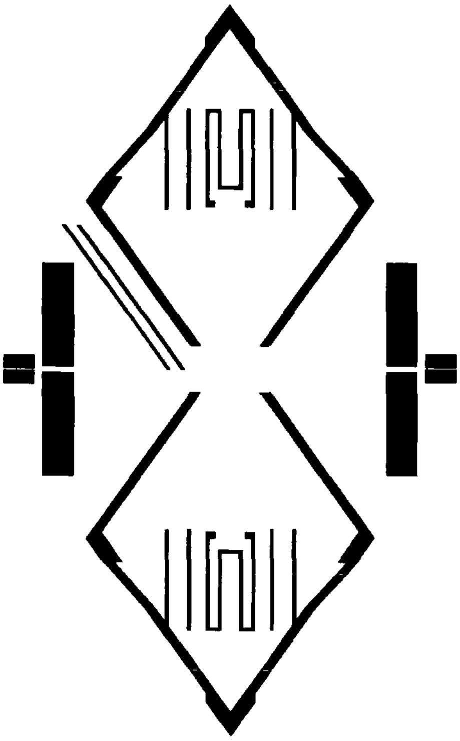

Figure 5.47 The mask pattern used to define the boron diffusion process.

Figure 5.47 shows the first mask stage. The primary and secondary piezoresistors are shown: these are the folded black lines inside the two near diamondpatterns. Either side of the piezoresistors are the sacrificial bridges which may be used to adjust the resonant frequency of the secondary mode. The thick broad lines forming the two diamond shapes define a region of boron doped silicon around each of the two wings of the bow-tie: this region acts as a corner compensation mask. Boron diffused silicon was found to be a more effective mask for corner compensation than silicon dioxide. The two thin parallel diagonal lines on the top left of the figure form the primary motion sensing piezoresistors. The rectangular structures either side of the device are alignment and orientation marks and do not form part of the final structure.

5.5.3 Anisotropic etch mask

Once the diffusion and boron glaze removal stages are complete the mask pattern for the anisotropic etch was formed in the silicon oxide. This mask also served to open contact windows through the thin oxide, created by the boron glaze removal, to the piezoresistors. This process is a straightforward oxide etch process as described previously.

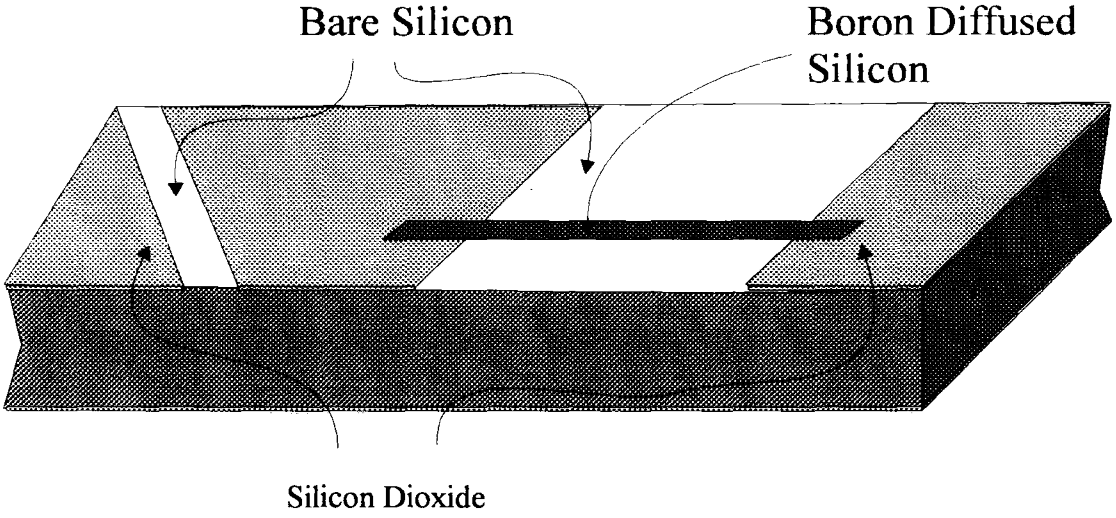

Figure 5.48 The wafer after the boron diffusion and etch mask stages.

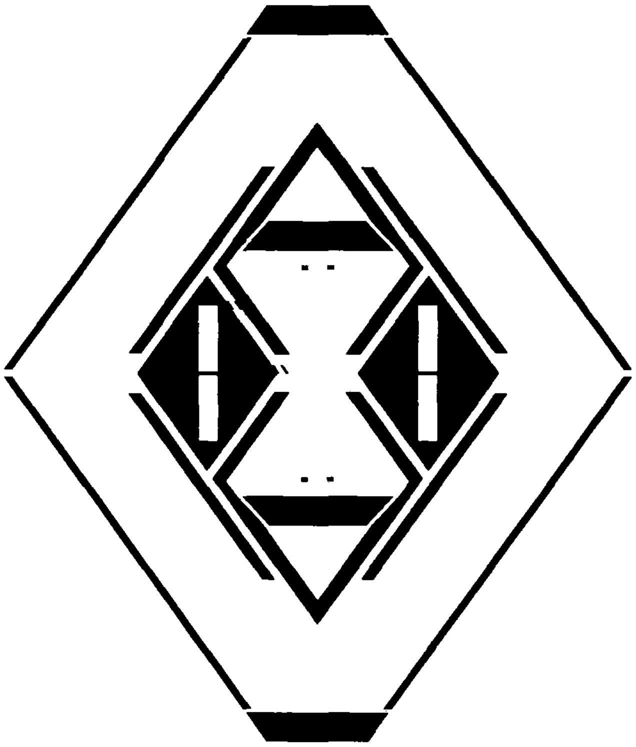

Figure 5.49 The mask pattern used to open the etch windows.

5.5.4 Metallisation

The next stage was to deposit the metal tracks that were used to form the interconnections to the piezoresistors and the wires carrying the drive current. The same gold/chromium combination was used as described previously. However, for this device a thicker layer of gold was used in order to allow the drive wires to carry a heavier current.

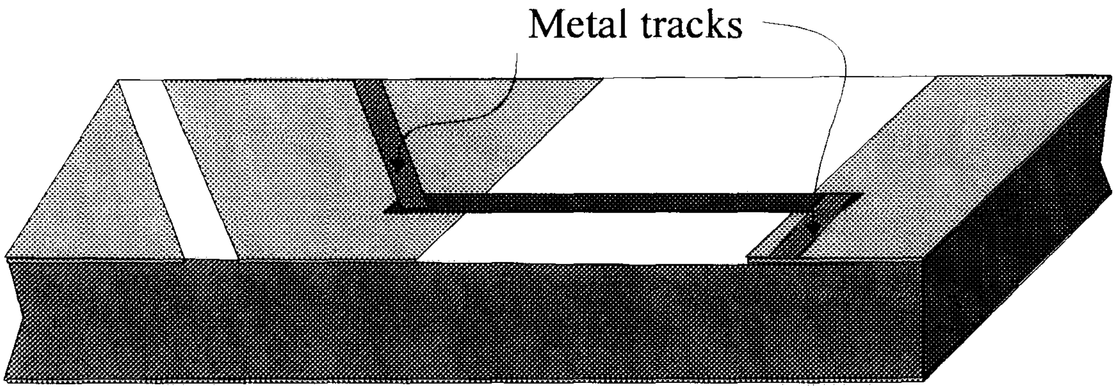

Figure 5.50 The wafer after metallisation and metal patterning

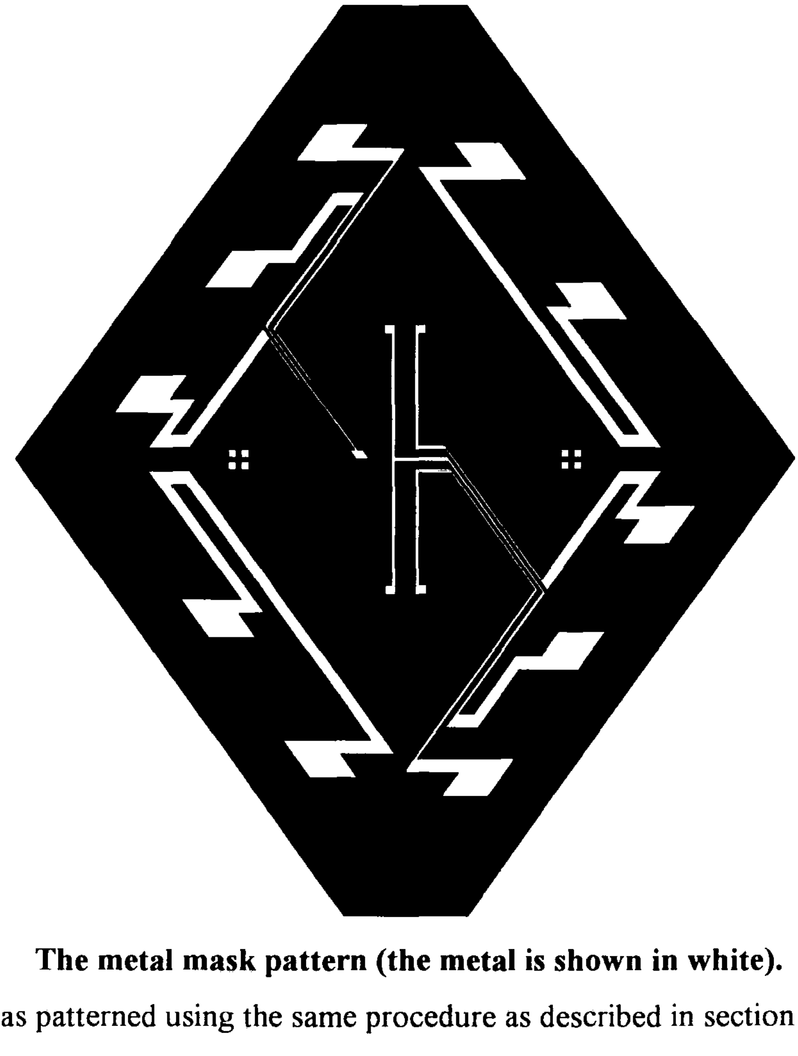

Figure 5.51 The metal mask pattern (the metal is shown in white).

The metal was patterned using the same procedure as described in section 4.4.

5.5.6 The anisotropic etch

The anisotropic etch was performed using the EDP process described in section 3.2.1. The {110} plane of silicon is attacked more rapidly in this etchant than is the {100} plane: as a consequence the etch took less time than with the previous device. The process typically took around 3 hours. As shown in figure 5.52 this process allowed the formation of both vertical trenches and V shaped trenches depending upon the orientation of the etch window.

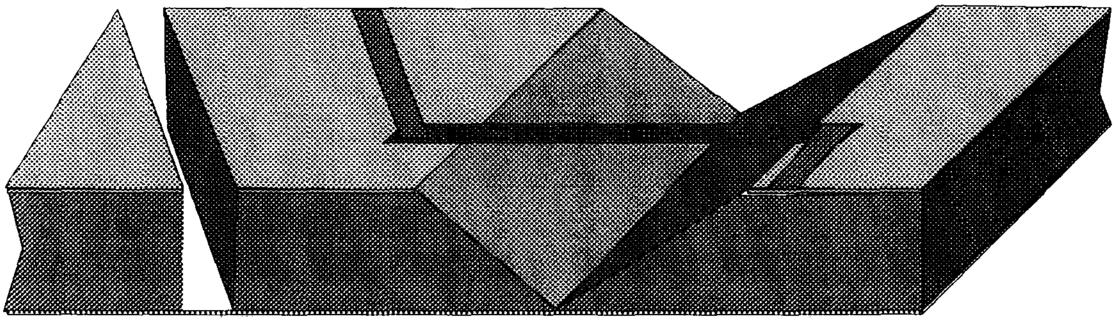

Fig 5.52 The wafer after the anisotropic etch.

During this process the back side of the wafer was protected from the etchant by the oxide layer grown during the first oxidation. At the end of the etch this oxide layer remained as a thin transparent membrane on the back surface of the wafer. This layer was removed with a HF etch lasting a few minutes.

5.5.7 Corner Compensation

The etching of the V grooved trenches which form the hinges for the sensing elements caused some manufacturing problems. The triangular section which forms the secondary sensing element is bounded by three acute convex corners. These corners undercut at a significant rate. As the corners undercut the V-groove becomes wider and correspondingly deeper, at each end. The result of this is that the ends of the V-groove etch all the way through the wafer. This situation is shown in figure 5.53. At the start of the etch process (figure 5.53a) the mask pattern is the desired shape. As the etch proceeds the corners of the structure are undercut: this undercutting effectively widens and deepens the V-groove at each side of the sensor causing the ends of the V-groove to etch right through the wafer (figure 5.53b). In the worst case the corner undercutting can lead to the entire V groove etching through the wafer and the mass becomes detached from the device (figure 5.53c).

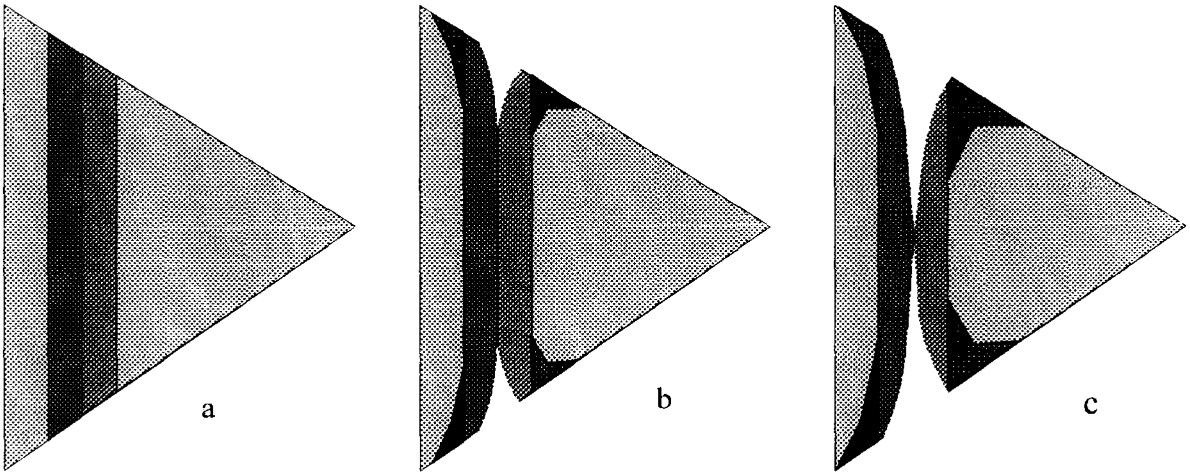

Figure 5.53 The effect of the corner undercutting on the V groove.

It was found that this problem could be successfully addressed by adjusting the mask layout of the anisotropic etch windows, in order to prevent these corners from being attacked. The compensated mask included a pair of beams extending from the triangular mass connecting to the body of the structure. These beams were slightly mis-oriented relative to the {111} direction. The misorientation allowed the etchant to undercut the beam during the etching process. As a result the beam would slowly etch away as the V-groove was formed. This misoriented beam is shown in figures 5.49 and 5.54. The photographs in figure 5.54 show three different structures: 5.54a had no compensation, 5.54b was over compensated with the result that the beam did not

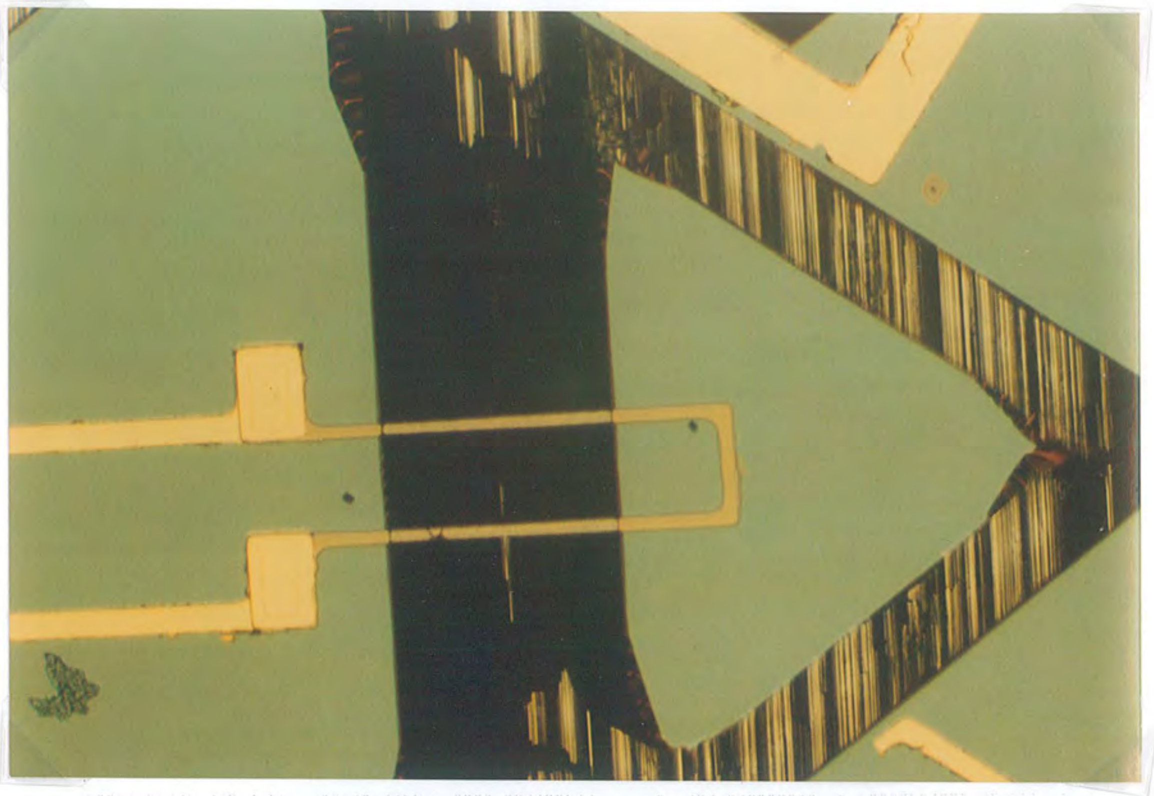

Figure 5.54a Without corner compensation the V-groove is attacked from either end and the sensing element becomes detached

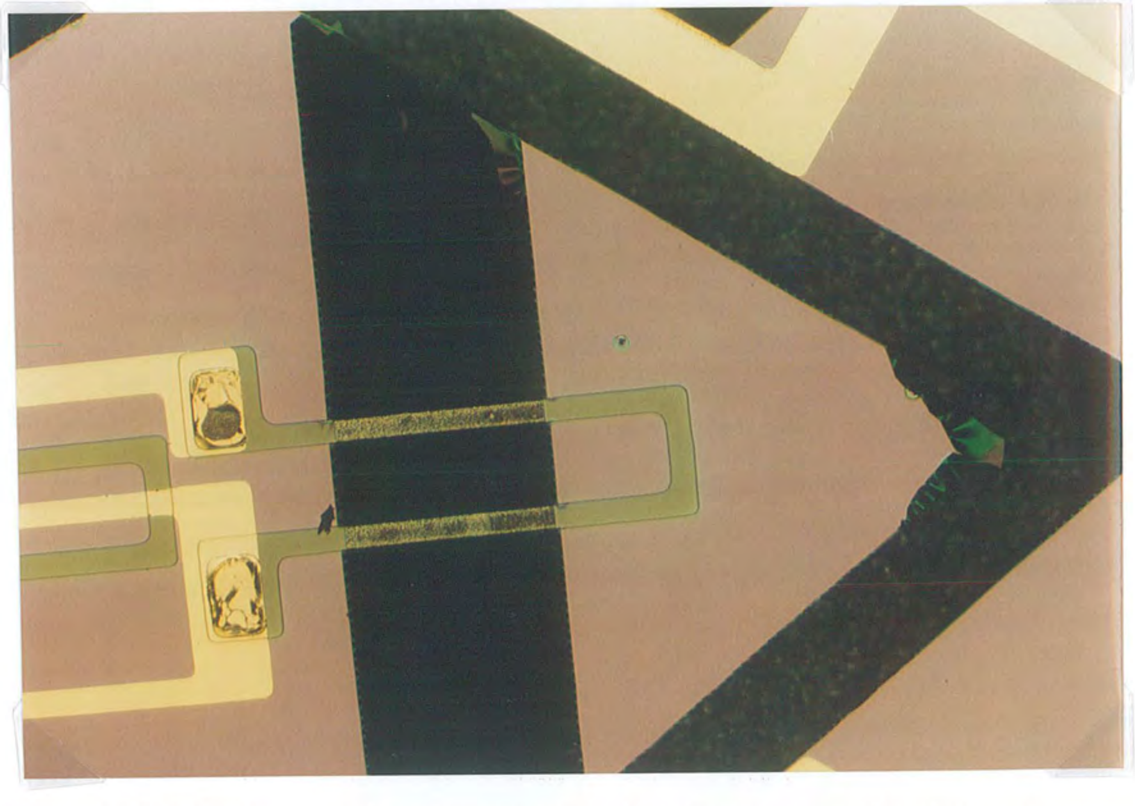

Figure 5.54b With correct corner compensation the corners of the triangular mass can be preserved during the etching process

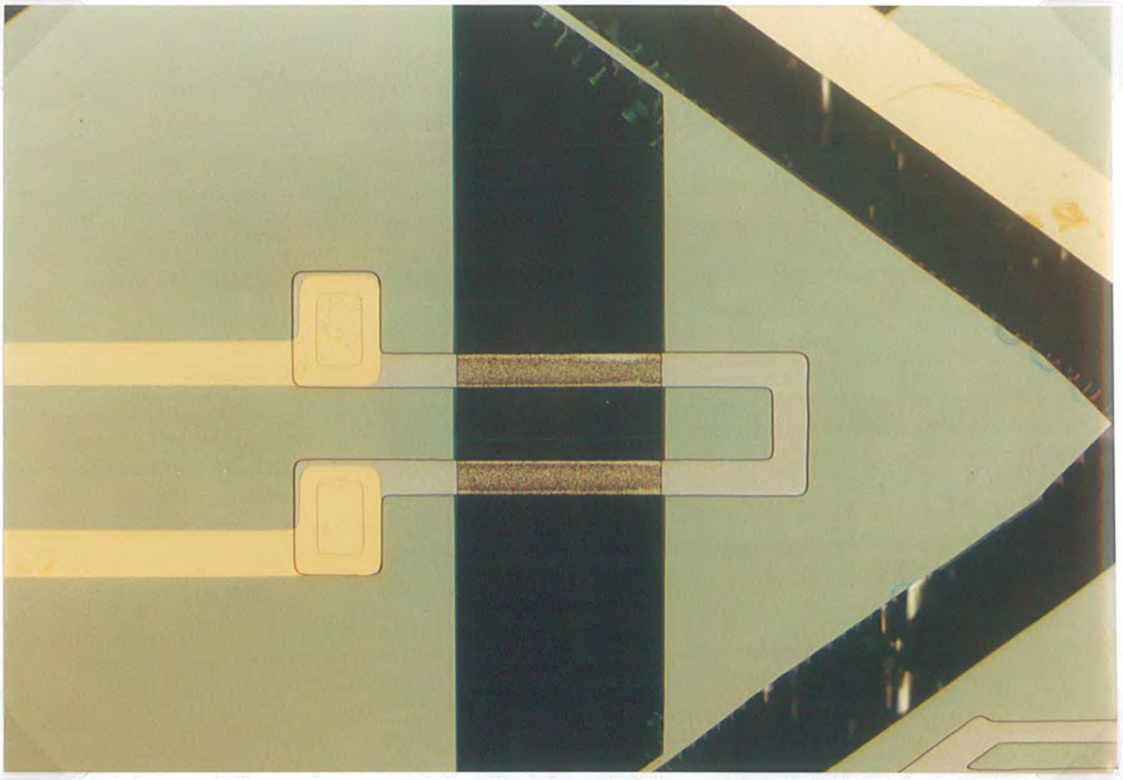

Figure 5.54c The corner compensation was achieved by making a sacrificial beam connecting the sensing elements corner to the gyroscope structure. Making the beam too wide results in a solid beam being left behind after etching.

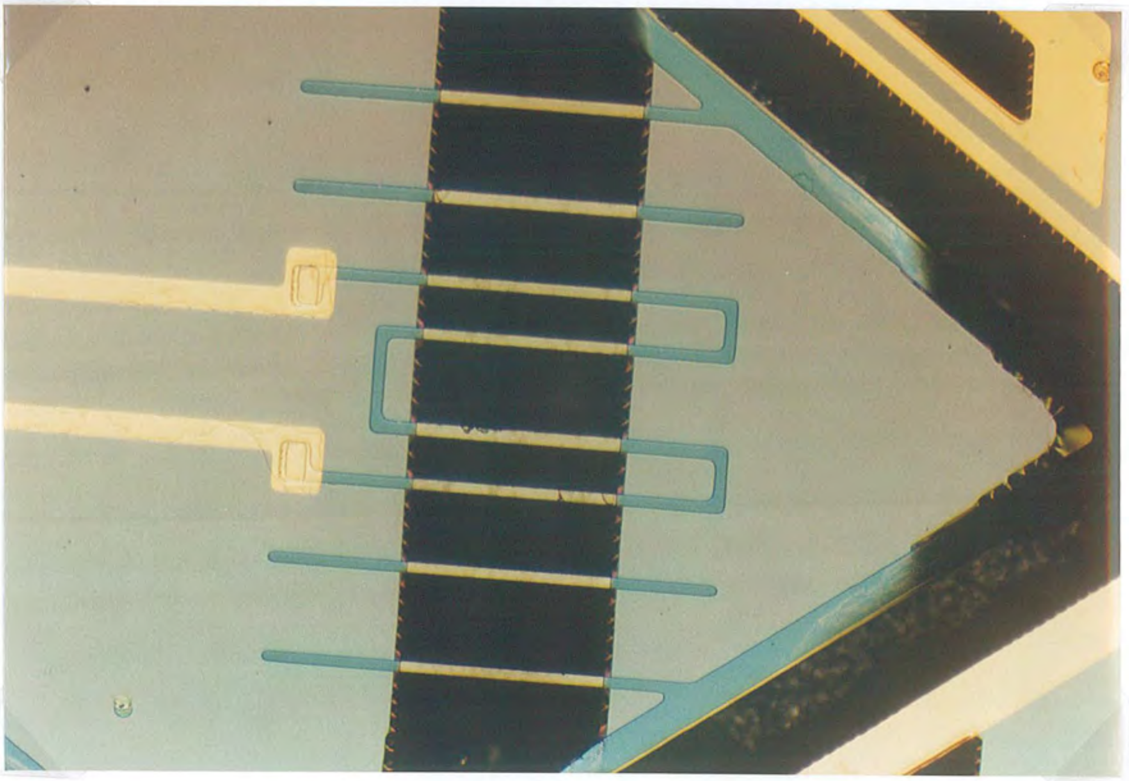

Figure 5.55 One of the secondary motion sensing piezoresistors, with the electrical contacts.

completely etch away. The undercut oxide layer is also visible in figure 5.54b: it is just possible to make out the shape of the original beam and see that it is mis oriented with respect to the remaining beam. Fig 5.54c shows one of the devices where the corner compensation worked as predicted.

Figure 5.55 shows a close up view of one of the secondary piezoresistors folded in a serpentine arrangement across the V-groove. Either side of this resistor are two further beams which may be broken to reduce the resonant frequency of the sensing element.

5.5.8 Dicing and bonding

After fabrication the device was then cut from the wafer. This process was facilitated by the trenches that were etched around the device during the final etch. The device was then stuck to a chip holder and the contact wires attached. For the test samples these wires were simply glued in place with a conducting epoxy.

The final device is shown in figures 5.56 - 5.57.

5.6 Testing

At the time of writing only a limited amount of testing of this device had been completed as the electronics necessary to interface with the piezoresistors had not yet been completed. This work is currently being carried out by colleagues at Newcastle University.

It was, however, possible to test, to a limited extent, the Lorentz drive mechanism simply by applying a sinusoidal signal from a signal generator. This was done and the resonances were observed acoustically.

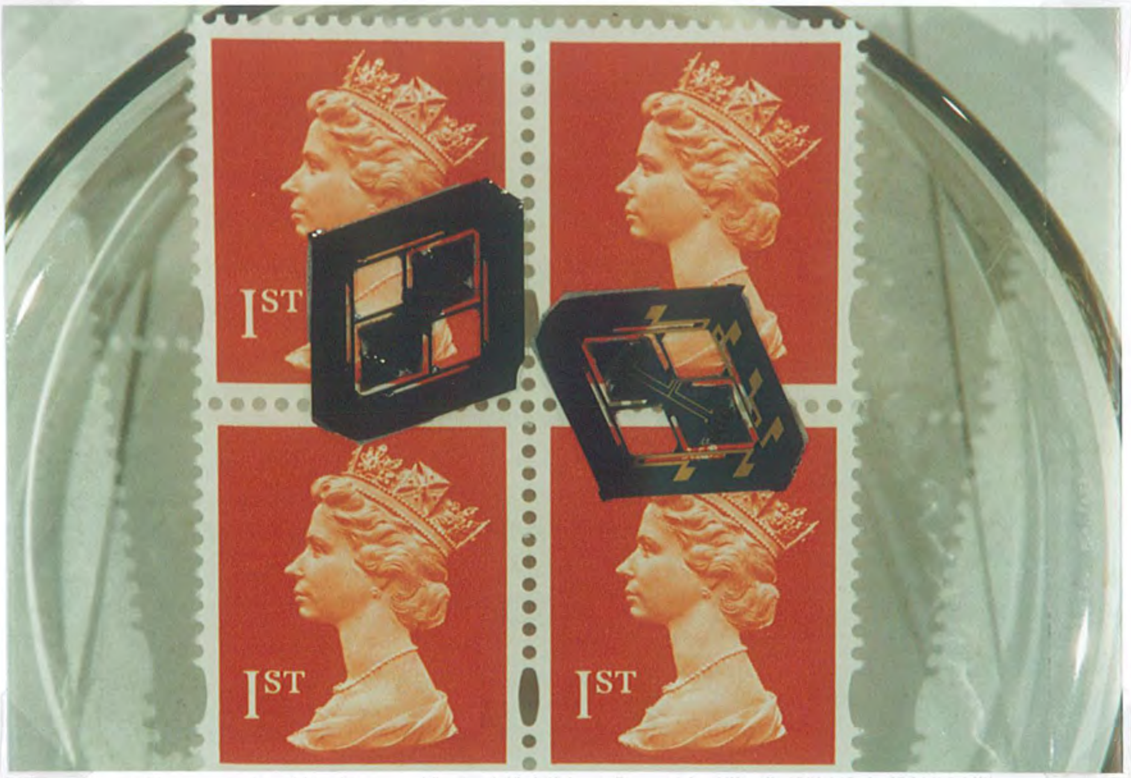

Figure 5.56 Two of the completed devices

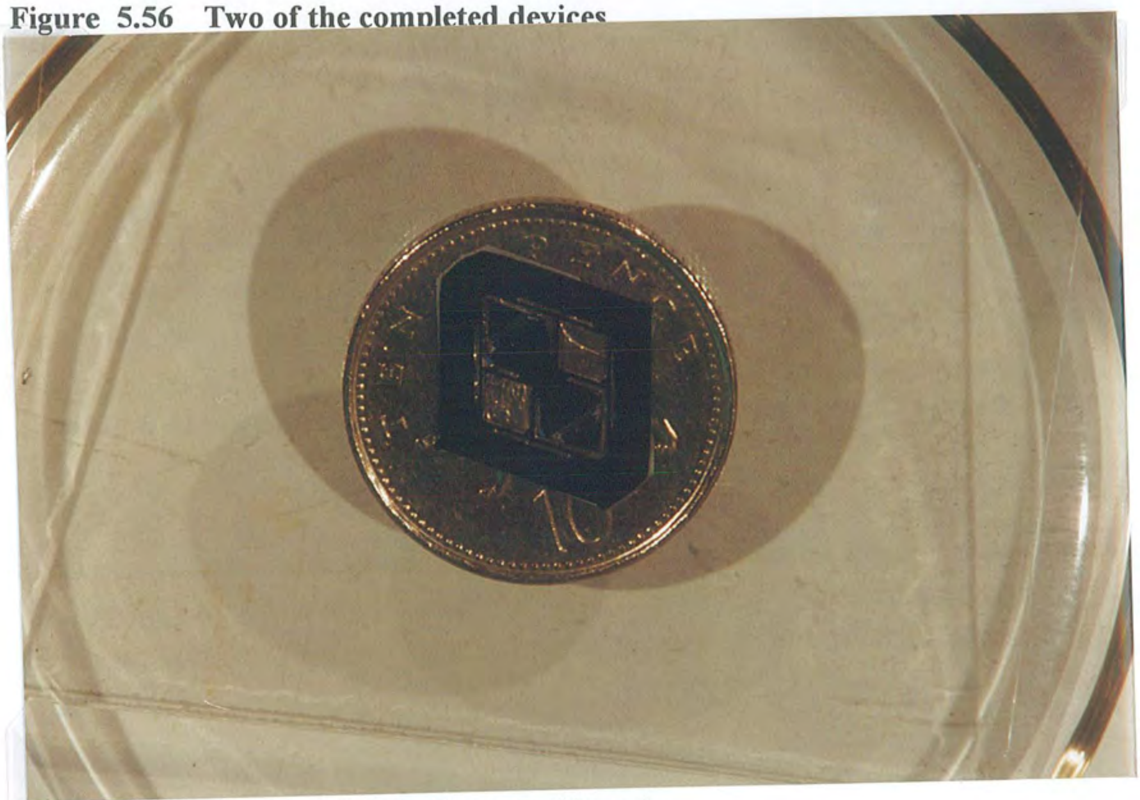

Figure 5.57 A completed device on a 10p coin.

The most dominant resonance could be heard at 11.6 kHz using the drive mechanism described in figure 5.20. This is slightly below the 12.6 kHz predicted by the FE analysis for this device. Given the limitations of the FE analysis and the errors introduced in the fabrication process, this is an acceptable result.

5.7 Conclusions

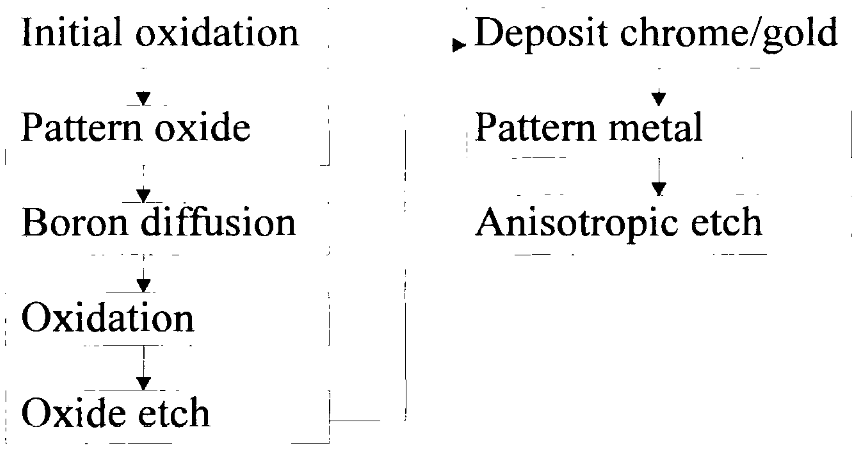

Figure 5.58 Flow Chart of the complete fabrication process

A resonant gyroscope suitable for mass production, from {110} silicon using a simple low cost three mask process, has been developed. The manufacturing process requires neither double sided alignment nor wafer to wafer bonding. This makes the manufacturing process significantly simpler than the process used to fabricate the design described in chapter 4.

The design has been tested theoretically using the finite element technique. The FE analysis indicates that the device should resonate in the desired manner and should be able to detect useful rates of turn.

The fabrication of prototype devices has been demonstrated. The testing of these prototype structures is still being carried out by colleagues at the University of Newcastle.

5.8 References

---

[1] Cermag Ltd. 94 Holywell Road, Sheffield,UK. Product data sheet

Chapter 6

Three Axis Gyroscope

6.1 Introduction

The gyroscopes presented in chapters 4 and 5 are single axis gyroscopes, meaning that they are able to sense a rate of turn about one axis only. This is also true of the resonant gyroscopes discussed in chapter 2. Optical gyroscopes are also single axis devices: flywheel gyroscopes may be configured as single or dual axis devices.

For many applications it is necessary to measure the rate of turn about all three axes simultaneously. For instance the semi-active suspension system as shown in figure 1.1. In order to measure a rate of turn about all three axes, using single axis devices, it is necessary to use three independent gyroscopes mounted so that their sensitive axes are all mutually perpendicular. Thus three components and a special packaging process are required.

In this chapter a third design of gyroscope is presented. This design is significant in that it is able to measure rates of turn about all three orthogonal axes. As a result only one device is required and the need for the special packaging of three independent devices is eliminated. This design is believed to be the first gyroscope, resonant or otherwise, with the ability to sense all three axes.

Section 6.2 describes the operation of the device. Section 6.3 describes the FE simulations of the structure, which serve to demonstrate that the device can be designed with matched modes and with reasonable dimensions. The manufacture of this design requires a number of processes which were not available at Durham at the time of writing, the most significant of these being the plasma etching process. It has not, therefore, been possible to demonstrate the manufacture of this device. These processes are however well documented and understood. Section 6.4 gives a brief description of how the device could be manufactured given the necessary equipment. Section 6.5 discusses the possibility of using the design as part of a full six axis inertial measurement system and section 6.6 contains the conclusions.

6.2 Method of Operation

The structure of the gyroscope is shown in figure 6.1. The whole device would be manufactured from a single silicon wafer. The square section in the centre of the structure is the mounting point, with all of the remaining structure being unrestrained. The device is square and thus has 90° rotational symmetry.

Each of the four sides of the square are composed of a rectangular solid section of silicon, connected to the corner sections via four beams. The beams are thin and deep so that the central rectangles are able to move radially outwards as shown in figure 6.1, while remaining rigid to flexing out of the plane.

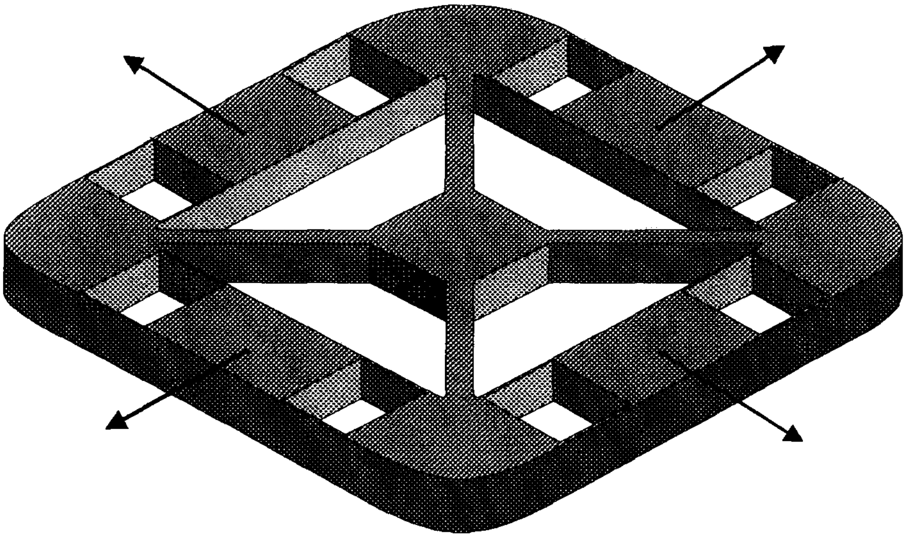

Figure 6.1 **The direction of motion in the primary mode**

This radial motion is the primary mode. Under the influence of a rate of turn this primary motion will then become coupled to three distinct secondary resonances. Each one of these secondary resonances are excited independently by a rotation about each of the X,Y and Z axis. Figure 6.2 shows the effect of a rate of turn about the X axis.

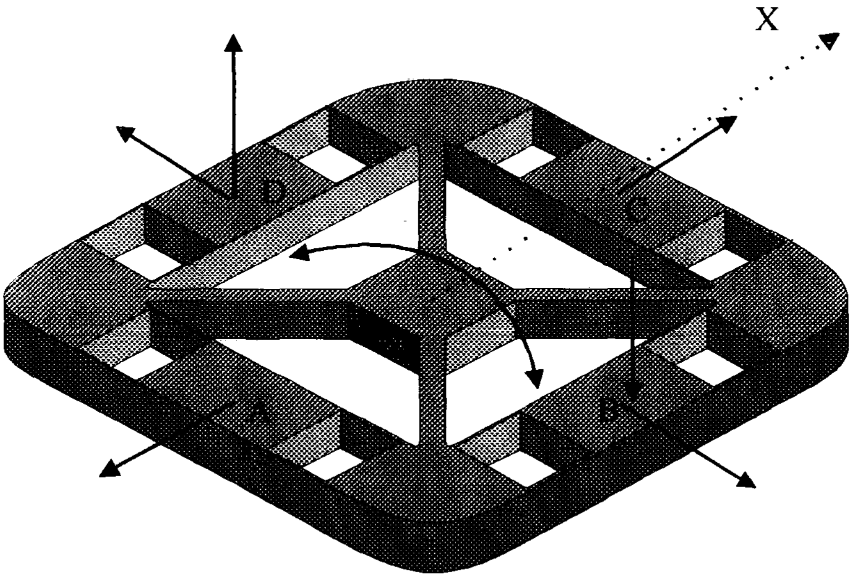

Fig 6.2 **The 'X' secondary motion**

In this situation the masses labelled A and C are moving parallel to the angular velocity vector: as a result they feel no Coriolis force. The masses B and D are moving orthogonal to the angular velocity vector, but in opposite directions, and therefore feel equal and opposite Coriolis forces normal to the plane of the device, as shown. This excites a rocking motion about the X axis (figure 6.2) referred to as the X secondary mode.

Due to the 90° symmetry of the structure the same is true of a rate of turn about the Y axis, but this time the masses A and C feel the Coriolis force, figure 6.3, this is referred to as the Y secondary mode.

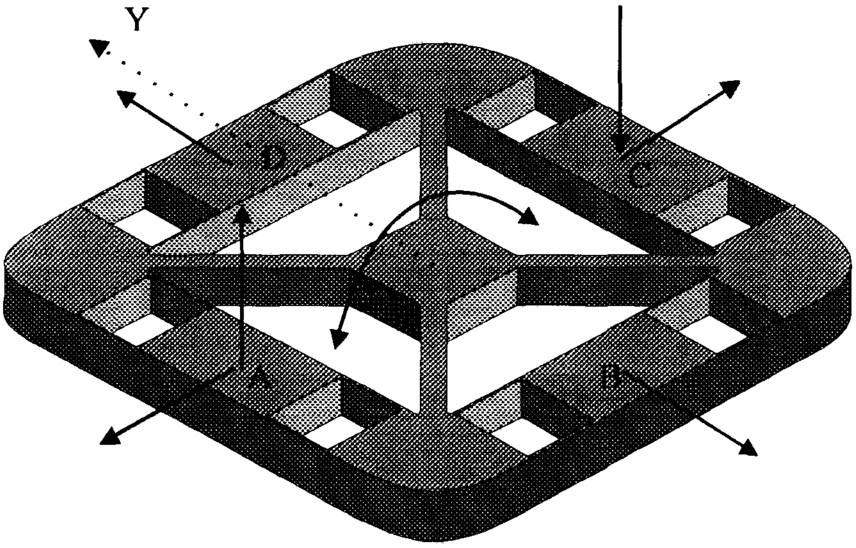

Figure 6.3 **The 'Y' secondary motion**

If a rate of turn is applied about the Z axis, normal to the wafer, then all four of the masses will experience a Coriolis force in the plane (figure 6.4). These forces all act together to produce a third rotational motion about the Z axis, the Z secondary motion.

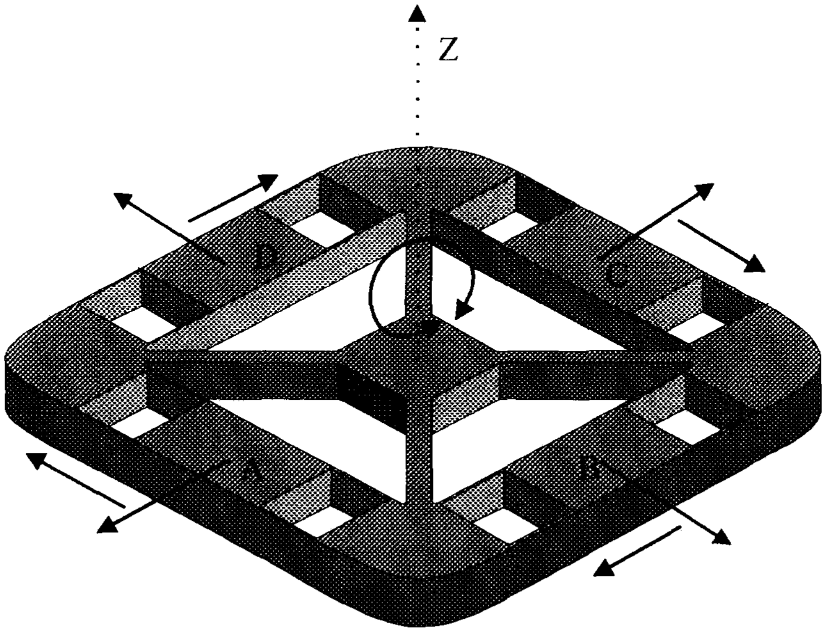

Fig 6.4 The 'Z' secondary motion

Thus the gyroscope has one primary and three secondary modes. Two of the secondary modes are degenerate by virtue of the symmetry of the structure. As a result of the design symmetry the four diagonal support beams in the centre of the device will experience only tensile and compressive forces along their length during the primary motion. In this mode the beams will be very stiff and as a result little energy should be dissipated: it is hoped that this will ensure that the primary motion will have a high value of Q.

6.2.1 Primary Drive Method

The primary motion of this device is ideally suited to Lorentz activation. If a track were deposited as shown in figure 6.5, and a sinusoidal current were to be passed along the track, then the radial motion of the primary mode could easily be generated. The diagonal beam carrying the drive current (top left) has zero net current flowing along it. The drive wires will therefore not cause any forces to be developed on this beam, as desired.

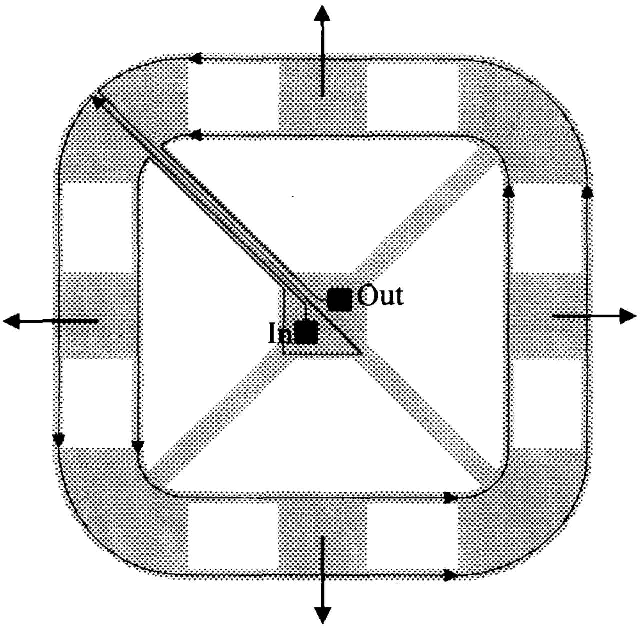

Figure 6.5 The primary drive method. The magnetic field lines would run normal to the plane of the page.

6.2.2 Secondary Sense Method

The secondary sensing could be performed in much the same way as used in the design described in chapter 4. The electrodes would be positioned beneath the square on a glass disc or second silicon wafer, which would also serve as the anchor point for the centre of the structure. Figure 6.6 shows one possible arrangement of electrodes which would be able to sense the amplitudes of the primary and three secondary modes. The electrodes beneath the moving masses would be able to sense the primary motion and the X/Y secondary motions. The electrodes beneath the corners of the structure would be able to sense all three of the secondary motions.

6.3 Finite Element Analysis

As with the previous devices the modelling of this design has been carried out using the properties of single crystal silicon. The device is square symmetric: it would therefore be more appropriate to manufacture the device on {100} silicon with one of the sides of the structure parallel to the {111} direction[*]. This was the assumption made in the following analysis, with the elastic properties being defined by the compliance matrix 3.14.

---

[*] Oriented at 45 degrees to the {111} direction would also preserve elastic symmetries of the final device.

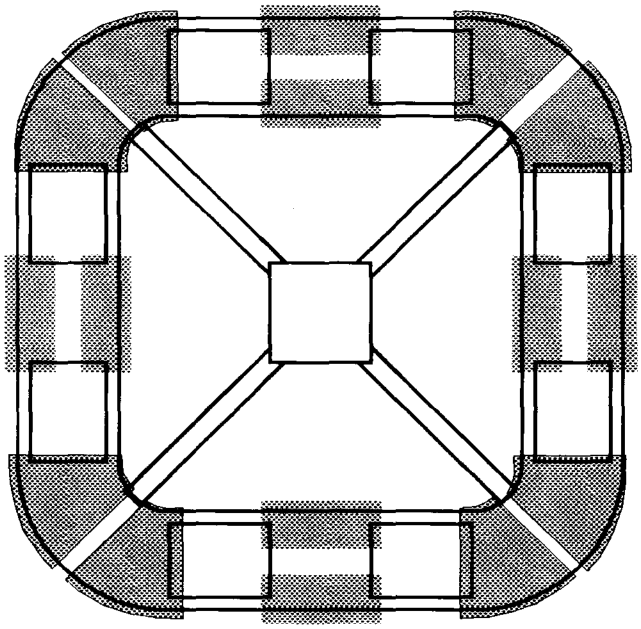

Figure 6.6 **One possible arrangement of electrodes (shaded).**

With this device there are 4 different modes which have to be matched by tuning the overall dimensions: the X and Y secondary modes are automatically matched by the symmetry of the device leaving only 3 independent modes to match. The device is uniform throughout its thickness (in the Z direction). This fact means that any resonance whose motion is purely in the plane of the device, that is whose motion is confined to the X and Y directions only, will be independent of the thickness of the structure. Both the primary and the secondary 'Z' modes meet this criterion and therefore have resonant frequencies which are independent of the device thickness. This was confirmed with FE analysis[†]. The secondary X and Y modes do move out of the plane, that is they posess a Z component, and therefore their resonant frequencies are dependent upon the thickness of the device.

This ability to separate the modes into those dependent upon the thickness of the device and those not is extremely useful in matching the frequencies of the various modes. In order to match the modes the shape of the design is first adjusted so as to match the primary and secondary Z modes. That is the two modes that are entirly in the

---

[†] The reason for these two modes being independent of the device thickness can be made more intuitive by considering a simple thought experiment. Imagine two identical devices, each resonating in the primary mode, with each resonance having the same frequency, amplitude and phase. The two resonating devices devices could be brought into contact, face to face. Since the two resonances are identical and in the plane no shear forces will be generated in the interface between the two devices. As a result the composite device will continue to move with the same frequency, though now it would have twice the thickness.

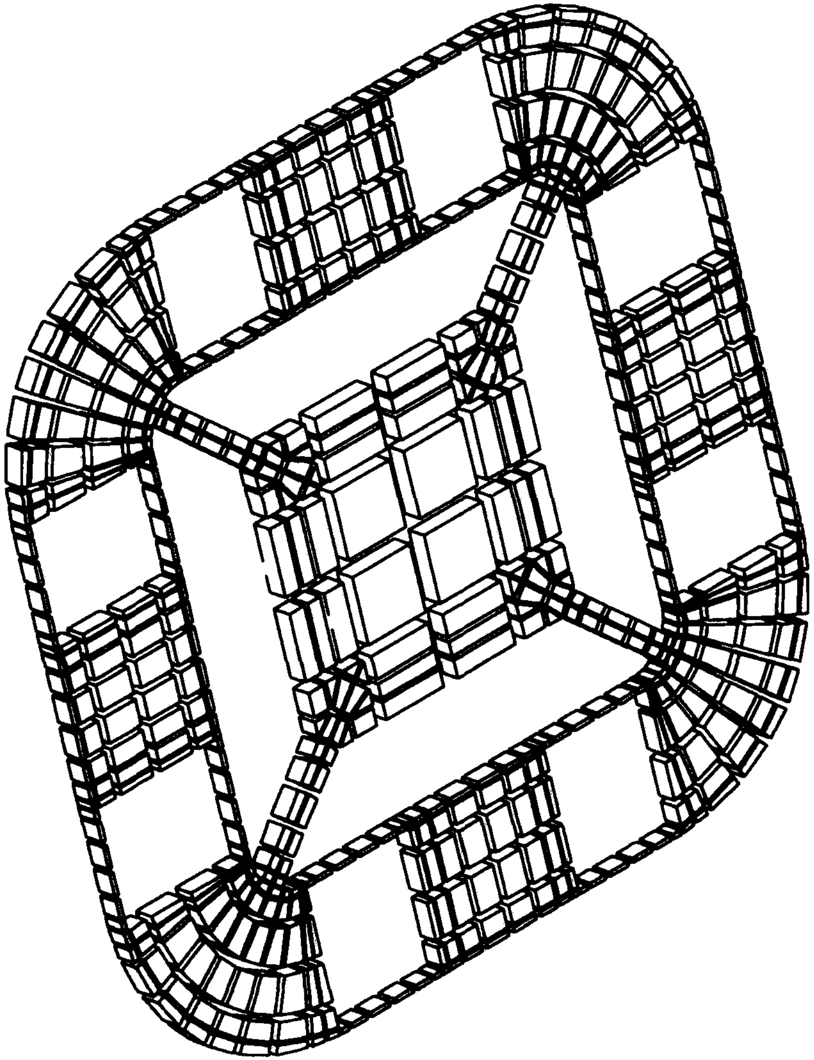

MODES-FREQ
MODE 0
0.000 E 0
(HZ)

ROTATION
X = 30
Y = 30
Z = 30

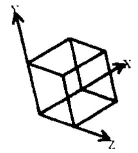

TITLE

FIG 6·7

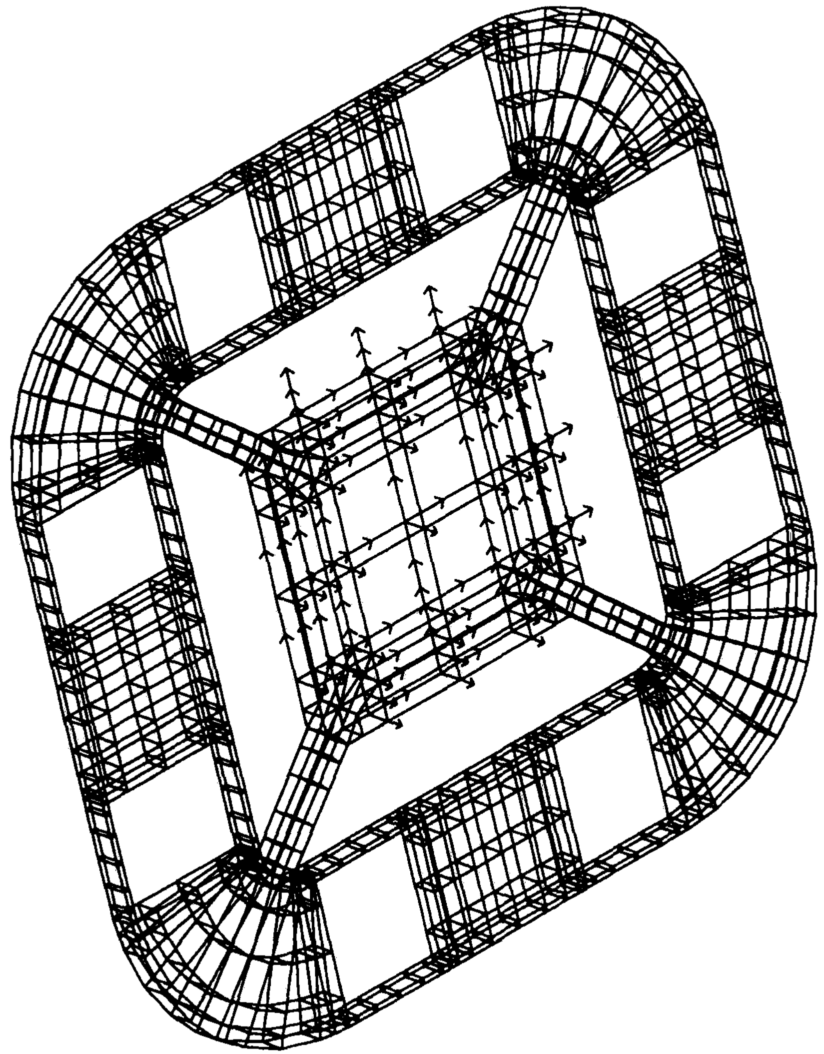

MODES-FREQ
MODE 5
2.833 E 4
(HZ)

ROTATION
X = 30
Y = 30
Z = 30

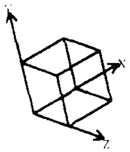

TITLE

FIG 6·8

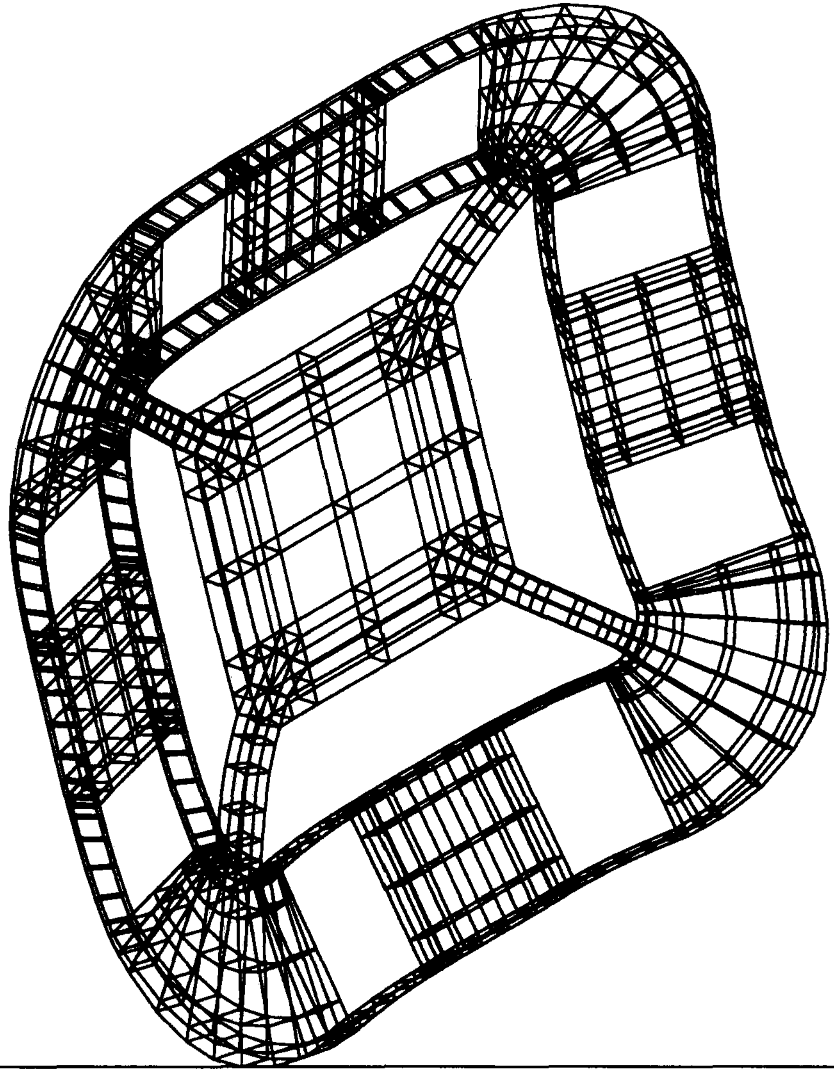

MODES-FREQ

MODE 1

2.759 E 4

(HZ)

ROTATION

X = 30

Y = 30

Z = 30

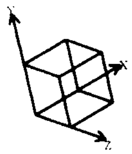

TITLE

FIG 6·9

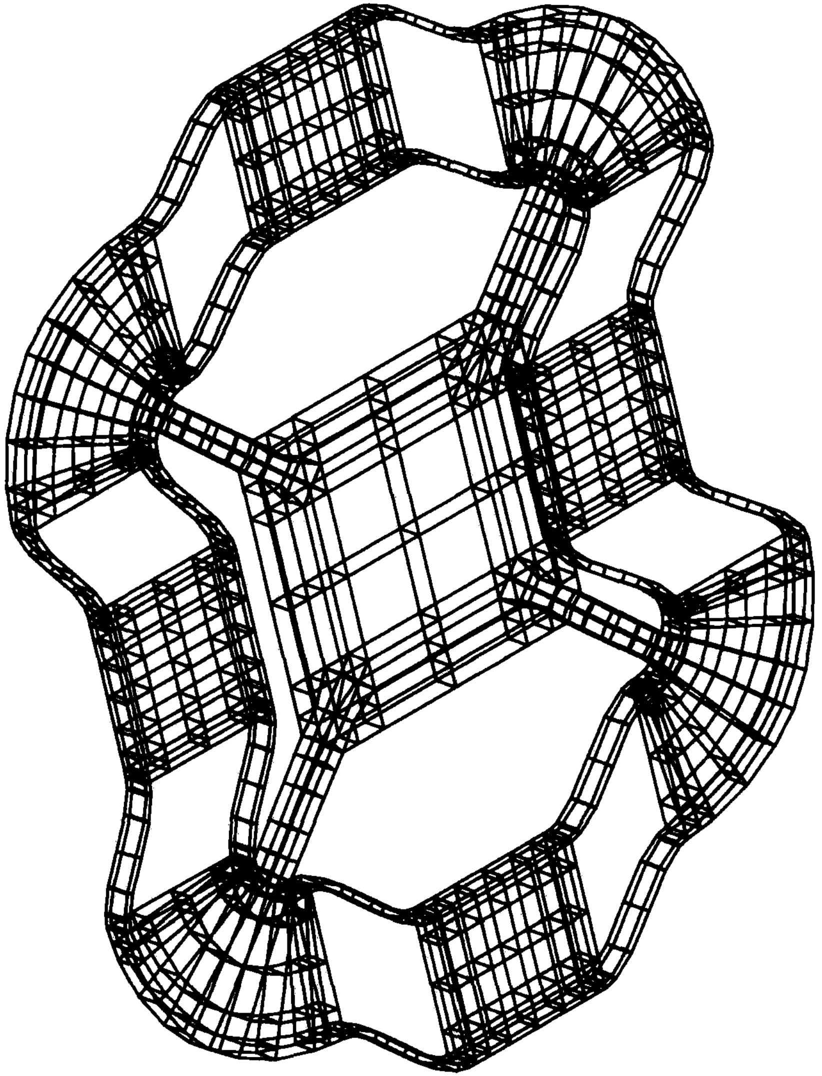

MODES-FREQ
MODE 2
2.815 E 4
(HZ)

ROTATION
X = 30
Y = 30
Z = 30

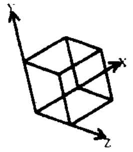

TITLE

FIG 6·10

MODES-FREQ
MODE 3
2.817 E 4
(HZ)

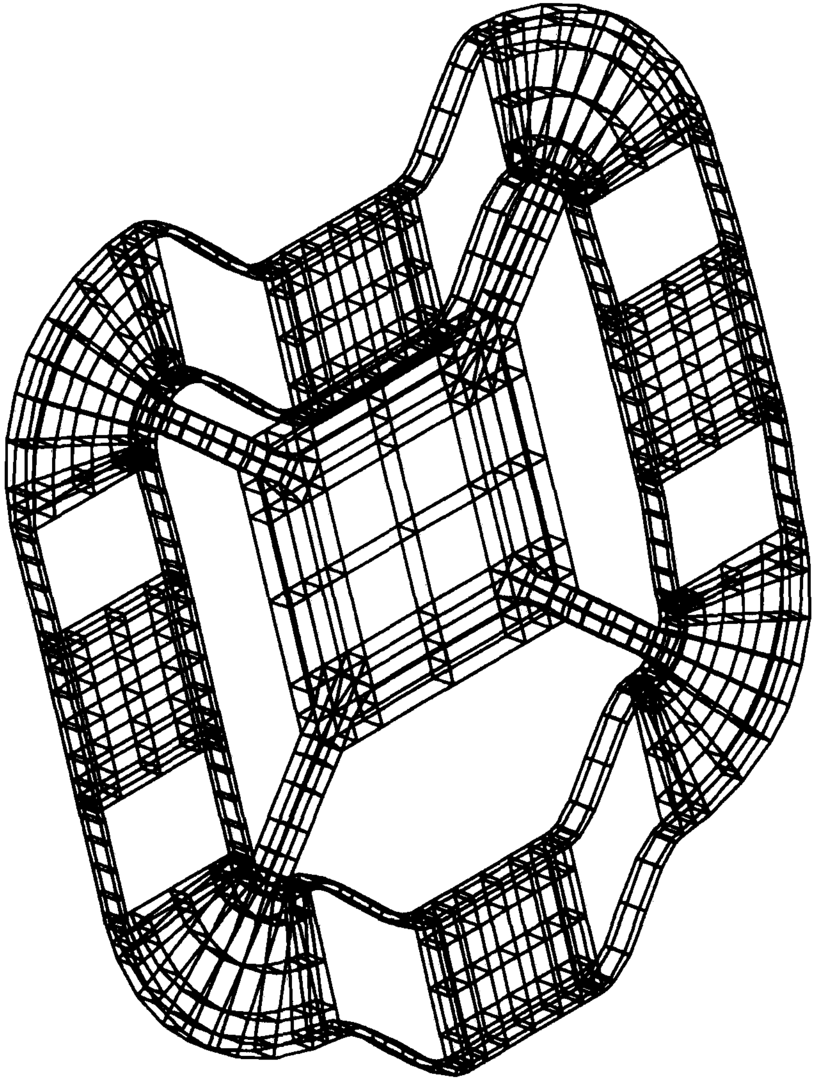

ROTATION
X = 30
Y = 30
Z = 30

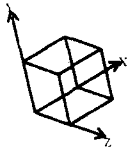

TITLE

FIG 6.11

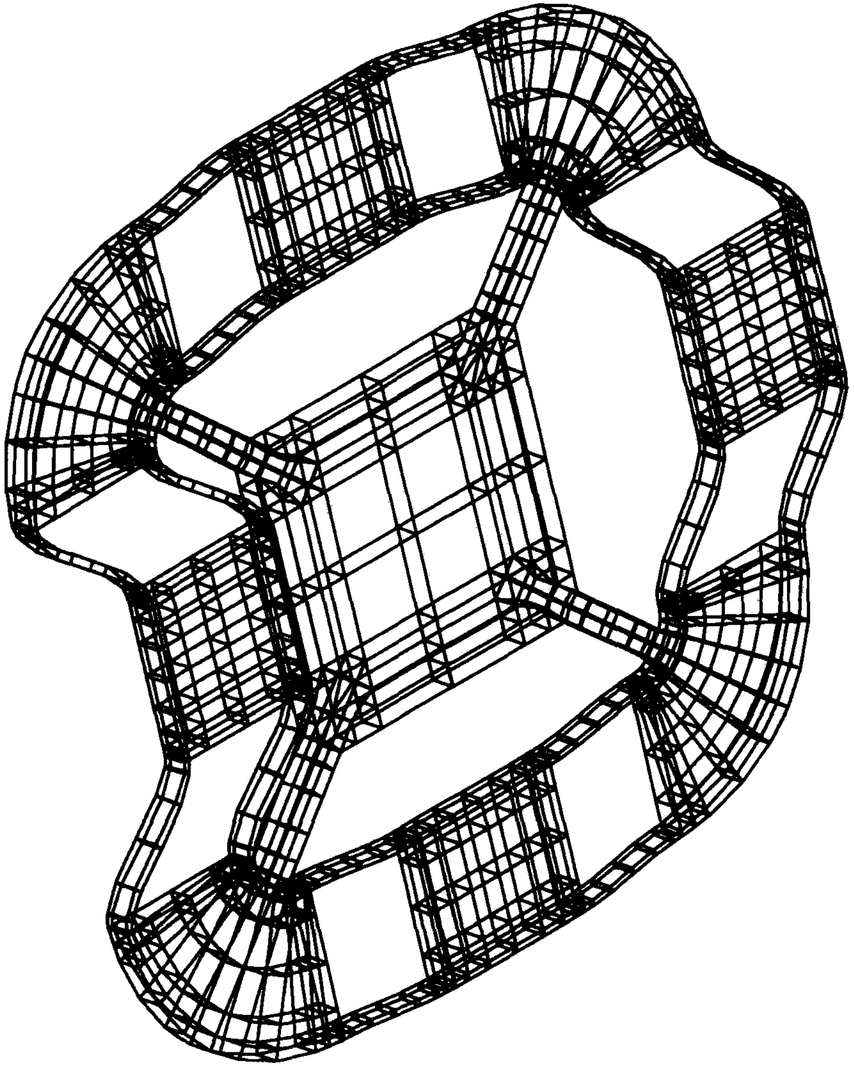

MODES-FREQ

MODE 4

2.818 E 4

(HZ)

ROTATION

X = 30

Y = 30

Z = 30

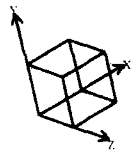

TITLE

FIG 6.12

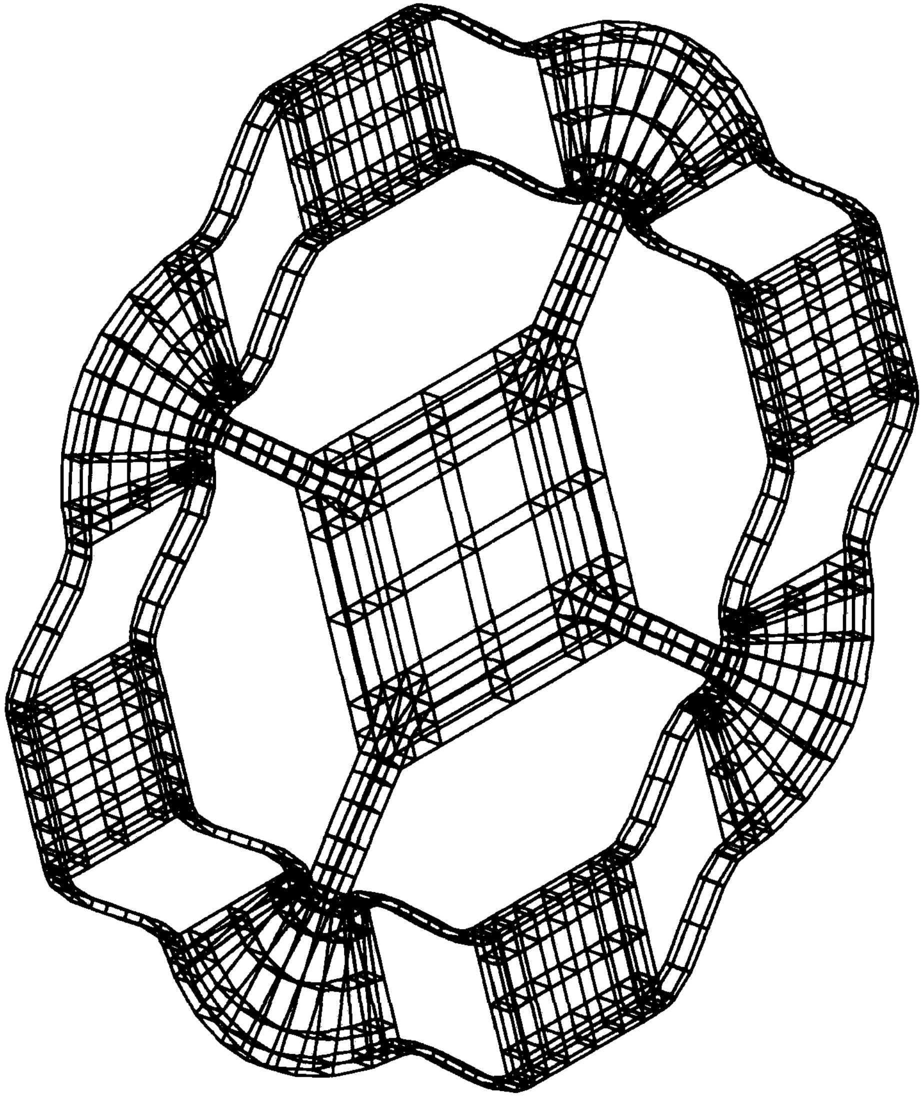

FIG 6.13

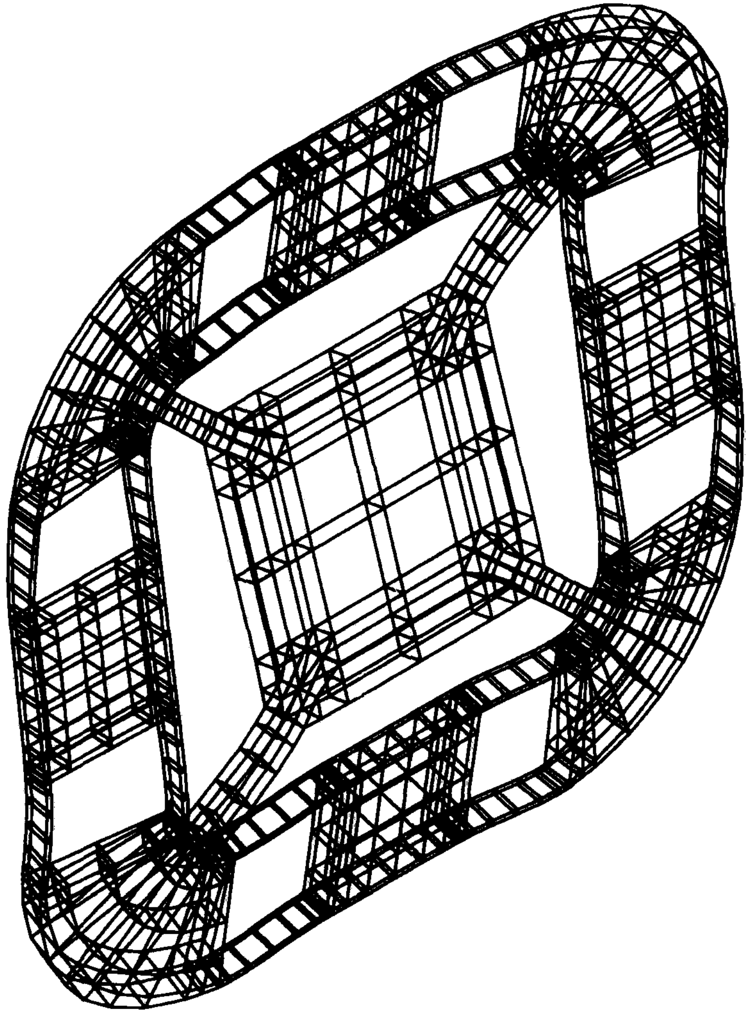

MODES-FREQ

MODE 5

2.833 E 4

(HZ)

ROTATION

X = 30

Y = 30

Z = 30

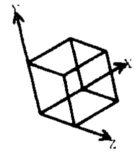

TITLE

FIG 6·14

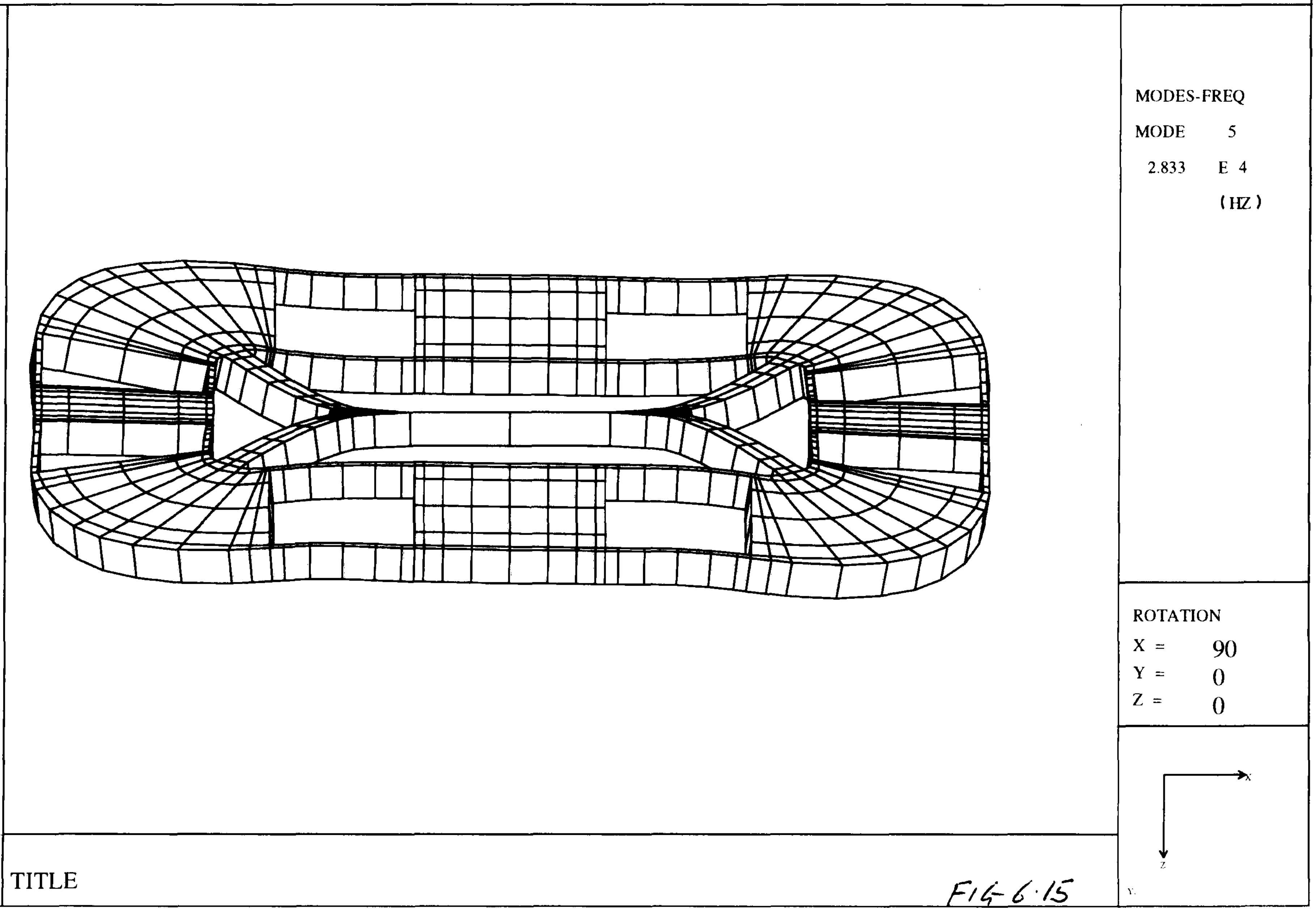

FIG 6.15

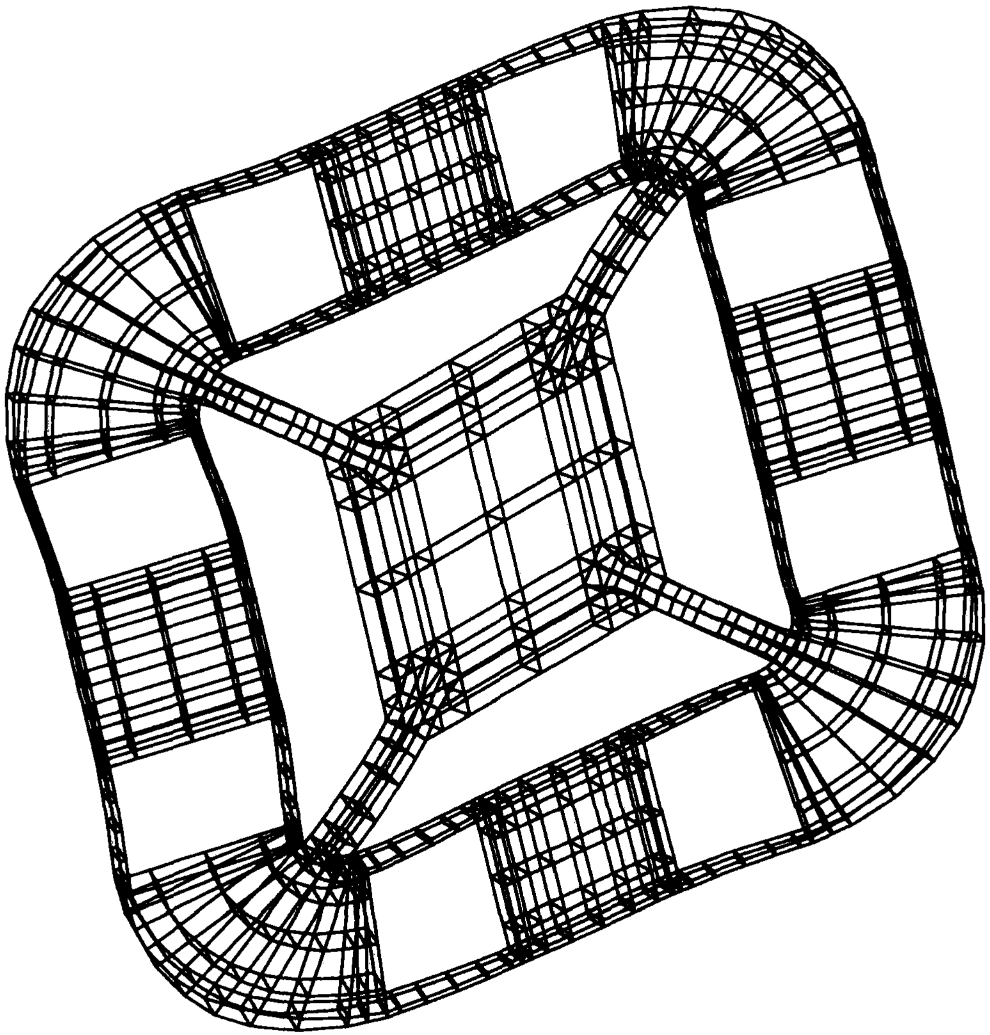

FIG 6.16

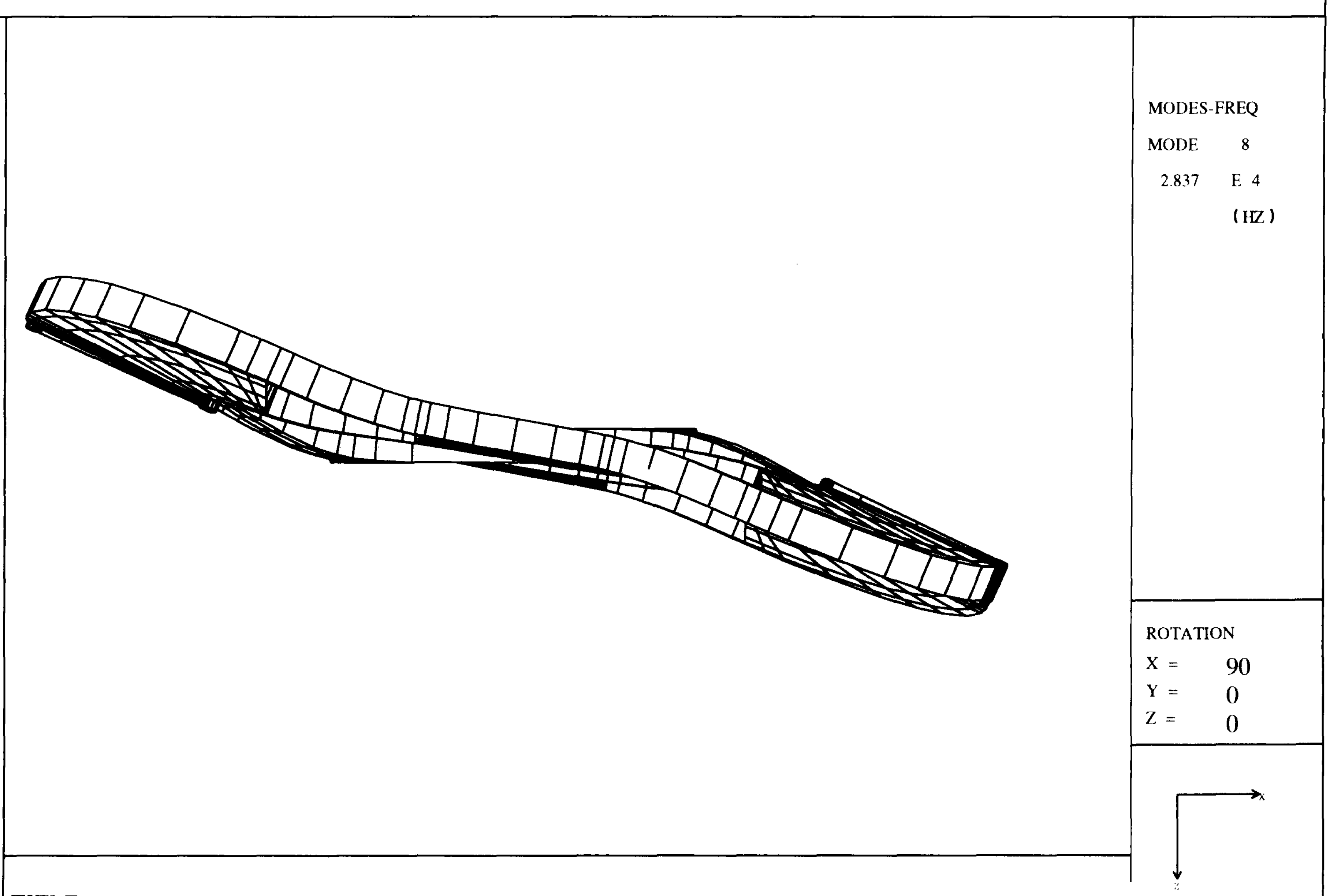

FIG 6.17

MODES-FREQ
MODE 7
2.836 E 4
(HZ)

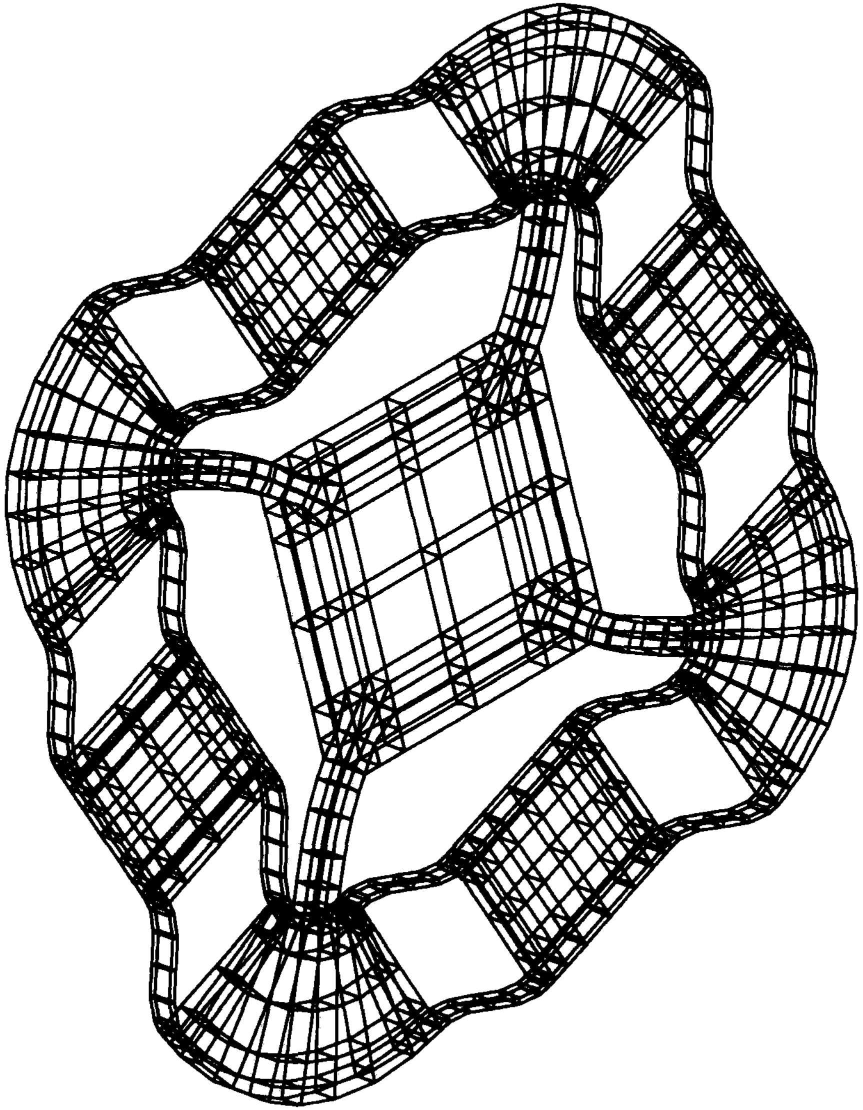

ROTATION
X = 30
Y = 30
Z = 30

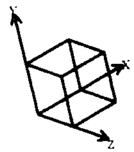

TITLE

FIG 6.18

MODES-FREQ

MODE 9

0.368 E 5

(HZ)

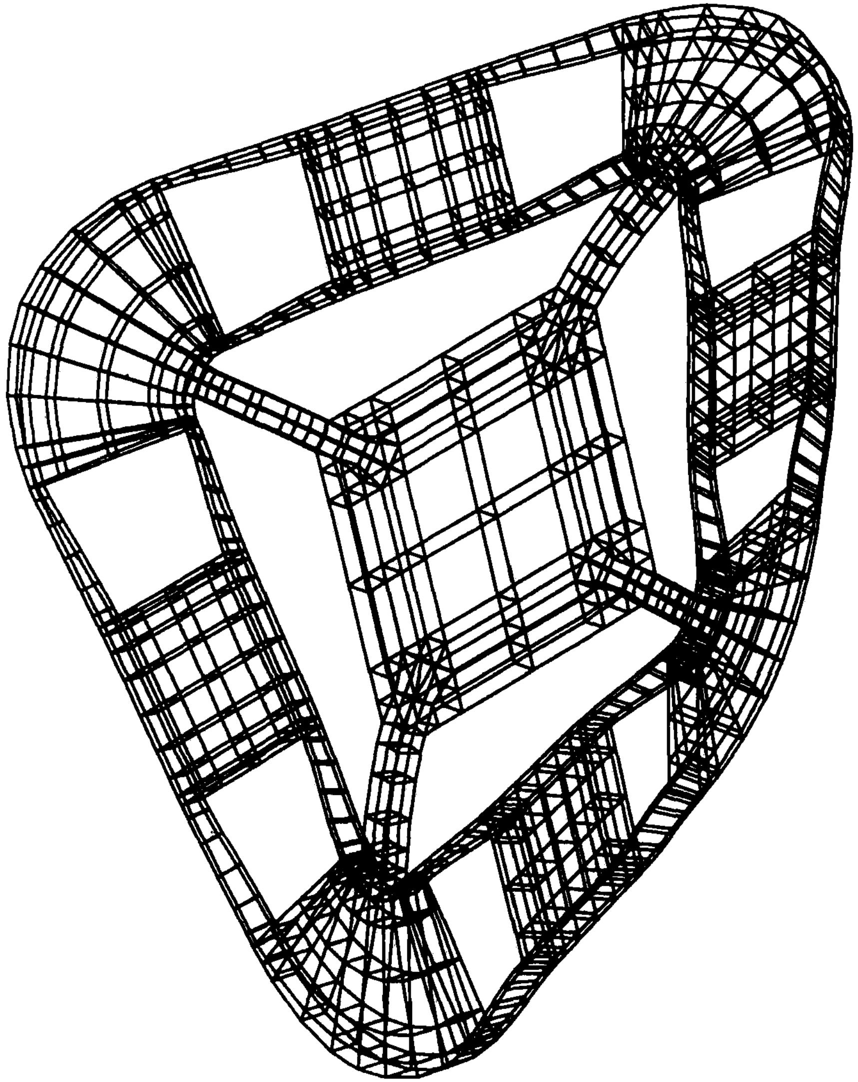

ROTATION

X = 30

Y = 30

Z = 30

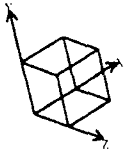

TITLE

FIG 6·14

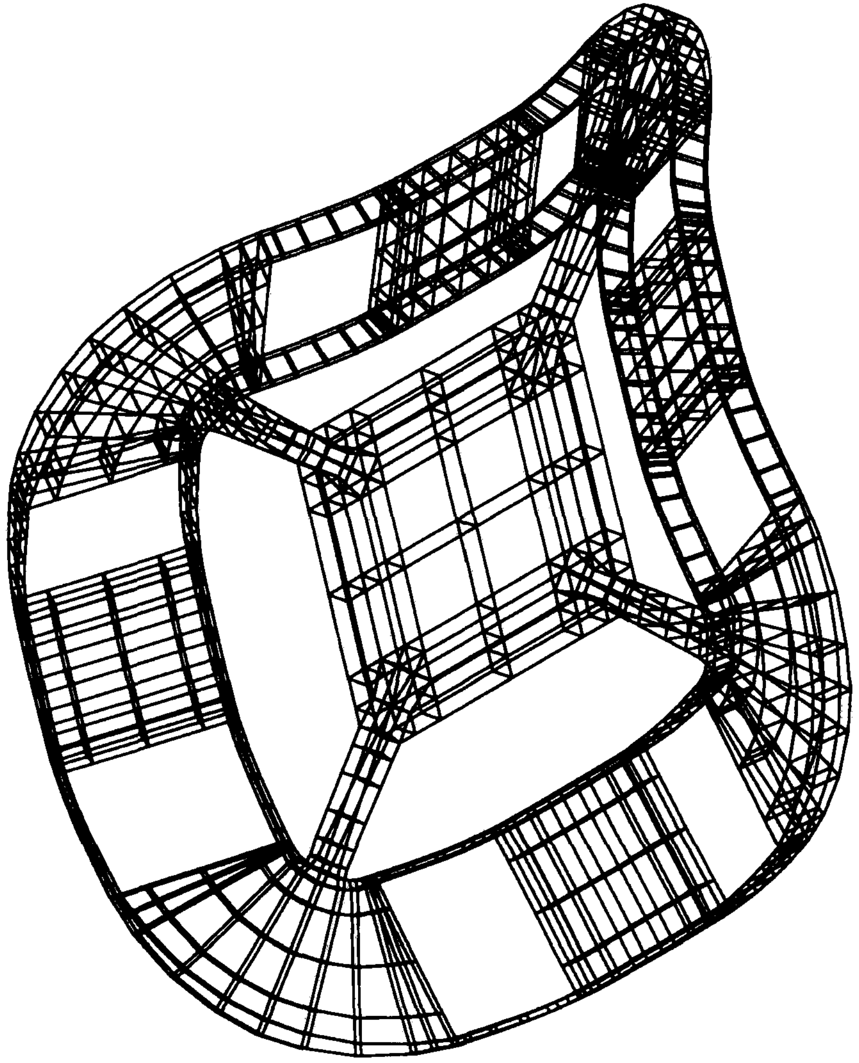

MODES-FREQ
MODE 10
0.369 E 5
(HZ)

ROTATION
X = 30
Y = 30
Z = 30

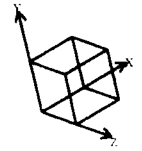

TITLE

FIG 6·20

plane of the device. This is done with a model haaving a constant thickness while the dimensions of the structure are varied. Once these in plane modes are matched the thickness of the device is adjusted, while keeping all other dimensions fixed, so as to bring the secondary X and Y modes into line with the primary and secondary Z modes. This algorithm was followed in order to achieve the design parameters described in figure 6.21.

As with the bow-tie gyroscope the dynamics of this design are quite complex and are best explained with reference to the mode shape plots produced by the finite element analysis of the structure. Figure 6.7 shows the FE mesh that was used to simulate the device. Figures 6.8 shows the restraints that were imposed on the structure. An ideal mechanical earth was assumed on one face of the central square region, the restrained freedoms are marked with arrows. Figure 6.9 shows the first mode of the structure: in this mode the whole unrestrained outer ring bounces in the Z-direction. Figure 6.10 is the first in-plane mode. Here all 4 masses move in the plane, with masses on opposite sides of the structure moving together while those on the other two sides move together but 180° out of phase with the first pair. Figures 6.11 shows a mode in which only two of the masses are moving, in the Y-direction. Figure 6.12 shows the same motion with the other two masses moving.

Figure 6.13 shows the first mode of interest, the primary mode. All four of the masses are moving radially in and out towards the centre of the structure phase. The plot shows the masses at their furthest point from the centre. The motion is entirely in the X-Y plane. Figures 6.14 shows the X secondary motion. The square ring is rocking about the X-axis: this motion would be excited by a rate of turn about the X-direction. This motion is also shown in figure 6.15 viewed along the Y-direction. Figures 6.16 and 6.17 show the same plots for the Y secondary motion. The X and Y secondary motions are the same, just rotated 90° with respect to the device. Figure 6.18 shows the last mode of interest, the Z secondary motion. This mode is a torsional resonance of the structure about the Z-direction and is excited by a rate of turn about the Z-direction. All of the four modes of interest, primary and X,Y&Z secondaries, are separated by only 45 Hz[‡]. Figures 6.19 and 6.20 show the next two resonances, these have been included for completeness and are not directly of interest.

The X and Y secondary modes are furthest apart at 28330 and 28375 Hz respectively. These two modes are in fact equivalent and as the model was symmetric they should be

---

[‡] This separation was between the X and Y secondary modes and is an indication of the numerical accuracy of the FE analysis as these two modes are, by symmetry, degenerate.

exactly matched. The 45 Hz mismatch was due to numerical errors in the model[§]. The dimensions of the structure with the 4 matched modes are shown in figure 6.21.

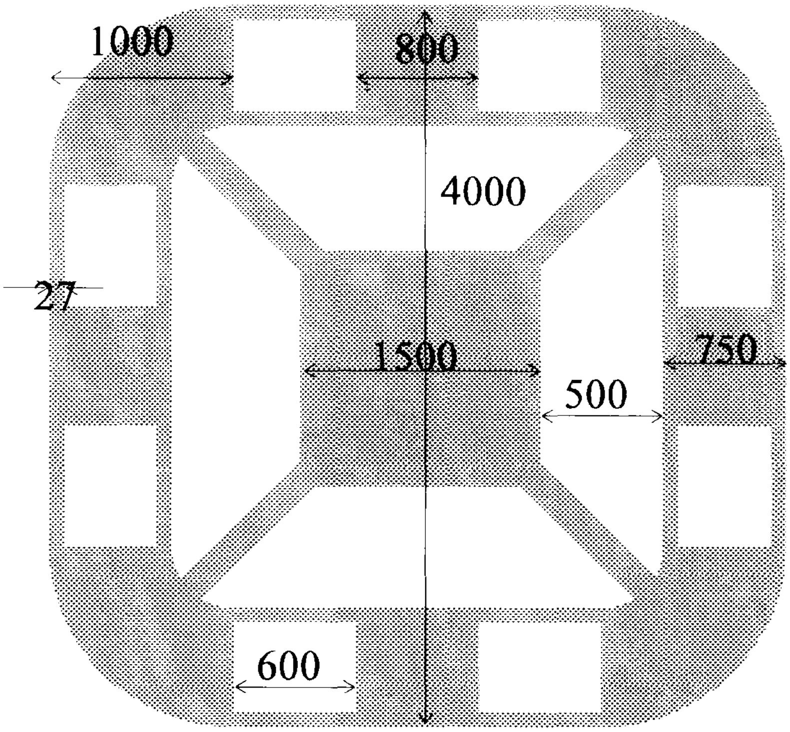

Figure 6.21 The dimensions of the structure necessary to produce a device with all 4 matched modes. (All dimensions in μm, wafer thickness 137μm)

6.4 Possible Manufacturing Methods

Figure 6.22 shows a brief summary of a possible manufacturing process which may be used to fabricate a device of this type. It is not intended to be a true process flow as only the major steps have been shown.

The main difference between this flow and the device described in chapter 4 is the need for deep anisotropic plasma etching. The device does not follow the {111} crystal planes: as a result the wet anisotropic etching process cannot be used and a plasma process must be substituted[1].

In steps A to C a base wafer is prepared with a recessed pit to contain the sensing electrodes: this is essentially the same process as used in the fabrication of the membrane gyroscope in chapter 4. In step D the silicon wafer is bonded to the substrate. The drive wires are then deposited and patterned (step E). Finally a photoresist mask layer would be deposited before the anisotropic etching, stage F.

[§] A similar mismatch was observed in the square membrane structure described in chapter 4, though in that case the effect was smaller due to the lower number of nodes in the model.

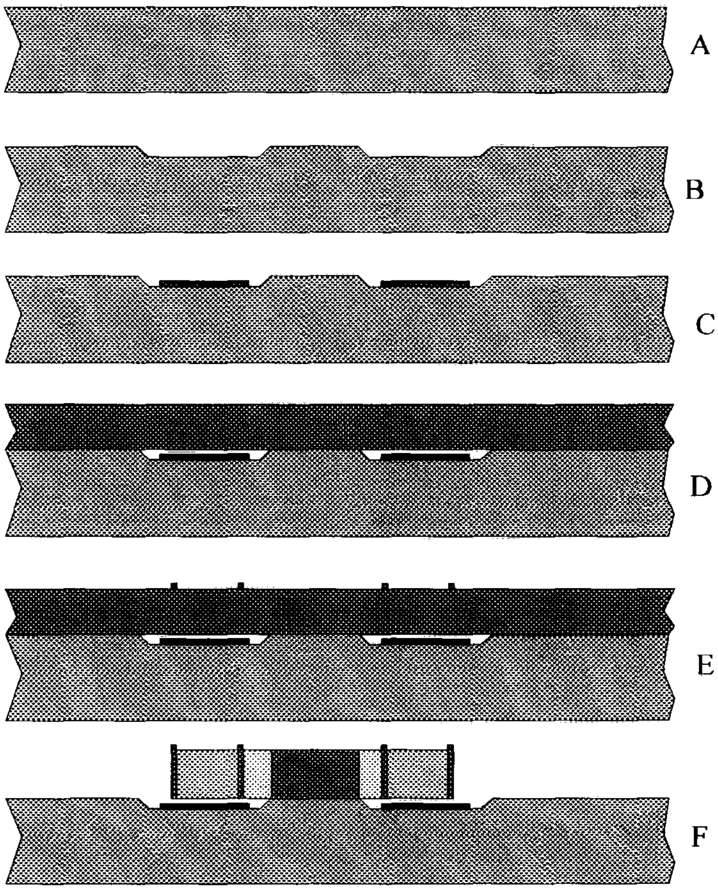

Figure 6.21 One possible processing sequence.

6.5 A Full Six Degree of Freedom Inertial Sensing System

The first three modes of the structure, shown in figures 6.9, 6.11 and 6.12 correspond to modes that would be excited by an acceleration force in the Z, X and Y directions respectively. If the detection plates and associated electronics were arranged to detect these modes it would be possible to use a structure of this type as a three axes accelerometer. In order to maximise the sensitivity as an accelerometer it is likely that the design dimensions would need to be adjusted to minimise the stiffness of the device, i.e. make the masses larger and beams thinner.

A similar device optimised for use as a three axis accelerometer could easily be fabricated alongside the gyroscope structure using exactly the same processing stages as used for the gyroscope. If this were done then the resulting combined device would be able to measure all six degrees of freedom, three rates of turn and three accelerations. The market for such a sensor is potentially very large.

6.6 Conclusions

A design of resonant gyroscope has been proposed with the ability to measure rate of turn about all three axis. A device of this type could yield very significant price savings over the conventional method of using three separate devices. Simulations of the proposed structure indicate that the device can be designed with dimensions suitable for fabrication with currently available silicon micromachining technology. A brief description of one possible manufacture process has been described. The design and fabrication process would also lend itself to integration with a three axis accelerometer.

6.7 References

---

[1] J. Bernstein, S.Cho, A.T.King, A. Kourepenis, P.Maciel,M.Weinberg A Micromachined Comb-Drive Tuning Fork Rate Gyroscope *Proc. IEEE Micro Electro Mechanical Systems Conference,* Florida, USA, Feb., 1993, P.143

Chapter 7

Conclusions and Suggestions for Future Work

7.1 Summary of the Plate Gyroscope

The plate gyroscope presented in chapter 4 has received the most development and testing. This device has been shown to function as a gyroscope, though the sensitivity is well below that which would be useful in a commercial device. The poor performance of the device can be explained by the mismatch between the primary and secondary modes. This mismatch is thought to be due to asymmetry in the device introduced by errors in the manufacturing process. More accurately manufactured samples have now been fabricated and are currently being evaluated. It is hoped that these will have a significantly improved sensitivity.

The non-linearity of the design, as discussed in chapter 4 and in appendix A, is potentially a serious problem as it causes a splitting of the primary and secondary modes. In addition the distortion in the shape of the resonance peak caused by the non-linearity is also unwanted. This distortion may effect the stability of the signal coming from the device.

Nevertheless the device has been shown to work using a relatively crude fabrication process. This is very encouraging and would indicate that with further improvements to both the fabrication and the sensing electronics the device may be developed into a viable low cost sensor.

7.1.1 Suggestions for Future Work on the Plate Gyroscope

There is still a great deal of work to be done before this device could be manufactured commercially. It would be desirable to change the fabrication process to one in which the silicon and glass substrates were anodically bonded prior to the anisotropic etching process. This would improve the mechanical properties of the device as the membrane would have a more rigid support structure leading to a higher Q. The bonding process would also avoid the need to handle the silicon membrane after etching, at which stage the membranes are extremely delicate and prone to fracture.

It is difficult to see how to address the issue of the non-linearity in the response of the device as this is inherent in resonant membranes. However, it may be possible to reduce the non-linearity by making the membrane both corrugated and much thicker, in an attempt to make the bending stiffness of the membrane dominate over the in-plane tensile forces.

7.2 Summary of the Bow-Tie design

The bow tie design is at a less advanced stage. Before a great deal of additional work is invested in this design it is necessary that the existing samples be tested to ensure that they are indeed resonating as expected and with reasonable amplitudes. The fabricated test structure has been made with dimensions suited to the relatively crude lithographic techniques available in the Durham facilities. This has meant that quite thick beams were employed. Reducing the thickness of these beams and correspondingly increasing the depth of the V groove on each of the wings will result in a more sensitive device. Employing a multi turn coil arrangement on the drive beams is also a logical progression of the design as this will reduce the drive current required by the device.

7.2.1 Suggestions for Future Work on The Bow-Tie design

Although the finite element analysis of the structure indicates that the fabricated device will have matched modes, these dimensions can realistically only be seen as a good starting point. In reality errors in both the FEA and the fabrication process will almost certainly cause a mismatch in the modes of the final structure. Achieving a real device with matched primary and secondary frequencies will therefore require the fabrication of a number of trial devices with differing dimensions.

This design, despite its complex mechanical structure, is in fact by far the simplest of the two devices. The fabrication process should be easily integrated with a conventional IC process, allowing the sensing electronics to be manufactured on the same wafer. The ease of fabrication and compatibility with circuit integration may well offer some significant commercial advantages over the plate gyroscope. Fabricating the device with integrated electronics would be a logical future step.

7.3 Summary and Suggestions for the Three Axis Design

The design proposed in chapter 6 is by far the most advanced of the three devices. The ability to sense rotational motion about all three orthogonal axes gives this design considerable advantages over both previously discussed devices, and all known commercial products. The fabrication process involved in making the device is not significantly more complex than that associated for the design in chapter 4: however the resulting device would be able to perform the tasks of three membrane devices. If the additional packaging processes needed to arrange three single axis devices in an orthogonal orientation were taken into account the fabrication of this structure may be even more simple.

As with the design of the Bow-tie structure the dimensions proposed in chapter 6 will only be a starting point in the development of a working device. The development of the final structure will be considerably more involved than that needed for the previous designs due to the need to match three independent modes.

Chapter 6 also suggests that this device could easily be integrated with a 3-axis accelerometer. From a commercial point of view a single chip that was able to measure all six degrees of freedom would be extremely valuable: it is difficult to imagine single axis devices prevailing over such a design.

7.4 Alternative Excitation Methods

During the early part of the project a number of different activation/detection methods were considered. Capacitive and Lorentz drive were eventually used for their simplicity of manufacture. An alternative activation method that is widely used in micromachining is the piezoelectric drive. Piezoelectric drive could be incorporated into either the membrane or the bow-tie design with the advantages of being able to remove the need for an additional wafer or the permanent magnets. Hence developing a piezoelectric activation method may be a worthwhile exercise.

An alternative to using the piezoelectric effect is the electrostrictive effect. This effect differs from the piezoelectric effect in that the shape change of the material is independent of the sign of the applied electric field. The result of this is that under the influence of an applied sinusoidal signal the material will increase or decrease in length on each half of the sine curve, the corresponding shape change being a rectified sine wave. The largest Fourier component of a rectified sine wave of frequency *f* is the *2f* component. Thus with an applied signal of frequency *f* it should be possible to excite a resonance of frequency *2f* using an electrostrictive material. In addition the electrostrictive material does not require the poling needed by the piezoelectric process. The magnitude of the electrostrictive phenomena in commercially available materials is comparable to the magnitude of the piezoelectric effect in some of the best PZT ceramics[1].

One of the recurring problems on resonant gyroscopes is the coupling of the drive signal into the sense signal by electrical interference. In a well designed gyroscope the drive signal will have the same resonant frequency as the sense signal and it is therefore difficult to distinguish the real sense signal from an erroneous signal induced by the primary drive. If the above method of using an electrostrictive material were used then it may be possible to have a primary drive signal at half the frequency of the primary resonance and associated secondary sense signal. This then would offer the potential of removing any component of the drive signal which happened to appear on the sense signal with a high pass filter.

---

[1] Morgan Matroc ltd. Product data sheet on ESC 1 Electrostrictive Ceramic 1994.

Appendix A

A Simplified model of the plate gyroscope

A much simplified model of the plate gyroscope is considered. This model is used to demonstrate the source of the non-linear respone which was observed in the resonance curves of the membrane gyroscope (section 4.8).

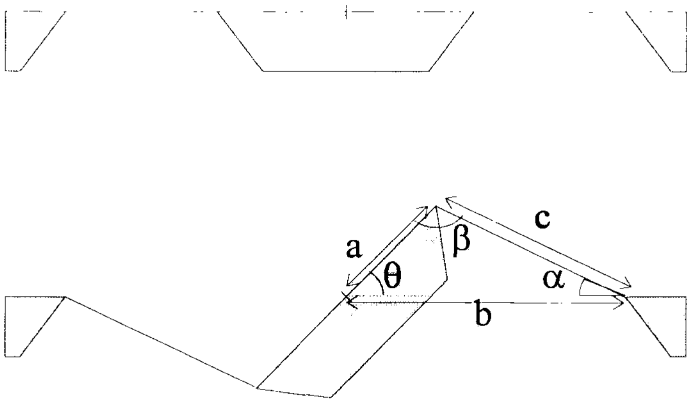

Figure A.1

Consider a two dimensional cross section through the gyroscope structure as shown in figure A.1 and neglecting any bending stiffness in the membrane. It is possible to calculate the restoring torque exerted on the central pyramid in terms of its angle of displacement.

The lengths a and b are constants. For the device described in chapter 4 a=0.1mm and b=1.5mm. It is useful later to have a expressed as a fraction of b, hence;

$b := 1.5$ $\qquad \theta := -90, -89..90$ $\qquad \mathrm{cosd}(v) := \cos(v\cdot\mathrm{deg})$

$\mathrm{acosd}(v) := \mathrm{acos}(v)\cdot\mathrm{deg}$

$a(r) := b\cdot r$

All of the variables in figure A.1 are now expressed in terms of a,b & q.

$$c(\theta,r) := \sqrt{\left(a(r)^2 + b^2\right) - 2\cdot a(r)\cdot b\cdot \mathrm{cosd}(\theta)}$$

$$\alpha(\theta,r) := \mathrm{acosd}\left[\frac{\left(b^2 + c(\theta,r)^2\right) - a(r)^2}{2\cdot b\cdot c(\theta,r)}\right]$$

$$\beta(\theta,r) := 180 - (\theta + \alpha(\theta,r))$$

Assuming that the material has linear elastic properies, then the tension T in the membrane will be related to the change in length of the membrane and to the amount of pre-tension in the membrane S. For convenience S is defined in terms of K, the spring constant of the membrane.

$K = 1 \qquad S(p) = K \cdot p$

$$T(\theta,r,p) = S(p) + K \cdot \left(\frac{c(\theta,r) - c(0,r)}{c(0,r)} \right)$$

From T it is possible to calculate the restoring couple acting on the pyramid. This is done by resolving T perpendicular to the face of the pyramid and multipying by 'a'. This situation is shown in figure A.2.

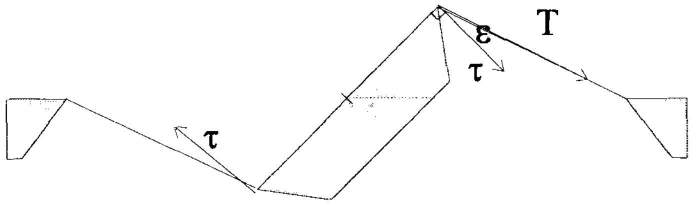

Fig A.2 Showing the restoring couple acting on the pyramid

$\varepsilon(\theta,r) = \beta(\theta,r) - 90$

$\tau(\theta,r,p) = T(\theta,r,p) \cdot \mathrm{cosd}(\varepsilon(\theta,r))$

The total couple is then given by:

$$\Gamma(\theta,r,p) = \frac{2 \cdot a(r) \cdot \tau(\theta,r,p)}{2 \cdot a(r) \cdot \tau(90,r,p)}$$

Setting r = 2/3 as is the situation for the gyroscope described in chapter 4 and setting the pre tension to zero the above function may be plotted

$r = \frac{2}{3} \qquad p =$

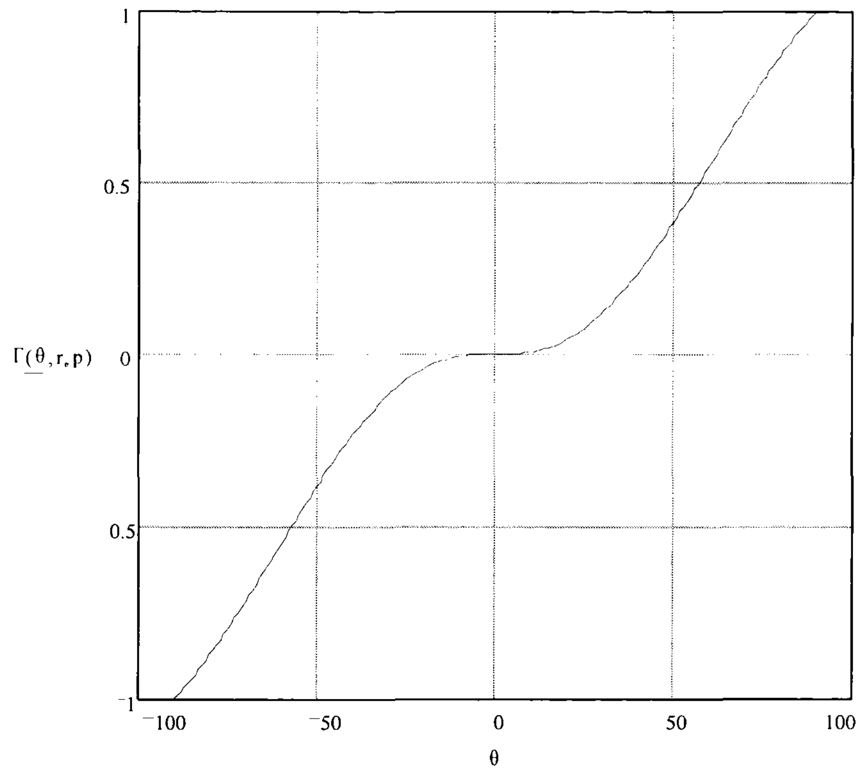

Figure A.3 Showing the non-linear restoring couple acting on the pyramid.

The form of this function is a classic non-linear restoring force. Figure A.3 shows the restoring force over the range -90 to + 90 degrees. However with the gyroscope the resonance is over a much smaller range. It is interesting to note that the shape of the function is still highly non-linear even over this small range, figure A4.

$\theta := -1,\ 0.99..0.99 \qquad \Gamma(\theta,r,p) := \dfrac{2\cdot a(r)\cdot\tau(\theta,r,p)}{2\cdot a(r)\cdot\tau(1,r,p)}$

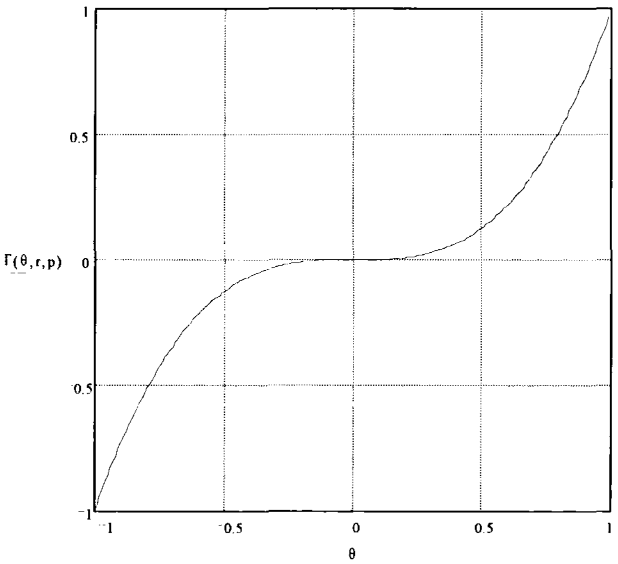

Figure A.4 showing the non-linearity of the restoring force over the range of -1 to 1 degree of rotation.

Another interesting plot is to look at the non-linearity of the system as a function of 'r', I.e. to note what happens as the size of the central pyramid is changed. Fig A5 shows the restoring function for 4 different values of r.

$r = 0.2, 0.25..0.75$ $\quad$ $\Gamma(\theta,r,p) = \dfrac{2\cdot a(r)\cdot\tau(\theta,r,p)}{2\cdot a(0.75)\cdot\tau(1,r,p)}$

$$\Gamma(\theta,r,p) \quad \frac{2\cdot a(r)\cdot\tau(\theta,r,p)}{2\cdot a(0.75)\cdot\tau(1,r,p)}$$

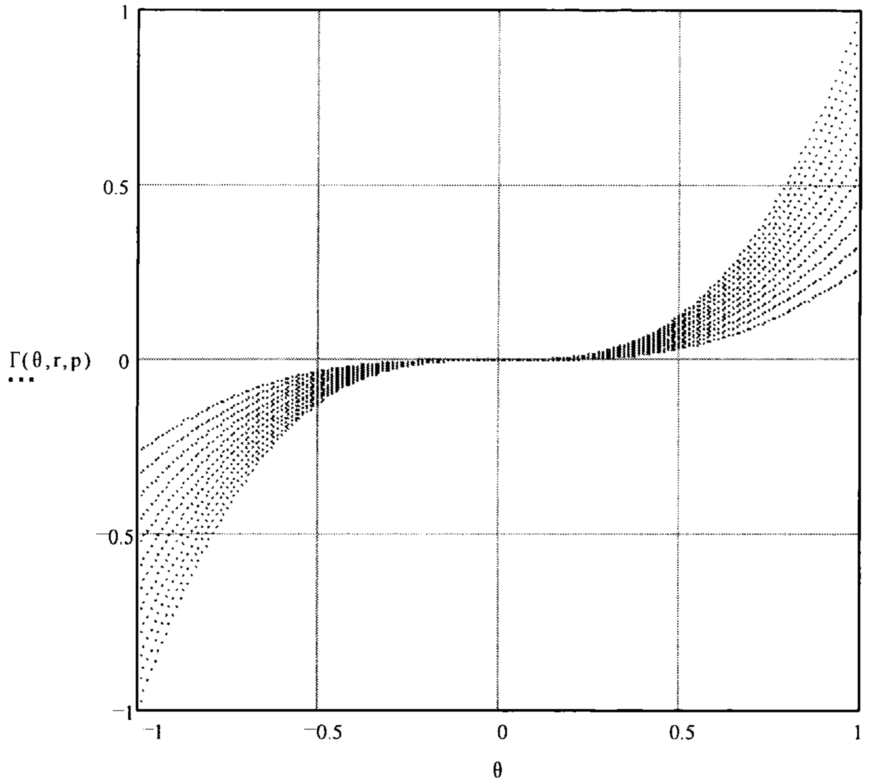

Figure A5 The non-linearity of the structure as a function of the pyramid size. The most none linear lines correspond to the larger pyramids.

Setting r back to 2/3 and considering the effect of pre-tension is also informative

$r = \dfrac{2}{3}$ $\quad$ $p = 0.00001, 0.0002..0.0010$ $\quad$ $\Gamma(\theta,r,p) = \dfrac{2\cdot a(r)\cdot\tau(\theta,r,p)}{2\cdot a(r)\cdot\tau(1,r,0.001)}$

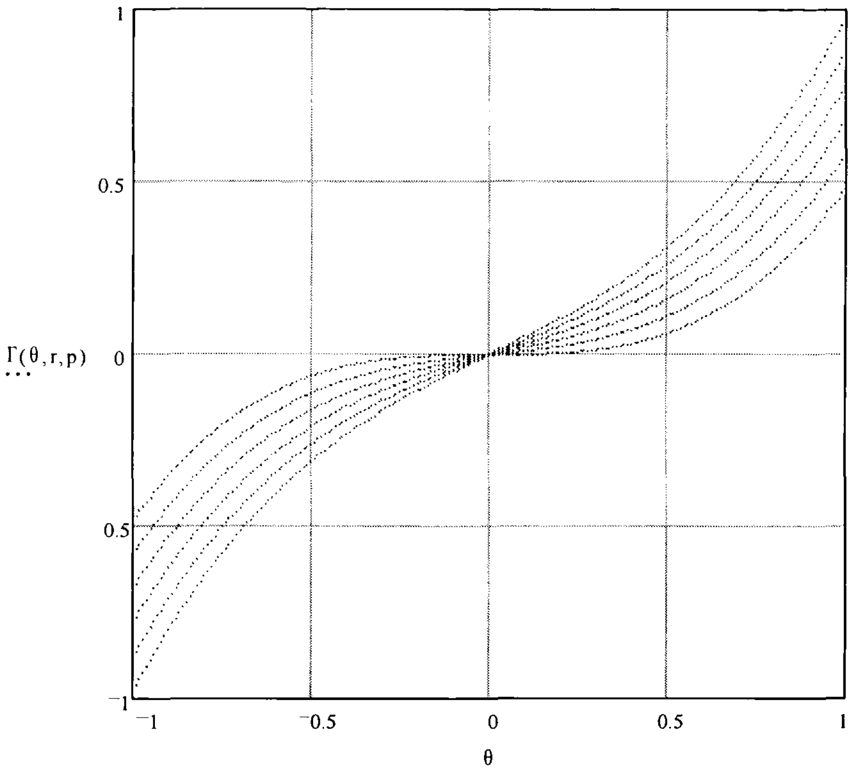

Figure A6 The effect of increasing the pre-tension in the membrane.

The increased pre-tension has the effect of making the curve more linear, at least for small vibrations. This is because at small vibrations the extra tension created in the membrane by stretching is dominated by the tension that is already there.